Ultrasound and Microwave Tomography Reconstruction Algorithms: Enhancement and New Approaches

by

Pedram Mojabi

A Thesis submitted to the Faculty of Graduate Studies of

The University of Manitoba

in partial fulfilment of the requirements of the degree of

DOCTOR OF PHILOSOPHY

Department of Electrical and Computer Engineering
University of Manitoba
Winnipeg, Manitoba, Canada

Abstract

New approaches to enhance ultrasound tomography (UT) and microwave tomography (MWT) as well as their combination are investigated. These nondestructive imaging techniques create five quantitative images of different properties of an object of interest (OI): (i) compressibility, (ii) acoustic attenuation, (iii) density, (iv) real part of the complex permittivity (related to the dielectric constant), and (v) the imaginary part of the complex permittivity (related to the conductivity and dielectric loss). These images are reconstructed by solving nonlinear ultrasound and electromagnetic inverse scattering problems, or using ray-based methods.

The overall objective of this research is to use UT and MWT so as to (1) enhance the achievable image accuracy related to the detection and identification of various tissues, and (2) to provide quantitative levels of confidence in those reconstruction. This is performed by combining the above five quantitative images into one image that is referred to as the composite tissue type image. For example, for the case of breast imaging, this provides an image of the breast whose pixels correspond to different tissue types (namely, fatty, fibroglandular, tumor, skin, or cyst) within the breast. In addition, each pixel of the image is associated with a probability value that determines the level of confidence regarding its corresponding reconstructed tissue type. This approach is important and novel since existing individual UT and MWT algorithms do not provide any indication regarding the level of confidence in their reconstruction. Furthermore, the approach is "user friendly" in the sense that one viewing the image for diagnosis of disease (e.g., a physician) does not have to interpret ultrasonic or electromagnetic properties in order to make a diagnosis.

Results of creating tissue-type images from various property images are shown for MRI-based numerical phantoms as well as an experimental tissue mimicking phantom and a human forearm. To perform the initial UT property reconstructions a new balancing method is introduced into the Born Iterative Method (BIM) to deal with the wide range of ultrasonic property values of breast tissues. The possibility of including anatomical and epidemiological information to enhance the reconstruction for the UT/MWT breast imaging application are also investigated.

Contributions

The research contributions shown in this Ph.D. thesis are reported as three peer-reviewed journal papers and one peer-reviewed conference paper (in Appendix B). The Introduction, Future Work and Appendix A Chapters are newly written, and a Background Chapter, which is a paper that was published based on the candidate's MSc research[*], is provided as background material. In all of these published works, the first author is the candidate, and the other author is the candidate's advisor with the supervisory role.

It should be noted that other candidate's papers in which the candidate is not the first author have not been included in this thesis, but are listed below. The candidate's research has been published in prestigious journals, namely the Journal of the Acoustical Society of America (JASA), the IEEE Journal[†] on Multiscale and Multiphysics Computational Techniques, and the IEEE Transactions on Computational Imaging. The full list of the candidate's publications are listed on the next page.

From the list of the publications presented below, the following articles have been included in this thesis, either in the form of a Chapter or an Appendix. These are [J1], [J2], [J3], [J4], and [C3].

---

[*] The writing of this paper and the answering of the reviewers's comments were done during the candidate's Ph.D. studies; however, the main body of this paper is based on his M.Sc. work

[†] IEEE Copyright Notice: In reference to IEEE copyrighted material which is used with permission in this thesis, the IEEE does not endorse any of University of Manitoba's products or services. Internal or personal use of this material is permitted. If interested in reprinting/republishing IEEE copyrighted material for advertising or promotional purposes or for creating new collective works for resale or redistribution, please go to `http://www.ieee.org/publications_standards/publications/rights/rights_link.html` to learn how to obtain a License from RightsLink.

- **Articles Published in Refereed Journals**

[J1]. **Pedram Mojabi** and Joe LoVetri, “Experimental Evaluation of Composite Tissue-Type Ultrasound and Microwave Imaging,” Accepted in *IEEE Journal on Multiscale and Multiphysics Computational Techniques*, 2019.

[J2]. **Pedram Mojabi** and Joe LoVetri, “Evaluation of Balanced Ultrasound Breast Imaging Under Three Density Assumptions,” *IEEE Transactions on Computational Imaging*, vol. 3, no 4, pp. 864-875, 2017.

[J3]. **Pedram Mojabi** and Joe LoVetri, “Composite Tissue-Type and Probability Image for Ultrasound and Microwave Tomography,” *IEEE Journal on Multiscale and Multiphysics Computational Techniques*, vol. 1, pp. 26-35, 2016.

[J4]. **Pedram Mojabi** and Joe LoVetri, “Ultrasound Tomography for Simultaneous Reconstruction of Acoustic Density, Attenuation, and Compressibility Profiles,” *Journal of Acoustical Society of America*, vol. 137, no. 4, pp. 1813-1825, 2015.

[J5]. N. Abdollahi, D. Kurrant, **Pedram Mojabi**, M. Omer, E. Fear and J. LoVetri, “Incorporation of Ultrasonic Prior Information for Improving Quantitative Microwave Imaging of Breast,” Accepted in *IEEE Journal on Multiscale and Multiphysics Computational Techniques*, 2019.

[J6]. M. Omer, **Pedram Mojabi**, D. Kurrant, J. LoVetri and E. Fear “Proof-of-Concept of the Incorporation of Ultrasound-Derived Structural Information into Microwave Radar Imaging,” *IEEE Journal on Multiscale and Multiphysics Computational Techniques*, vol. 3, pp. 129-139, 2018.

- **Conference Papers and Abstracts**

[C1]. **Pedram Mojabi**, Nasim Abdollahi, Muhammad Omer, Douglas Kurrant, Ian Jeffrey, Elise Fear and Joe LoVetri , “Tissue-Type Imaging for Ultrasound-Prior Microwave Inversion,” *18th International Symposium on Antenna Technology and Applied Electromagnetics (ANTEM)*, Waterloo, Canada, Aug 2018.

[C2]. Muhammad Omer, **Pedram Mojabi**, Nasim Abdollahi, Douglas Kurrant, Ian Jeffrey, Joe LoVetri and Elise Fear, “Breast Imaging with Multiphysics Prior for Improved Tumour Detection and Localization,” *18th International Symposium on Antenna Technology and Applied Electromagnetics (ANTEM)*, Waterloo, Canada, Aug 2018.

[C3]. **Pedram Mojabi** and Joe LoVetri, “On the potential use of anatomical and epidemiological information to enhance microwave and ultrasound breast imaging,” *2nd URSI AT-RASC,* Gran Canaria, Spain, May 2018. (Invited)

[C4]. Joe LoVetri, Elise Fear, Ian Jeffrey, Muhammad Omer, **Pedram Mojabi**, Douglas Kurrant, Nasim Abdollahi, “A Multimodal Ultrasound-Microwave Quantitative Imaging Technique for Breast Cancer,” *EuCap*, London, UK, Aug 2018.

[C5]. Muhammad Omer, **Pedram Mojabi**, Douglas Kurrant, Anastasia Baran, Joe LoVetri and Elise Fear, “Strategies for Integrating Ultrasound and Microwave Data for Improved Breast Imaging,” *URSI*, Montreal, Canada, Aug 2017.

[C6]. **Pedram Mojabi** and Joe LoVetri, “Development of an ultrasound tomography system: Preliminary results,” *5th Joint Meeting of the Acoustical*

Society of America and the Acoustical Society of Japan, Honolulu, Hawaii, Dec 2016.

[C7]. P. Mojabi, N. Firoozy, N. Bayat, T. Brown, C. Narendra, **Pedram Mojabi**, C. Niu, T. Tiede, T. Neusitzer, X. Li, I. Jeffrey, J. LoVetri, D. Barber, "Electromagnetic Inversion for Biomedical Imaging, Antenna Characterization, and Sea Ice Remote Sensing Applications," *URSI AP-RASC 2016*, Seoul, Korea, Aug 2016. (Invited)

[C8]. **Pedram Mojabi** and Joe LoVetri, "Tissue-Type Imaging Using Ultrasound Tomography," *IEEE MTT-S International Conference on Numerical Electromagnetic and Multiphysics Modeling and Optimization for RF, microwave and Terahertz Applications (NEMO)*, Ottawa, Canada, Aug 2015.

[C9]. **Pedram Mojabi** and Joe LoVetri, "Microwave and Ultrasound Imaging for Biomedical Tissue Identification," *International Symposium on Antennas and Propagation (APS) and URSI*, Memphis, USA, July 2014.

[C10]. **Pedram Mojabi** and Joe LoVetri, "A Fast and Efficient MoM Forward Solver for Ultrasound Tomography of Inhomogeneous Compressibility and Density Profiles," *International Symposium on Antennas and Propagation (APS) and URSI*, Orlando, USA, July 2013.

[C11]. **Pedram Mojabi** and Joe LoVetri, "Simultaneous Reconstruction of Compressibility and Density Profiles in Multiple Frequency Acoustic Inverse Scattering," *International Symposium on Antennas and Propagation (APS) and URSI*, Orlando, USA, July 2013.

Acknowledgments

I would like to thank my advisor, Prof. Joe LoVetri, for his guidance and support during my Ph.D. studies. I would also like to thank my friends at the Electromagnetic Imaging Laboratory at the University of Manitoba.

I would like to express my appreciation for the time taken by my examining committee members: Prof. Greg Bridges and Prof. Daniel Rickey from the University of Manitoba, and my External Examiner, Prof. Mahta Moghaddam, from the University of Southern California. The financial support of NSERC and the University of Manitoba Graduate Fellowship (UMGF) is also appreciated.

I would like to thank my family in Canada, Puyan, Shiva, and Hamid, Jelveh for their kindness and support. Last but not least, my biggest thank-you goes to my parents, Amir and Parvin, and my grandmother.

Table of Contents

List of Tables

List of Figures

1

Introduction

Ultrasound tomography (UT) and microwave tomography (MWT) are nondestructive imaging modalities which can be used for different applications such as biomedical imaging and industrial non-destructive testing [2–19]. The ultrasonic properties of the object of interest (OI) to be determined in UT are compressibility, attenuation, density and sound speed and the dielectric properties of the OI to be determined in MWT are the real and imaginary parts of the complex permittivity profile [2].

In UT and MWT, the OI is surrounded by some transceivers as shown in Fig 2.1. When the first transceiver works as a transmitter, the other transceivers operate as receivers. This procedure continues until all the transceivers are used as transmitters [20]. The collected data can be used by different methods to create qualitative and/or quantitative images. For example, some of the main methods are: 1) ray-based methods [5,21–25] , 2) diffraction tomography [26,27], and 3) full-wave inverse scattering algorithms [4,20,28–36].

The reconstruction algorithm is chosen based on different criteria. The form of data (number of available data) and computational resources are two important parameters for choosing the reconstruction algorithms. Ray-based methods are computationally efficient, and in contrast to full-wave inverse scattering algorithms, do not suffer from not converging to a proper solution due to being trapped in a local minimum [5]. In addition, full-wave inverse scattering algorithms often require many data points and are computationally expensive. It should be noted that full-wave inversion methods use a more accurate wave model than ray-based and diffraction tomography methods. Thus, multiple scattering events are taken into account in full-wave inversion [28]. Therefore, full-wave inversion methods lead to better reconstruction[*] of the ultrasonic and/or dielectric properties of the OI as compared to the ray-based and diffraction tomography methods. In the full-wave inversion algorithms, the UT and MWT problems are mathematically formulated as non-linear inverse scattering problems. Different inversion algorithms such as the Born Iterative Method (BIM) [4, 20, 29, 37], the Distorted Born Iterative Method (DBIM) [30, 34, 38, 39] (or, equivalently, the Gauss-Newton inversion algorithm), and the Contrast Source Inversion (CSI) algorithm [40, 41] can be used to solve this non-linear problem. The full-wave inversion problem is non-linear and ill-posed. To handle the ill-posedness of this problem, different regularization techniques need to be used, such as the standard Tikhonov [32, 42], the L_1-norm Tikhonov [43, 44], multiplicative regularizers [45, 46], the truncated singular value decomposition [47, 48] and the conjugate gradient least squares (CGLS) subspace regularization methods [8, 9, 20, 47].

In this thesis, full-wave inversion algorithms are used to create the ultrasonic and dielectric properties of the OI. The OI of primary interest in this thesis is the human breast with the detection of breast tumours being the primary biomedical application. Numerical MRI-based breast phantoms[†] are used to validate much of the research. We

---

[*] In the context of this thesis, the terms *inversion* and *reconstruction* are used interchangeably. However, we note that the term reconstruction may be considered broader than the term inversion. The inversion is the step in which the measured data is inverted to produce property images. However, the reconstruction may include other steps such as filtering and post processing in addition to the inversion step.

[†] Within the context of this thesis, these numerical breast phantoms are the numerical models that have been derived from magnetic resonance imaging (MRI) scans.

also use some ray-based methods for ultrasound imaging to create both quantitative and qualitative properties of the OI.

Several quantitative property images can be obtained from UT (such as attenuation, compressibility, density and sound speed) and from MWT (real and imaginary parts of complex permittivity). One of the main ideas pursued in this thesis is to create a *single* image that can interpret one or more of the five quantitate images for end users (especially, medical doctors). This approach is more practical since medical doctors not familiar with the properties of different tissues may have a difficult time interpreting the quantitative property images (either individually or together). Inspired by this idea, it was proposed, for the first time by the author, to introduce the concept of creating a composite tissue type image that can integrate the quantitative property images obtained from UT and MWT (including their combination). This new approach is not limited to these two modalities, but can be extended to other modalities as well. As part of this new approach, the probability of assigning a tissue type to each pixel in the final image is also provided. This probability indicated the level of confidence in assigning that particular tissue-type for a given pixel. In this thesis, the reconstructions of the tissue-type along with the probability image for MRI-based phantoms are shown for UT, MWT and their combination. In addition to synthetic data, the experimental reconstruction of tissue-type for a tissue mimicking phantom using UT data and a human forearm using MWT data are also shown. In the following, the contents of each chapter are explained.

In Chapter 2, which is a background chapter based on a paper that resulted from the candidate's MSc research and published in the *Journal of Acoustical Society of America*‡ [20], a fast and efficient forward scattering solver for ultrasound tomography

---

‡The writing of this paper and the answering of the reviewers's comments were done during the candidate's Ph.D. studies; however, the main body of this paper is based on his M.Sc. work [33]

is explained. This is important as having a fast and efficient forward solver is essential in the use of inversion algorithms in ultrasound tomography as (nonlinear) inversion algorithms require repeated calls to a forward solver, which solves the associated wave equation for a given predicted ultrasound profile[§] and a given excitation. This forward solver can handle large and relatively high contrast objects in which all the ultrasonic properties of the OI (*i.e.,* compressibility, attenuation, and density) can vary simultaneously, and the OI's properties can also be inhomogeneous. This forward solver is also equipped with some acceleration features based on marching-on-source, fast Fourier transform (FFT), and the symmetric block Toeplitz matrix with symmetric Toeplitz blocks property of the Green's function matrix to increase efficiency and to only store the first row of the resulting matrix to reduce the memory requirement.

Chapter 3 investigates the use of non-linear inversion algorithms for the breast imaging applications under three scenarios for UT. To have more relevance to the breast imaging application, MRI-based numerical breast phantoms are considered. The Born Iterative method (BIM) is investigated first for all three scenarios. Then the multiplicative regularized Gauss-Newton inversion (GNI) method, originally developed for MWT, is adapted to the ultrasound imaging problem but is only applied to the reconstruction of the compressibility and the attenuation. The use of GNI is investigated because of the availability of a more sophisticated regularization technique. For all these algorithms, a balancing method is introduced; it is shown how this balancing technique can improve the reconstruction accuracy. (The balancing method considered in this chapter for UT was adapted from the balancing method

---

[§] In the context of this thesis, the term profile refers to a (property or contrast) function that can vary with respect to position vector. This is important for inhomogeneous objects since their properties are a function of position. For example, for two dimensional imaging in the xy plane, an attenuation profile will be a function of (x, y), i.e., $\alpha(\boldsymbol{r}) = \alpha(x, y)$.

proposed for MWT [49,50].) In this chapter, the properties to be reconstructed are the inhomogeneous compressibility, density and attenuation of breast tissues. Three scenarios related to the interdependence of the ultrasonic properties are considered in this paper. The first scenario corresponds to the case that all the ultrasonic properties are assumed to be independent and unknown. The assumption of a linear relation between the contrast of compressibility and the contrast of inverse density [4] is used in the second scenario and finally the variation of density is neglected completely in the last scenario. The balancing method substantially improves the reconstruction of all the contrast profiles especially for the case that the contrast profiles for the breast imaging application. As will be seen in this Chapter, the contrast corresponding to the attenuation in the breast imaging application is much smaller than the other contrast profiles and the image corresponding to this contrast is important because tumor can be better identified using this image [51–53]. However, as will be seen, we cannot obtain a good reconstruction for this contrast without applying the balancing method. This is due to the fact that most optimization-based inversion algorithms favour the reconstruction of unknowns with a larger magnitude. The balanced BIM is used as an inversion algorithm for all the scenarios. Reconstructions of the contrast profiles as performed for MRI-based numerical phantoms. We have also adapted the MR-GNI method for the last scenario of our ultrasound tomography problem. This inversion algorithm was originally developed for microwave tomography [50]. The regularization used in MR-GNI is more advanced compared to the regularization used in the BIM. Thus, it leads to better reconstruction of the contrast profiles. However, the MR-GNI is computationally more expensive in comparison with the BIM algorithm. In any case, we see that the balancing method is also required for this inversion algorithm. This chapter is based on the author's journal paper published in the *IEEE*

Transactions on Computational Imaging [28].

In Chapter 4, the concept of creating a composite tissue type image (cTTI) along with an associated composite probability image is introduced for the first time for UT, MWT, and their combination. This new imaging technique uses Bayes' Theorem to make a decision on the most probable tissue type occupying a pixel given the reconstructed properties at the same pixel. The proposed concept not only integrates the information available from different reconstructed quantitative property images (obtained from different imaging modalities), but also provides an indication for the level of confidence regarding the reconstructed tissue type. This tissue-type image represents the most probable tissue type at each pixel. This work has the potential to significantly impact the area of biomedical imaging as the proposed method not only facilitates the diagnosis process by the physicians, but also provides indications for the level of confidence for each image pixel, which is very crucial in some sensitive situations such as making the decision for breast mastectomy. In addition, the proposed method provides a mechanism to perform multi-physics imaging within an inverse scattering approach. The reconstructions of the composite tissue type image along with the probability image for the MRI-based phantoms based on the quantitative reconstructions of the ultrasonic properties and dielectric properties of the breast phantoms as well as their combination are shown in this chapter. This chapter is based on the author's journal paper published in the *IEEE Journal on Multiscale and Multiphysics Computational Techniques* [2].

In Chapter 5, the concept of a composite tissue-type image along with the probability image is experimentally evaluated based on the data provided by two different systems: an ultrasound system as well as a microwave imaging system. The experimental ultrasound data set for a tissue-mimicking phantom is provided by the

Multimodal Ultrasound Breast Imaging (MUBI) system developed by the Ultrasound Systems and Technology Group at the Spanish National Research Council (USTG-CSIC) and the Group of Nuclear Physics at the Complutense University of Madrid (GFN-UCM) [54–56]. The experimental Microwave data set for a human forearm is provided by an in-house system at the University of Manitoba. The enhancement of the cTTI algorithm based on differences in the accuracy of reconstructing one property compared to another property is also shown using the experimental ultrasound data. The cTTI algorithm is also improved based on changing the prior probabilities. In the cTTI algorithm, we should define the prior probabilities of each tissue-type occupying each pixel; in Chapter 4 [2] these probability values are chosen to be equal. However, in this work, we show that the change of the prior probabilities can lead to improved reconstruction of the cTTI. Some prior knowledge about the object of interest can be used to provide improved prior probabilities (for example anatomical and epidemiological information of the OI as explained in Appendix B). As will be seen, two sets of improved prior probabilities based on the estimated skin and fat regions for the numerical MRI-based phantom are considered. The results of this improvement are shown with the simulated data using combined ultrasound and microwave tomography property images. The ray-based methods are used for the reconstruction of the ultrasonic properties (sound speed and attenuation) of the OI for the experimental ultrasound data. These ray-based algorithms are described in this chapter. Calculating the time-of-arrival (TOA) of the signal is critical in the time-domain ray-based algorithms. In this chapter, the modified energy ratio (MER) [57, 58] is used to calculate the TOA of the experimental ultrasound measured signal. The MR-GNI method is used for reconstruction of electromagnetic properties using experimental microwave data and simulated ultrasound and microwave data for the MRI-based breast phantom. This chapter is based on the author's journal paper accepted in the *IEEE Journal on Multiscale and Multiphysics Computational Techniques* [59].

This thesis also consists of two appendices, which also include the author's work during his PhD studies. However, due to the fact that this thesis is presented in the sandwich style format with the author's peer-reviewed journal papers as its chapters, these two works are included as appendices.

Appendix A presents the experimental reconstructions of the ultrasonic properties (sound speed and attenuation) of an OI using an in-house ultrasound system at the University of Manitoba. This system has a small number of transducers situated in a circular ring. Due to the limited number of transducers in our UT system, we restrict the testing to simple homogenous objects. The preprocessing of ultrasound raw data and also the calculation of the time-of-arrival of the signal using Akaike information criterion (AIC) [60, 61] are also explained.

Appendix B presents the potential use of anatomical and epidemiological information to enhance the cTTI reconstruction for the breast imaging application for both UT and MWT, and their combination. A general procedure for introducing this information is first considered. It is shown how anatomical prior information can be based on the expected position of different tissue-types in the breast. For example, the skin position is in the outer region of the breast and tumors mainly emerge within the radiodense tissue (specifically radiodense fibroglandular tissue) [62]. A discussion of how epidemiological prior information consisting of where in the breast certain pixels belong and the age of the patient, can be incorporated into the cTTI procedure. For example, the chance of having tumor varies in different breast quadrants [63]. This information can be taken into account in the future to improve the cTTI reconstruction. This chapter is based on the author's International Union of Radio Science

(URSI) AT-RASC conference paper [64].

2

Background*: Ultrasound Tomography for Simultaneous Reconstruction of Acoustic Density, Attenuation, and Compressibility Profiles

2.1 abstract

A fast and efficient forward scattering solver is developed for use in ultrasound tomography. The solver is formulated so as to enable the calculation of scattering from large and high-contrast objects with inhomogeneous physical properties that vary simultaneously in acoustic attenuation, compressibility, and density. It is based on the method of moments in conjunction with a novel implementation of the conjugate gradient algorithm which requires the use of the adjoints of the scattering operators. The solver takes advantage of the symmetric block Toeplitz matrix with symmetric Toepltiz blocks property of the Green's function matrix to increase efficiency and only stores the first row of this matrix to reduce memory requirements. This row is then used for the matrix-vector multiplication using the fast Fourier transform

---

*Reprinted with permission from Pedram Mojabi and Joe LoVetri, "Ultrasound Tomography for Simultaneous Reconstruction of Acoustic Density, Attenuation, and Compressibility Profiles," *Journal of Acoustical Society of America*, vol. 137, no. 4, pp. 1813-1825, 2015. © 2015, Acoustic Society of America.

technique, thus, resulting in the computational complexity $O(n \log n)$. The marching-on-source technique is also used to provide a good initial guess which allows the conjugate gradient technique to converge faster than initializing with an arbitrary guess. This feature is important in tomographic inversion algorithms which require that the object to be imaged be interrogated via several incident fields. Forward scattering and inversion examples, based on the Conjugate Gradient Least Squares regularized Born Iterative method, are shown, in two-dimensions, for objects varying in all three physical properties.

2.2 INTRODUCTION

Ultrasound tomography (UT) can be mathematically formulated as an inverse scattering problem [4, 29, 33, 34, 65, 66]. In this inverse scattering problem, the goal is to find the shape, location, and some quantitative ultrasonic properties of the object of interest (OI). Images of the acoustic attenuation, compressibility, and density of materials can provide substantial information regarding the internal structure and composition of the OI. Quantitative reconstructions of these properties can be found using various nonlinear inversion algorithms. Such inversion algorithms iteratively minimizes the discrepancy between measurements of scattered pressure and those simulated from predicted profiles. Thus, one important component of these inversion algorithms is the forward solver which calculates the corresponding simulated data due to a predicted profile. The main focus of this paper is the development of an appropriate forward solver for this purpose, which is then used in the Born Iterative Technique (BIM) [4, 29, 37, 67] to invert scattered pressure data and create images of three contrast parameters related to the acoustic attenuation, compressibility, and density of the OI.

In UT, the object of interest is surrounded by several transducers as shown in Fig 2.1, and is located within a known background medium [33, 68, 69]. Each of these transducers can work either as a transmitter or receiver. When one transducer operates as a transmitter, the others work as receivers. This procedure continues until all the transducers are utilized as transmitters. The pressure data at each transducer is collected in two different scenarios. The pressure data collected in the absence of the OI is called the incident pressure, and the pressure data collected in the presence of the OI is called the total pressure. The scattered pressure is then defined as the numerical difference between the total and incident pressure and serves as the measurement data that is inverted by the inversion algorithm to create one or more property images.

Some desirable features of the forward scattering solver used within the inversion algorithm are: (1) it should be able to handle inhomogeneous compressibility, density and attenuation profiles, (2) it should handle large objects with respect to the wavelength of operation, and (3) it must be computationally and memory efficient. The first requirement is desirable so as to broaden the range of materials that can be imaged within the OI. For example, human tissue at ultrasound frequencies typically vary in all three of these properties. To the authors' knowledge, most of the forward solvers developed to-date for ultrasound imaging assume that the density profile of the OI is constant; this is true, e.g., in the biconjugate gradient (BCG) imaging technique presented in [70], in the formulation of the inverse operator incorporated in the DBIM as developed in [71], the parabolic approximation in [72], the multilevel fast multipole algorithm (MLFMA) incorporated in the DBIM as developed in [30], as well as in the time-domain and frequency-domain eigenfunction methods described in [73, 74]. It is well known that the density profile in many biomedical applications such as breast imaging is not constant [4, 34, 75, 76]. Using inversion algorithms that assume a constant density profile can result in a large amount of modelling error, defined as the discrepancy between the numerical model used in the inversion algorithm and the actual measurement system, producing erroneous reconstructions. Although inversion algorithms have been reported wherein the forward solvers do not assume a constant density profile; e.g., the T-matrix and DF-DBIM approach as presented in [34,35], the FMM method as used in [31], and the time-domain forward solver used in [29], none of these simultaneously and quantitatively invert all three properties that are considered herein. The only work the authors are aware of where three acoustic parameters are simultaneously inverted is the work presented in [77] wherein speed of sound, density, and absorption are simultaneously inverted. It should be noted that treating these three profiles as independent unknowns have the potential to result in more accurate reconstruction accuracy in different application areas ranging from biomedical to non-destructive applications. On the other hand, this may result in the increase of the number of unknowns to be reconstructed. Therefore, more ultrasound scattering data points are then needed to be collected and used for the inversion.

The second desirable feature is due to the fact that for some biomedical UT applications, e.g., breast cancer imaging, the size of the OI is very large with respect to the wavelength of operation. This relates to the third important feature, computational efficiency, because it is typical for nonlinear inversion algorithms to call the forward solver many times for accurate quantitative reconstructions. For example, if we assume that the number of ultrasonic transducers in a UT system is 30, collecting scattered field data at 10 different frequencies, and that the inversion algorithm converges after 10 iterations, then the forward solver will be called 3000 times. This simple example demonstrates the need for having a fast and efficient forward solver.

To handle this computational burden, a forward solver based on the Neumann series was recently proposed in [4]. This forward solver assumes that there exists a fixed linear relationship between the contrast of compressibility and contrast of density throughout the OI. Such an assumption is not valid for a broad range of materials and thereby limits the use of such imaging algorithms.

Finally, it is beneficial to utilize a forward solver that can handle OIs with large contrast. Sometimes the use of a proper background immersion medium, such as a matching fluid, can help reduce the contrast of the OI. When this is not feasible it is important that the forward solver be able to handle large contrast values. This is not true of the forward solver proposed in [4], which is based on the Neumann series.

In this paper, a Method of Moments (MoM) [78–81] forward solver, in conjunction with the Conjugate Gradient method [82], is used to handle the scattering from inhomogeneous objects which simultaneously vary in compressibility, attenuation, and density. This forward solver can also deal with large high contrast objects [33, 66]. To handle the computational burden associated with the UT problem, this solver is equipped with some accelerating and memory reduction features. It makes use of the block Toeplitz matrix properties [83, 84] of the resulting Green's function matrices to significantly reduce the memory requirements. Secondly, it uses the Fast Fourier Transform (FFT) method to accelerate the matrix-vector multiplications in the Conjugate Gradient (CG) method. Finally, the so-called marching-on-source technique is used to find a good initial guess for the CG method; thus, accelerating its convergence. To use the CG method with the integral equation formulation described herein, the adjoint of the integral operators for the inhomogeneous compressibility, attenuation and density profiles are required. These adjoint operators are provided in the continuous domain, that is, before discretization using the Method of Moments.

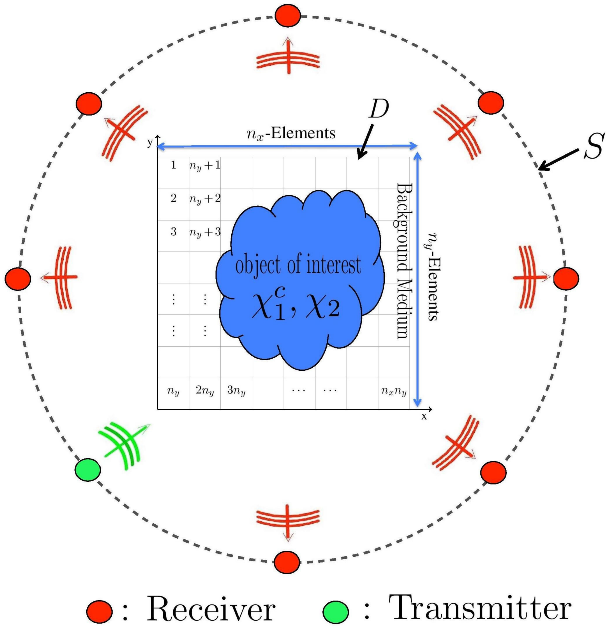

Figure 2.1: UT setup in which the OI is enclosed by an array of ultrasound transmitters/receivers. The discretization scheme employed in this work is also shown.

The structure of this paper is as follows. In Section 2.3, we provide the mathematical formulation of the UT problem for objects having inhomogeneous complex-valued compressibility, which takes into account the attenuation and compressibility, as well as inhomogeneous density profiles. We then describe the MoM operators required in the formulation of the forward scattering problem in Section 2.4, providing details on the adjoints of these operators required in the CG solution. The accelerating features of the MoM-CG forward solver are described in Section 2.5. In Section 2.6 we outline the Born Iterative Method (BIM) in conjunction with Conjugate Gradient Least Squares (CGLS) regularization which is then used to invert some 2D data obtained synthetically. Although only 2D data is considered herein, the basic method is easily extended to 3D problems. Section 2.7 presents some numerical forward and inverse scattering results to demonstrate the effectiveness and efficiency of the forward solver and simultaneous reconstruction of all the contrast profiles. Discussion and conclusions are presented in Section 2.8 and 2.9.

2.3 Problem Formulation

The acoustic wave equation can be written as [31,33,36,85,86]

$$\rho(\mathbf{r})\nabla\cdot[\rho^{-1}(\mathbf{r})\nabla p(\mathbf{r})]+\hat{k}^2(\mathbf{r})p(\mathbf{r})=-S(\mathbf{r}) \tag{2.1}$$

where ρ is density, p is pressure and S is an arbitrary acoustical source. The effect of attenuation can be modelled by assuming a complex valued wavenumber [31,36] as

$$\hat{k}(\mathbf{r})\triangleq\frac{\omega}{c(\mathbf{r})}-j\alpha(\mathbf{r}) \tag{2.2}$$

where ω is the angular frequency, $c(\mathbf{r})$ is the speed of propagation, and $\alpha(\mathbf{r})$ is the attenuation. The minus sign in (2.2) is due to the fact an $e^{+j\omega t}$ time dependancy is assumed. Similarly, the complex-valued background wavenumber, $\hat{k}_b(\mathbf{r})$, is defined as [33]

$$\hat{k}_b\triangleq\frac{\omega}{c_0}-j\alpha_0 \tag{2.3}$$

where $c_0(\mathbf{r})$ is the background speed of sound and $\alpha_0(\mathbf{r})$ is the background attenuation, both assumed to be constants. The scattered pressure for the inhomogeneous compressibility and density profiles can be found as [4,29,33,66]

$$p^{scat}(\mathbf{r})=k_0^2\int_D g(\mathbf{r},\mathbf{r}')\chi_1^c(\mathbf{r}')p(\mathbf{r}')\mathrm{d}\mathbf{r}'+\int_D g(\mathbf{r},\mathbf{r}')\nabla\cdot\left[\chi_2(\mathbf{r}')\nabla p(\mathbf{r}')\right]\mathrm{d}\mathbf{r}' \tag{2.4}$$

where p and p^{scat} are the total pressure and the scattered pressure. D is a domain containing the OI within the known background medium. Note that the contrast profiles, to be defined below, are zero outside D. The scattered pressure is defined as the numerical difference between the total pressure and the incident pressure, p^{inc}, that is, $p^{scat} \triangleq p - p^{inc}$. In these equations, k_0 is the real part of the complex background wavenumber, $g(\mathbf{r}, \mathbf{r}')$ is the Green's function for the background medium, and $\chi_1^c(\mathbf{r})$ is the contrast of complex compressibility. The complex compressibility profile takes into account the contrast of compressibility and the variation of attenuation via its real and imaginary parts[†], respectively. It is defined as [33,66]

$$\chi_1^c(\mathbf{r}) \triangleq \chi_1(\mathbf{r}) - j\frac{2\delta\alpha(\mathbf{r})}{k_0} \tag{2.5}$$

where the superscript c denotes that this contrast is complex valued. The contrast of compressibility $\chi_1(\mathbf{r})$, which is real valued, is defined as

$$\chi_1(\mathbf{r}) \triangleq \frac{\kappa(\mathbf{r}) - \kappa_b}{\kappa_b} \tag{2.6}$$

Here, $\kappa(\mathbf{r})$ is the compressibility at position $\mathbf{r}$ and κ_b is the background compressibility. $\delta\alpha(\mathbf{r})$ is defined as the difference between the attenuation at position $\mathbf{r}$ and the background attenuation ($\delta\alpha(\mathbf{r}) \triangleq \alpha(\mathbf{r}) - \alpha_b$). The contrast of inverse density, $\chi_2(\mathbf{r})$, is defined as

$$\chi_2(\mathbf{r}) \triangleq \frac{\rho^{-1}(\mathbf{r}) - \rho_b^{-1}}{\rho_b^{-1}} \tag{2.7}$$

where ρ_b^{-1} and $\rho^{-1}(\mathbf{r})$ are the background inverse density and the inverse density at position $\mathbf{r}$. This completes a brief description of the acoustic scattering problem. The UT problem can then be formulated as finding $\chi_1^c(\mathbf{r})$ and $\chi_2(\mathbf{r})$ of an OI based on the knowledge of $p^{scat}(\mathbf{r})$ at certain measurement points outside the OI. To this end, we need to know the total pressure due to a predicted $\chi_1^c(\mathbf{r})$ and $\chi_2(\mathbf{r})$. This will be

---

[†] The real and imaginary parts of χ_1^c are denoted by χ_{1r}^c and χ_{1i}^c in this thesis.

done through an appropriate forward solver, which is the focus of the next section.

2.4 Forward Solver

The MoM technique [78–81] has been widely used for different scattering problems to discretized the problem into a linear system of equations of the form $\mathcal{A}x = b$. In this section, the CG version of the MoM forward solver for solving the scattering from inhomogeneous attenuation, density, and compressibility profiles will be described. As noted above, the effect of inhomogeneous attenuation and compressibility will be embedded in the inhomogeneous complex compressibility profile. This CG version of the MoM forward solver requires the definition of the so-called domain operators as well as their adjoints. In Section 2.4.1, these adjoint operators are provided in the continuous domain. These are then discretized and used to solve the scattering problem numerically.

Two fundamental physical domains are introduced for the UT problem. The first one, called the imaging domain, contains the OI within the background medium and is denoted by D, as shown in Fig 2.1. The data domain, which is outside the imaging domain, is denoted by S. This domain contains the transmitters and receivers as shown in Fig 2.1. The goal of the forward solver is to determine the total pressure in the imaging domain given a transmitter location and predicted material profiles of the OI. It is assumed herein that the incident field is known analytically and the scattered field within D is then to be determined using 2.4. In this case, both $\boldsymbol{r}$ and $\boldsymbol{r}'$ in (2.4) belong to the imaging domain ($\boldsymbol{r}, \boldsymbol{r}' \in D$). Once this total pressure in D is found by the forward solver, the scattered pressure on S can be found using (2.4) with $\boldsymbol{r} \in S,$ and $\boldsymbol{r}' \in D$.

2.4.1 Method of Moments (MoM) Forward Solver

The CG-MoM forward solver is described using two new operators which are defined as [33]

$$\mathcal{G}_{1d}(\cdot) \triangleq k_0^2 \int_D g(\mathbf{r}, \mathbf{r}')\chi_1^c(\mathbf{r}')(\cdot)\mathrm{d}\mathbf{r}' \qquad \mathbf{r}, \mathbf{r}' \in D \tag{2.8}$$

$$\mathcal{G}_{2d}(\cdot) \triangleq \int_D g(\mathbf{r}, \mathbf{r}')\nabla' \cdot \left[\chi_2(\mathbf{r}')\nabla'(\cdot)\right] \mathrm{d}\mathbf{r}' \qquad \mathbf{r}, \mathbf{r}' \in D \tag{2.9}$$

both of which operate on the total pressure in the imaging domain. The subscript d indicates that these operators are domain operators. The total-pressure equation can now be written as

$$p(\mathbf{r}) = p^{inc}(\mathbf{r}) + \mathcal{G}_{1d}\big\{p(\mathbf{r}')\big\} + \mathcal{G}_{2d}\big\{p(\mathbf{r}')\big\} = p^{inc}(\mathbf{r}) + (\mathcal{G}_{1d} + \mathcal{G}_{2d})\big\{p(\mathbf{r}')\big\} \tag{2.10}$$

Defining $\mathcal{G}_d$ as the sum of $\mathcal{G}_{1d}$ and $\mathcal{G}_{2d}$ we have

$$(\mathcal{I} - \mathcal{G}_d)\big\{p(\mathbf{r})\big\} = p^{inc}(\mathbf{r}) \tag{2.11}$$

As a linear system of equations in the form $\mathcal{A}x = b$, x is the unknown total pressure inside the imaging domain, b is the known incident pressure within the imaging domain and the operator $\mathcal{A}$ is

$$\mathcal{A} = \mathcal{I} - \mathcal{G}_d = \mathcal{I} - \mathcal{G}_{1d} - \mathcal{G}_{2d} \tag{2.12}$$

We solve this linear-operator equation using the CG algorithm [82]. To use the CG algorithm, the adjoint of $\mathcal{A}$, denoted as $\mathcal{A}^a$, is required. The adjoint of operator $\mathcal{A}$

can be found by taking the adjoint of $\mathcal{G}_1$ and $\mathcal{G}_2$:

$$\mathcal{A}^a = (\mathcal{I} - \mathcal{G}_d)^a = (\mathcal{I} - \mathcal{G}_{1d} - \mathcal{G}_{2d})^a = \mathcal{I} - \mathcal{G}_{1d}^a - \mathcal{G}_{2d}^a \tag{2.13}$$

Therefore, to obtain $\mathcal{A}^a$, we need to determine $\mathcal{G}_1^a$ and $\mathcal{G}_2^a$. To find $\mathcal{G}_1^a$ we use the definition for the adjoint operator:

$$< \mathcal{G}_{1d}\big\{p(\mathbf{r}')\big\}, \psi(\mathbf{r}) >_D = < p(\mathbf{r}'), \mathcal{G}_{1d}^a\big\{\psi(\mathbf{r})\big\} >_D \tag{2.14}$$

where $< \cdot, \cdot >$ is the inner product and the subscript D denotes that this inner product is taken over the domain D. Here $\psi(\mathbf{r})$ is an arbitrary function over D. After some algebraic manipulation, the adjoint operators, $\mathcal{G}_{1d}^a$ and $\mathcal{G}_{2d}^a$, are found as

$$\mathcal{G}_{1d}^a\{\,\cdot\,\} = \big[k_0^2\chi_1^c(\mathbf{r})\big]^* \int_D g^*(\mathbf{r}', \mathbf{r})(\cdot)\mathrm{d}\mathbf{r}' \tag{2.15}$$

and

$$\mathcal{G}_{2d}^a\{\,\cdot\,\} = \nabla\chi_2^*(\mathbf{r}) \cdot \nabla \int g^*(\mathbf{r}', \mathbf{r})(\cdot)\mathrm{d}\mathbf{r}' + \chi_2^*(\mathbf{r})\nabla^2 \int g^*(\mathbf{r}', \mathbf{r})(\cdot)\mathrm{d}\mathbf{r}' \tag{2.16}$$

where * denotes the complex conjugate operation [33].

After discretizing $\mathcal{A}$ and $\mathcal{A}^a$, the CG algorithm can be applied to solve $\mathcal{A}x = b$, for the total pressure x in the imaging domain. It should be noted that the only assumption used to find the adjoint operators is that the contrast of the reciprocal of the density is zero on the boundary of D [33]. This assumption is true in practice because the OI is surrounded by the background medium, and the contrast value is zero anywhere on the background medium. That being said, it can be concluded that no approximations have been used in the derivation of this analytical formula. Note that in this paper the imaging domain is discretized into square cells using 2D pulse basis functions and Dirac delta weighting functions are utilized [33, 78–81].

The next task is to incorporate features in the numerical algorithm that will allow us to handle large numerical values of the contrast and also large objects as compared to the wavelength. The standard CG algorithm turns out to be too computationally expensive for the UT problem. Thus, in the next section we focus on three acceleration techniques that are used in conjunction with this CG-MoM forward solver.

2.5 Acceleration Techniques for CG-MoM Forward Solver

As noted in the Introduction, the UT problem requires having a fast and efficient forward solver due to the fact that (1) the size of the imaging domain is usually large as compared to the wavelength of operation [4, 66], and (2) the forward solver is called several times within the utilized inversion algorithm. To handle this issue, three accelerating features are incorporated into the standard CG-MoM forward solver, which will now be described.

2.5.1 Marching-on-source Technique

This technique was developed for the electromagnetic forward scattering problems [87–89]. Herein, we apply this method to the ultrasound forward scattering problem. The fundamental idea of the marching-on-source technique is to provide a good initial guess for the CG algorithm. The initial guess given to the CG algorithm plays a very important role in the number of iterations needed for its convergence. When there is no prior information related to the distribution of the total field for a given source, the initial guess is usually chosen to be either zero or the incident pressure. The intuitive idea behind the marching-on-source technique method can be explained as follows. First, note that in an ultrasound tomography setup, we have several transducers which are co-resident on a ring close to the object of interest. That we have several transducers close to the OI indicates that neighbouring transducers “see” the object similarly. This indicates that the corresponding total pressure distributions of these neighbouring transmitters will be similar. The level of similarity can then be determined based on comparing their incident pressure distributions. Therefore, having the total pressure distributions for some previous neighbouring transducers to the transducer of interest, and knowing the incident pressure for these transducers, a good estimate for the total pressure of the transducer of interest can be calculated.

The marching-on-source technique is well suited for the UT problem in which the forward solution needs to be found for several transmitters usually located close to each other. For the first few transmitters, a typical initial guess, *e.g.,* zero or incident pressure, is used to find the total pressure in the imaging domain. An improved initial guess for the next transmitter is then based on the total pressure that has been calculated for these previous transmitters. For example, assume that we are looking for a good initial guess for the forward scattering problem corresponding to the m^{th} transmitter. This initial guess is written as a linear combination of Q previously found total pressures due to Q previous transmitters. The initial guess for the m^{th} transmitter is denoted by x_m^0 and the total pressure corresponding to the $(m-q)^{\text{th}}$ transmitter is denoted by x_{m-q}. Thus, the initial guess for the m^{th} transmitter is written as [33]

$$x_m^0 = \sum_{q=1}^{Q} a_q x_{m-q} \tag{2.17}$$

where a_q is the weighting coefficient for the total pressure inside the domain due to transmitter $m-q$. To find these coefficients, it should be noted that a good initial guess should be close to the exact solution. In other words, we minimize the following norm [33]

$$\underset{x_m^0}{\operatorname{argmin}}\left\{||\mathcal{A}x_m^0 - b||^2\right\} = \underset{a_q}{\operatorname{argmin}}\left\{||\sum_{q=1}^{Q} a_q \mathcal{A} x_{m-q} - b||^2\right\} \tag{2.18}$$

where b is the incident field due to transmitter m. It should be noted that when $\mathcal{A}$ operates on x_{m-q}, it gives the incident pressure inside the domain due to transmitter $m-q$. Thus, (2.18) can be written as

$$\underset{a_q}{\operatorname{argmin}}\left\{||\sum_{q=1}^{Q} a_q p_{m-q}^{inc} - p_m^{inc}||^2\right\} \tag{2.19}$$

where p_{m-q}^{inc} is the incident pressure inside the domain due to the transmitter $m-q$. This minimization can be written in the following form:

$$\underset{a_q}{\operatorname{argmin}}\left\{\left|\left| \begin{pmatrix} p_{m-1}^{inc} & p_{m-2}^{inc} & \cdots & p_{m-Q}^{inc} \end{pmatrix} \begin{pmatrix} a_1 \\ a_2 \\ \vdots \\ a_Q \end{pmatrix} - p_m^{inc} \right|\right|^2\right\} \tag{2.20}$$

where $\begin{pmatrix} p_{m-1}^{inc} & p_{m-2}^{inc} & \cdots & p_{m-Q}^{inc} \end{pmatrix}$ is an $N \times Q$ matrix, and N is the number of cells in the imaging domain. The solution to this least-squares minimization is easily found as

$$\begin{pmatrix} a_1 \\ a_2 \\ \vdots \\ a_Q \end{pmatrix} = \left[\begin{pmatrix} p_{m-1}^{inc} & p_{m-2}^{inc} & \cdots & p_{m-Q}^{inc} \end{pmatrix}^H \begin{pmatrix} p_{m-1}^{inc} & p_{m-2}^{inc} & \cdots & p_{m-Q}^{inc} \end{pmatrix} \right]^{-1} \times \begin{pmatrix} p_{m-1}^{inc} & p_{m-2}^{inc} & \cdots & p_{m-Q}^{inc} \end{pmatrix}^H p_m^{inc} \tag{2.21}$$

Once these coefficients are found, the appropriate initial guess can be given to the CG algorithm. Note that the calculation of these coefficients can be pre-calculated and stored since they are only dependent on the incident pressures. Therefore, their calculation does not impose any additional computational cost to the forward solver.

2.5.2 Symmetric Block Toeplitz Matrix with Symmetric Toepltiz Blocks

The other method used in this forward solver to make it efficient in terms of memory storage is based on using the block Toeplitz matrix properties. The key to this method is that the Green's function matrix in the domain equation is a symmetric block Toeplitz matrix with symmetric Toeplitz blocks. It will be shown that only the first row of this matrix is needed to be stored instead of storing all of the matrix elements. This method was originally used in electromagnetic problems and signal processing [83, 84].

We start by noting that the term $g(\mathbf{r}, \mathbf{r}')$ is a common term in both integrals in (2.4). If we assume that we have a 2D time-harmonic problem with $e^{+j\omega t}$ time dependancy, the Green's function for each frequency is solely dependent on the distance between positions $\mathbf{r}$ and $\mathbf{r}'$ and can be found as [34, 85] $\frac{1}{4j}H_0^{(2)}(k_0|\mathbf{r}-\mathbf{r}'|)$ where H_0^2 is the zeroth-order Hankel function of the second kind. If we assume that the number of cells in the pulse basis function is $N = n_x \times n_y$ (see Fig 2.1) where n_x and n_y are the number of discretized elements along the x and y axes respectively, then each integral results in an $N \times N$ matrix of the form shown in Fig 2.2. This $N \times N$ matrix is not only a symmetric block Toeplitz matrix but also each of its block is a symmetric Toeplitz matrix. The size of each Toeplitz matrix in Fig 2.2 is $n_y \times n_y$ and the total number of Toeplitz blocks is $n_x \times n_x$. If each Toeplitz block is considered as an element of the matrix, these elements make another Toeplitz matrix.

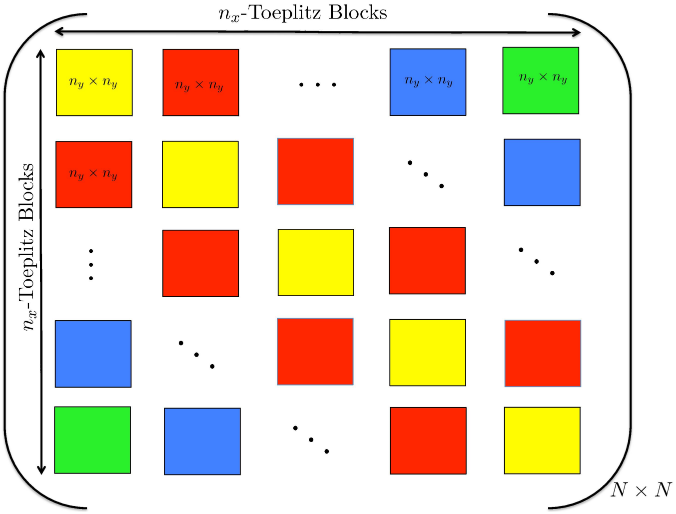

Figure 2.2: A symmetric block Toeplitz Matrix. Each block is also a symmetric Toeplitz matrix of the size of $n_y \times n_y$.

This specific structure allows us to store only the first row of the whole matrix instead of all the N^2 elements, thus saving significantly on storage memory. As will be seen in the next section, only this first row is used for our matrix-vector multiplications. That is, the whole matrix is never actually constructed. This is possible because the CG algorithm needs only matrix-vector product operations on appropriately chosen vectors and not the actual operators themselves. Finally, we note that this Toeplitz structure can also be applied to the 3D cases [83].

2.5.3 FFT Matrix-Vector Multiplication

The matrix-vector multiplications required in the CG algorithm are implemented using FFT-based multiplication. This reduces the computational complexity from order $\mathcal{O}(n^2)$ to $\mathcal{O}(n\log(n))$ as compared to performing standard matrix-vector products.

Circulant matrix-vector multiplication can be performed using the FFT multiplication [90–93]. For example, the following circulant-matrix vector multiplication can be found as

$$\begin{pmatrix} w_0 & w_1 & \cdots & w_{p-1} & w_p \\ w_p & w_0 & \ddots & w_{p-2} & w_{p-1} \\ \vdots & w_p & w_0 & \ddots & \vdots \\ w_2 & \ddots & w_p & \ddots & w_1 \\ w_1 & w_2 & \cdots & w_p & w_0 \end{pmatrix} \begin{pmatrix} k_0 \\ k_1 \\ k_2 \\ \vdots \\ k_p \end{pmatrix} = \mathrm{IDFT}\Big[\mathrm{DFT}[W(1,:)] \odot \mathrm{DFT}[K(:,1)]\Big] \tag{2.22}$$

where W and K are the above circulant matrix and column vector respectively. The Hadamard product (element-wise product) is denoted by $\odot$. IDFT and DFT are the inverse discrete Fourier transform and discrete Fourier transform, respectively. $W(1,:)$ is the first row of the circulant matrix and $K(:,1)$ is the column vector that should be multiplied with a circulant matrix.

To apply this technique to the block Toeplitz matrix of Section 2.5.2 each Toeplitz block is first converted to a circulant matrix. As shown in Fig 2.2, the first row corresponds to the first rows of n_x Toeplitz blocks where the size of each row is n_y. Therefore, the first row of each n_x Toeplitz block is converted to the first row of a corresponding circulant matrix. This is done in a similar fashion as reported in [92, 93], where it was shown how to convert an asymmetric Toeplitz matrix to a circulant matrix. For our symmetric Toeplitz matrix of size $n_y \times n_y$, $n_y - 2$ columns are added to this matrix as shown in Fig 2.3 [33]. Specifically, a matrix having the elements shown in the second box, which has a size of $n_y \times (n_y - 2)$, is added to the original matrix shown in the first box. This converts our matrix to a circulant matrix. As before, this is created implicitly via the first row only. That is, $n_y - 2$ elements are added to the first row of each Toeplitz matrix. Note that this conversion makes the size of the corresponding vector to be multiplied different than in the original multiplication. This means that $n_y - 2$ elements should also be added to the corresponding vector that is to be multiplied. These elements are denoted by $c_1, c_2, \cdots c_{n_y-2}$. To have the same results for both matrix-vector multiplications as shown in Fig 2.4, (1) the value of $c_1, c_2, \cdots c_{n_y-2}$ are set to zero and (2) the last $n_y - 2$ elements of resulting vector after multiplication are removed. This procedure

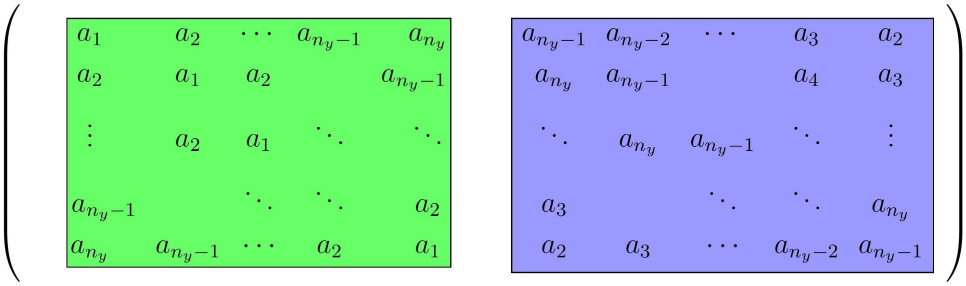

$$\left(\begin{array}{ccccc|ccccc}
a_1 & a_2 & \cdots & a_{n_y-1} & a_{n_y} & a_{n_y-1} & a_{n_y-2} & \cdots & a_3 & a_2 \\
a_2 & a_1 & a_2 & & a_{n_y-1} & a_{n_y} & a_{n_y-1} & & a_4 & a_3 \\
\vdots & a_2 & a_1 & \ddots & \ddots & \ddots & a_{n_y} & a_{n_y-1} & \ddots & \vdots \\
a_{n_y-1} & & \ddots & \ddots & a_2 & a_3 & & \ddots & \ddots & a_{n_y} \\
a_{n_y} & a_{n_y-1} & \cdots & a_2 & a_1 & a_2 & a_3 & \cdots & a_{n_y-2} & a_{n_y-1}
\end{array}\right)$$

Figure 2.3: Converting a symmetric Toeplitz matrix to a circulant matrix. The first block corresponds to a symmetric Toeplitz matrix. The second block is added to the first block to create a circulant matrix.

is performed for the first row of each n_x Toeplitz matrices and column vectors that correspond to these Toeplitz matrices.

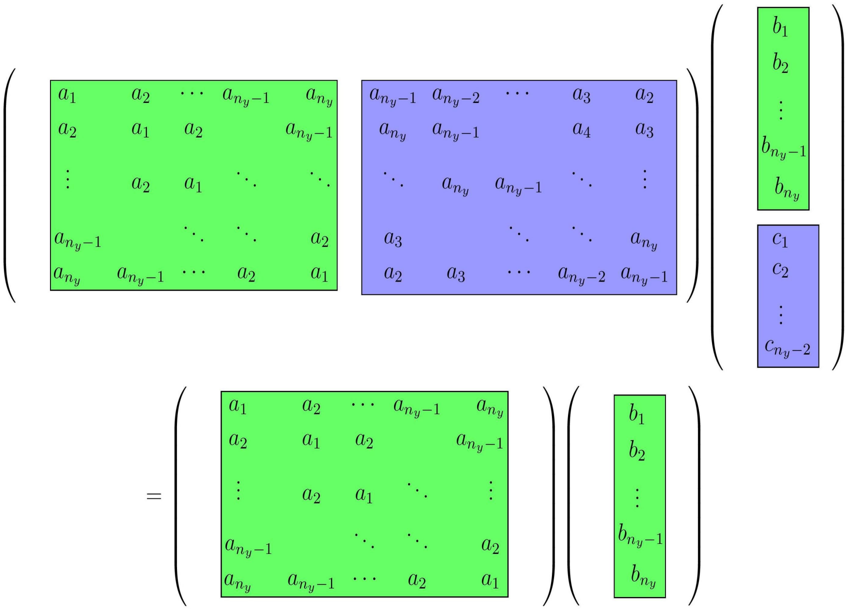

Figure 2.4: A circulant matrix-vector multiplication and a Toepliz matrix-vector multiplication.

The basic idea behind the FFT matrix-vector multiplication for this matrix can now be summarized as follows. To this end, consider the matrix shown in Fig 2.2 that consists of n_x block rows. Since the whole matrix is symmetric block Toeplitz, all the block rows can be simply generated merely by knowing the first block row. In addition, since the first block row consists of Toeplitz matrices, its first row can be simply used to generate the whole block row. Therefore, the very first row of the first block row can represent the entire matrix. That's why we only store this single row instead of the entire matrix. Also, as described above, this single row can be used with the FFT to operate on a vector of appropriate size so as to implicitly calculate the operation of the entire matrix on that vector. To this end, this single row needs to be divided into n_x parts, each of which belongs to one of the n_x different Toeplitz matrices of the first block row. Likewise, the vector by which the entire matrix is to be multiplied are divided into n_x parts. These n_x parts of the first row operate on the corresponding n_x parts of the vector. The results of these n_x operations will then be summed up to produce the result of the operation of the first block row on the vector. Using the result of this calculation, and re-ordering them, the results of the operation of other block rows on that vector can also be found. Therefore, the result of the operation of the entire matrix on that vector is now found.

Finally, we note that the whole idea behind this acceleration lies in the fact that the Green's function relies on $|\mathbf{r}-\mathbf{r}'|$. Since the complex conjugate of the Green's function also shares this property, the adjoint of the forward operators can also be accelerated using this technique. (Note that these adjoint operators utilize the complex conjugate of this Green's function in their kernels.)

2.6 Inversion Algorithm

2.6.1 Born Iterative Method

The Born Iterative Method is used as the non-linear inversion algorithm to simultaneously reconstruct the contrast profiles. In the BIM, we start by assuming that the unknown total pressure distribution within the imaging domain is the same as the known incident pressure distribution. Using this approximation, we then solve for the contrast profiles. These predicted contrast profiles are then used to find a new total pressure distribution within the imaging domain. Using the new predicted total pressure distribution, the new predicted contrast profiles are found. This procedure continues until the convergence criterion is met. The steps of this algorithm can then be summarized as [4, 29, 37, 67, 94]:

1. Set the unknown total pressure inside the imaging domain to be equal to the incident pressure in the first iteration (Born approximation).
2. Find the contrasts of OI by solving the resulting linearized integral equation.
3. Call the forward solver to find the total pressure inside the imaging domain based on the predicted contrast profiles of the previous step.
4. Find the simulated scattered pressure at the receiver locations.
5. Calculate the discrepancy between the measured and simulated scattered pressure (data misfit).
6. Go back to step 2 until the data misfit becomes sufficiently small.

Finally, as noted in [27], the BIM is capable of handling multiple-scattering events within the OI. The BIM achieves this via its iterative nature. Intuitively speaking, each iteration of the BIM attempts to recover one scattering event.

2.6.2 Data Operator

To find the contrast profiles, a linear equation, $\mathcal{A}x = b$, for the scattered pressure at the receiver points, b, is formulated where x now contains the discretized values of the unknown contrast profiles, and $\mathcal{A}$ is now the data operator that takes these contrast profile values and calculates the scattered pressure at the receiver locations. This data operator is decomposed into two operators denoted by $\mathcal{G}_{1s}$ and $\mathcal{G}_{2s}$. The scattered pressure based on these operators can be written as [65]

$$p^{scat}(\mathbf{r}) = \mathcal{G}_{1s}\left\{\chi_1^c(\mathbf{r}')\right\} + \mathcal{G}_{2s}\left\{\chi_2(\mathbf{r}')\right\} \tag{2.23}$$

where subscript s denotes that these operators output field variables on the S domain.[‡] $\mathcal{G}_{1s}$ and $\mathcal{G}_{2s}$ operate on the complex contrast of compressibility and contrast of inverse density and are defined as

$$\mathcal{G}_{1s}(\cdot) \triangleq k_0^2 \int_D g(\mathbf{r}, \mathbf{r}')(\cdot) p(\mathbf{r}') \mathrm{d}\mathbf{r}' \qquad \mathbf{r}' \in D, \ \mathbf{r} \in S \tag{2.24}$$

$$\mathcal{G}_{2s}(\cdot) \triangleq \int_D g(\mathbf{r}, \mathbf{r}') \nabla \cdot \big[(\cdot) \nabla p(\mathbf{r}')\big] \mathrm{d}\mathbf{r}' \quad \mathbf{r}' \in D, \ \mathbf{r} \in S \tag{2.25}$$

When discretized, the data equation[§] produces an ill-conditioned matrix equation which requires regularization to invert. We perform this regularization using the Conjugate-Gradient Least-Squares (CGLS) technique which will be described in the next section. The CGLS algorithm requires the use of the adjoint of the data operator which operates on field values on S. These adjoints can be found as [4,33,65]

$$\mathcal{G}_{1s}^{a}\{\,\cdot\,\} = \big[k_0^2 p(\mathbf{r}')\big]^* \int_S g^*(\mathbf{r}, \mathbf{r}')(\cdot) \mathrm{d}\mathbf{r} \tag{2.26}$$

$$\mathcal{G}_{2s}^{a}\{\,\cdot\,\} = -\nabla' p^*(\mathbf{r}') \cdot \nabla' \int_S g^*(\mathbf{r}, \mathbf{r}')(\cdot) \mathrm{d}\mathbf{r} \tag{2.27}$$

2.6.3 CGLS Regularization

The UT problem is an ill-posed problem which requires a regularization technique to obtain a physical solution. The CGLS regularization used herein is a well-known technique which implicitly effects the truncated singular-value decomposition for solving the ill-conditioned matrix that results from discretizing the data operator [8,9,47].

[‡] The equation presented in (2.23) connects the unknown profiles to the measured data, and is often referred to as the *data equation*. For microwave imaging, we have a similar data equation that relates the unknown complex permittivity to the measured scattered fields.

[§] The data equation is shown in (2.23).

The main reason for choosing this regularization is the computational efficiency with which it can be implemented for our UT problem. In the implementation of BIM for our problem, at each step 2 the data operator changes because the total field inside D is updated. Thus, it is not efficient to store the complicated matrix representation corresponding to these new data and adjoint operators at each step in the BIM iterations. This is easily accommodated by CGLS because it only requires matrix-vector multiplications which represent the action of the data operator on contrast values and the operation of the data-operator adjoint on discretized functions defined on S. Therefore, it does not require the full storage of the matrix representing the data operator and its adjoint (even if it could be found).

The CGLS method projects the solution into a Krylov subspace for the problem at each of its iterations [47, 95]. The CGLS iteration loop must be terminated to obtain a stable solution to the poorly conditioned matrix equation. At early iterations of the BIM, where the estimation of the total field within the imaging domain is poor, the CGLS iterations are terminated early. This corresponds to approximating the contrast using low spatial frequency components. As the BIM gets closer to the solution, higher frequency components for the contrast can be determined using CGLS by allowing more iterations. This *ad hoc* technique was proposed in [9] to terminate the CGLS iterations for microwave imaging algorithms. The number of CGLS iterations, which determine the final size of the Krylov subspace being projected onto, acts as a regularization parameter in CGLS regularization. The details of this regularization technique are explained in [9, 33, 47].

Finally, we again emphasize that the computational efficiency of the CGLS algorithm which requires only a few matrix-vector multiplications is an important advantage of this regularization technique. In addition, that the CGLS regularization method does not require the full storage of the matrix provides another important advantage for this method specially when dealing with large scale problems. On the other hand, the appropriate dimension of the Krylov subspace should be determined using *ad hoc* techniques [9].

2.7 Results

2.7.1 Forward Solver

In this section, the effects of the accelerating features of the CG-MoM forward solver are demonstrated. We first tabulate the computational time required for standard matrix-vector multiplication compared with the case that only the first row of the matrix is stored and FFT matrix-vector multiplication is utilized. We next show the effect of marching-on-source on the convergence of the CG algorithm, by applying the forward solver to a scattering problem which contains inhomogeneities in all three physical acoustic parameters.

Consider imaging domains of various increasing sizes with respect to the wavelength. Imaging domains for 16 different cases are tabulated in Table 2.1, where the domain size varies from $2\lambda \times 2\lambda$ to $150\lambda \times 150\lambda$. The number of unknowns in the domain increases dramatically, given as $n_x \times n_y$, where we have considered a minimum discretization requirement of 10 cells per wavelength. For small domains the time required to store the whole matrix (T_1) and the time required to perform standard matrix-vector multiplication (T_2) are almost comparable to the time required for storing the first row of the matrix (T_3), and the time required to perform FFT matrix-vector multiplication using only this row, (T_4). However, as the size of the imaging domain increases, the values of T_1 and T_2 become significantly larger. Specifically, when the size of the imaging domain reaches $22\lambda \times 22\lambda$, the standard method, when implemented on MATLAB running on a computer with 32 GB of RAM, fails to provide the matrix-vector multiplication due to lack of memory. However, on the same computer, MATLAB took less than a second to calculate the same matrix-vector multiplication that the standard method fails to calculate. Interestingly, when the size of the imaging domain reaches $100\lambda \times 100\lambda$, the proposed method takes less than 100 seconds to calculate the matrix-vector multiplication. Therefore, the use of such fast and efficient forward solvers is essential to solving UT problems.

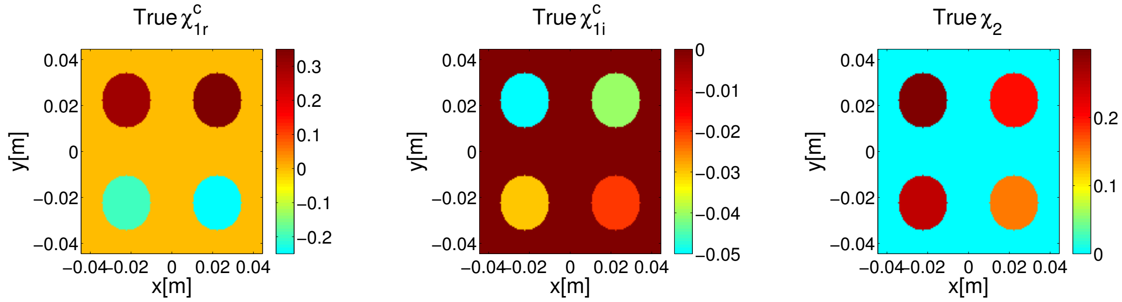

Figure 2.5: True contrast profiles for comparison between the final calculated total pressure within the imaging domain with two different initial guesses.

UT problems also typically have a large number of incident fields where the marching-on-source technique is able to find a good initial guess for the CG algorithm, thus, leading to faster convergence. To demonstrate this feature of our forward solver, consider a 2D scattering problem consisting of four cylinders each having a diameter of 4λ. This scattering object is enclosed within a $15\lambda \times 15\lambda$ imaging domain and the frequency of operation is 250 kHz. The total number of transducers used in this example is 400. (It should be noted that recent UT systems often have many more transducers. For example, in [96, 97], 2048 transducers are used in a ring.) The UT properties (χ_1^c and χ_2) of this OI are shown in Fig 2.5. In this example, the total pressure in the imaging domain for the first Q transmitters are found using our forward solver when the incident pressure is given as the initial guess to the CG algorithm. The calculation of the total pressure corresponding to the remaining transmitters is substantially accelerated by the use of the marching-on-source technique, which uses the already-calculated total pressure of the previous transmitters. Table 2.2 shows the number of CG iterations needed to converge to the solutions for the first 20 transmitters using six different categories of initial guesses. The first column, denoted by C_1, simply uses the incident pressure as the initial guess. In the remaining five columns of the Table, we show the required CG iterations based on using the marching-on-source technique with varying values of Q, ranging from 2 to 6. For this example, using the marching-on-source technique using the previous four transmitters, $Q = 4$, leads to an overall fewer number of CG iterations. Using more transmitters may not lead to a better initial guess if the total field due to the transmitters used in the linear approximation are not very similar. Therefore, the criteria of using $Q = 4$ will change depending on the separation between transmitters.

2.7.2 Inversion Results

We now consider a total of four different 2D inversion examples based on synthetically generated data. The first two examples have imaging domains that are $8\lambda_{\min} \times 8\lambda_{\min}$, and contain two cylinders each. In the first, the two cylinders have the same physical properties whereas in the second the two cylinders differ. The third example has a much larger imaging domain of $15\lambda_{\min} \times 15\lambda_{\min}$ and contains two identical cylinders. The fourth example is a very large problem of $20\lambda_{\min} \times 20\lambda_{\min}$ and contains two cylinders where now the density is assumed to be the same as the background, that is, $\chi_2 = 0$. A summary of the information regarding the number of transmitters, receivers, domain size, the diameter of the OI, frequency of operations and the contrast profiles of the OI for all these example are listed in Table 2.3. In all examples, three percent noise, $NP = 3\%$, is added to the synthetic data using the following formula

$$p_{noisy}^{scat} = p_{simulated}^{scat} + |\overline{p_{simulated}^{scat}}| \times \frac{NP \times RV}{\sqrt{2}} \tag{2.28}$$

where $-1 < RV < 1$ is a uniformly distributed random vector. The range of frequencies utilized for the inversions is $200 \leq f \leq 270$ kHz. The multiple-frequency data sets are utilized simultaneously to reconstruct the contrast profiles of the OI [65, 98, 99]. Assuming we have data from nRx receivers, nTx transmitters and at n_f frequencies, then the total amount of information used by the inversion algorithm at each frequency is $nRx \times nTx$. Thus, inverting using all frequencies simultaneously results in n_f complex valued data-vectors of length $nRx \times nTx$ concatenated into a single vector of length $nRx \times nTx \times n_f$. For these examples the background medium is chosen to be water where the speed of the sound is set to $c_b = 1483[\frac{\text{m}}{\text{s}}]$. Contrast values for these examples are chosen within ranges corresponding to the physical parameters of human tissue. These specific contrast values are within the range of values typically used to model breast tissues, as reported in [4].

The first example considers the reconstruction of two cylinders, each having a diameter of $2\lambda_{min}$ and the contrast profiles of $\chi_1^c = 0.15 - j0.08$ and $\chi_2 = 0.1$, enclosed within an $8\lambda_{\text{min}} \times 8\lambda_{\text{min}}$ imaging domain, as shown in the first row of Fig 2.6. Three frequencies, $f = [250, 260, 270]$ kHz, are simultaneously used for the reconstruction. Thus, at these chosen frequencies the minimum wavelength with respect to the background medium is $\lambda_{min} \simeq 5.5$mm. The number of transmitters and receivers utilized in this example are 100. The BIM with CGLS regularization inversion algorithm took only 10 iterations to converge. The reconstruction of the contrast profiles for the 10th iteration of the BIM is shown in the second row of Fig 2.6[¶]. The results of the comparison between the exact value of the contrast profiles with the reconstructed contrast profiles for the pixels on the main diagonal are shown in Fig 2.7. The first and second rows of this figure correspond to the reconstruction of the contrast profiles after the first and 10th iterations of the BIM. The number of CGLS iterations was set to 2 in the first iteration and was increased systematically reaching a value of 200 by the 10th iteration. As can be seen in Fig 2.7, the first iteration of the BIM (Born approximation) provides a reasonable qualitative reconstruction of the two cylinders but does not reconstruct the actual values of the contrasts well. By the 10th iteration the BIM achieves good accuracy in reconstructing these values.

The second example is similar to the first, but the contrasts of the two cylinders differ. The contrast profiles for the top cylinder is $\chi_1^c = 0.2 - j0.03, \chi_2 = 0.08$ and the contrast profiles for the bottom cylinder is $\chi_1^c = 0.1 - j0.06, \chi_2 = 0.05$, as shown in the top row of Fig 2.8. The BIM converged at the 10th iteration and the final contrast profiles are shown in the second row of Fig 2.8. The exact value of the contrast profiles as well as the reconstructed contrast profiles for the elements on the main diagonal are shown in Fig 2.9. The number of CGLS iterations at the last iteration of the BIM was set to 200.

The reconstruction of two cylinders each with a diameter of $4\lambda_{\min}$ and contrast profiles of $\chi_1^c = 0.14 - j0.08$ and $\chi_2 = 0.1$ enclosed within $15\lambda_{\min} \times 15\lambda_{\min}$ imaging

---

[¶] There are artifacts in the reconstructed images. Broadly speaking, these artifacts are related to the signal-to-noise ratio (SNR) of the data, the modeling accuracy (similarity between the actual system and the inversion model), the choice of the regularization operator and its weight, etc. To reduce these artifacts, the best approach is to make sure that the SNR of the data and the modelling accuracy have been improved as much as possible. Then, the choice of regularization and its weight are important. For example in Chapter 3, the effects of the regularization term can be seen in Figures 3.5h and 3.9d in which the CGLS regularization and the weighted L_2 norm total variation regularization have been used for the same data.

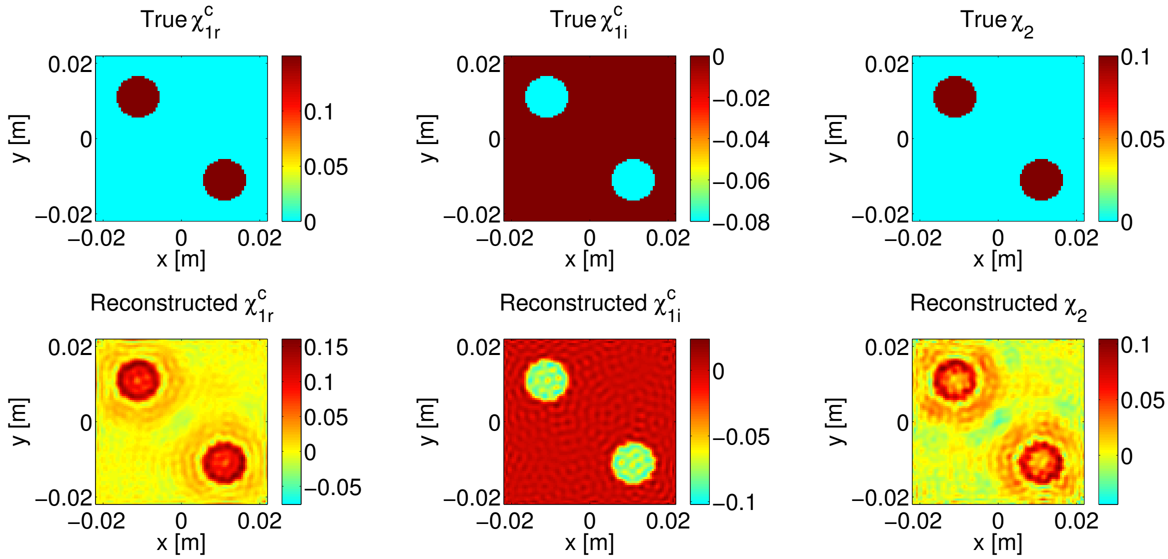

Figure 2.6: Simultaneous reconstruction of χ_1^c and χ_2 for two cylinders with the same contrast profiles enclosed within a $8\lambda_{\min} \times 8\lambda_{\min}$. The first row is the true contrast profiles. The second row corresponds to the reconstruction of contrast profiles for the 10^{th} iteration of the BIM.

domain is considered next. The true profiles are shown in the first row of Fig 2.10. The number of transmitters and receivers were increased to 120 for this example and now five frequencies, $f = [200, 210, 220, 230, 240]$ kHz, were simultaneously used for the inversion. Thus, the minimum wavelength at these chosen frequencies is $\lambda_{\min} \simeq 6.18mm$. The reconstructions of the contrast profiles for the 8^{th} iteration of the BIM, in which the maximum number of CGLS iterations was set to 200, are shown in the second row of Fig 2.10.

The final example shows the reconstruction of two cylinders each having a diameter of $5\lambda_{\min}$ and contrast profiles of $\chi_1^c = 0.07 - j0.03$ and $\chi_1^c = -0.07 - j0.05$ enclosed within $20\lambda_{\min} \times 20\lambda_{\min}$ imaging domain. The density is assumed to be the same as the background, giving $\chi_2 = 0$. The true profiles are shown in the first row of Fig 2.11. The number of transmitters and receivers for this example was set to

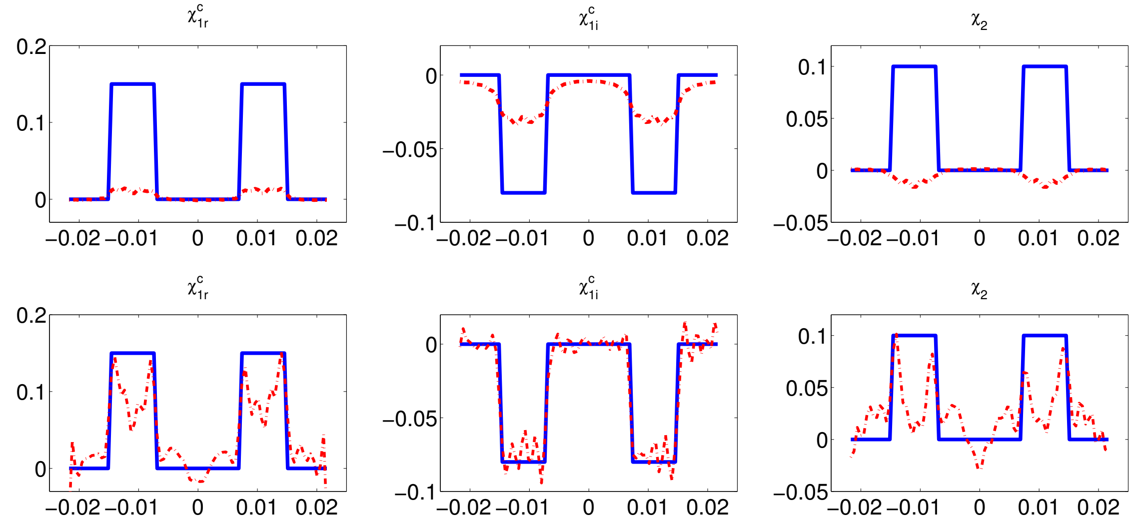

Figure 2.7: Diagonal cut from top left to the bottom right for the case that the OI consists of two cylinders with the same contrast profiles. The first and second rows correspond to the 1st and 10th iterations of the BIM. The solid line corresponds to the actual contrast profiles and the dashed line corresponds to the reconstructed contrast profiles. (The horizontal axis corresponds to the x value of the diagonal cut from the top left to the bottom right with the unit of [m] and the vertical axis corresponds to the value of the corresponding contrast).

200. Four frequencies, $f = [200, 210, 220, 230]$ kHz, were used for the inversion. The reconstructions of the contrast profiles for the fourth iteration of the BIM in which the number of CGLS iterations was set to 80 are shown in the second row of Fig 2.11.

2.8 Discussion

These inversions provide promising results for using this algorithm within a practical biomedical UT device. The size of the imaging domain is sufficient for biomedical applications such as breast imaging and the contrast values shown are also within the ranges required for such applications. The value of the attenuation in the tissue,

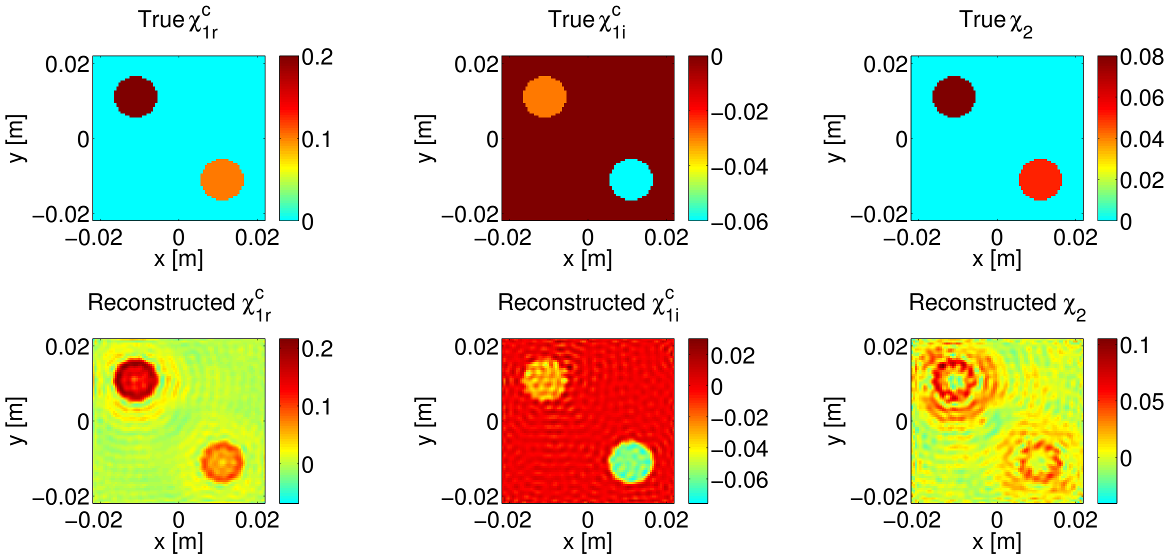

Figure 2.8: Simultaneous reconstruction of χ_1^c and χ_2 for two cylinders with the different contrast profiles enclosed within a $8\lambda_{\min} \times 8\lambda_{\min}$. The first row is the true contrast profiles. The second row corresponds to the reconstruction of contrast profiles for the tenth iteration of the BIM.

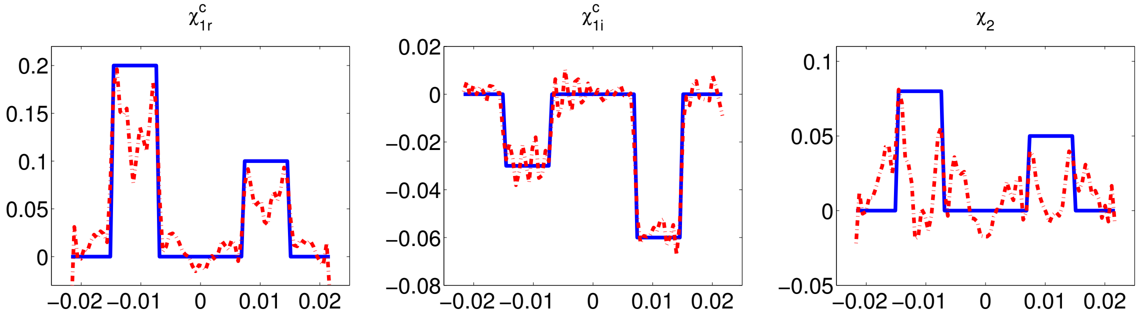

Figure 2.9: Diagonal cut from top left to the bottom right for the case that the OI consists of two cylinders with different contrast profiles. It corresponds to the tenth iteration of the BIM. The solid line corresponds to the actual contrast profiles and the dashed line corresponds to the reconstructed contrast profiles. (The horizontal axis corresponds to the x value of the diagonal cut from the top left to the bottom right with the unit of [m] and the vertical axis corresponds to the value of the corresponding contrast).

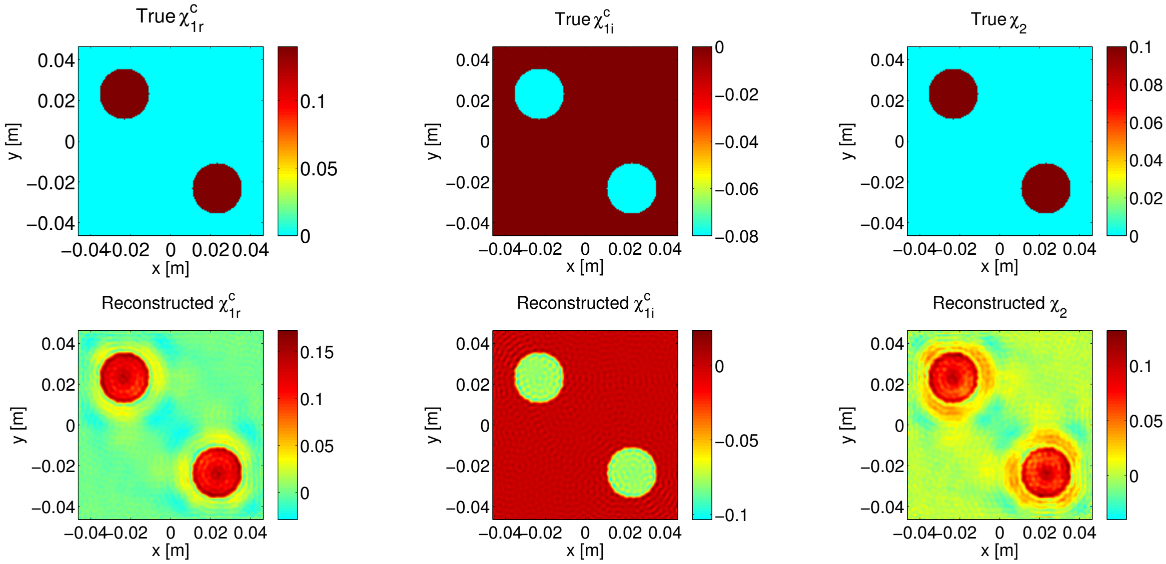

Figure 2.10: Simultaneous reconstruction of χ_1^c and χ_2 for two cylinders with the same contrast profiles enclosed within a $15\lambda_{\min} \times 15\lambda_{\min}$. The first row shows the true contrast profiles. The second row corresponds to the reconstruction of contrast profiles for the 8th iteration of the BIM.

which is related to the imaginary part of χ_1^c, was chosen slightly higher than expected values for breast tissue in order to balance out the relative values of the three parameters being inverted. Future work will report on a new balancing technique which we have developed to overcome this constraint, allowing any relative range of values between the reconstructed parameter values. As can be seen from the figures, the quantitative values for the inverse of density, χ_2, are not reconstructed as well as for the complex contrast of compressibility. This is most certainly due to the fact that the inverse of density shows up in the more complicated field operator, (2.25), which includes gradient and divergence operations within the integral. These differential operators were discretized using simple finite differences and thus the numerical approximation may not be sufficient to recover the inverse of density in the inversions. Similar observations were made in [77].

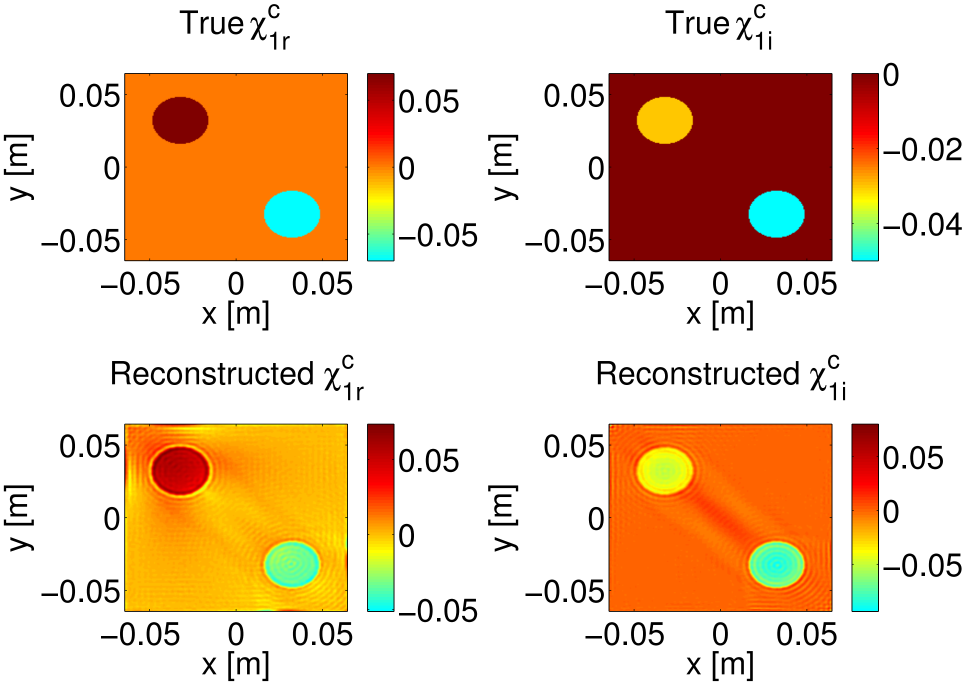

Figure 2.11: Simultaneous reconstruction of χ_1^c for two cylinders with different contrast profiles enclosed within a $20\lambda_{\text{min}} \times 20\lambda_{\text{min}}$ imaging domain. The first row shows the true contrast profiles. The density is assumed to be constant and equal to that of the background. The second row corresponds to the reconstruction of the contrast profiles for the fourth iteration of the BIM.

Although, the inversions take several hours of computation time, the algorithm is well suited to parallelization and the time could easily be reduced. Extending the algorithm to full 3D inversions is straight-forward from an algorithmic perspective, but computation time will certainly have to be reduced. Future work will investigate the application of this algorithm to physically realistic breast phantoms, the extension to 3D, and the use of experimental scattered-field data from an in-house UT system.

2.9 Conclusion

In this paper, we have presented an inversion algorithm to simultaneously reconstruct three properties of the OI. This algorithm requires a fast and efficient forward solver to compute the scattering from objects with inhomogeneous density, attenuation, and compressibility profiles. The presented forward solver requires the use of the adjoint of the operator which governs the scattering phenomenon in the imaging domain. To make use of this forward solver for large domain problems, three computational features have been implemented. The first provides a good initial guess to make the convergence of the algorithm faster. The second provides an efficient way for storing the elements of the matrix, and the third provides an FFT matrix-vector multiplication for the algorithm. Inversion results for synthetically generated data representative of data that would be collected in a UT system designed for breast imaging are shown. The inversion algorithm produces three images in each of the three properties of the OI. Although the OI is qualitatively reconstructed well in all three images, the quantitative value of the inverse density profile is not as well reconstructed as are the two images associated with the complex contrast of compressibility. A procedure for enhancing the accuracy of the all three reconstructions using a novel balancing technique is the topic of future work, which will also investigate the use of the algorithm on more realistic breast phantoms.

Acknowledgment

The financial support of the Natural Sciences and Engineering Research Council of Canada (NSERC) is appreciated.

Table 2.1: Calculation time required for the standard matrix storage and matrix-vector multiplication as compared to the time required for storage and matrix-vector multiplication as presented in this paper.

case	n_x	n_y	Domain size	T_1[s]	T_2[s]	T_3[s]	T_4[s]
1	20	20	$2\lambda \times 2\lambda$	0.26	0.009	0.02	0.007
2	40	40	$4\lambda \times 4\lambda$	2.86	0.012	0.021	0.013
3	60	60	$6\lambda \times 6\lambda$	12.97	0.070	0.023	0.045
4	80	80	$8\lambda \times 8\lambda$	40.27	0.225	0.027	0.052
5	100	100	$10\lambda \times 10\lambda$	89.69	0.495	0.029	0.065
6	120	120	$12\lambda \times 12\lambda$	188.2	1.034	0.034	0.103
7	140	140	$14\lambda \times 14\lambda$	326.3	1.84	0.041	0.378
8	160	160	$16\lambda \times 16\lambda$	1324	23.74	0.047	0.464
9	180	180	$18\lambda \times 18\lambda$	5836	1979	0.053	0.545
10	200	200	$20\lambda \times 20\lambda$	11387	4094	0.061	0.655
11	220	220	$22\lambda \times 22\lambda$			0.069	0.817
12	300	300	$30\lambda \times 30\lambda$			0.1132	4.4582
13	400	400	$40\lambda \times 40\lambda$			0.1707	7.681
14	500	500	$50\lambda \times 50\lambda$			0.236	12.32
15	1000	1000	$100\lambda \times 100\lambda$			0.8614	97.36
16	1500	1500	$150\lambda \times 150\lambda$			1.9763	471.3

n_x: Number of discretized elements in the x axis.
n_y: Number of discretized elements in the y axis.
T_1: Time taken to make the whole matrix.
T_2: Time taken for standard matrix-vector multiplication.
T_3: Time taken to make the first row of the matrix.
T_4: Time taken to perform FFT matrix-vector multiplication by using the first row of the matrix.

Table 2.2: Comparison between the number of CG iterations required for converging to the solution for some transmitters using six different initial guesses. The first one uses the incident pressure as the initial guess, and the remaining columns show results using the marching-on-source technique with varying Q to generate the initial guess.

Transmitter Index	C_1	C_2	C_3	C_4	C_5	C_6
Tx_1	178	178	178	178	178	178
Tx_2	178	178	178	178	178	178
Tx_3	179	92	179	179	179	179
Tx_4	179	96	86	179	179	179
Tx_5	181	91	90	57	181	181
Tx_6	181	93	86	71	31	181
Tx_7	181	93	88	60	52	23
Tx_8	180	91	83	73	50	44
Tx_9	180	90	84	53	57	46
Tx_{10}	180	90	83	67	65	70
Tx_{11}	180	89	84	69	64	85
Tx_{12}	180	89	81	76	76	92
Tx_{13}	180	88	80	66	80	102
Tx_{14}	180	89	78	76	89	99
Tx_{15}	180	89	79	65	94	106
Tx_{16}	180	89	78	77	93	116
Tx_{17}	179	88	77	74	98	135
Tx_{18}	177	87	76	81	97	131
Tx_{19}	176	88	76	77	97	126
Tx_{20}	175	89	77	80	100	173

Required iterations for the CG algorithm using the following initial guesses:
C_1: incident pressure.
C_2: marching-on-source Technique with $Q = 2$.
C_3: marching-on-source Technique with $Q = 3$.
C_4: marching-on-source Technique with $Q = 4$.
C_5: marching-on-source Technique with $Q = 5$.
C_6: marching-on-source Technique with $Q = 6$.

Table 2.3: The information of the examples shown in the inversion results. nRx and nTx denote the number of transmitters and receivers respectively.

Example	nTx	nRx	Size Domain	Diameter OI	Frequencies [kHz]	Cylinder 1	Cylinder 2
1	100	100	$8\lambda_{\min} \times 8\lambda_{\min}$	$2\lambda_{\min}$	$f_1 = 250$ $f_2 = 260$ $f_3 = 270$	$\chi_{1r} = 0.15$ $\chi_{1i} = -0.08$ $\chi_2 = 0.1$	$\chi_{1r} = 0.15$ $\chi_{1i} = -0.08$ $\chi_2 = 0.1$
2	100	100	$8\lambda_{\min} \times 8\lambda_{\min}$	$2\lambda_{\min}$	$f_1 = 250$ $f_2 = 260$ $f_3 = 270$	$\chi_{1r} = 0.2$ $\chi_{1i} = -0.03$ $\chi_2 = 0.08$	$\chi_{1r} = 0.1$ $\chi_{1i} = -0.06$ $\chi_2 = 0.05$
3	120	120	$15\lambda_{\min} \times 15\lambda_{\min}$	$4\lambda_{\min}$	$f_1 = 200$ $f_2 = 210$ $f_3 = 220$ $f_4 = 230$ $f_4 = 240$	$\chi_{1r} = 0.14$ $\chi_{1i} = -0.08$ $\chi_2 = 0.1$	$\chi_{1r} = 0.14$ $\chi_{1i} = -0.08$ $\chi_2 = 0.1$
4	200	200	$20\lambda_{\min} \times 20\lambda_{\min}$	$5\lambda_{\min}$	$f_1 = 200$ $f_2 = 210$ $f_3 = 220$ $f_4 = 230$	$\chi_{1r} = 0.07$ $\chi_{1i} = -0.03$ $\chi_2 = 0$	$\chi_{1r} = -0.07$ $\chi_{1i} = -0.05$ $\chi_2 = 0$

3

Paper 1*: Evaluation of Balanced Ultrasound Breast Imaging Under Three Density Profile Assumptions

---

3.1 abstract

A balanced inverse scattering algorithm for ultrasonic breast imaging is developed to simultaneously reconstruct quantitative images of the breast's ultrasonic properties. These properties are the inhomogeneous compressibility, attenuation, and density. Three scenarios are considered for this inversion algorithm. First, all the properties are assumed to be independent. The assumption of a linear relation between the contrast of compressibility and inverse density is then considered in the second scenario whereas the density variation is neglected in the third scenario. The image corresponding to the attenuation is of particular importance because breast tumors can be better identified using this property in comparison with compressibility and density images. However, this contrast is often poorly reconstructed because the magnitude of this contrast in the mathematical formulation of the problem is generally

---

*© 2017 IEEE. Reprinted, with permission, from Pedram Mojabi and Joe LoVetri, "Evaluation of Balanced Ultrasound Breast Imaging Under Three Density Assumptions," *IEEE Transactions on Computational Imaging*, 2017.

smaller than the magnitude of the contrasts of the other two properties. To overcome this problem, a novel balancing method is applied to all these three inversion algorithms so as to enhance the reconstruction results. Using synthetic data from MRI-based breast models, it is demonstrated that the use of the proposed balancing scheme enhances the reconstruction results of all these algorithms, and in particular enhances their reconstructed images corresponding to the attenuation profile.

3.2 Introduction

Ultrasound tomography (UT) is a non-destructive imaging method that creates quantitative images corresponding to some of the acoustical properties of an object of interest (OI). This information is useful for several application areas such as biomedical imaging and industrial non-destructive testing [3–7]. In biomedical imaging, the main focus of this work, it can be used to distinguish healthy tissues from malignant tissues without the use of biopsy.

The ultrasonic properties of interest for breast imaging applications are compressibility, attenuation and density. In most of the published work related to the use of quantitative UT for biomedical imaging, the effect of the variation of density is neglected [30, 32, 72, 73]. However, this assumption is shown to be not accurate for breast imaging and all three parameters are allowed to vary in the one of the algorithms considered herein [4, 20, 31, 34, 35, 75]. The constant density assumption increases the modelling error in the inversion problem and thereby adversely affects the accuracy of the reconstructed contrast profiles. An improved approach based on assuming a linear relationship between the contrast of compressibility and the density was introduced in [4]. The effect of the variation of density is partially considered using this linear relationship assumption while keeping the same number of unknowns for the OI in the imaging domain. However, this linear relationship assumption is not always accurate for the types of tissues found inside the breast [100, 101].

In this paper, we consider three different scenarios: 1) independent density, 2) linear relation between the contrast of compressibility and inverse density and 3) no variation of density. When the density is considered as an independent unknown, it leads to a more accurate model in the inverse problem; but, the price we pay for this is having one extra unknown function in the imaging domain. However, we can compensate for this extra unknown by providing more measurement data; e.g., by collecting scattering data at multiple frequencies.

Broadly speaking, the papers taking into account the variation of the density as an independent variable to be imaged can be classified into two categories [35]. In the first category, the scattered pressure integral equation is formulated based on one unknown function that depends on both density and the speed of sound [31, 34, 35]. In the second category, the scattered pressure integral equation is formulated as two separate integrals. The first one is a function of a complex-valued compressibility and the second one is a function of density [4, 20, 29, 33, 41, 102]. In this paper, we take the second approach for the independent density case which builds on the work of [20]. Noting that the complex compressibility profile consists of real and imaginary parts, we formulate the UT problem as finding three real unknown profiles (three quantitative images) from scattered data collected outside the OI.

To create the required ultrasonic images of the OI, the scattered-pressure data set is inverted using a nonlinear inversion algorithm to create quantitative images of the OI. There are several alternative set-ups and methods that have been used to collect ultrasonic scattering information and create images from the acquired data. For example: (1) time-of-flight tomography (TFT) [5, 21–24], (2) diffraction tomography (linear inversion algorithm) [26, 27], and (3) full-wave inversion algorithms (nonlinear inversion algorithms) similar to the one considered herein [4, 20, 29–36].

Full-wave UT methods can produce better reconstructions of the OI than the TFT and diffraction tomography methods. This is because the full behaviour of the interrogating wave is modelled with fewer simplifying assumptions; specifically, multiple scattering events are taken into account using this method. Thus, full-wave methods suffer much less from modelling errors as compared to techniques based on TFT and diffraction tomography formulations. In full-wave methods, the UT problem is mathematically formulated as a non-linear inverse scattering problem where total pressure and contrast profiles are unknown and non-linearly related to each other [4, 20, 33]. Different inversion algorithms, some of which have also been used in microwave tomography, can be applied to this non-linear problem; *e.g.,* the Contrast Source Inversion Method (CSI) [41], the Born Iterative Method (BIM) [4, 20, 29], and the Distorted Born Iterative Method (DBIM) [30, 32, 34, 39]. In this paper, BIM is chosen as the non-linear inversion algorithm. We choose BIM because it is computationally more efficient than CSI and DBIM and can therefore manage the resulting large UT problems [4]. It should be noted that DBIM and CSI provide better reconstruction as compared to the BIM for the high contrast objects [4, 27]. Low contrast profiles for breast imaging applications can be obtained by the appropriate choice of the background medium. For example, if water is chosen as a background medium for breast imaging, the variation of the speed of sound will be ±6% [4, 103]. In addition, arranging a low contrast using a specifically chosen background medium allows more interrogation energy to penetrate into the OI, thus, allowing the possibility to extract more useful information for the reconstruction.

The BIM inversion algorithm used in this paper is able to perform simultaneous frequency inversion. This is important as the number of unknowns in the UT inversion algorithm is usually large due to the small operating wavelength(s). To obtain good reconstructions of the contrast profiles, one requires sufficient information about the OI, and utilizing multiple-frequency data sets achieves this. Two methods can be implemented for using multiple-frequency data: (1) frequency hopping techniques [104,105] or (2) simultaneous frequency techniques [33,98]. In this work we implement a simultaneous frequency technique because we've found that it results in enhanced reconstructions.

The UT inverse scattering problem is ill-posed. Therefore, regularization in conjunction with the BIM inversion algorithm is required. Different regularization methods have been proposed to handle the ill-posedness of inverse scattering problems; *e.g.* the Truncated Singular Value Decomposition (TSVD) [47, 48], the standard Tikhonov [32, 42], the L_1-norm Tikhonov [43, 44], Multiplicative [45, 46] and Conjugate Gradient Least squares methods [8, 9, 20, 47]. In this work, the CGLS regularization in conjunction with the BIM inversion algorithm is used as a regularization method to handle the ill-posedness of the UT inverse scattering problem. The main reason to choose CGLS regularization is the computational efficiency of this method. It can be implemented efficiently using some additional matrix-vector multiplications at each iteration of the inverse algorithm. Furthermore, it can be implemented in a such way that it does not require the full storage of the associated ill-posed matrix [33]. The CGLS-BIM method used herein is sufficiently computationally efficient to allow the inversion of large multiple-frequency data sets using a desk-top computer.

This paper contributes to the enhancement of ultrasound inversion results by introducing a balancing method for all the three scenarios that have been described above to effectively normalize the contrasts being inverted. This balancing scheme, which is borrowed from microwave tomography algorithms [49, 50], is necessary when reconstructing tissues where the contrast profiles of interest have significantly different numerical magnitudes. It is well known that most optimization-based inversion algorithms favour the reconstruction of unknowns with a larger magnitude [49]. For example, if the overall value of the real part of the complex compressibility profile is larger than the other two profiles, the inversion algorithm will tend to provide more accurate reconstruction for the real part of the complex compressibility profile at the expense of the reconstruction of the other two profiles. To overcome this numerical issue, we balance all the contrast profiles by creating balanced unknown contrast variables which are used in the optimization problem. The actual unknown contrast variables are then recovered from the reconstructed balanced unknowns. This method requires one to have prior estimates of the expected ranges of the contrast profiles. These expected ranges are readily available in the research literature. It should be noted that in UT the overall value of the contrast profile corresponding to the attenuation is much smaller than the overall values of the other two contrast profiles. (This will be shown in Table 3.1.) Therefore, if these three contrasts are blindly reconstructed, the inversion algorithm often favours the reconstruction of the other two contrast profiles. This is problematic since the image associated with the contrast corresponding to the attenuation is of particular importance compared to the compressibility and density images. As can be seen later in the paper, this is due to the fact that the tumor is more readily identified in the attenuation profile image in comparison with compressibility and density images [51–53]. Thus, having this image leads to an improved method of distinguishing the tumor from healthy tissues.

It is essential to take advantage of the balancing method introduced here. As will be shown in this paper using numerical MRI-based breast phantoms, the balancing method enhances the reconstruction results of all the three scenarios considered in this paper. Therefore, the proposed method in this paper holds promise to be used for ultrasound breast imaging.

The structure of this paper is as follows. We first present the problem statement and mathematical formulation in Section 3.3. The inversion algorithm in conjunction with a balancing method for all the scenarios is then described in Section 3.4. The results are then presented and discussed in Section 3.5. Finally, conclusions and recommendations for future work are presented in Section 3.6.

3.3 Problem Statement

In the UT setup assumed herein, the OI is surrounded by an array of ultrasound transducers. The object is then successively irradiated by each of these transducers operating at several chosen single frequencies over a wide-band frequency spectrum. Thus, a time-harmonic formulation can be used where a time dependency of $e^{j\omega t}$ is assumed (here $j^2 = -1$, t is time, and ω is the angular frequency). Furthermore, we consider UT applications in which images of a cross-section of the OI are created using a 2D assumption for the wave propagation.

To reconstruct the unknown contrast profiles, the discrepancy between the measured and simulated scattered pressure is iteratively minimized. That is,

$$\underset{\chi_1^c,\chi_2}{\operatorname{argmin}} \left\{ \sum_{f=1}^{n_f} \sum_{k=1}^{nTx} \sum_{q=1}^{nRx} \frac{\left\| p^{\text{scat}}_{\text{meas}_{(f,k,q)}} - p^{\text{scat}}_{\text{simu}_{(f,k,q)}} \right\|^2}{\left\| p^{\text{scat}}_{\text{meas}_{(f,k,q)}} \right\|^2} \right\} \tag{3.1}$$

where subscripts "meas" and "simu" denote the measurement and simulated pressure. The simulated pressure is a function of two contrast variables: χ_1^c is the complex-valued variable which holds the contrast of the complex compressibility, and χ_2 holds the contrast of the inverse density. In addition, $\|\cdot\|$ denotes the L^2-norm, n_f, nTx and nRx denote the total number of frequencies, transmitters and receivers, and p^{scat} is the scattered pressure, which is defined as the difference between the total pressure and the incident pressure ($p^{\text{scat}} \triangleq p - p^{\text{inc}}$).

The integral equation for the simulated scattered pressure due to given inhomogeneous compressibility, attenuation and density profiles can be written as [4,20,29,33]

$$\begin{aligned} p^{scat}(\mathbf{r}) &= k_0^2 \int_D g(\mathbf{r},\mathbf{r}') \left[\chi_1(\mathbf{r}') - j\frac{2\delta\alpha(\mathbf{r}')}{k_0}\right] p(\mathbf{r}')\mathrm{d}\mathbf{r}' \\ &+ \int_D g(\mathbf{r},\mathbf{r}')\nabla\cdot\left[\chi_2(\mathbf{r}')\nabla p(\mathbf{r}')\right]\mathrm{d}\mathbf{r}' \end{aligned} \tag{3.2}$$

where $g(\mathbf{r},\mathbf{r}')$ is the Green's function of the background medium and k_0 is the real part of the complex background wavenumber. The contrast of compressibility and inverse density are defined as

$$\chi_1(\mathbf{r}) \triangleq \frac{\kappa(\mathbf{r}) - \kappa_b}{\kappa_b} \tag{3.3}$$

$$\chi_2(\mathbf{r}) \triangleq \frac{\rho^{-1}(\mathbf{r}) - \rho_b^{-1}}{\rho_b^{-1}} \tag{3.4}$$

where κ_b and $\kappa(\mathbf{r})$ are the background compressibility and compressibility at position $\mathbf{r}$. Also, ρ_b^{-1} and $\rho^{-1}(\mathbf{r})$ are the background inverse density and the inverse density at position $\mathbf{r}$. Also, $\delta\alpha(\mathbf{r})$ with the unit of 1/cm is defined as [30]

$$\delta\alpha(\mathbf{r}) \triangleq f \times \frac{\ln 10}{20}\left[\alpha(\mathbf{r}) - \alpha_b\right] \tag{3.5}$$

where $\alpha(\mathbf{r})$ and α_b are the attenuation at position $\mathbf{r}$ and the background attenuation respectively with the units of dB/cm/MHz, and f is the frequency of operation. The complex contrast of compressibility is defined as

$$\chi_1^c(\mathbf{r}) \triangleq \chi_1(\mathbf{r}) - j\frac{2\delta\alpha(\mathbf{r}')}{k_0} \tag{3.6}$$

Thus, in the inverse UT problem we must find the real and imaginary parts of χ_1^c, denoted by χ_{1r}^c and χ_{1i}^c, as well as χ_2, which is assumed to be a real value, from $p_{\text{meas}}^{\text{scat}}$ by minimizing (3.1). In the next section, we discuss how we minimize the above norm using the BIM in conjunction with a balancing method.

3.4 Inversion algorithm in conjunction with a balancing method

In this paper, the Born iterative method (BIM) is utilized as an inversion algorithm. The steps of this method are explained in [4, 20, 33]. Implementation of the BIM requires an efficient solver for the forward scattering problem. The forward solver utilized in this work with some accelerating techniques is explained in [20]. The BIM also requires an operator that maps the contrast profiles into the scattered pressure at the receivers locations. This operator is described next.

3.4.1 Data Operator

At the core of the BIM algorithm are linearized so-called data operators that operate on the contrast profiles to generate the simulated scattered pressure. These linearized operators change at each iteration of the BIM as the estimated total pressure inside the imaging domain is updated. In our formulation, we have two data operators, one operates on the contrast of the complex compressibility, and the other operates on the contrast of the inverse density. The scattered pressure can be written as [20, 33]

$$p^{scat}(\mathbf{r}) = \boldsymbol{\mathcal{G}}_{1s}\left\{\chi_1^c(\mathbf{r}')\right\} + \boldsymbol{\mathcal{G}}_{2s}\left\{\chi_2(\mathbf{r}')\right\} \tag{3.7}$$

where $\boldsymbol{\mathcal{G}}_{1s}$ and $\boldsymbol{\mathcal{G}}_{2s}$ are the required data operators. The subscript s denotes that these operators map to the data domain and the bold sign denotes that the contrasts which these operators operate on are in the continuous domain. These operators and their adjoints denoted by $\boldsymbol{\mathcal{G}}_{1s}^a$ and $\boldsymbol{\mathcal{G}}_{2s}^a$ are shown in [20]. It should be noted that inverting the data operators in the UT problem is an ill-posed problem requiring some form of regularization. The conjugate gradient least squares (CGLS) regularization chosen here requires both the data operators and their adjoints.

3.4.2 Balancing of the Contrasts

In this paper, we consider OIs having contrast variables with significantly different ranges of values such as those encountered in biomedical breast imaging applications where the imaginary part of the complex contrast of compressibility (χ_{1i}^c) is much smaller than the real part of complex contrast of compressibility (χ_{1r}^c) as well as smaller than the contrast of inverse density (χ_2). This can be problematic for optimization-based inversion algorithms because such algorithms favour the reconstruction of variables having larger values and contrasts with variables having small magnitudes are reconstructed poorly. To rectify this issue we introduce new variables to balance the unknowns of the optimization. (This is inspired by a balancing approach in microwave tomography applications [49].) Thus, instead of reconstructing profiles based on the contrast variables, we reconstruct profiles based on the newly balanced variables. This requires prior information regarding the expected ranges of the contrast variables as well as a reformulation of the scattered field equations based on the new balanced contrast variables. The required prior information for the expected contrast ranges in the biomedical breast imaging application can be obtained from the literature [51,52,75,101,103,106]. This balancing method is applied to three different scenarios of the inversion described next.

Scenario 1 (Independent Density)

The reformulated scattered-pressure integral equations, based on the balanced contrast variables, can easily be written in the discretized domain. The data operators and corresponding contrast profiles are first split into their real and imaginary parts [33]. The operation of $\boldsymbol{\mathcal{G}}_{1s}$ on the complex contrast of compressibility in a discretized form can be written as

$$\begin{aligned}\mathcal{G}_{1s}\{\underline{\chi}_1^c\} &= (\mathcal{G}_{1s_r} + j\mathcal{G}_{1s_i})\{\underline{\chi}_{1r}^c + j\underline{\chi}_{1i}^c\} \\ &= \left[\mathcal{G}_{1s_r}\{\underline{\chi}_{1r}^c\} - \mathcal{G}_{1s_i}\{\underline{\chi}_{1i}^c\}\right] \\ &+ j\left[\mathcal{G}_{1s_i}\{\underline{\chi}_{1r}^c\} + \mathcal{G}_{1s_r}\{\underline{\chi}_{1i}^c\}\right] \end{aligned} \tag{3.8}$$

where the underscore identifies the discretized variables and bold-face type has been removed from the operators to signify that they now operate on discretized variables. The subscripts r and i, denote the real and imaginary parts of the variables. These same subscripts on the operators signify that the real and imaginary parts are chosen after the operator is applied, that is

$$\mathcal{G}_{1s_r}\{\cdot\} \triangleq \mathrm{Re}\left(\mathcal{G}_{1s}\{\cdot\}\right), \quad \mathcal{G}_{1s_i}\{\cdot\} \triangleq \mathrm{Im}\left(\mathcal{G}_{1s}\{\cdot\}\right) \tag{3.9}$$

The same procedure is applied for the operation of $\mathcal{G}_{2s}$ which operates on the real-valued contrast of inverse density:

$$\mathcal{G}_{2s}\{\underline{\chi}_2\} = \mathcal{G}_{2s_r}\{\underline{\chi}_{2r}\} + j\mathcal{G}_{2s_i}\{\underline{\chi}_{2r}\} \tag{3.10}$$

The discretized scattered pressure can be formally written in matrix form as

$$\begin{pmatrix} \underline{p}_r^{scat} \\ \underline{p}_i^{scat} \end{pmatrix} = \begin{pmatrix} \mathcal{G}_{1s_r} & -\mathcal{G}_{1s_i} & \mathcal{G}_{2s_r} \\ \mathcal{G}_{1s_i} & \mathcal{G}_{1s_r} & \mathcal{G}_{2s_i} \end{pmatrix} \begin{pmatrix} \underline{\chi}_{1r}^c \\ \underline{\chi}_{1i}^c \\ \underline{\chi}_{2r} \end{pmatrix} \tag{3.11}$$

where $\underline{p}_r^{scat}$ and $\underline{p}_i^{scat}$ are the real and imaginary parts of the discretized scattered pressure. Note that in the above equation, each of the "matrix blocks" which operates on a real vector containing one of the three contrasts, cannot easily be written down as a matrix. In fact, each block represents a series of matrix operations which depend on the form of the discretization chosen (i.e, the basis and weighting functions in the Method of Moments, as well as the discretization of the gradient and divergence operations). The overall result of these block-operations on the vector of discretized contrast profiles gives a real vector containing the real and imaginary parts of the scattered pressure.

Scalar balancing coefficients are now applied to this equation to balance the contrast variables. To this end, the right hand side of (3.11) is written as

$$\begin{pmatrix} Q_1\,\mathcal{G}_{1s_r} & -Q_2\,\mathcal{G}_{1s_i} & Q_3\,\mathcal{G}_{2s_r} \\ Q_1\,\mathcal{G}_{1s_i} & Q_2\,\mathcal{G}_{1s_r} & Q_3\,\mathcal{G}_{2s_i} \end{pmatrix} \begin{pmatrix} Q_1^{-1}\,\underline{\chi}_{1r}^c \\ Q_2^{-1}\,\underline{\chi}_{1i}^c \\ Q_3^{-1}\,\underline{\chi}_{2r} \end{pmatrix} \tag{3.12}$$

where Q_1, Q_2 and Q_3 are the chosen scalar balancing coefficients. These coefficients are chosen based on the prior information about the expected ranges of the contrast profiles. Thus, we can define the normalized contrast variables as

$$\underline{\chi}_{1r}^{cn} \triangleq \frac{\underline{\chi}_{1r}^{c}}{Q_1}, \quad \underline{\chi}_{1i}^{cn} \triangleq \frac{\underline{\chi}_{1i}^{c}}{Q_2}, \quad \underline{\chi}_{2r}^{n} \triangleq \frac{\underline{\chi}_{2r}}{Q_3} \tag{3.13}$$

where the superscript n denotes that these contrast variables are normalized. It should be noted that these scalar coefficients are chosen to ensure that the overall magnitudes of all these normalized contrast profiles are within the same range. Then, the normalized contrast profiles having the same range of magnitude are reconstructed instead of the actual contrast profiles. As will be see later, this leads to much better reconstruction for the small contrast profiles.

This problem can now be considered as an $\mathcal{A}x = b$ where b is a real vector of length $2 \times nRx \times nTx$ containing the real and imaginary parts of the measured scattered pressure, x is a real unknown vector of length $3N$ containing the normalized contrast variables, and $\mathcal{A}$ is a balanced data operator that operates on the normalized contrast variables. The result of this operation is a real vector containing the real and imaginary parts of the scattered pressure which can be found as [33]

$$\begin{aligned} \underline{p}_r^{scat} &= Q_1 \mathrm{Re}\left(\mathcal{G}_{1s}\{\underline{\chi}_{1r}^{cn}\}\right) - Q_2 \mathrm{Im}\left(\mathcal{G}_{1s}\{\underline{\chi}_{1i}^{cn}\}\right) \\ &+ Q_3 \mathrm{Re}\left(\mathcal{G}_{2s}\{\underline{\chi}_{2r}^{n}\}\right) \end{aligned} \tag{3.14}$$

$$\begin{aligned} \underline{p}_i^{scat} &= Q_1 \mathrm{Im}\left(\mathcal{G}_{1s}\{\underline{\chi}_{1r}^{cn}\}\right) + Q_2 \mathrm{Re}\left(\mathcal{G}_{1s}\{\underline{\chi}_{1i}^{cn}\}\right) \\ &+ Q_3 \mathrm{Im}\left(\mathcal{G}_{2s}\{\underline{\chi}_{2r}^{n}\}\right) \end{aligned} \tag{3.15}$$

As mentioned in Section 3.4.1, the CGLS regularization requires the adjoint of the data operator. Thus, the balancing coefficients must be incorporated into the adjoint of the data operator. It should be noted that this adjoint operator operates on the result of the operation of the balanced data operator on the predicted normalized contrast variables.

To find the adjoint of the balanced data operator, we perform the same procedure explained for the balanced data operator. Thus, both the predicted scattered pressure and the adjoint operator should be split into real and imaginary parts. The operation of $\boldsymbol{\mathcal{G}}^a_{1s}$ on the scattered pressure in a discretized form can be written as [33]

$$\mathcal{G}^a_{1s}\{\underline{p}^{scat}\} = (\mathcal{G}^a_{1s_r} + j\mathcal{G}^a_{1s_i})\{\underline{p}^{scat}_r + j\underline{p}^{scat}_i\} \tag{3.16}$$

where $\mathcal{G}^a_{1s_r}\{\cdot\}$ and $\mathcal{G}^a_{1s_i}\{\cdot\}$ can formally be defined as the following operations

$$\mathcal{G}^a_{1s_r}\{\cdot\} \triangleq \mathrm{Re}\Big(\mathcal{G}^a_{1s}\{\cdot\}\Big), \quad \mathcal{G}^a_{1s_i}\{\cdot\} \triangleq \mathrm{Im}\Big(\mathcal{G}^a_{1s}\{\cdot\}\Big) \tag{3.17}$$

Thus, the real and imaginary parts of the result can be found as

$$\begin{aligned} \mathcal{G}^a_{1s}\{\underline{p}^{scat}\} &= \Big[\mathcal{G}^a_{1s_r}\{\underline{p}^{scat}_r\} + \mathcal{G}^a_{1s_r}\{j\underline{p}^{scat}_i\}\Big] \\ &+ j\Big[\mathcal{G}^a_{1s_i}\{\underline{p}^{scat}_r\} + \mathcal{G}^a_{1s_i}\{j\underline{p}^{scat}_i\}\Big] \end{aligned} \tag{3.18}$$

The same procedure is performed for $\mathcal{G}^a_{2s}$ as

$$\mathcal{G}^a_{2s}\{\underline{p}^{scat}\} = (\mathcal{G}^a_{2s_r} + j\mathcal{G}^a_{2s_i})\{\underline{p}^{scat}_r + j\underline{p}^{scat}_i\} \tag{3.19}$$

The real and imaginary parts of $\mathcal{G}^a_{2s}\{p^{scat}\}$ can be written as

$$\begin{aligned}\mathcal{G}^a_{2s}\{\underline{p}^{scat}\} &= \left[\mathcal{G}^a_{2s_r}\{\underline{p}^{scat}_r\} + \mathcal{G}^a_{2s_r}\{j\underline{p}^{scat}_i\}\right] \\ &+ j\left[\mathcal{G}^a_{2s_i}\{\underline{p}^{scat}_r\} + \mathcal{G}^a_{2s_i}\{j\underline{p}^{scat}_i\}\right] \qquad (3.20)\end{aligned}$$

At each iteration of the algorithm, this last equation returns a predicted contrast of inverse density which is known to have a zero imaginary part. Thus, the imaginary part is forced to be zero. The final form of the adjoint operator on the predicted scattered pressure is written as

$$\begin{pmatrix}\underline{x}_1\\ \underline{x}_2\\ \underline{x}_3\end{pmatrix} = \begin{pmatrix}\mathcal{G}^a_{1s_r} & \mathcal{G}^a_{1s_r}\\ \mathcal{G}^a_{1s_i} & \mathcal{G}^a_{1s_i}\\ \mathcal{G}^a_{2s_r} & \mathcal{G}^a_{2s_r}\end{pmatrix}\begin{pmatrix}\underline{p}^{scat}_r\\ j\underline{p}^{scat}_i\end{pmatrix} \qquad (3.21)$$

In accordance with the balanced data operator, we must apply the same balancing coefficients in the adjoint operation

$$\begin{pmatrix}\underline{x}_1\\ \underline{x}_2\\ \underline{x}_3\end{pmatrix} = \begin{pmatrix}Q_1\,\mathcal{G}^a_{1s_r} & Q_1\,\mathcal{G}^a_{1s_r}\\ Q_2\,\mathcal{G}^a_{1s_i} & Q_2\,\mathcal{G}^a_{1s_i}\\ Q_3\,\mathcal{G}^a_{2s_r} & Q_3\,\mathcal{G}^a_{2s_r}\end{pmatrix}\begin{pmatrix}\underline{p}^{scat}_r\\ j\underline{p}^{scat}_i\end{pmatrix} \qquad (3.22)$$

The adjoint operator returns a real vector of length $3N$. The elements of this vector are denoted by $\underline{x}_1$, $\underline{x}_2$, and $\underline{x}_3$; each of which is a real vector of length N. These vectors can be found as

$$\underline{x}_1 = Q_1\mathrm{Re}\Big(\mathcal{G}^a_{1s}\{\underline{p}^{scat}_r\}\Big) + Q_1\mathrm{Re}\Big(\mathcal{G}^a_{1s}\{j\underline{p}^{scat}_i\}\Big) \qquad (3.23)$$

$$\underline{x}_2 = Q_2\mathrm{Im}\Bigg(\mathcal{G}^a_{1s}\{\underline{p}^{scat}_r\}\Bigg) + Q_2\mathrm{Im}\Bigg(\mathcal{G}^a_{1s}\{j\underline{p}^{scat}_i\}\Bigg) \tag{3.24}$$

$$\underline{x}_3 = Q_3\mathrm{Re}\Bigg(\mathcal{G}^a_{2s}\{\underline{p}^{scat}_r\}\Bigg) + Q_3\mathrm{Re}\Bigg(\mathcal{G}^a_{2s}\{j\underline{p}^{scat}_i\}\Bigg) \tag{3.25}$$

The balanced contrast variables which are reconstructed at each iteration of the BIM are converted to the actual contrast variables based on (3.13).

Scenario 2 (assumption of a linear relationship between the contrast of compressibility and inverse density)

Herein, the balancing method is applied for the scattered pressure equation with the assumption of a linear relationship between the contrast of compressibility and contrast of inverse density. Specifically, based on [4], we assume $\chi^c_{1r} = 2.4\chi_2$. To apply a balancing method, the same procedure explained in 3.4.2 is utilized. It should be noted that the inversion algorithm reconstruct the real and imaginary part of χ^c_1 in each iteration. Therefore, only one scalar balancing coefficient denoted by Q is utilized as shown below

$$\underline{\chi}^{cn}_{1i} \triangleq \frac{\underline{\chi}^c_{1i}}{Q}. \tag{3.26}$$

The result of the operation of the data operator on the contrast profiles with this assumption is a real vector containing the real and imaginary part of the scattered pressure which can be found as

$$\begin{aligned} \underline{p}^{scat}_r &= \mathrm{Re}\left(\mathcal{G}_{1s}\{\underline{\chi}^c_{1r}\}\right) - Q\mathrm{Im}\left(\mathcal{G}_{1s}\{\underline{\chi}^{cn}_{1i}\}\right) \\ &+ \frac{1}{2.4}\mathrm{Re}\left(\mathcal{G}_{2s}\{\underline{\chi}^c_{1r}\}\right) \end{aligned} \tag{3.27}$$

$$
\begin{aligned}
\underline{p}_i^{scat} &= \mathrm{Im}\left(\mathcal{G}_{1s}\{\underline{\chi}_{1r}^{c}\}\right) + Q\mathrm{Re}\left(\mathcal{G}_{1s}\{\underline{\chi}_{1i}^{cn}\}\right) \\
&+ \frac{1}{2.4}\mathrm{Im}\left(\mathcal{G}_{2s}\{\underline{\chi}_{1r}^{c}\}\right) \qquad (3.28)
\end{aligned}
$$

The adjoint of this operator returns a real vector of length $2N$. The elements of this vector are denoted by $\underline{x_1}$ and $\underline{x_2}$. It should be noted that each of them is a real vector of length N and can be found as

$$
\begin{aligned}
\underline{x}_1 &= \mathrm{Re}\Bigg(\mathcal{G}_{1s}^{a}\{\underline{p}_r^{scat}\}\Bigg) + \mathrm{Re}\Bigg(\mathcal{G}_{1s}^{a}\{j\underline{p}_i^{scat}\}\Bigg) \qquad (3.29) \\
&+ \frac{1}{2.4}\mathrm{Re}\Bigg(\mathcal{G}_{2s}^{a}\{\underline{p}_r^{scat}\}\Bigg) + \frac{1}{2.4}\mathrm{Re}\Bigg(\mathcal{G}_{2s}^{a}\{j\underline{p}_i^{scat}\}\Bigg)
\end{aligned}
$$

$$
\underline{x}_2 = Q\mathrm{Im}\Bigg(\mathcal{G}_{1s}^{a}\{\underline{p}_r^{scat}\}\Bigg) + Q\mathrm{Im}\Bigg(\mathcal{G}_{1s}^{a}\{j\underline{p}_i^{scat}\}\Bigg) \qquad (3.30)
$$

Scenario 3 (assumption of no variation in the density profile)

Neglecting the variation of density, *i.e.*, $\chi_2 = 0$, is another assumption which can be utilized in the inversion algorithm to simplify the scattered pressure equation. This assumption leads to removing the second integral in (3.2). In this case, the inversion algorithm reconstruct two contrast profiles, χ_{1r}^{c} and χ_{1i}^{c}, so that only one scalar balancing coefficient is required. In our implementation, the balancing coefficient is applied to χ_{1i}^{c} as shown in (3.26) to make the overall magnitude of χ_{1i}^{cn} be in the same range of χ_{1r}^{c}. The procedure of finding the balancing method for this case is similar to 3.4.2. It should be noted that only $\mathcal{G}_{1s}$ and its adjoint are utilized in this case.

3.5 Results

Herein, two 2D inversion examples using synthetically generated data are considered. The first example is the reconstruction of the contrast profiles for an MRI-based breast phantom containing a medium-sized tumor [2, 107] within a $12\lambda_{\min} \times 12\lambda_{\min}$ imaging domain. In the second example, we consider an MRI-based numerical phantom of a dense breast (*i.e.*, one containing a substantial amount of fibroglandular tissue) [2, 107] enclosed within a $12\lambda_{\min} \times 12\lambda_{\min}$ imaging domain. The true tissue image of these phantoms are shown in Fig 3.1. It should be noted that the use of 2D inversion algorithms for a 3D object results in some extra errors in the reconstruction. In this paper, our MRI-based numerical phantoms are 2D, and therefore, we have not considered the errors associated with applying a 2D inversion algorithm to a 3D object.

The ranges of the chosen values of the speed of sound, density and attenuation for each tissue of these synthetic breast phantoms are chosen based on [2, 51, 52, 100, 101, 108]. To set the property values for each tissue we apply a uniformly distributed random function to set values for every pixel within that tissue. For example, if the upper and lower ranges of a property associated with a given tissue type are UR and LR respectively, the true quantitative values for that property within that tissue are chosen to be $UR + (LR - UR) \times rand$, where $rand$ is a uniformly distributed random number between 0 and 1. The range of the contrast profiles for each tissue based on the chosen ranges of speed, attenuation and density is shown in Table 3.1. Water is chosen as the background medium where the speed of sound, density and attenuation at $22°C$ are $c_b = 1483$ $[\frac{\text{m}}{\text{s}}]$, $\rho_b = 1000$ $[\frac{\text{kg}}{\text{m}^3}]$ and $\alpha_b = 0.0022$ $[\frac{\text{dB}}{\text{cm MHz}}]$ [33, 108].

For all the examples, we first show reconstructions with and without balancing assuming an independent density variation (scenario 1). Then, we show the reconstruction with and without the balancing method with the assumption of $\chi_{1r}^{c} = 2.4\chi_2$ and $\chi_2 = 0$ (scenario 2 and scenario 3). It should be noted that all the synthetic measured data are generated based on assuming inhomogeneous complex compressibility and inverse density contrasts. For scenario 3, we also show reconstructions, with and without the balancing method, using the Multiplicatively Regularized Gauss-Newton Inversion (MR-GNI) method. The number of transmitters and receivers for these examples are set as 120. The transducers are placed outside of the imaging domain on a circle of radius 11 cm as depicted in Fig 3.2. In all the breast phantom examples except the one that we consider different noise levels, the synthetic data is contaminated with two percent noise using the following equation [109]

$$p_{noisy}^{scat} = p_{simulated}^{scat} + \max\left(|p_{simulated}^{scat}|\right) \times \frac{NP \times RV}{\sqrt{2}} \tag{3.31}$$

$$-1 < RV < 1$$

where RV is a uniformly distributed random vector and NP is a noise percentage. It should be noted that although this type of synthetic noise has been already utilized in literature to create synthetic noisy data, we are unsure whether this type of additive noise is representative of that inherent in real US systems. The multiple frequencies that are utilized are in the range defined by: $110 \leq f \leq 200$ kHz. It should be noted that these frequency ranges are not representative of current US technology [51,110,111]; *e.g.*, frequency ranges between 0.4-1MHz are utilized in [110]. The only reason that the 100 to 200 kHz frequency range was chosen in this paper is to avoid having a very large domain due to the increased computational complexity. However, this balancing method can still be utilized for higher range of frequencies, but we would require a faster computer with more memory and a parallel implementation.

Table 3.1: The range of the contrast profiles for breast tissues.

Tissue	χ_{1r}^{c}	χ_{1i}^{c}	χ_2
Fat	$(0.0891, 0.1756)$	$(-0.0054, -0.0005)$	$(0.0411, 0.0627)$
Cyst	$(-0.0995, -0.0472)$	$(-0.0019, -0.0005)$	$(-0.029, -0.012)$
Glandular	$(-0.0886, -0.037)$	$(-0.0081, -0.0043)$	$(0.0215, 0.0384)$
Tumor	$(-0.1654, -0.0975)$	$(-0.0163, -0.0120)$	$(0.0021, 0.0183)$
Skin	$(-0.3728, -0.3333)$	$(-0.0046, -0.0035)$	$(-0.1266, -0.1135)$

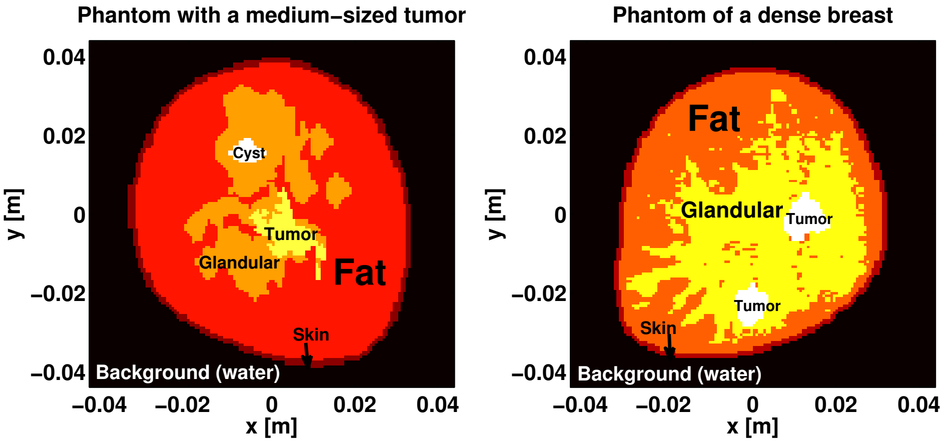

Figure 3.1: The true tissue type images for MRI-based numerical breast phantoms.

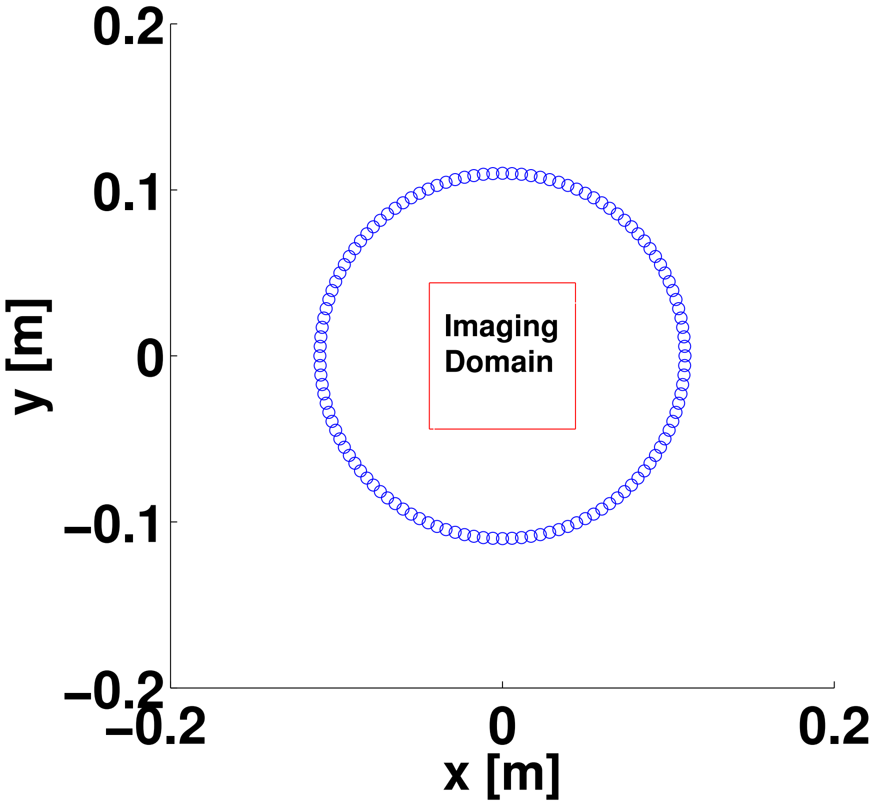

Figure 3.2: Transmitters and receivers positions. The transducers are in a circle with a radius of 11 cm.

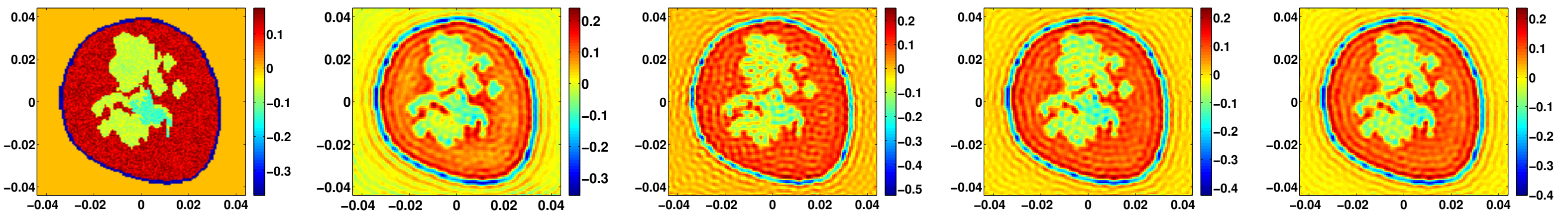

(a) True χ_{1r}^{c} (b) χ_{1r}^{c}-No Balancing (c) χ_{1r}^{c}-Balancing set 1 (d) χ_{1r}^{c}-Balancing set 2 (e) χ_{1r}^{c}-Balancing set 3

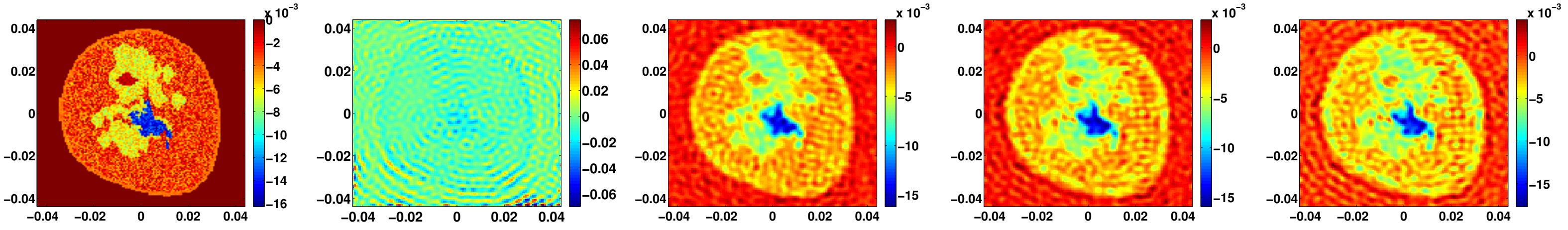

(f) True χ_{1i}^{c} (g) χ_{1i}^{c}-No Balancing (h) χ_{1i}^{c}-Balancing set 1 (i) χ_{1i}^{c}-Balancing set 2 (j) χ_{1i}^{c}-Balancing set 3

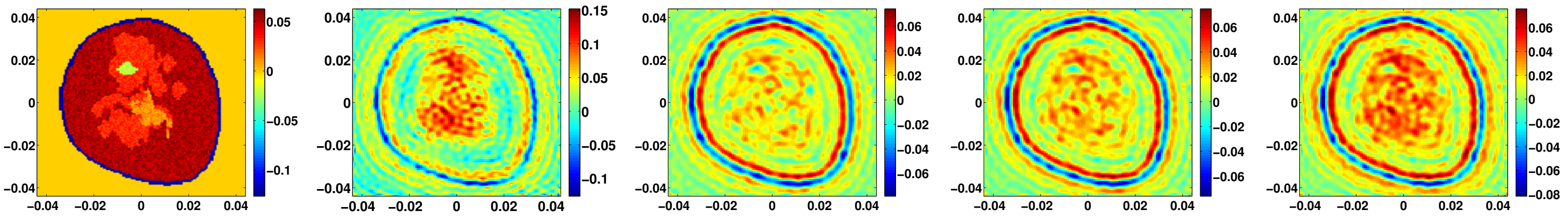

(k) True χ_2 (l) χ_2-No Balancing (m) χ_2-Balancing set 1 (n) χ_2-Balancing set 2 (o) χ_2-Balancing set 3

Figure 3.3: The first column corresponds to the true contrast profiles for the MRI-based breast phantom with medium size tumor. The second column corresponds to the reconstruction without using a balancing method ($Q_1 = Q_2 = Q_3 = 1$). The third, fourth and fifth columns correspond to the simultaneous reconstruction of independent χ_{1r}^{c} and χ_2 using a balancing coefficients set 1, set 2, and set 3 respectively.

3.5.1 How to determine the balancing coefficients

To choose proper balancing coefficients, we utilize the available tissue contrast information shown in Table 3.1. As noted earlier, the balancing coefficients should be chosen so that the overall magnitude of all the normalized contrast variables are within the same range. In this paper, we try to keep the values of all the contrast profiles within the same range of the real part of complex compressibility contrast. Thus, Q_1 is chosen to be one. The ranges of Q_2 and Q_3 can be calculated as

$$\frac{\sum_{T=1}^{N_T} \left|\chi^c_{1i_{(T)}}\right|_{\min}}{\sum_{T=1}^{N_T} \left|\chi^c_{1r_{(T)}}\right|_{\max}} < Q_2 < \frac{\sum_{T=1}^{N_T} \left|\chi^c_{1i_{(T)}}\right|_{\max}}{\sum_{T=1}^{N_T} \left|\chi^c_{1r_{(T)}}\right|_{\min}} \tag{3.32}$$

$$\frac{\sum_{T=1}^{N_T} \left|\chi_{2_{(T)}}\right|_{\min}}{\sum_{T=1}^{N_T} \left|\chi^c_{1r_{(T)}}\right|_{\max}} < Q_3 < \frac{\sum_{T=1}^{N_T} \left|\chi_{2_{(T)}}\right|_{\max}}{\sum_{T=1}^{N_T} \left|\chi^c_{1r_{(T)}}\right|_{\min}} \tag{3.33}$$

where N_T is the number of the chosen tissue types. The ranges obtained for Q_2 and Q_3 via (3.32) and (3.33) for the case that we consider five different tissue types (*i.e,* skin, fat, glandular, tumor and cyst) are

$$0.0231 < Q_2 < 0.06, \qquad 0.2109 < Q_3 < 0.4552$$

To show the robustness of our algorithm with respect to balancing coefficients chosen from the above ranges, three sets of balancing coefficients are chosen for scenario 1. The first, second and third sets are based on minimum ($Q_1 = 1, Q_2 = 0.023$, and $Q_3 = 0.21$), average ($Q_1 = 1, Q_2 = 0.04$, and $Q_3 = 0.33$) and maximum ($Q_1 = 1, Q_2 = 0.06$, and $Q_3 = 0.45$) ranges of balancing coefficients respectively. However, the result of the contrast profiles using a balancing method for scenario 2 and scenario 3 is only shown for the average range (*i.e,* $Q = 0.04$).

3.5.2 MRI-based numerical phantom with a medium-sized tumor

This example corresponds to the MRI-based numerical phantom having five regions specified with properties corresponding to skin, fat, glandular, tumor and cyst (or, Fibroadenoma) enclosed within about a $12\lambda_{\min} \times 12\lambda_{\min}$ imaging domain as shown in Fig 3.1 (the cyst region is added to the numerical phantom that was developed at the University of Calgary, Canada [107]). The true contrast profiles for this breast model are shown in the first column of Fig 3.3. Three frequencies, $f = [110, 150, 200]$ kHz, are simultaneously utilized for the inversion. The results of the reconstruction of the contrast profiles for the independent density formulation without applying the balancing method, *i.e,* $Q_1 = Q_2 = Q_3 = 1$, is shown in the second column of Fig 3.3. As can be seen, χ^c_{1i} is poorly reconstructed due to small value of this contrast in comparison with the other contrast profiles. Also, as can be seen, the reconstruction of χ_2 is not good either.

Three different sets of balancing coefficients are utilized for the scenario 1 explained in Section 3.4.2 (independent density). These sets are mentioned in Section 3.5.1. The result of the reconstruction of the contrast profiles using these sets of balancing coefficients are shown in the third, fourth and fifth columns of Fig 3.3. Comparing the results obtained with and without a balancing method, it can be seen that the reconstruction of χ^c_{1i} and χ_2 are improved using the balancing method. Furthermore, the imaginary part of the complex contrast of compressibility is significantly improved. The image obtained from χ^c_{1i} is important due to the fact that it is easier to distinguish the tumor from the healthy tissues in this image as compared to the other two images [53]. This can be better understood by noting that the attenuation in tumor tissue is much higher than the other tissues [51, 52]. It should be noted that although the reconstruction of inverse density is not very good, as will be shown later the independent variation of density leads to better reconstructions of χ^c_{1r} and χ^c_{1i}. This is consistent with the observation made in [29]. Finally, it should be noted that three sets of values for balancing coefficients resulted in the enhancement of the reconstruction results. Thus, based on this result, and other results (not shown here), we speculate that the algorithm is not very sensitive to the choice of balancing coefficients.

The reconstructions of χ^c_{1r} and χ^c_{1i} based on the scenario 2 explained in Section 3.4.2 ($\chi^c_{1r} = 2.4\chi_2$) without and with applying the balancing method are shown in the first and second rows of Fig 3.4. The reconstructions of χ^c_{1r} and χ^c_{1i} based on the scenario 3 explained in Section 3.4.2 ($\chi_2 = 0$) without and with using a balancing method are shown in the third and fourth rows of Fig 3.4. As can be seen, the reconstruction of χ^c_{1i} is significantly improved using the balancing method for both scenarios.

The residual errors for the real and imaginary parts of χ^c_1 for different cases of applying or not applying the balancing method for all the scenarios are tabulated in Table 3.2. In this table, the residual errors for the skin, fat, glandular, and tumor regions as well as the total errors (the background medium is not considered in calculating the total errors) are calculated. This means that the error formulas listed at the bottom of the table are applied to either the whole breast, for the total error, or only in the region where each tissue is supposed to be reconstructed based on the true model. It should be noted that to calculate the residual error the meshes utilized in the inversion algorithm are interpolated to the mesh utilized in the true value mesh of the contrast profiles. The interpolation is based on the linear interpolation. As can be seen, the residual errors for scenario 1 with different balancing sets (case 2, 3 and 4) are much smaller than the residual errors for scenario 1 without the balancing method (case 1), especially for Error_2 which corresponds to the imaginary part of χ_1^c. The residual errors are also decreased using a balancing method for scenarios 2 and 3 compared to unbalanced cases. Furthermore, the total residual errors and also the residual errors for most of the tissue types are decreased in the balanced scenario 1 in comparison with the balanced scenario 2 and scenario 3.

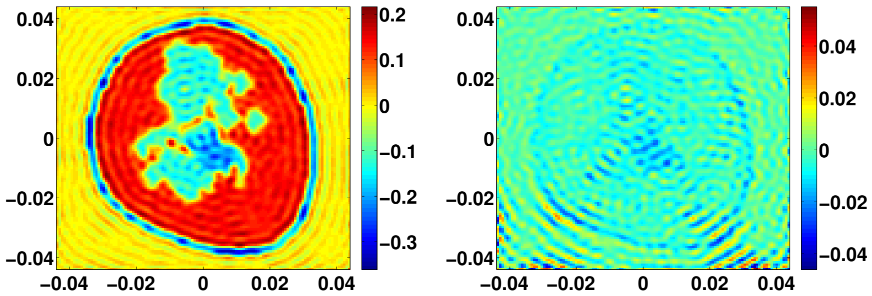

(a) χ_{1r}^{c}-No Balancing (b) χ_{1i}^{c}-No Balancing

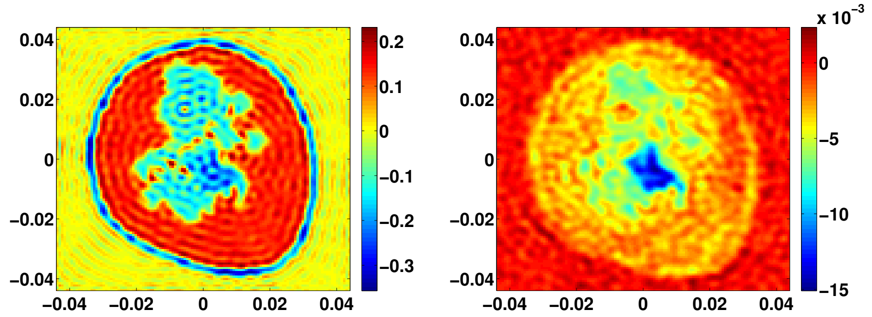

(c) χ_{1r}^{c}-Balancing (d) χ_{1i}^{c}-Balancing

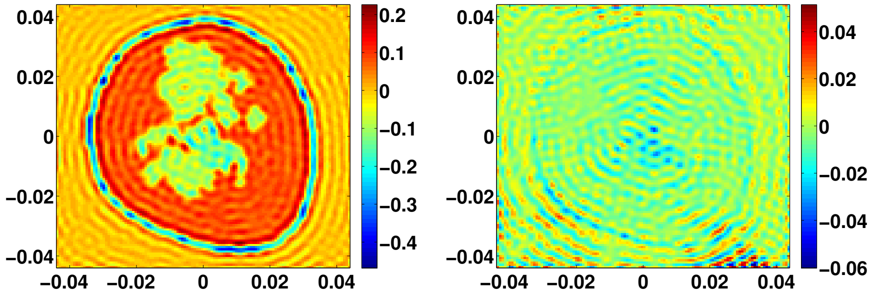

(e) χ_{1r}^{c}-No Balancing (f) χ_{1i}^{c}-No Balancing

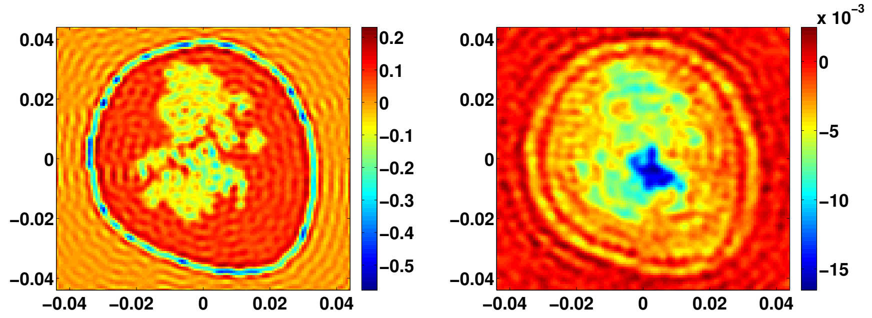

(g) χ_{1r}^{c}-Balancing (h) χ_{1i}^{c}-Balancing

Figure 3.4: The first and second rows correspond to the reconstruction of the χ_1^c based on the scenario 2 without and with using the balancing method. The third and fourth rows correspond to the reconstruction of χ_1^c based on scenario 3 without and with using the balancing method.

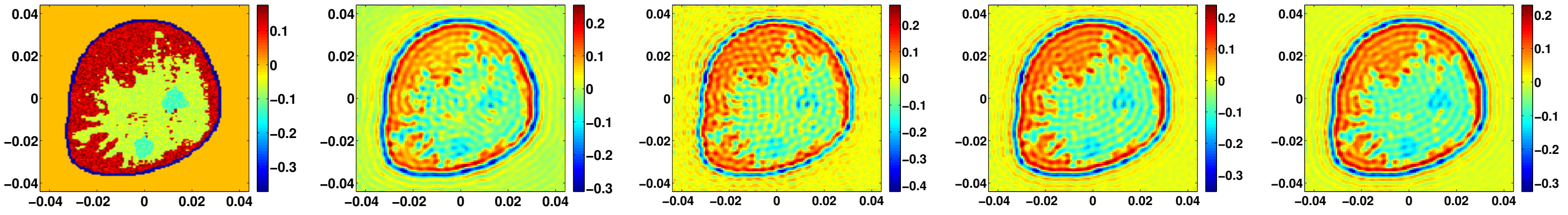

(a) True χ_{1r}^{c} (b) χ_{1r}^{c}-No Balancing (c) χ_{1r}^{c}-Balancing set 1 (d) χ_{1r}^{c}-Balancing set 2 (e) χ_{1r}^{c}-Balancing set 3

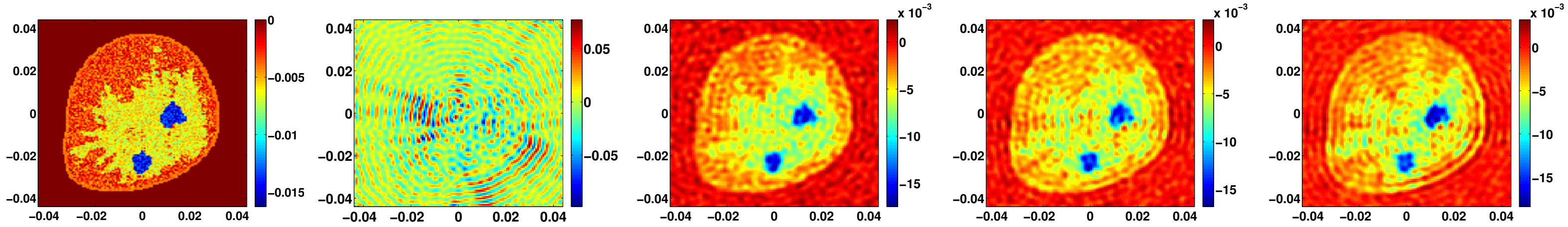

(f) True χ_{1i}^{c} (g) χ_{1i}^{c}-No Balancing (h) χ_{1i}^{c}-Balancing set 1 (i) χ_{1i}^{c}-Balancing set 2 (j) χ_{1i}^{c}-Balancing set 3

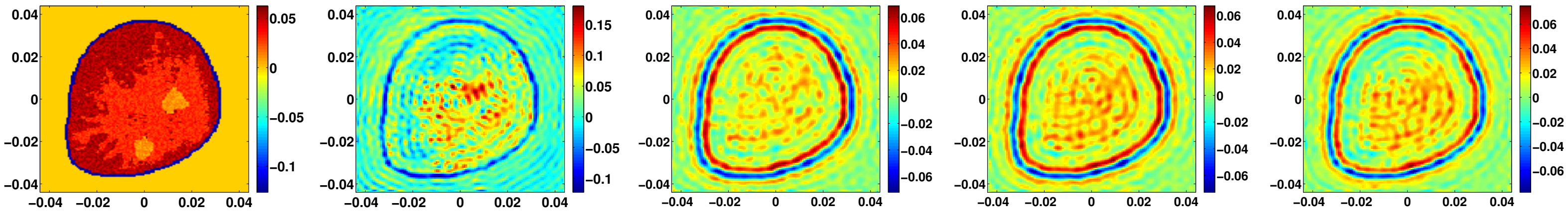

(k) True χ_2 (l) χ_2-No Balancing (m) χ_2-Balancing set 1 (n) χ_2-Balancing set 2 (o) χ_2-Balancing set 3

Figure 3.5: The first column corresponds to the true contrast profiles for the MRI-based breast phantom of a dense breast. The second column corresponds to the reconstruction without using a balancing method ($Q_1 = Q_2 = Q_3 = 1$). The third, fourth and fifth columns correspond to the simultaneous reconstruction of independent χ_{1r}^{c} and χ_2 using a balancing coefficients sets 1, 2, and 3 respectively.

3.5.3 MRI-based numerical phantom of a dense breast

The MRI-based numerical phantom of a dense breast having four tissue regions specified with properties corresponding to skin, fat, glandular and tumor enclosed within a $12\lambda_{\text{min}} \times 12\lambda_{\text{min}}$ imaging domain is considered in this example [107]. The true tissue image and contrast profiles for this breast phantom are shown in the Fig 3.1 (right side) and the first column of Fig 3.5, respectively. Three frequencies, $f = [110, 150, 200]$ kHz, are simultaneously utilized for the inversion. The reconstructions of the independent χ_1^c and χ_2 (scenario 1) without using a balancing method ($Q_1 = Q_2 = Q_3 = 1$) are shown in the second column of Fig 3.5. As can be seen, χ_{1i}^c and χ_2 are poorly reconstructed. Three sets of the balancing coefficients used in the first example are utilized to improve this results. The result of the reconstruction using these three sets of balancing coefficients for the scenario 1 are shown in the third, fourth, and fifth columns of Fig 3.5. As can be seen in Fig 3.5, the reconstructions of the contrast profiles using the newly introduced balancing method are much better than the reconstructions obtained without balancing the contrasts. Furthermore, all the three balancing sets resulted in the enhancement of the reconstruction results.

The reconstructions of the real and imaginary parts of complex contrast of compressibility using the balancing method based on scenario 2 are shown in the first column of Fig 3.6. Results of the reconstruction of the contrast profiles based on scenario 3 using different noise levels ranging from two to eight percent without and with using the balancing method are also shown in Fig 3.6. The second column of this figure corresponds to the reconstruction of the contrast profiles based on scenario 3 without applying the balancing method for the case that the data is contaminated with two percent noise. The third, forth and fifth columns of Fig 3.6 correspond to the reconstruction of the real and imaginary parts of χ_1^c based on scenario 3 using

Table 3.2: Residual Error for the different reconstructions of χ_1^c with respect to the true value of the corresponding contrast profile for the MRI-based numerical phantom with a medium sized tumor. Errors are provided for all three scenarios.

Case	Phantom	Error Skin	Error Fat	Error Glandulart	Error Tumor	Error Total
1	Scenario 1 Independent ρ No Balancing	$\text{Error}_1 = 0.227$ $\text{Error}_2 = 4.29$	$\text{Error}_1 = 0.218$ $\text{Error}_2 = 4.03$	$\text{Error}_1 = 0.772$ $\text{Error}_2 = 1.03$	$\text{Error}_1 = 0.352$ $\text{Error}_2 = 0.25$	$\text{Error}_1 = 0.247$ $\text{Error}_2 = 1.925$
2	Scenario 1 Independent ρ Balancing set1	$\text{Error}_1 = 0.155$ $\text{Error}_2 = 0.111$	$\text{Error}_1 = 0.243$ $\text{Error}_2 = 0.247$	$\text{Error}_1 = 0.679$ $\text{Error}_2 = 0.072$	$\text{Error}_1 = 0.174$ $\text{Error}_2 = 0.061$	$\text{Error}_1 = 0.223$ $\text{Error}_2 = 0.126$
3	Scenario 1 Independent ρ Balancing set2	$\text{Error}_1 = 0.178$ $\text{Error}_2 = 0.103$	$\text{Error}_1 = 0.234$ $\text{Error}_2 = 0.269$	$\text{Error}_1 = 0.493$ $\text{Error}_2 = 0.076$	$\text{Error}_1 = 0.167$ $\text{Error}_2 = 0.063$	$\text{Error}_1 = 0.22$ $\text{Error}_2 = 0.135$
4	Scenario 1 Independent ρ Balancing set3	$\text{Error}_1 = 0.19$ $\text{Error}_2 = 0.125$	$\text{Error}_1 = 0.225$ $\text{Error}_2 = 0.341$	$\text{Error}_1 = 0.471$ $\text{Error}_2 = 0.074$	$\text{Error}_1 = 0.176$ $\text{Error}_2 = 0.051$	$\text{Error}_1 = 0.219$ $\text{Error}_2 = 0.154$
5	Scenario 2 $\chi_{1r}^c = 2.4\chi_2$ No Balancing	$\text{Error}_1 = 0.215$ $\text{Error}_2 = 2.878$	$\text{Error}_1 = 0.22$ $\text{Error}_2 = 2.501$	$\text{Error}_1 = 0.934$ $\text{Error}_2 = 0.604$	$\text{Error}_1 = 0.296$ $\text{Error}_2 = 0.171$	$\text{Error}_1 = 0.248$ $\text{Error}_2 = 1.199$
6	Scenario 2 $\chi_{1r}^c = 2.4\chi_2$ $Q = 0.04$	$\text{Error}_1 = 0.199$ $\text{Error}_2 = 0.169$	$\text{Error}_1 = 0.237$ $\text{Error}_2 = 0.266$	$\text{Error}_1 = 1.081$ $\text{Error}_2 = 0.078$	$\text{Error}_1 = 0.347$ $\text{Error}_2 = 0.079$	$\text{Error}_1 = 0.259$ $\text{Error}_2 = 0.142$
7	Scenario 3 $\chi_2 = 0$ No Balancing	$\text{Error}_1 = 0.168$ $\text{Error}_2 = 4.04$	$\text{Error}_1 = 0.311$ $\text{Error}_2 = 3.392$	$\text{Error}_1 = 0.526$ $\text{Error}_2 = 1.029$	$\text{Error}_1 = 0.157$ $\text{Error}_2 = 0.359$	$\text{Error}_1 = 0.258$ $\text{Error}_2 = 1.735$
8	Scenario 3 $\chi_2 = 0$ $Q = 0.04$	$\text{Error}_1 = 0.143$ $\text{Error}_2 = 0.076$	$\text{Error}_1 = 0.297$ $\text{Error}_2 = 0.348$	$\text{Error}_1 = 0.673$ $\text{Error}_2 = 0.076$	$\text{Error}_1 = 0.207$ $\text{Error}_2 = 0.061$	$\text{Error}_1 = 0.248$ $\text{Error}_2 = 0.16$

$$\text{Error}_1 = \frac{\left\|\chi_{1r}^{c(True)} - \chi_{1r}^{c(simu)}\right\|_2^2}{\left\|\chi_{1r}^{c(True)}\right\|_2^2}, \qquad \text{Error}_2 = \frac{\left\|\chi_{1i}^{c(True)} - \chi_{1i}^{c(simu)}\right\|_2^2}{\left\|\chi_{1i}^{c(True)}\right\|_2^2}$$

the balancing method for the 2%, 6% and 8% noise levels respectively. As can be seen, the balancing method works properly for different noise levels. It should also be noted that as the noise level increases, the image corresponding to the imaginary part of the complex contrast of compressibility cannot reach to the exact quantitative values.

The cut passing through two tumours from bottom left to the top right for the real and imaginary parts of the complex contrast of compressibility using the average value of balancing coefficients for the independent density, $\chi_{1r}^c = 2.4\chi_2$ and $\chi_2 = 0$ are shown in Fig 3.7 (data contaminated with 2% noise). As can be seen in this figure, the reconstruction of χ_1^c is more accurate when density is inverted independently (scenario 1). Therefore, it can be seen that although the reconstruction of inverse density is not as good as the other contrast profiles (based on scenario 1), it leads to a better reconstruction of the complex contrast of compressibility in comparison with the reconstruction of χ_1^c using the assumption of $\chi_{1r}^c = 2.4\chi_2$ and $\chi_2 = 0$ utilized in scenario 2 and scenario 3. We speculate that this will be the case in general.

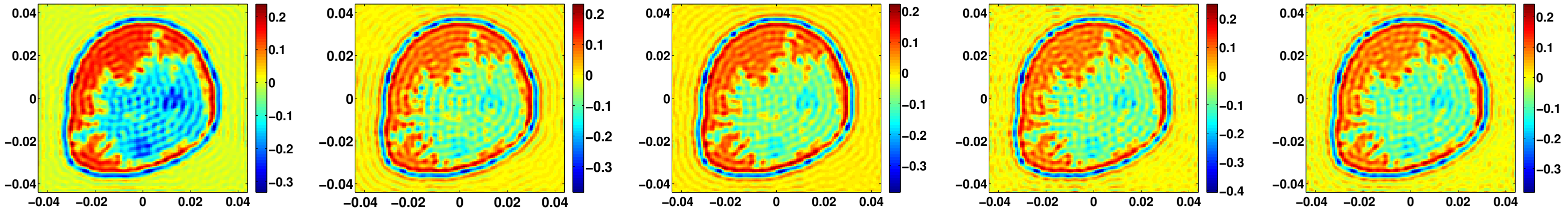

(a) χ_{1r}^c-Scenario2-2%noise (b) χ_{1r}^c-No Balance-2%noise (c) χ_{1r}^c-Balance-2%noise (d) χ_{1r}^c-Balance-6%noise (e) χ_{1r}^c-Balance-8%noise

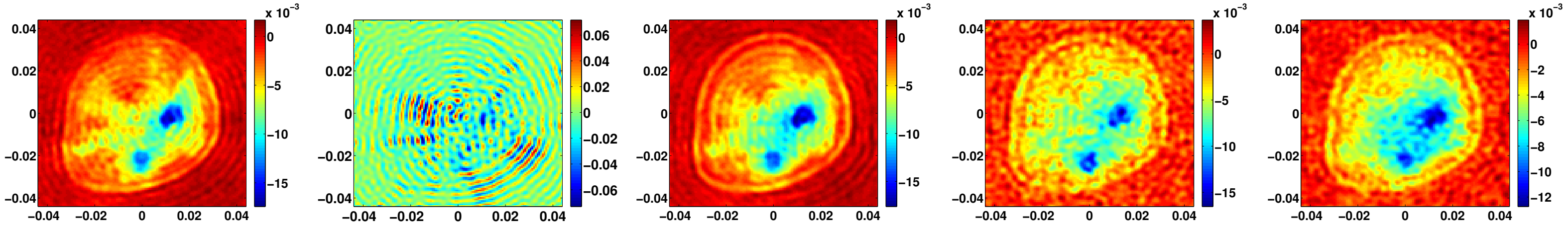

(f) χ_{1i}^c-Scenario2-2%noise (g) χ_{1i}^c-No Balance-2%noise (h) χ_{1i}^c-Balance-2%noise (i) χ_{1i}^c-Balance-6%noise (j) χ_{1i}^c-Balance-8%noise

Figure 3.6: Reconstruction of the dense breast phantom based on scenario 2 and scenario 3. The first column corresponds to the reconstruction of χ_1^c based on scenario 2 using the balancing method. The second column corresponds to the reconstruction based on scenario 3 without applying the balancing method. The third, fourth, fifth columns correspond to the reconstruction based on scenario 3 using the balancing method for the case that the data is contaminated with 2%, 6% and 8% noise.

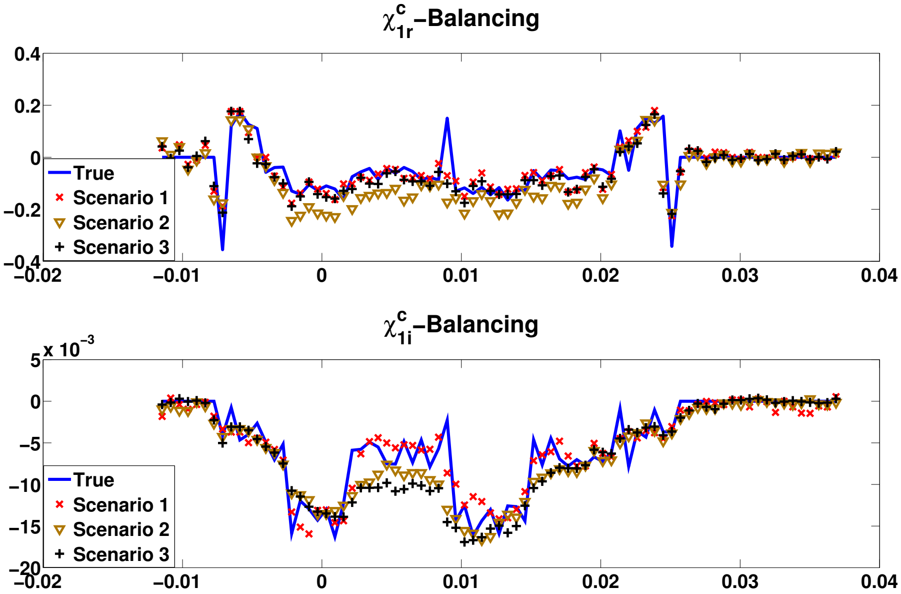

Figure 3.7: Comparison of the reconstruction of χ_1^c using the balancing method based on scenarios 1, 2 and 3 for a cut passing through two tumours from the bottom left to the top right. The average balancing coefficients are utilized and the noise level is 2%. (The horizontal axis corresponds to the x value of the cut passing through two tumors from the bottom left to the top right with the unit of [m] and the vertical axis corresponds to the value of the corresponding contrast).

3.5.4 Reconstructions using the MR-GNI method

In this section, we demonstrate that the balancing method considered herein is not only applicable to the BIM-CGLS inversion algorithm but also to other inversion algorithms where one of the contrast variables is much smaller than the others. To this end, the MR-GNI algorithm is utilized for the reconstruction of the ultrasonic properties of the OI for scenario 3 ($\chi_2 = 0$). We have adapted the MR-GNI algorithm that was developed for the reconstruction of complex permittivity in microwave tomography [50] to our scenario 3 of ultrasound tomography where complex compressibility is inverted. Only inversions for scenario 3 are possible using this code because there is no equivalent of density in microwave tomography. The details of this algorithm are presented in [50]. The utilized MR is a weighted L^2-norm total variation regularizer exhibiting two features: Laplacian regularization for smooth areas and edge-preserving regularization for sharp transitions. Thus, the utilized MR is a more advanced regularization compared to the CGLS regularization used in BIM. It leads to better reconstructions and reduced image noise. However, MR-GNI is computationally much more expensive in comparison with our BIM-CGLS algorithm. The result of the reconstruction of the medium-sized tumor breast phantom based on scenario 3 using the MR-GNI algorithm without and with using the balancing method are shown in the first and second rows of Fig 3.8. The results of the reconstruction of a dense breast using the MRGNI algorithm are shown in Fig 3.9. As can be seen, the reconstruction of χ^c_{1i} is poor without using the balancing method.

3.6 Conclusion

The performance of a balanced ultrasound tomography inversion algorithm for breast imaging is studied for the reconstruction of up to three ultrasonic properties: compressibility, attenuation, and density. These are represented as contrasts with respect to a homogeneous background and constitute the variables to be inverted given scattered-pressure data surrounding an object-of-interest. Numerical results are presented for three different scenarios that correspond to different approximations related to the density profile. The first scenario considers a density variation that is completely independent of the other two properties. The second and third scenarios, assume that either the contrast of density is linearly dependent on the contrast of compressibility or that there exists no variation in the density profile.

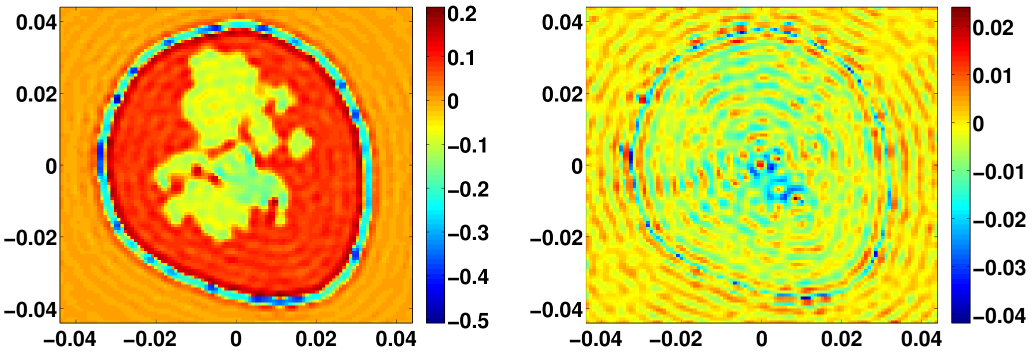

(a) χ^c_{1r}-No Balancing- 2% Noise (b) χ^c_{1i}-No Balancing- 2% Noise

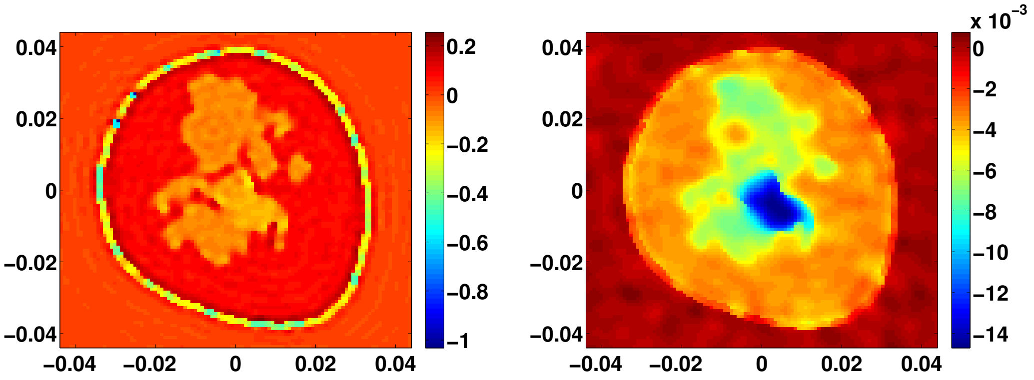

(c) χ^c_{1r}-Balancing- 2% Noise (d) χ^c_{1i}-Balancing- 2% Noise

Figure 3.8: Reconstruction of a medium sized tumor based on scenario 3 ($\chi_2 = 0$) using the MR-GNI algorithm. The first and second rows correspond to the reconstruction of the complex contrast of compressibility without and with using the balancing method respectively.

The CGLS regularization in conjunction with the BIM inversion algorithm is used for all the scenarios. The MR-GNI algorithm is also used for the last scenario to show that the balancing method is also applicable and required for other inversion algorithms, especially for the case where one of the contrast variables is much smaller than the others. It is observed that the reconstruction of the complex contrast of compressibility is improved when considering an independent variation of the density in comparison with the results obtained using the other two assumptions. For all the

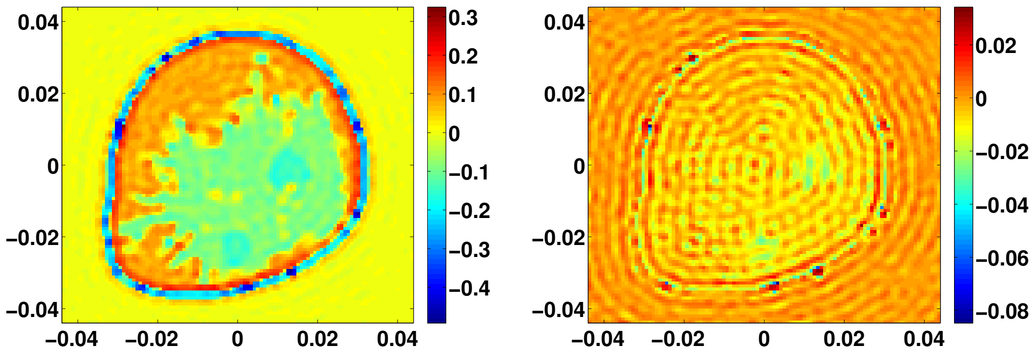

(a) χ^c_{1r}-No Balancing- 2% Noise (b) χ^c_{1i}-No Balancing- 2% Noise

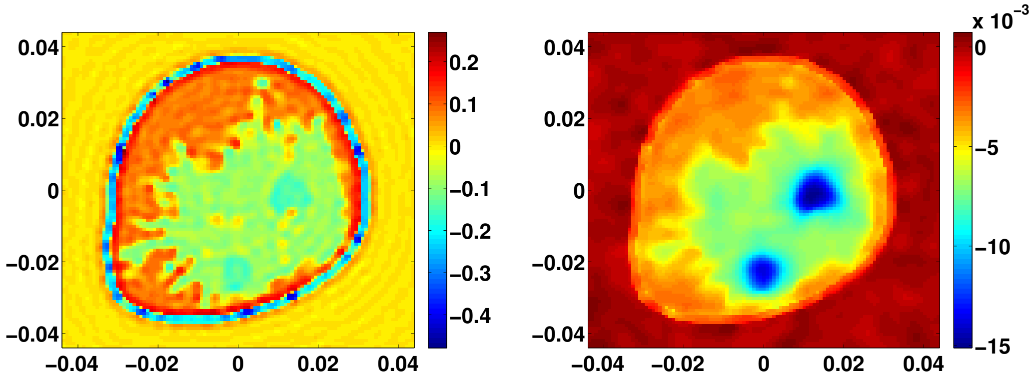

(c) χ^c_{1r}- Balancing- 2% Noise (d) χ^c_{1i}- Balancing- 2% Noise

Figure 3.9: Reconstruction of a dense breast based on scenario 3 ($\chi_2 = 0$) using the MR-GNI algorithm. The first and second rows correspond to the reconstruction of the complex contrast of compressibility without and with using the balancing method respectively.

scenarios the use of the balancing algorithm that has been introduced improves the reconstruction of the attenuation profile. This is important as the attenuation allows for a better detection and identification of tumor tissue compared to using only the compressibility and density images.

In summary, this paper addresses two issues. First, it is shown that as we enhance our numerical model, we achieve better imaging results due to reducing the modelling error. Second, the concept of balancing may be viewed as an effective way of incorporating prior information about the imbalance between different contrasts. For application-specific imaging scenarios, such as breast imaging, we are often aware of the imbalance between the unknown contrasts since we have prior knowledge about the expected ranges for different properties. In this paper, we have shown that our proposed balanced inversion algorithm, with a trivial initial guess (zero contrast), can enhance the quantitative images. In particular, an enhanced quantitative attenuation image is very important for breast imaging applications since it is easier to detect tumor in the quantitative attenuation image.

ACKNOWLEDGMENT

The authors would like to thank Dr. Puyan Mojabi for providing us with the MR-GNI code for microwave tomography.

4

Paper 2*: Composite Tissue-Type and Probability Image for Ultrasound and Microwave Tomography

4.1 abstract

The concept of creating a composite tissue-type-image (cTTI) along with an associated probability image is introduced for ultrasound and microwave tomography. The cTTI integrates information available within different quantitative property-images, and the associated probability image provides an indication of the level of confidence regarding the reconstructed tissue types. It is shown that the cTTI concept can be applied to ultrasound tomography property images, microwave tomography property images, as well as to their combination. Thus, the concept is generalizable to the amalgamation of quantitative information derived from a wide variety of modalities with the goal of increasing the confidence in the reconstructed cTTI. Validation of the concept is performed on MRI-derived numerical breast phantoms containing up to five different tissue types.

---

[*] from Pedram Mojabi and Joe LoVetri, "Composite Tissue-Type and Probability Image for Ultrasound and Microwave Tomography," *IEEE Journal on Multiscale and Multiphysics Computational Techniques*, 2016.

4.2 Introduction

ultrasound tomography (UT) and microwave tomography (MWT) are two quantitative imaging modalities which are being investigated for several industrial non-destructive testing and biomedical imaging applications [3, 5, 6, 8–12]. The focus of this work is on the application of these techniques to biomedical breast tissue imaging. Both of these imaging modalities rely on irradiating the object of interest (OI) using incident waves (pressure waves in UT, and electromagnetic waves in MWT). The scattered waves from the OI are collected, and are then utilized to reconstruct images of related properties of the OI. In UT, these properties are the ultrasonic properties; for example, in this work we consider the compressibility, attenuation and density profiles. In MWT, the properties of interest are the real and imaginary parts of the complex permittivity profile of the OI.

Both of these modalities can be mathematically formulated as an inverse scattering problem, which is non-linear and ill-posed. Several non-linear inversion algorithms have been utilized in the past to solve these problems, for example, the Born iterative method (BIM) [4, 20, 29, 37], the distorted Born iterative method [30, 34, 38, 39] and the contrast source inversion (CSI) algorithm [40, 41]. Generally, such methods need to be applied in conjunction with regularization techniques, such as the standard Tikhonov [32, 42], the L_1-norm Tikhonov [43, 44], multiplicative regularizers [45, 46], truncated singular value decomposition [47, 48] and conjugate gradient least squares (CGLS) subspace regularization methods [8,9,20,47]. These regularization techniques are used to deal with the ill-posedness of inverse problem.

We have recently shown how to reconstruct the three aforementioned ultrasonic properties of the OI using the BIM inversion algorithm in conjunction with the CGLS regularization technique [20]. We have also shown how to improve the reconstruction of the contrast profiles using a balancing method for the case that the ranges of the contrast profiles are significantly different from each other [28]. Similarly, several inversion algorithms have been proposed to reconstruct the complex permittivity profile of the OI using MWT data [8, 9]. Thus, UT and MWT inversion algorithms exist to solve the inverse scattering problem and thereby produce quantitative images corresponding to the relevant physical properties associated with the respective wave propagation.

Often, especially in biomedical imaging, the goal is to infer the tissue type within the image, but this can be quite difficult working from a single property image such as ultrasonic wave-speed. Even when three ultrasonic properties are reconstructed simultaneously, as in [20], it is difficult to infer the tissue-type at a particular pixel location. Techniques to do so are typically *ad hoc*, relying on the expertise of the person examining the image. Recently, we have proposed preliminary systematic techniques to create such tissue type images (TTIs) [112, 113]. In this paper we introduce a general systematic procedure, based on Bayesian inference, to derive a tissue-type image from one or more property images.

Thus, three quantitative property images obtained from UT data, and/or two quantitative property images obtained from MWT, are utilized to form a single TTI which we refer to as the composite tissue type image (cTTI). Each tissue-type in the inferred composite TTI is represented by a single colour. This approach offers the following advantages. First, the cTTI is more robust and reliable than a TTI derived from a single quantitative image because the most accurately reconstructed part of each property-image is used toward the creation of the cTTI. Secondly, for each pixel of the cTTI we construct an associated probability value that indicates the level of confidence regarding the assignment of the final tissue-type to that pixel.

(It should be emphasized that current UT and MWT algorithms do not provide any indications regarding the level of confidence in their reconstruction, which is a serious disadvantage for risk assessment associated with a diagnosis.) Thirdly, a physician can more easily understand the cTTI without knowing the ultrasonic or complex permittivity values of different tissues. The cTTI, along with the associated probability image, can provide the physician with better information that is required to evaluate patient health and risk factors. In addition, the physician would be provided with a single image as opposed to several images obtained from different imaging modalities.

For the creation of this cTTI, we require (1) quantitative reconstructions of at least two properties of the OI, and (2) the probability density functions (PDF) for the property values corresponding to the different tissues within the object being imaged. The quantitative property reconstructions can be obtained using any available inversion algorithm. The PDFs of different properties for each tissue are estimated from property-value ranges available in the published literature [9, 51, 52, 100, 101, 108, 114, 115].

We further show that single-property TTIs, or the cTTI, can be used to improve the quantitative reconstructions of the OI. In this method, we first utilize the quantitative reconstructions of the properties to create the TTIs, or the cTTI, and then utilize these to provide a good initial guess for the inversion algorithm (for any of the property reconstructions). As is well-known, the appropriate choice of an initial guess is very important for avoiding local minima, and converging to a good solution.

The TTI concept presented in this paper can be applied to different biomedical or industrial applications. However, in this paper, we limit ourselves to the breast imaging application. In addition, although we consider two-dimensional MWT and UT, the framework presented in this paper can be applied to three-dimensional problems as well. The structure of this paper is as follows. In Section 4.3, the problem statement is presented. Then, two methods to create the composite TTI based on using the quantitative reconstruction of the properties of the OI are described in Section 4.4. Results of applying the techniques to MRI derived numerical phantoms are then presented and discussed in Section 4.5.

4.3 Problem Statement and Methodology

The methodology for creating the TTIs and the cTTI is independent of the number and type of property images that are used. We thus describe the methodology as a general procedure, but subsequently apply it to three cases in the Results section. That is, we validate the methodology using quantitative UT images, or quantitative microwave (MW) images, or combinations of these.

4.3.1 Tissue Property Data

A basic assumption of creating TTIs is that, not only is there some correlation between tissue properties and tissue types, but that the tissue properties provide a means of discriminating between different tissues of interest. As the discrimination capacity of a single property may not be ideal, the use of several properties reinforces the discrimination. In order to perform such a function quantitatively and in a systematic way, it is assumed that typical property values for specific tissue types are available and that PDFs of the property values for the tissues of interest can be estimated. This basic assumption is required for the methodology that will be presented, and the inferences made about the tissue type at any particular pixel depend on the form of the PDFs that are assumed. None the less, the procedure itself is independent of the form of the PDFs. If future experimental work reveals more accurate property distributions for some or all of the tissues of interest the methodology can easily incorporate these. For the examples shown in the Results section of this paper, we describe how we approximate Gaussian PDFs for five properties of five different tissue-types.

4.3.2 MW and US Property-Image Formation

The TTIs are inferred from property-images and thus a means of creating US and MW property images is required. In this work we focus on three US properties: compressibility, attenuation, and density, as well as two MW properties: the real and imaginary parts of the complex permittivity. It is assumed that the US and MW inverse scattering problems have been solved resulting in five quantitative images for these properties. For the results considered herein the ultrasound inverse scattering problem is solved using the algorithm presented in [20, 28], and the microwave inverse scattering problem is solved using the algorithm presented in [116]. These are representative of state-of-the-art inversion algorithms available in the literature.

4.4 Formation of the Composite TTI

Two methods to create cTTIs are described and investigated. The first method first forms single property TTIs along with their corresponding probability images and then uses these to construct a cTTI. In the second method, all the property images of interest are used simultaneously to create the cTTI, bypassing the creation of the single-property TTIs. Along with the reconstructed quantitative images obtained from UT and/or MWT, both require approximate PDFs of property values for each

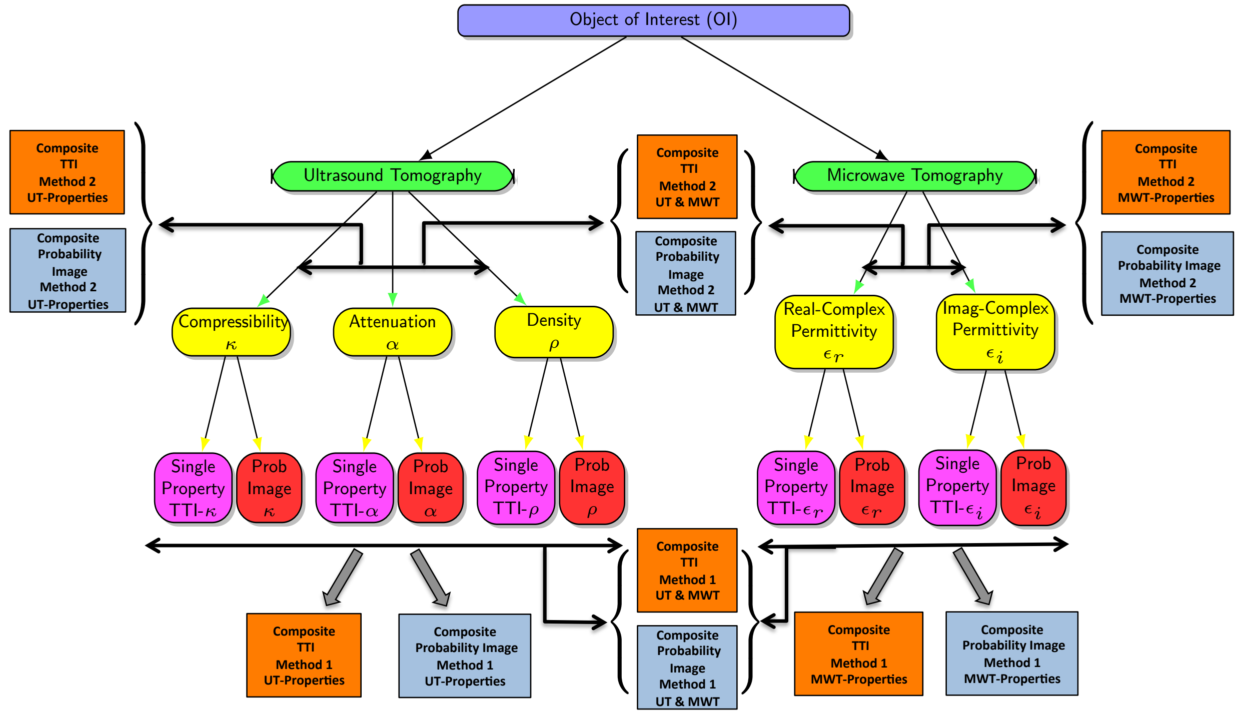

Figure 4.1: The flowchart of creating a composite TTI (cTTI) using Method 1 and Method 2 for both UT and MWT. In Method 1, single-property TTIs and single-property probability images for all the properties of interest are created. This information is then utilized to create the cTTI along with its composite probability image. In Method 2, we do not create single-property TTIs. All the properties of interest are simultaneously utilized to directly create the cTTI along with its composite probability image.

tissue being considered. The first method requires only single variate PDFs for each combination of property/tissue-type pair, whereas the second method utilizes multivariate PDFs for all the properties for each tissue-type. The flowchart showing how these two methods work is depicted in Fig 4.1.

The goal of the methodology is to construct a cTTI wherein each pixel is labeled, via a specific color, with the most-probable tissue type. The probability of the label being correct is provided by the corresponding probability image. This probability represents the confidence one should have that the particular pixel corresponds to that tissue-type given all of the available information.

4.4.1 Method 1: cTTI derived from single-property TTIs

The first step of this method is to first construct a single-property TTI and its corresponding probability image for each quantitative property image. Thus, for example, if we have available three quantitative property images, we will obtain six images. These six images are then used to form one composite TTI with a corresponding composite probability image. For ultrasound imaging the properties being imaged will be, e.g., compressibility, attenuation and density, whereas for microwave imaging the properties will be the real and imaginary parts of the complex permittivity.

The number of tissue types of interest should also be specified. For example, four or five different tissue types can be chosen for breast imaging; namely, skin, fat, glandular, tumor and/or cyst. (The number of chosen tissue types can be adjusted for different applications.)

The steps for creating the single-property tissue-type and probability images are summarized below.

1. Consider each of the quantitative property images in turn.

2. At each pixel within the quantitative property image, we calculate the probability that that pixel corresponds to tissue type, T_k, using Bayes' formula [117]:

$$P(T_k|x) = \frac{p(x|T_k)P(T_k)}{\displaystyle\sum_{i=1}^{N_t} p(x|T_i)P(T_i)} \tag{4.1}$$

   where x is the property value of that pixel in the property image. In this formula N_t is the total number of tissues, and $p(x|T_k)$ is the value of the PDF at property value x for tissue T_k. The term $P(T_k)$ is the prior probability of assigning tissue-type T_k for that pixel. In this work, we assume no prior information and therefore set all of the prior probabilities to be equal amongst the tissues being considered. That is, for the case that we consider five tissue types, we set $P(T_k) = 0.2$. At the end of this step we will have N_t probabilities assigned to each pixel, one for each tissue-type.

3. To form the TTI, we assign each pixel the tissue type with the highest probability calculated in step 2. Thus,

$$\text{if} \quad P(T_k|x) > P(T_j|x) \Longrightarrow \text{choose tissue } T_k \tag{4.2}$$

$$\text{where} \quad j = 1, \cdots, N_t \quad \text{and} \quad j \neq k$$

   We also keep this highest probability of each pixel and introduce it at the corresponding pixel in the probability image. Thus, we have two images for each property of interest as shown in Fig 4.1. The first image is called the single-property TTI and the second image is called the single-property probability image.

4. Once we obtain the single-property TTI and single-property probability image for this property, we go back to Step 1, and repeat these procedures until all the properties are covered.

Now, we can utilize all these single-property TTIs and single-property probability images to create a cTTI. To this end, for each pixel within the cTTI, we scan all the corresponding pixels in single-property TTIs and their single-property probability images. We then choose the tissue type of the highest probability, and assign it to that pixel of the cTTI. We also keep this highest probability to form the composite probability image. This procedure continues until all the pixels of the cTTI are covered.

4.4.2 Method 2: cTTI derived from simultaneous use of different properties

Whereas Method 1 treated the information within the individual quantitative property images as independent, Method 2 makes some assumptions regarding how this information is correlated. That is, Method 2 forms the cTTI by simultaneously considering all the quantitative images, without creating single-property TTIs, and assumes that for each tissue-type we have available a multivariate PDF that takes into account all of the properties. Although having an accurate multivariate PDF may seem demanding, we will show that simple assumptions as to the form of this multivariate PDF improves the predicted cTTI. Specifically, we assume that a multivariate normal PDF, in d dimensions (corresponding to the number of properties), can be used. Thus, we assume that the multivariate normal PDF for tissue T_k is of the form [117]

$$p(\mathbf{x}|T_k) = \frac{1}{(2\pi)^{d/2}|\mathbf{\Sigma}|^{1/2}} \times \mathrm{e}^{\left[-\frac{1}{2}(\mathbf{x}-\mu)^t\mathbf{\Sigma}^{-1}(\mathbf{x}-\mu)\right]} \tag{4.3}$$

where $\mathbf{x}$ is a vector of length d corresponding to the value of d properties for each pixel, μ is the mean vector of length d corresponding to the mean value of each property, and $\mathbf{\Sigma}$ is the $d \times d$ covariance matrix. Also, $|\mathbf{\Sigma}|$ and $\mathbf{\Sigma^{-1}}$ are the determinant and the inverse of the covariance matrix. For simplicity, it is assumed that the properties are statistically independent; thus, the covariance matrix is diagonal.

The steps of this method are summarized below.

1. For each pixel, considering all the property images of interest simultaneously, the value of multivariate PDF for each tissue type is calculated based on (4.3), *i.e*, $p(\mathbf{x}, T_1), p(\mathbf{x}, T_2), \cdots, p(\mathbf{x}, T_k)$.

2. The probability that any particular tissue, T_k, occupies a pixel is calculated using Bayes' formula, where (4.1) is used with vector argument $\mathbf{x}$ rather than x.

3. Bayesian decision theory [117] is then applied where the tissue-type with the highest probability is assigned to each pixel. As in Method 1, two images will be obtained from this method. The first image is the composite TTI and the second image is the composite probability image (*i.e.*, the highest probability).

4.5 Results

To validate the effectiveness of the TTI methodology, numerical experiments with synthetically derived data were performed. For these experiments two different 2D

MRI-based numerical phantoms were considered [107]. The first phantom contains a medium sized tumor and a total of five tissue types: skin, fat, glandular, cyst, and tumor. The second phantom is a dense breast having four tissue types (no cyst) and two medium sized tumors. The true tissue images of these phantoms are shown in Fig 4.2. The discrete colorbar of each image is used to identify the tissue-type. Note that for all of the synthetic examples considered herein noise is added to the scattered field data according to a percentage value of the maximum scattered field. Details are provided in [109].

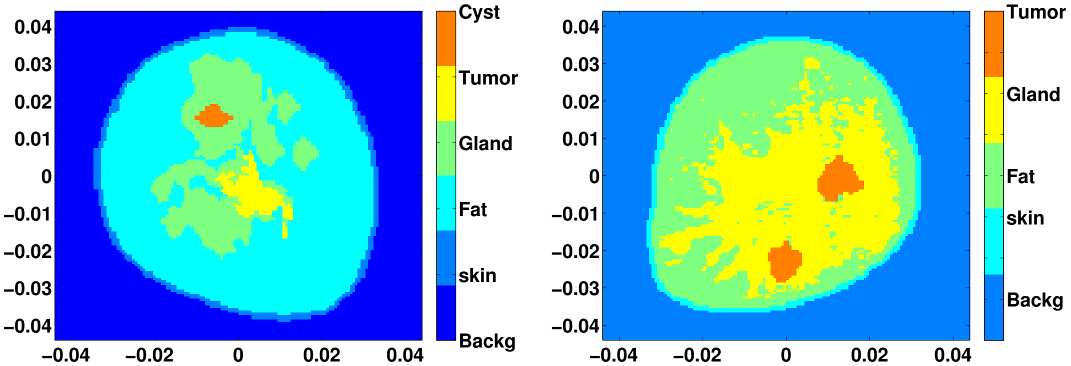

(a) Phantom with a medium sized tumor

(b) Phantom of a dense breast

Figure 4.2: The true TTI for MRI-based numerical breast phantoms.

The results are presented in the following format. First, in Section 4.5.1, the reconstructions of the ultrasonic properties for each phantom are shown. Then, these reconstructions are utilized to create single-property TTIs and cTTIs using Method 1 and Method 2. In Section 4.5.2, the reconstructions of the electromagnetic properties for the phantoms are shown. Then, these quantitative MWT properties are utilized to create single-property TTIs and a cTTI. In Section 4.5.3, UT and MWT are utilized together to create a cTTI. Finally, in Section 4.5.4, we show how the concept of cTTI can be used to provided an enhanced initial guess for the inversion algorithm. It should be noted that the prior probabilities for all the tissue types are assumed to be the same unless otherwise stated.

4.5.1 cTTI for UT

Formation of the true quantitative profile

The ranges of the ultrasonic properties for breast are shown in Table 4.1[†]. These ranges are chosen based on [51, 52, 100, 101, 108]. To create numerical phantoms from the MRI-based tissue-phantoms for each property being considered we randomize the property values at each pixel for each tissue. That is, to set the property values for each tissue we apply a uniformly distributed random function to pick up values for every pixel within that tissue. For example, if the upper and lower ranges of a property associated with a given tissue type is a and b respectively, the true quantitative values for that property within that tissue are chosen to be $a + (b - a) \times rand$ where $rand$ is a uniformly distributed random number from 0 to 1.

Formation of the PDFs

Based on the expected ranges of each property for a given tissue, we create the required PDFs. For example, if we consider 5 tissue types and 5 properties, we will have 25 single variate PDFs. These PDFs are all assumed to have normal distributions with their mean values coinciding with the mean value of the expected range for each property associated with a certain tissue. Furthermore, to find the standard deviation

---

[†] It should be noted that the units of these ultrasonic properties have been provided in this Table, and therefore for brevity, we do not repeat these units in the reconstructed images. In the reconstructed images, the colorbars of reconstructions represent the quantitative values of these properties.

Table 4.1: The ranges of the speed of the sound ($c = \frac{1}{\sqrt{\kappa\rho}}$), attenuation and density for breast tissues.

Tissue	Speed of Propagation [m/s]	Attenuation[$\frac{\text{dB}}{\text{cm MHz}}$]	Density[$\frac{\text{kg}}{\text{m}^3}$]
Skin	$1710 < c < 1750$	$0.65 < \alpha < 0.85$	$1128 < \rho < 1145$
Fat	$1410 < c < 1450$	$0.1 < \alpha < 1$	$941 < \rho < 960.5$
Glandular	$1540 < c < 1570$	$0.8 < \alpha < 1.5$	$963 < \rho < 979$
Tumor	$1575 < c < 1625$	$2.2 < \alpha < 3$	$982 < \rho < 998$
Cyst	$1510 < c < 1540$	$0.1 < \alpha < 0.35$	$1012 < \rho < 1030$

of the PDF, it is assumed that the value of the PDF at the minimum and maximum values of the expected range is 40% of the maximum value of the PDF. These standard deviations and means are also utilized to create the multivariate normal PDF for Method 2.

Inversion setup

Three ultrasonic frequencies of operation, $f = [110, 150, 200]$ kHz, are considered. The number of transmitters and receivers is set to be 120 and water is chosen as the background medium‡. The datasets corresponding to these three frequencies are simultaneously inverted. Due to the fact that attenuation is dependent on frequency, we reconstruct the slope of the attenuation at these frequencies (which can be assumed to be a constant). The term attenuation is used throughout the paper to refer to this quantity.

First phantom (phantom with a medium sized tumor)

The true TTI for this phantom is shown in Fig 4.2a. The true compressibility, attenuation and density profiles for this phantom are shown in the top row of Fig 4.3.

---

‡Although the choice of the background medium has not been investigated in this thesis, it should be noted that an important criterion toward the choice of the background medium, also known as the matching fluid, is to choose a safe medium that minimizes the reflection from the object so as to maximize interrogation of the internal regions of the object.

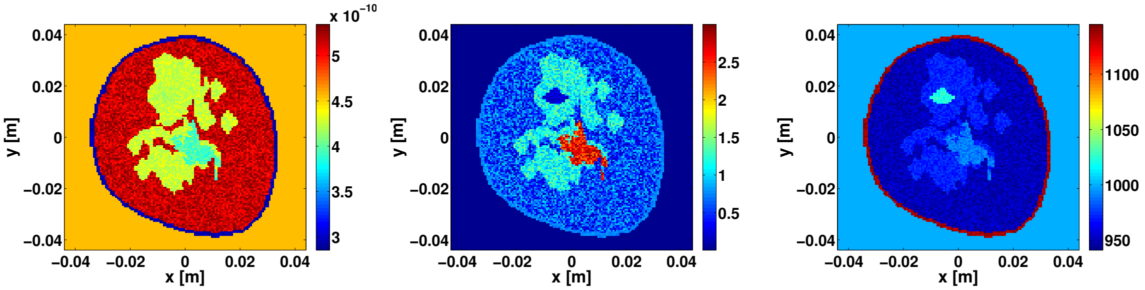

(a) True κ (b) True α (c) True ρ

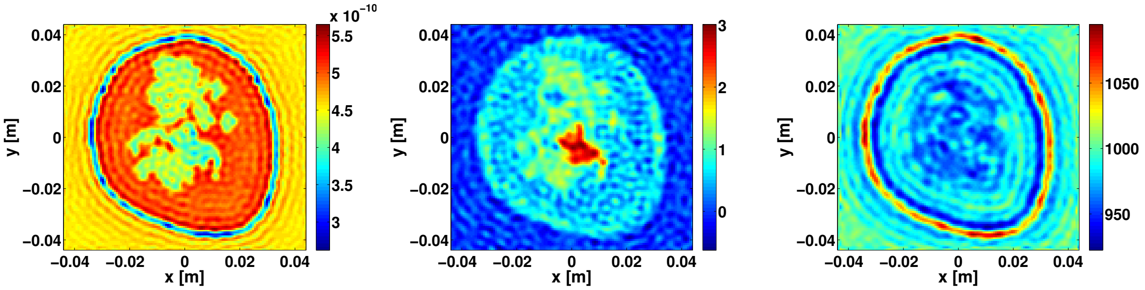

(d) Reconstructed κ (e) Reconstructed α (f) Reconstructed ρ

Figure 4.3: The first row corresponds to the true compressibility, attenuation and density profiles. The second row corresponds to the reconstruction of compressibility, attenuation and density profiles for the data contaminated with 2% noise.

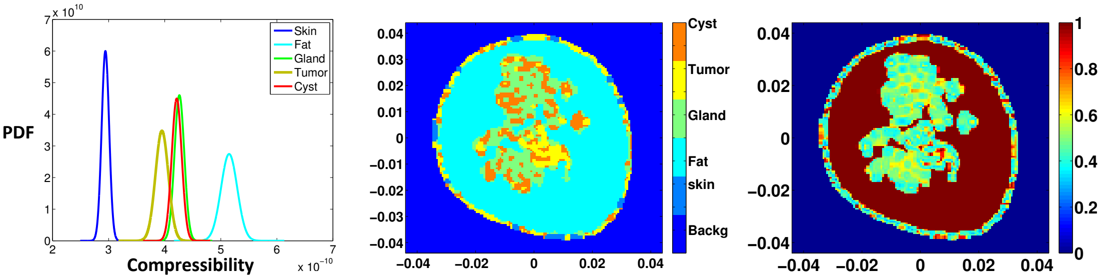

(a) PDF κ (b) Single Prop TTI-κ (c) Probability Image κ

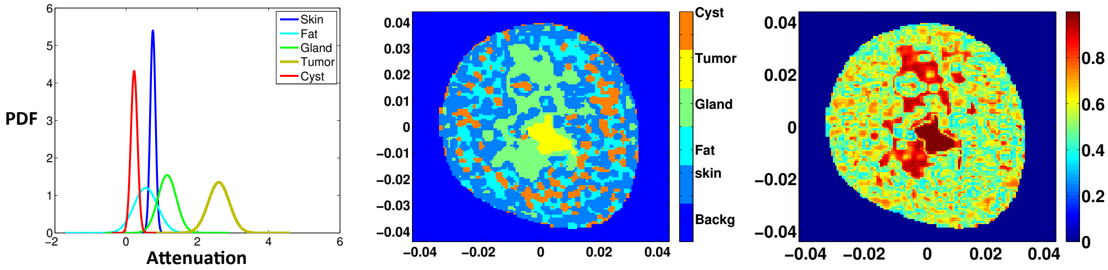

(d) PDF α (e) Single Prop TTI-α (f) Probability Image α

Figure 4.4: The PDF, single property TTI and probability image for the compressibility (top row) and attenuation (bottom row) are shown.

The reconstruction of the properties with two percent noise added to the data are shown in the bottom row of Fig 4.3[§]. As can be seen the reconstruction of the density is poor and we thus do not use this property for creating the composite TTI. That is, we only use reconstructed compressibility and attenuation property images. (It will be shown in Section 4.5.4 that the reconstruction of density can be improved using a good initial guess based on the reconstructed composite TTI.) The PDFs for the compressibility and attenuation for all tissue types are shown in the first column of Fig 4.4. Using these PDFs and the reconstructed properties, a single-property TTI and a single-property probability image for each property are constructed. These are shown in the second and third columns of Fig 4.4, respectively. It is worthwhile to note that the fat region can be well distinguished from the other tissues, with high probability values, using the single-property compressibility TTI. The tumor is also well detected using the single-property attenuation TTI, again with high probability values. Note though, that if one were to utilize only the attenuation property there would be many false skin designations within the fat region. Similarly, using only compressibility, there would be many false cyst designations within the glandular region.

The cTTI based on κ and α properties can then be created by either Method 1 or Method 2. The cTTI, correct-pixel image and probability image using Method 1 and Method 2 are shown in the first and second rows of Fig 4.5, respectively. Here, using two properties, we already see a substantial reduction in the number of false designations of tissue type. As can be seen in the title bar of the correct-pixel images, the error which is defined as the ratio of the number of wrong pixels to the total

---

[§] The achievable resolution may be enhanced by utilizing higher frequencies of operation. To the best of the author's knowledge, the achievable resolution using the inverse scattering approaches is object dependent, e.g., see [118].

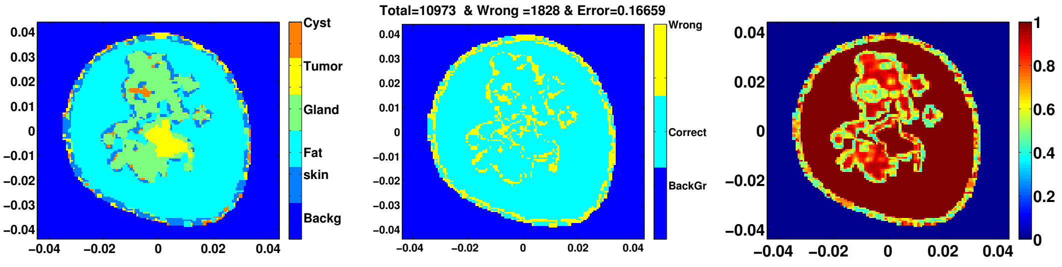

(a) cTTI-Method 1 (b) Correct pixels (c) Probability Image

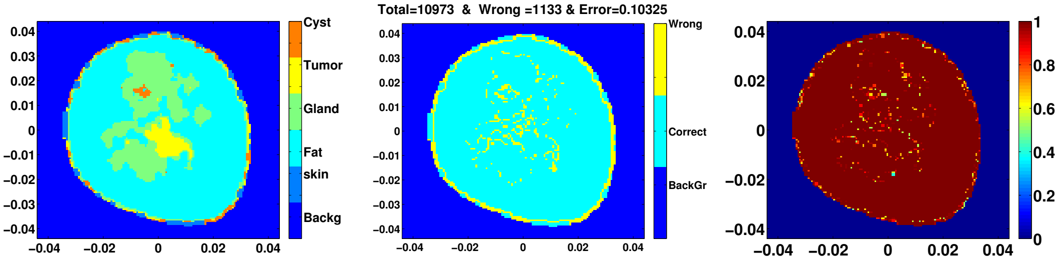

(d) cTTI-Method 2 (e) Correct pixels (f) Probability Image

Figure 4.5: The first and second rows correspond to the reconstruction of a cTTI, correct pixel image and probability image using Method 1 and Method 2, respectively.

number of pixels within the OI for the reconstructed cTTI using Method 2 (0.10325) is smaller than that using Method 1 (0.16659).

Second phantom (dense breast with two tumors)

The true TTI for this phantom is shown in Fig 4.2b. The true compressibility, attenuation, and density profiles for this phantom are shown in the first row of Fig 4.6. The reconstruction of these properties for two different noise levels (2% and 9%) are shown in the second and third rows of Fig 4.6, respectively. The PDF and TTI as well as the probability image for the compressibility and attenuation are shown in the first and second rows of Fig 4.7 for the case that the noise level is 2%. Similar to the previous example, it can be seen in Fig 4.7 that fat can be well distinguished, with high probability values, from the other tissues using the single-property TTI

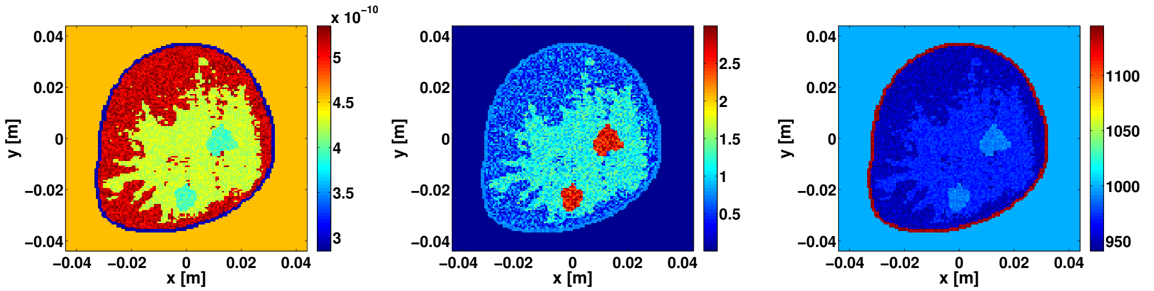

(a) True κ (b) True α (c) True ρ

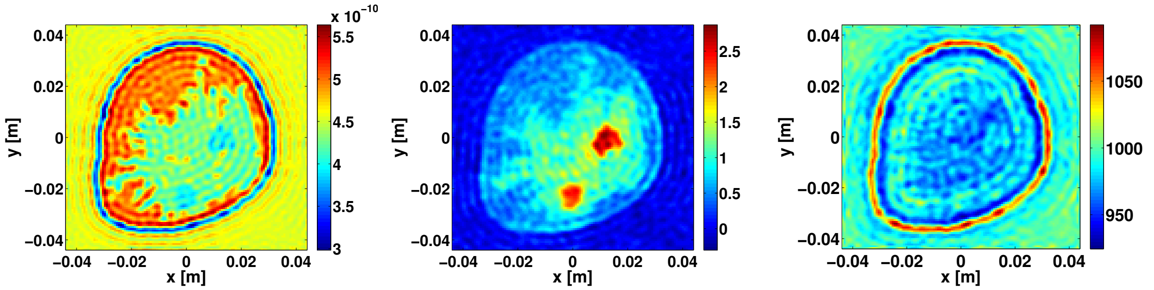

(d) Reconstructed κ (e) Reconstructed α (f) Reconstructed ρ

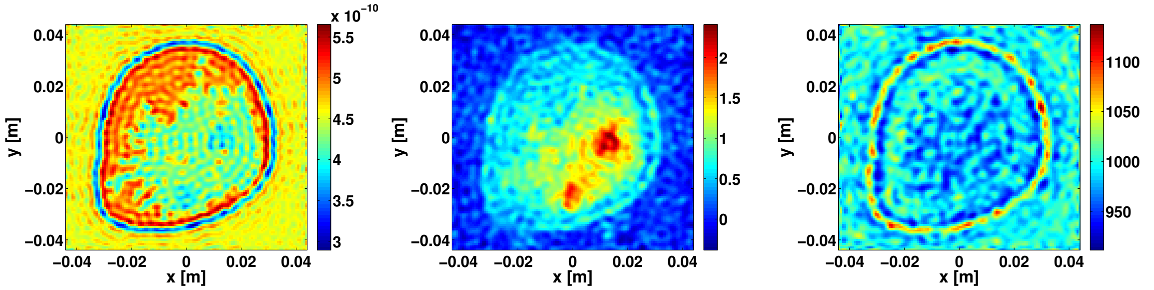

(g) Reconstructed κ (h) Reconstructed α (i) Reconstructed ρ

Figure 4.6: The first row corresponds to the true compressibility, attenuation and density profiles for dense breast. The second and third rows correspond to the reconstruction of the profiles for 2% and 9% noise respectively.

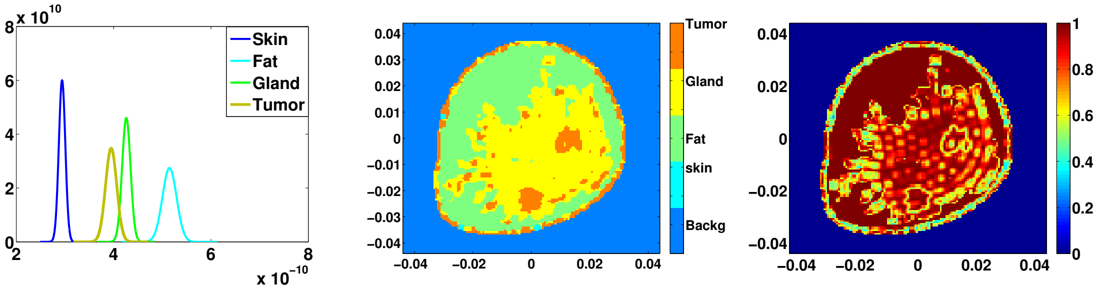

(a) PDF κ (b) Single Prop TTI-κ (c) Probability Image κ

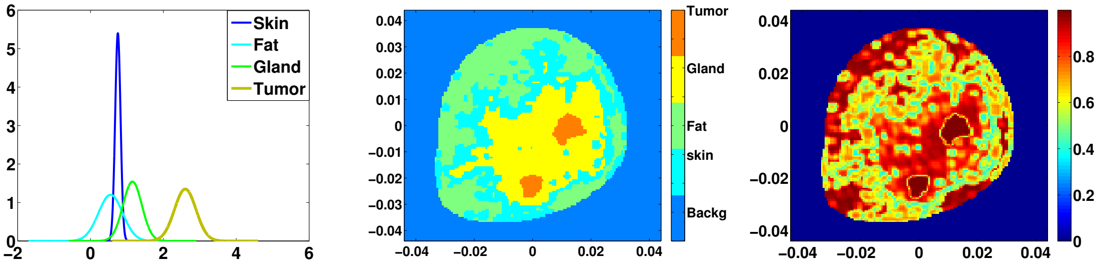

(d) PDF α (e) Single Prop TTI-α (f) Probability Image α

Figure 4.7: The PDF, single property TTI and probability image for the κ and α are shown in the first and second rows for 2% noise.

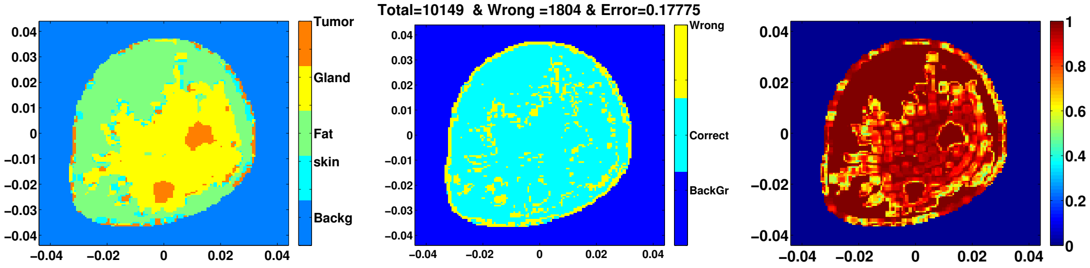

(a) cTTI-Method1-2PN (b) Correct pixels (c) Probability Image

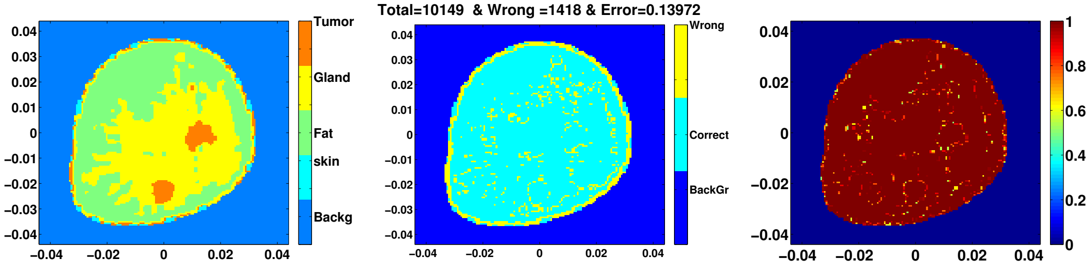

(d) cTTI-Method2-2PN (e) Correct pixels (f) Probability Image

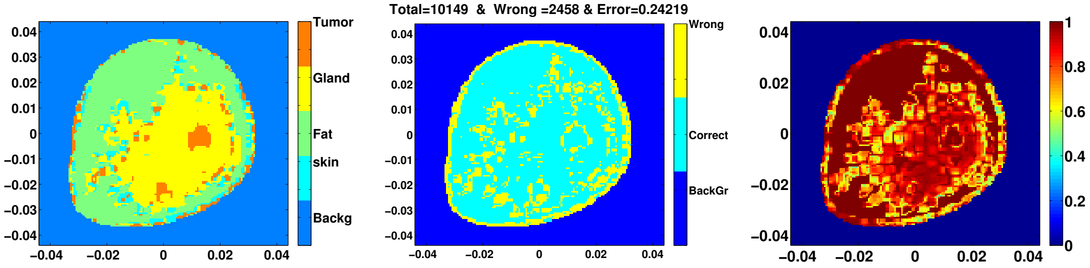

(g) cTTI-Method1-9PN (h) Correct pixels (i) Probability Image

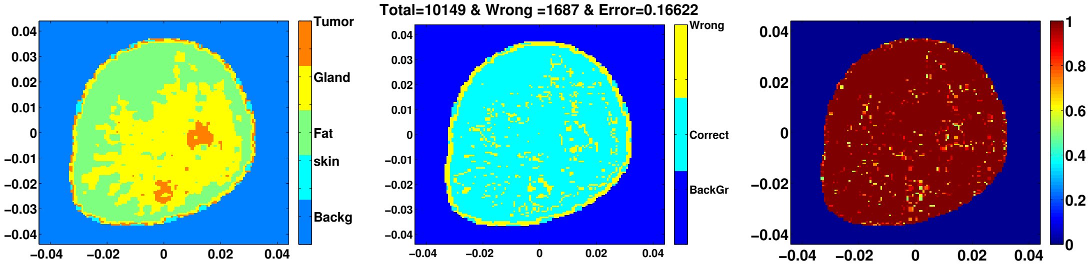

(j) cTTI-Method2-9PN (k) Correct pixels (l) Probability Image

Figure 4.8: Create a cTTI based on the reconstruction of κ and α. The first and second rows correspond to the reconstruction of a cTTI, correct pixel image and probability image based on Method 1 and Method 2 for the 2% noise. The third and fourth rows correspond to the cTTI, correct pixel image and probability image based on Method 1 and Method 2 for a 9% noise level.

derived from compressibility. The tumor region can also be well distinguished using the single-property TTI derived from attenuation. The cTTI, correct-pixel image as well as probability image for both noise levels using Method 1 and Method 2 are shown in Fig 4.8. As can be seen, this TTI obtained from the nine percent noise still allows one to distinguish the tissue types.

4.5.2 cTTI for MWT

Formation of the true quantitative profile and PDFs

The range of electromagnetic properties for breast at a frequency of 1.1 GHz are shown in Table 4.2. These value are chosen based on values published in [9,114,115]. For each value in this table, we consider ±10% variation. The complex permittivity of the background is assumed to be $23.3-j18.46$ as in [9]. To create the true quantitative values for each tissue within this phantom, we utilize the same method used for UT explained in Section 4.5.1. The formation of PDFs is also the same as the method for UT explained in Section 4.5.1.

Inversion setup

Five frequencies of operation, $f = [1.1, 1.5, 2, 2.4, 2.8]$ GHz are considered. The datasets corresponding to these frequencies are simultaneously utilized for the inversion. The number of transmitters and receivers are set to be 30. We note that the inversion algorithm takes into account the variation of the imaginary part of the complex permittivity with respect to frequency of operation using the so-called Maxwell model [119].

Table 4.2: The values of the electromagnetic properties (real and imaginary parts of the relative complex permittivity) of the breast tissues at 1.1 GHz. We consider ±10% variation for these values.

Tissue	ϵ_r	ϵ_i
Skin [115]	35	-23
Fat [9]	12.6	-10.13
Glandular [9]	32.7	-20.92
Tumor [9]	53.4	-18.8
Cyst [114]	60	-16.34

First Phantom (phantom with a medium sized tumor)

The true TTI and the complex permittivity of this phantom are shown in Fig 4.2a and the top row of Fig 4.9. The reconstruction of the complex permittivity for the case that the data is contaminated with 9% noise is shown in the bottom row of Fig 4.9. The PDF, single-property TTI and its probability image for the real and imaginary parts of complex permittivity are shown in the first and second rows of Fig 4.10. The cTTI using Method 1 and Method 2 are shown in the third and fourth rows of Fig 4.10.

Second Phantom (dense breast with two tumors)

The true TTI and electromagnetic properties for this phantom are shown in Fig 4.2b and the first row of Fig 4.11. The reconstruction of the complex permittivity for the case that the data is contaminated with 9% noise is shown in the second row of Fig 4.11. The cTTI, true pixel and probability images obtained using Method 2 are shown in Fig 4.12.

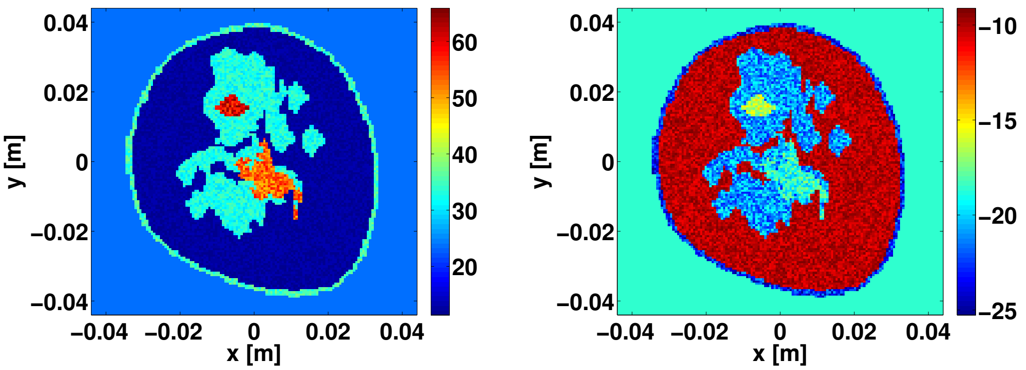

(a) True ϵ_r (b) True ϵ_i

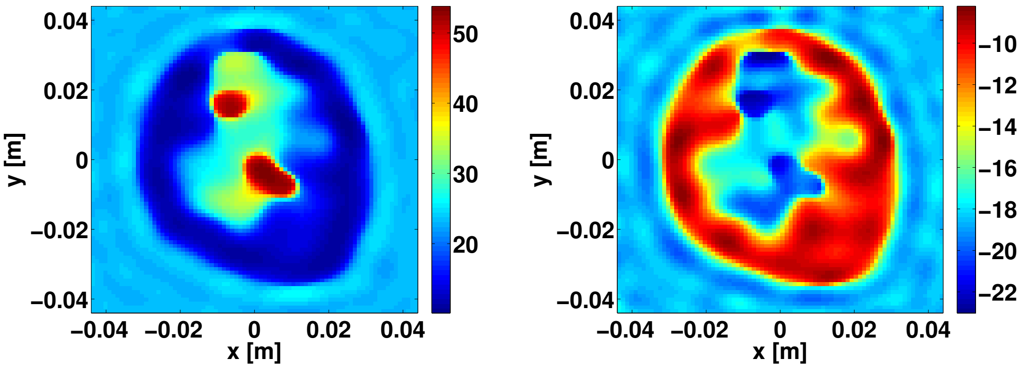

(c) Reconstructed ϵ_r (d) Reconstructed ϵ_i

Figure 4.9: The first and second rows correspond to the true and reconstructed real and imaginary parts of the complex permittivity for the case that the noise is 9 percent.

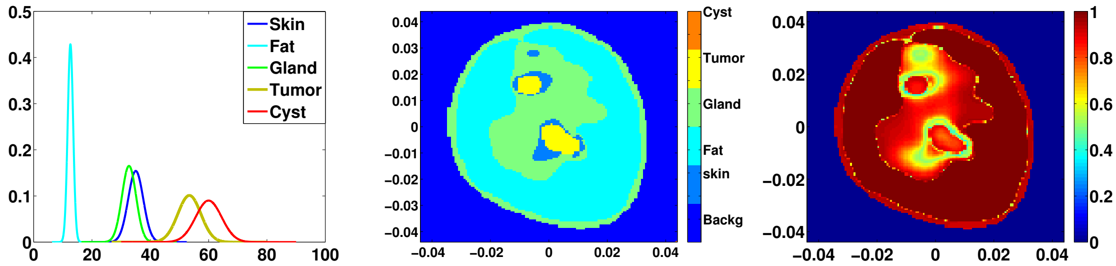

(a) PDF ϵ_r (b) Single Prop TTI-ϵ_r (c) Probability Image ϵ_r

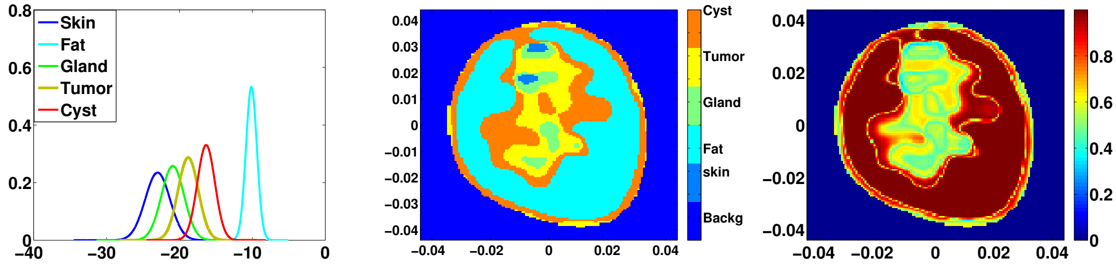

(d) PDF ϵ_i (e) Single Prop TTI-ϵ_i (f) Probability Image ϵ_i

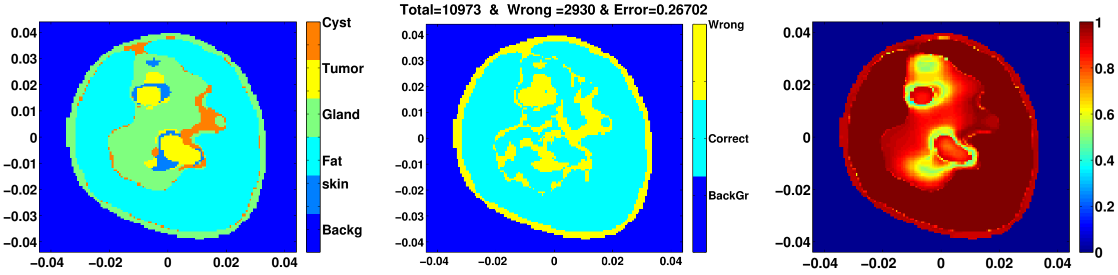

(g) cTTI-Method 1 (h) Correct Pixels (i) Probability Image

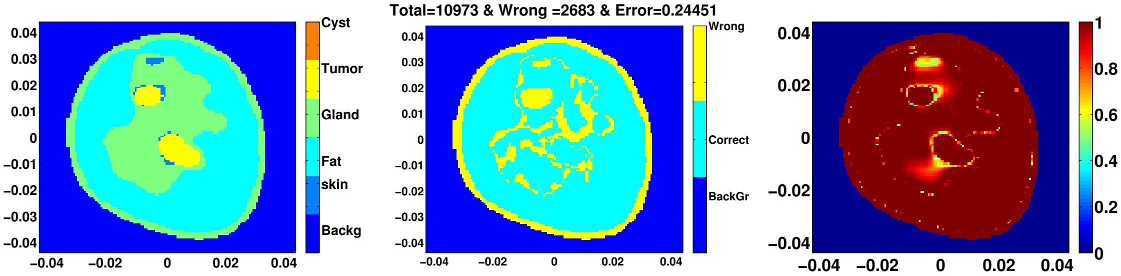

(j) cTTI-Method 2 (k) Correct Pixels (l) Probability Image

Figure 4.10: The first and second rows correspond to a single property TTI for the ϵ_r and ϵ_i respectively. The third and fourth rows correspond to the cTTI and its probability using Method 1 and Method 2 respectively.

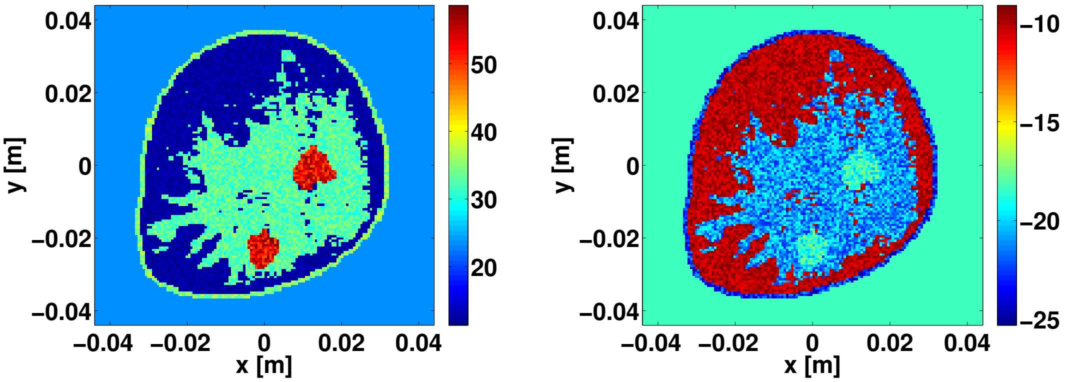

(a) True ϵ_r (b) True ϵ_i

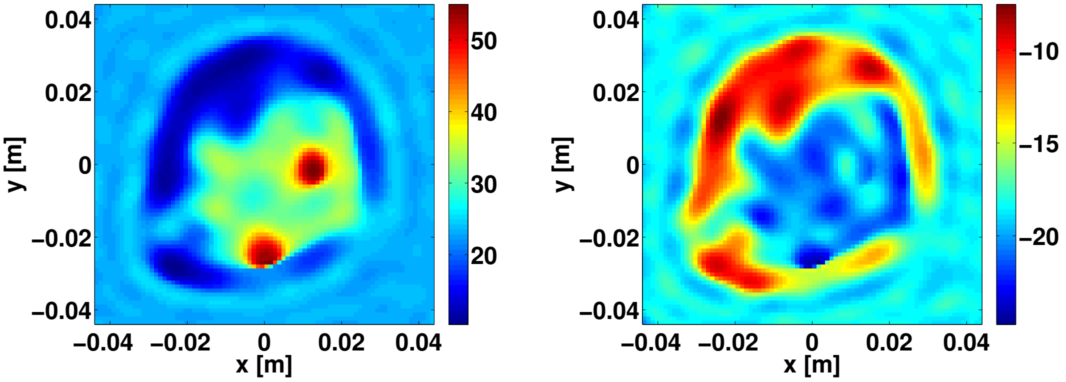

(c) Reconstructed ϵ_r (d) Reconstructed ϵ_i

Figure 4.11: The first and second rows correspond to the true and reconstruction of real and imaginary parts of permittivity for the case that the noise percentage is 9 percent.

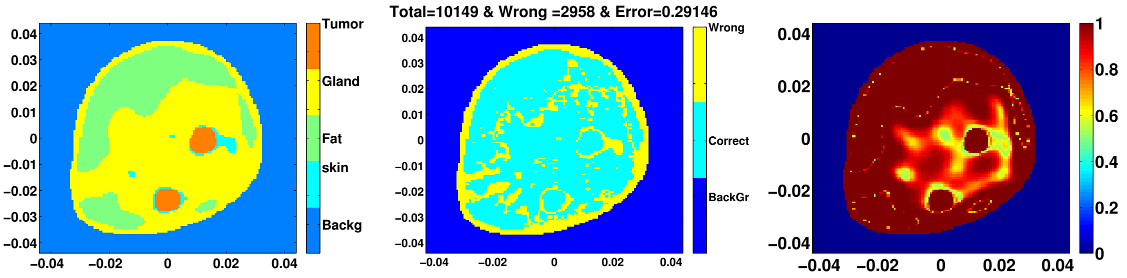

(a) cTTI-Method 2 (b) Correct Pixels (c) Probability Image

Figure 4.12: cTTI, correct pixel and probability images obtained using Method 2 for the second phantom using MWT properties.

4.5.3 cTTI for Combined UT and MWT

We now consider the case where both UT and MWT properties are utilized together to create a composite TTI. The first phantom with a true TTI shown in Fig 4.2a is utilized in this example. The true UT and MWT properties for this phantom are shown in the top row of Fig 4.3 and Fig 4.9 respectively. The data for both UT and MWT are contaminated with 9% noise. The reconstruction of the UT properties and MWT properties for 9% noise are shown in first row of Fig 4.14 and the bottom row of Fig 4.9 respectively. The cTTI obtained using Method 2 for UT properties is shown in the last row of Fig 4.14. The cTTI obtained using Method 2 for MWT properties is shown in the last row of Fig 4.10.

Next, both UT and MWT properties are simultaneously utilized based on Method 2 to create a cTTI. The result of the cTTI using UT and MWT properties are shown in Fig 4.13. As can be seen, the cTTI using both UT and MWT properties leads to a better reconstruction in comparison with the cTTIs based solely on UT properties or MWT properties. It should be noted that the cyst region is not detected in the cTTIs using UT and MWT separately. However, when both UT and MWT prop-

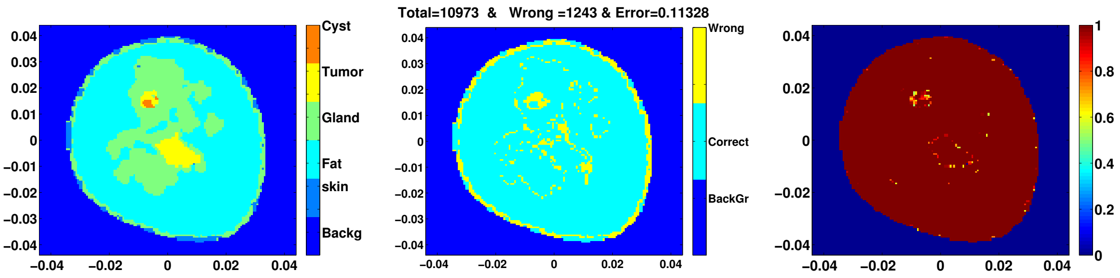

(a) cTTI-Method 2 (b) Correct Pixels (c) Probability Image

Figure 4.13: Composite TTI, correct pixel and probability images obtained using Method 2 for the case that both UT and MWT properties are utilized.

erties are simultaneously utilized, some parts of cyst region start to appear in the cTTI. Furthermore, note that the probabilities of those pixels which are mistakenly assigned as tumor (instead of cyst) are low. That is, even in the case of wrong reconstruction for some pixels, the fact that one cannot be confident in the reliability of the reconstructed tissue type for those pixels is indicated in the composite probability image.

It should be noted that the fat region is well distinguished using the single-property compressibility TTI with high probability values as shown in the second row of Fig 4.14. Therefore, for the previous example, we utilized this information to provide better prior probabilities for those pixels. To this end, we gave higher prior probabilities for fat compared to other tissues for those pixels.

4.5.4 Enhanced Reconstruction using TTI

Next, we show that the concept of TTI can be used to enhance the quantitative reconstruction. As will be explained below, in this approach, we use the TTI to create a better initial guess for the inversion algorithm. That is, the TTI concept is used as a feedback mechanism: we first reconstruct the quantitative properties using a blind initial guess (e.g., an initial guess of zero which was used in all the examples above), form the TTI images, and then finally use these TTI images to create a better initial guess for the inversion algorithm so as to converge to a more accurate quantitative reconstruction. It should be noted that the choice of initial guess is important for the success of inversion algorithms as a bad choice for the initial guess may cause the inversion algorithm to be trapped in wrong local minima.

The proposed method to create a good initial guess for each property can be explained as follows. For a given property, say compressibility, consider its corresponding single-property TTI and its associated probability image. Now, consider one pixel of this single-property compressibility TTI. If its corresponding probability value is above a threshold level, say 0.9, we consider this as a ‘fit’ pixel. Therefore, for that pixel, we use its corresponding reconstructed compressibility value in our initial guess. Otherwise, for that pixel, we consider the single-property TTI of the next property, say attenuation. For that pixel, if the corresponding attenuation probability value is greater than the threshold level, we consider the tissue-type of that pixel as a ‘fit’ tissue type, and assign this pixel a compressibility value as the average of the expected minimum and maximum compressibility values of of that tissue. This process continues until we cover all the single-property TTIs. If the probability value of that pixel is never above the threshold level, we simply use the reconstructed values as there is no ‘smart’ estimate on the value of that pixel. This procedure continues until all the properties associated with each pixel are estimated. Then, the resulting initial guess will be provided to the inversion algorithm.

To understand this approach better, we apply it to the first MRI-based phantom in the UT framework. For this case, we consider that the UT data is contaminated with

9% noise. The reconstruction of the UT properties is shown in the first row of Fig 4.14. (These have been obtained assuming a zero initial guess.) The PDF, tissue-type and probability images for compressibility and attenuation property using Method 1 based on each single property are shown in the second and third rows of Fig 4.14. The composite image, correct-pixel image as well as probability image using the κ and α based on Method 2 are shown in Fig 4.14. We then apply our method to create an enhanced initial guess. To this end, we utilize the single-property TTI and probability images obtained from κ and α. We also utilize the composite TTI obtained from κ and α using Method 2 to create an initial guess for the density property. The initial guess obtained from this method for compressibility, attenuation and density are shown in the first row of Fig 4.15. The reconstruction of the ultrasound properties using this initial guess is shown in the second row of Fig 4.15. The diagonal cut from top left to the bottom right for the true, previous reconstruction and the reconstruction using the initial guess provided by TTI are shown in the third and fourth rows of Fig 4.15. Comparing this result with the previous reconstruction shown in the first row of Fig 4.14, it can be seen that all the property reconstructions are improved. For example, the density reconstruction is significantly improved, the attenuation is also improved, and the value of the tumor attenuation is now more accurate.

4.6 Conclusion

We have introduced the concept of composite TTI and probability image for UT, MWT, and their combination. To arrive at the composite TTI, we have utilized reconstructed quantitative images, and the PDFs associated with these properties for different tissue types. The reconstructed quantitative properties are obtained by the use of inverse scattering algorithms, whereas the PDFs are constructed based

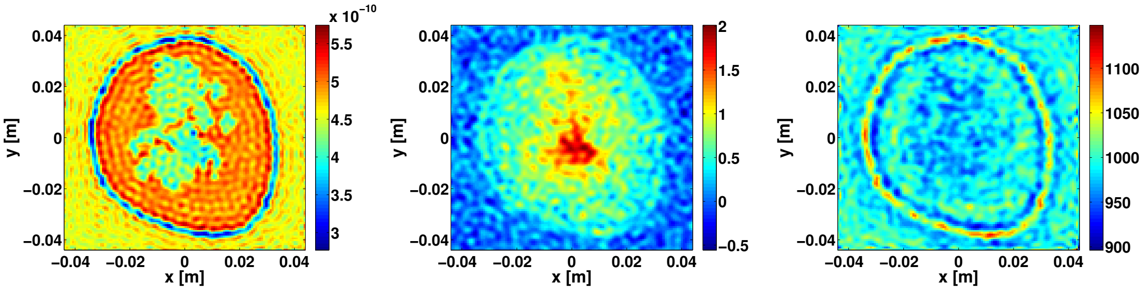

(a) Reconstructed κ (b) Reconstructed α (c) Reconstructed ρ

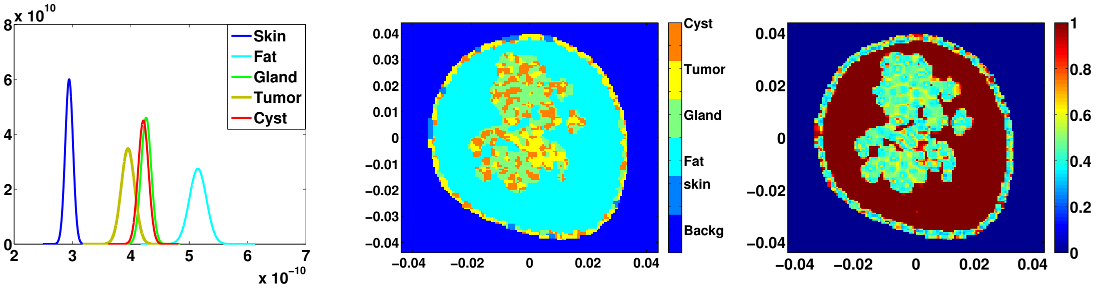

(d) PDF κ (e) Single Prop TTI-κ (f) Probability Image κ

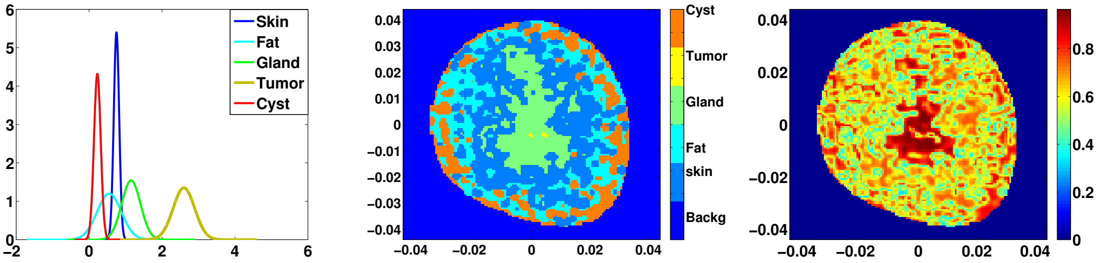

(g) PDF α (h) Single Prop TTI-α (i) Probability Image α

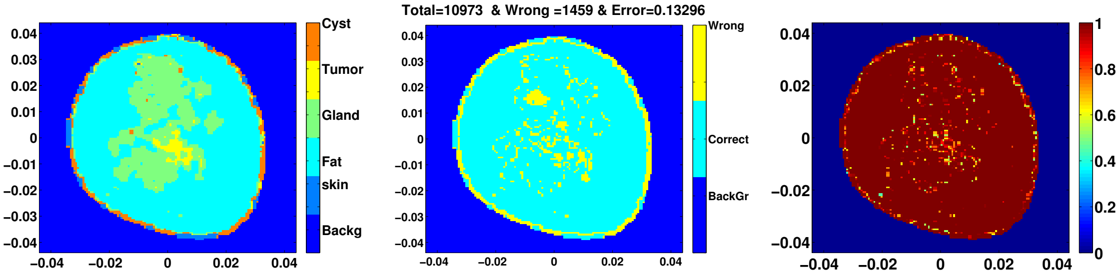

(j) cTTI-Method 2 (k) Correct pixels (l) Probability Image

Figure 4.14: The first row corresponds to the the reconstruction of ultrasonic properties for the case that the noise level is 9%. The second and third rows correspond to the PDF, single property TTI and probability image for κ and α respectively. The last row corresponds to the composite TTI, correct pixel and probability images obtained from Method 2.

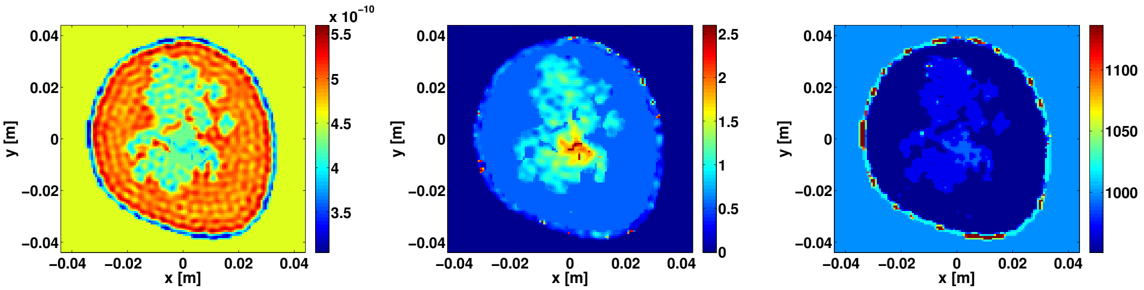

(a) Initial Guess-κ (b) Initial Guess-α (c) Initial Guess-ρ

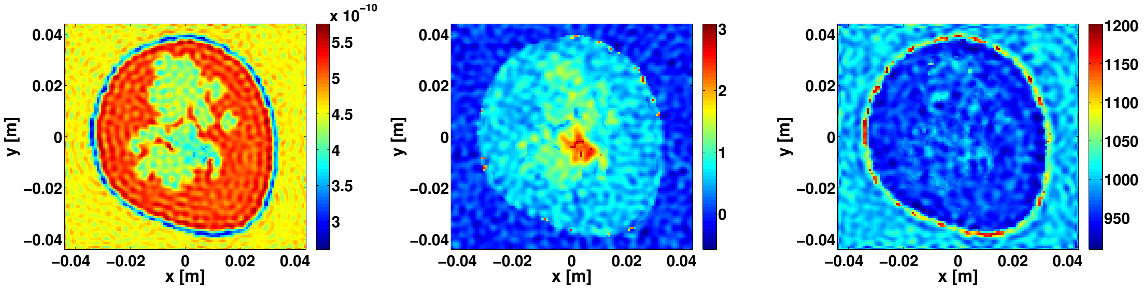

(d) Reconstructed κ (e) Reconstructed α (f) Reconstructed ρ

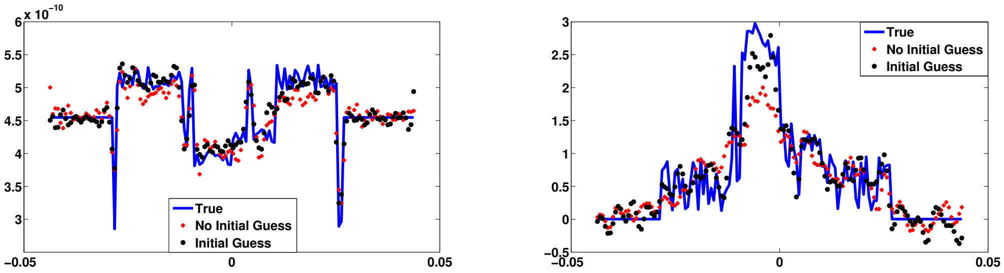

(g) Diagonal cut κ (h) Diagonal cut α

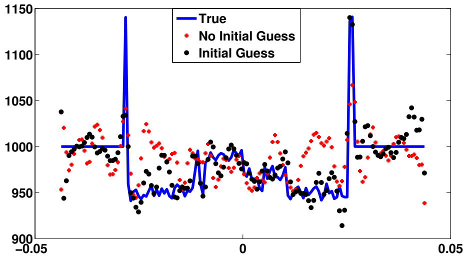

(i) Diagonal cut ρ

Figure 4.15: The first row corresponds to the initial guess provided by TTI. The second row corresponds to the reconstruction of the properties using this initial guess. The third and fourth rows correspond to the diagonal cut for the true and the reconstruction with and without using an initial guess (the horizontal axis corresponds to the x value of the diagonal cut from the top left to the bottom right with the unit of [m] and the vertical axis corresponds to the value of the corresponding properties).

on the expected range of values that tissue properties can take. Specifically, we have utilized two methods to create the composite TTI. The first method utilizes the single variate PDF of each tissue property whereas the second method uses the multivariate PDF for the all tissue properties. For the examples considered here, Method 2 outperformed Method 1 in creating the composite TTI. The main advantage of the proposed concept is that it integrates all the quantitative information of the reconstructed property images into one composite image that represents the most probable tissue type at each pixel. The use of multimodality imaging based on multiphysics properties provides and enhanced ability to identify tissue types within images and better reveals their structure. This will have important advantages for the diagnosis of disease by physicians.

5

Paper 3*: Experimental Evaluation of Composite Tissue-Type Ultrasound and Microwave Imaging

5.1 abstract

The recently proposed concept of composite tissue-type image (cTTI), which provides an easy-to-interpret image constructed from quantitative ultrasonic and electromagnetic properties, is experimentally investigated. The experimental data set used for the ultrasound investigation is obtained from the Multimodal Ultrasound Breast Imaging (MUBI) system. The experimental data set utilized for microwave imaging is provided by an in-house system at the University of Manitoba. To this end, a tissue mimicking phantom and a human forearm are utilized for experimental ultrasound and microwave imaging. In addition, the cTTI algorithm is modified to take into account differences in the quantitative accuracy of reconstructing one property compared to other properties so as to increase the achievable accuracy in the resulting

---

*© 2019 IEEE. Reprinted, with permission, from Pedram Mojabi and Joe LoVetri, "Experimental Evaluation of Composite Tissue-Type Ultrasound and Microwave Imaging," *IEEE Journal on Multiscale and Multiphysics Computational Techniques*, 2019.

cTTI. In addition to experimental ultrasound and microwave data, the cTTI method is also applied against synthetic data obtained from an MRI-based numerical breast phantom to further demonstrate the performance of the cTTI not only with respect to microwave and ultrasound tomography data but also with respect to their combination. Finally, the improvements of the cTTI reconstructions based on changing the prior probabilities compared with equal prior probability distribution are shown for combined ultrasound and microwave tomography of a numerical breast phantom.

5.2 Introduction

Ultrasound tomography (UT) and microwave tomography (MWT) are non-destructive imaging modalities which can provide both qualitative and quantitative images of the object of interest (OI) by processing the measured ultrasound and microwave data collected by transceivers outside the OI. These imaging modalities are being investigated for various industrial non-destructive testing and biomedical applications [1,2,6,10,17,20,28,120–133].

In UT and MWT, the OI is illuminated by an incident wave using a transceiver. The resulting scattered waves are then collected by other transceivers and this process continues for, possibly, all the remaining available transceivers. The collected data is then used by an appropriate reconstruction algorithm to yield ultrasonic and electromagnetic images of the OI. The choice of reconstruction algorithms depends on various parameters including the form of the data, how many data points are available, and the available computational resources. For example, full-wave inverse scattering algorithms [1,4,20,28,30,34,39,110,126,129,134] often require many data points, and are computationally expensive. On the other hand, ray-based techniques, e.g., time-of-flight tomography (TFT) [21,22], are computationally efficient, and in contrast to inverse scattering algorithms, do not suffer from not converging to an appropriate solution due to being trapped in a local minimum [5]. Note that both methods provide quantitative images but based on the measurement configuration and the choice of reconstruction algorithm images can be obtained of different quantitative parameters for a given OI. In this paper, ray-based algorithms[†] are used for reconstruction of the ultrasonic properties for the experimental ultrasound data and Multiplicatively Regularized Gauss-Newton Inversion (MR-GNI) method [1, 28, 136] are utilized for reconstruction of the electromagnetic properties using experimental microwave data and simulated ultrasound and microwave data for the MRI-based breast phantom (for reconstruction of both ultrasound and microwave tomography properties). Having knowledge of several physical properties at a pixel location is an advantage to more accurately infer the tissue-type associated with that pixel. In our case, we consider ultrasound and microwave tomography modalities to reconstruct ultrasonic and electromagnetic properties respectively. (The individual use of these properties to form cTTIs is investigated experimentally, whereas their simultaneous use is merely considered using synthetic data.) The use of ultrasound data with microwave radar imaging has been synthetically considered in [128]. We have also showed the advantage of simultaneously using microwave and ultrasound tomography data for numerical breast phantoms in [2]. (The method to create the numerical breast models from MRI scans as well as some available numerical breast models are reported in [137–139]). In addition, a combined microwave and ultrasound

---

[†] The choice of the ray-based methods for the MUBI experimental ultrasound imaging system is due to the following reason. The MUBI system uses a high center frequency (3.5 MHz) which corresponds to a wavelength of about 0.42 [mm] (with the background medium of water). For an imaging domain with the size of 13 [cm] × 13 [cm], this will translate to $307\lambda \times 307\lambda$. Therefore, the problem will be very large compared to the wavelength. Thus, it will be extremely computationally expensive for the inverse scattering algorithms. In addition, the inverse scattering algorithms often require the calibration of the data using a calibration object, e.g., see [135]. Unfortunately, we did not have access to a calibration dataset for the MUBI system.

tomography system has been proposed in [140].

As far as the end users (medical doctors) are concerned, it is important to be able to provide one image which represents the most important and most practical information. To this end, the composite tissue-type imaging (cTTI) concept was recently introduced in [2], along with other methods such as those based on artificial neural networks (ANNs) [141], and Support Vector Machines (SVM) classifiers [142]. The objective of this work is to combine the reconstructed quantitative images of the ultrasonic and/or electromagnetic properties of an OI, obtained using experimental systems or simulated data, into one image, referred to as the composite tissue type image (cTTI). Instead of associating a quantitative value to each pixel of the cTTI, we associate tissue types and probability levels to the pixels of the cTTI. The probability level is represented by a probability image which can potentially help medical doctors toward making a more reliable diagnosis.

The cTTI approach is important because 1) it can integrate all the available quantitative ultrasonic or electromagnetic images of the OI into a single cTTI image, 2) it can be used for multi-physics imaging such as combined ultrasound and microwave imaging, thus, impacting the worldwide efforts toward integrating different imaging modalities to harness the complementary benefits thereof, 3) in contrast to current ultrasound or microwave tomography algorithms, it provides a probability image representing the level of confidence in the obtained reconstruction, and 4) it provides a user-friendly image in the sense that the end user (*e.g.,* a medical doctor) only needs to look at the resulting tissue-type image, and evaluate the risk based on the associated probability values instead of looking at many different quantitative images corresponding to ultrasonic and/or electromagnetic properties of the OI.

When the cTTI concept was originally proposed in [2], its performance was evaluated utilizing merely synthetically generated ultrasound and microwave data from numerical (breast) phantoms. In particular, in [2], we synthetically evaluated this concept using quantitative reconstruction of compressibility, attenuation, and density as well as complex permittivity obtained from both ultrasound and microwave imaging techniques. In this paper, the main focus is on the experimental evaluation of this approach for ultrasound and microwave imaging. Differences in the accuracy of reconstructing one property compared to another property are also now taken into account in the cTTI algorithm to improve the reconstruction of the composite tissue type. This improvement is shown using the experimental ultrasound data. We also further improve the cTTI algorithm based on changing the prior probabilities[‡]. In the cTTI algorithm, we should define the prior probabilities of each tissue-type occupying each pixel; in [2] these probability values are chosen to be equal. However, in this work, we show that the change of the prior probabilities can lead to improved reconstruction of the cTTI. The results of this improvement are shown with the simulated data using combined ultrasound and microwave tomography property images.

In the ultrasound experimental study reported herein, we utilized data provided by the Multimodal Ultrasound Breast Imaging (MUBI) system developed by the Ultrasound Systems and Technology Group at the Spanish National Research Council (USTG-CSIC) and the Group of Nuclear Physics at the Complutense University of Madrid (GFN-UCM) [54–56][§]. The MUBI data set used herein is freely available to the public based on the USCT Data Exchange and Collaboration initiative [143] and can be accessed at [144]. More detailed information on their system is also available on that web-site. For the microwave experimental study, an in-house microwave

---

[‡] In the context of this thesis, prior probabilities refer to the prior information that is available regarding probability values of each tissue types occupying each pixel.

[§] Experimental results using ultrasound system at the University of Manitoba are also shown in Appendix A.

tomography system at the University of Manitoba [1] is utilized. It should be noted that the reconstruction of the complex permittivity profile of the human forearm used in this paper was already published in [1]; herein, we utilize these quantitative reconstructions to create a tissue-type image along with a probability image.

The structure of the paper is as follows. In Section 5.3, we present the cTTI method along with the associated probability image and we also present some improvements of this method based on changing the prior probabilities. In Section 5.4, we briefly describe the experimental ultrasound and microwave systems from which data were collected. The algorithms for the reconstruction of the ultrasonic and electromagnetic properties of the OI based on ray-based methods and full-wave inversion algorithm are briefly explained in Section 5.5. Results are presented in Sections 5.6, 5.7 and 5.8. Finally, conclusions are presented in Section 5.9.

5.3 Composite Tissue Type Image and Probability Image

The composite tissue type image (cTTI) along with the composite probability image can be created using the quantitative reconstruction of the object of interest. In [2] three quantitative property reconstructions based on synthetic date were utilized: compressibility, attenuation and density. Herein, experimental reconstruction of the sound-speed and attenuation for UT and complex permittivity for MWT are utilized to create the cTTIs. Some improvements on the cTTI algorithm based on 1) changing the prior probabilities and 2) taking into account differences in the accuracy of reconstructing one property compared to another are also presented and shown using experimental and simulated data. The other requirement for creation of the cTTI is some knowledge (assumptions) of the probability density functions (PDFs) for the different properties of each tissue type expected within the object being imaged. These PDFs can be created based on the expected ranges of the tissue properties. These ranges are available in the literature for different biological tissues. For example, the property ranges for skin, fat, fibroglandular, cyst, and tumor for the breast have been studied and can be found in [51, 52, 100]. Information of what these property ranges are is required for the cTTI method, even if only in an approximate fashion. We have utilized two different methods of creating cTTIs and the associated composite probability image [2]. These two methods are now briefly described.

5.3.1 Method 1

In Method 1, we first create a single property TTI and a single probability image for all the properties of interest. These TTI images are then utilized to form a single cTTI; the individual probability images are also converted to a single probability image, which we refer to as the composite probability image. To create a single property TTI, at each pixel of the previously reconstructed property image, the probability that tissue type (T_k) occupies that pixel is calculated based on Bayes' formula [2, 117]

$$P(T_k|x) = \frac{p(x|T_k)P(T_k)}{\sum_{i=1}^{N_t} p(x|T_i)P(T_i)} \tag{5.1}$$

where N_t refers to the total number of tissue types and x is the quantitative value of that pixel in the corresponding property image. $p(x|T_k)$ is the value of the conditional PDF for property value x assuming the tissue type is T_k. The prior probability of assigning tissue type T_k for that pixel is denoted by $P(T_k)$. Then, the tissue type with the highest probability is chosen for each pixel to create a single property TTI. The highest probability for the tissue type occupying that pixel is also stored to create a probability image. The same procedure is performed for all the properties to create a single TTI and an individual probability image for each property. To create a cTTI and composite probability image, we utilize all the single property TTIs and their probability images. To assign a tissue value and probability to each pixel in the cTTI, we first check the probability of each single property probability image and choose the tissue type corresponding to the highest probability. We also assign this highest probability at each pixel as the probability for that pixel in the composite probability image.

5.3.2 Method 2

In this method, all the quantitative properties are utilized simultaneously to create a cTTI along with the probability image without first creating individual TTIs and probability images for each property. In this method, as opposed to Method 1, a multivariate PDF is required instead of single-variate PDFs. For details, see [2]. In summary, in Method 2, the probability of each tissue type occupying a particular pixel is again calculated based on (5.1), but this time using the multivariate PDFs with x being a vector of properties. Then, we choose the tissue type with the highest probability and we also keep the highest probability to create a composite probability image.

5.3.3 Setting the Prior Probabilities

The prior probability of each tissue type, $P(T_k)$, is required in Bayes' formula as shown in (5.1). If we do not have any prior information about the OI, then one can do no better than to set the prior probability of all the tissue types for each pixel the same (obviously, adding up to one). For example in breast imaging application, if we consider five different tissue types (skin, fat, glandular, tumor and cyst), then we set $P(T_k) = 0.2$ letting each of the five tissue types have the same chance of occupying that pixel.

Prior information about the OI, can be incorporated by modifying these prior probabilities in the composite tissue type method [64]. For example, for most biomedical imaging cases, one could increase the prior probability of the skin tissue-type in the outer regions of the reconstruction and set these to zero deep within the reconstructed volume. More complicated scenarios are possible. For example, for breast cancer imaging, if one knows that the tumor is mainly contained within radiodense fibroglandular tissue [62] then the neighbouring pixels of a pixel that has been tissue-typed as tumor can be checked. If the tissue types of neighbouring pixels are fat or skin, then we might reduce the prior probability of the pixel in question being tumor. The probabilities for a region being a cyst or solid lesion varies as a function of the sound speed [145]. This information can be incorporated in the cTTI algorithm to provide a better prior probability, potentially leading to distinguishing these two regions more accurately.

Epidemiological information can also be taken into account in the cTTI algorithm to enhance the discrimination between cyst and tumor [64][¶]. For example, the chances of finding a tumor varies among different breast quadrants. Based on a

---

[¶] More information about the potential use of anatomical and epidemiological information to enhance microwave and ultrasound breast imaging can be found in Appendix B.

study that included 13,984 women having breast tumors the location of the breast having the greatest chance within which the tumor was located was the upper-outer quadrant (UOQ) (58%) compared to upper-inner quadrant (14%), the lower-inner quadrant (9%), the lower-outer quadrant (10%), and the nipple complex (9%) [63]. Furthermore, the chance of having a tumor or cyst is also dependent on the age of patient [146, 147]. This information might be used in future work to set the prior probability values for cancerous tissues at a pixel.

The above description shows some of the potentials for this approach. In this paper, we show the use of improved prior probabilities for both experimental and synthetic data. For example, for the synthetic study, the first set of prior probabilities is based on estimating the skin region and the second set is based on estimating skin and fat regions. The reconstruction of the cTTI using these sets of prior probabilities are compared with the reconstruction of the cTTI with the assumption of equal prior probability.

5.4 Experimental Ultrasound and Microwave Imaging Systems

The ultrasound and microwave systems from which data were collected are now briefly described. Note that these ultrasound and microwave systems produce sampled time-domain and frequency-domain data respectively.

5.4.1 Multimodal Ultrasound Breast Imaging (MUBI) System

The MUBI system [54–56,144] consists of two arrays of movable transducers[‖]. One of the array is used as a transmitter array and the other is used as a receiver array. For each fixed position of the transmitter array, the receiver array can be moved to different positions, allowing one to cover a large angle of interest. For the example shown in this paper, for each fixed position of the transmitter array, the receiver array is moved to 11 different positions in front of the transmitter array as shown in Fig 5.1a. Each 0.22 mm pitch array (P2-4/30EP, Prosonic, Korea) consists of 128 transducers each radiating with a centre frequency of 3.5 MHz, but only 16 elements of each array are used. Thus, for each fixed position of the transmitter array, we have 2816 so-called A-scans. It should be noted that the transmitter array is also moved to 23 different positions to cover 360° of the object of interest. Thus, the total number of A-scans is 64768. A depiction of the tissue mimicking phantom that is part of the USCT Data Exchange and provided by the USTG-CSIC and GFN-UCM groups is shown in Fig 5.1b.

5.4.2 Experimental Microwave Imaging System

We consider an in-house experimental microwave imaging system at the University of Manitoba for the reconstruction of the TTI and probability image of the human forearm. This system consists of 24 dipole antennas with the operation frequency of around 1 GHz immersed in salt water matching fluid as shown in Fig 5.9. More details and calibration methods for this system are explained in [1].

[‖] Each transmitting transducer transmits a pulse waveform in the MUBI system.

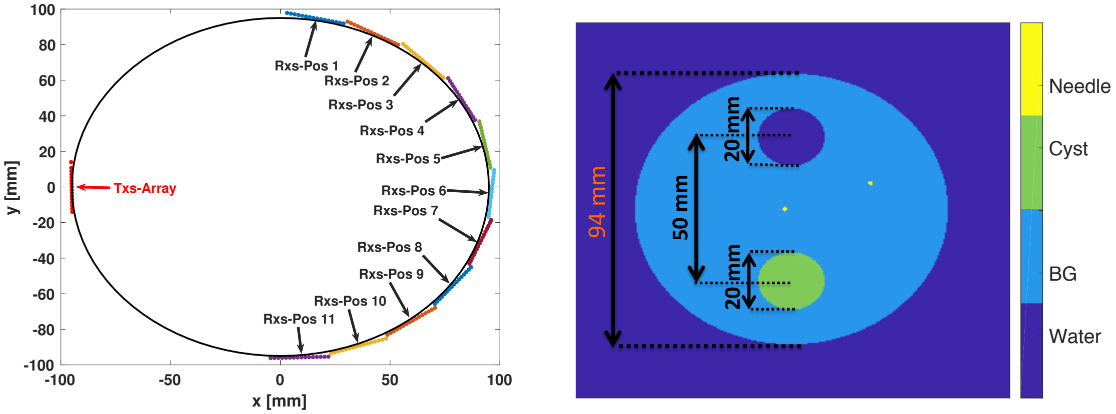

(a) First transmitter array and corresponding receivers array position

(b) True TTI of tissue mimicking phantom

Figure 5.1: Experimental system configuration and the tissue mimicking phantom for the Multimodal ultrasound breast imaging (MUBI) system. (a) Positions of the first transmitter array and the corresponding receivers array position (11 positions of the receiving arrays are utilized per transmitter array). (b) The true tissue type image for the tissue mimicking phantom used for the MUBI system.

5.5 Quantitative Reconstruction of ultrasonic and electromagnetic properties

In order to construct tissue-type images one requires quantitative reconstruction of material properties expected in the object being imaged. The quantitative reconstruction of the complex permittivity profile, which is an electromagnetic property, is addressed in Section 5.5.1, whereas the reconstruction of ultrasonic properties are discussed in Sections 5.5.2, 5.5.3 and 5.5.4.

5.5.1 Complex Permittivity Reconstruction

The MR-GNI method is utilized for the reconstruction of the complex permittivity profile from microwave imaging data. The details for the MR-GNI method for the reconstruction of the complex permittivity are explained in [1], and therefore is not presented herein.

5.5.2 Sound-Speed Reconstruction

To create a sound-speed image one works with the travel time between each transmitter and receiver pair while making the assumption that the ultrasonic wave propagates as a ray between the two. Herein, we follow the work of Duric et. al. for the two-dimensional (2D) case [21]. Travel time, $\mathcal{T}_{tr}$, between transmitter t and receiver r is written as

$$\mathcal{T}_{tr} = \sum_{m=1}^{n_y} \sum_{n=1}^{n_x} \frac{d_{tr_{m,n}}}{c_{m,n}} \tag{5.2}$$

where $c_{m,n}$ is the sound-speed associated with pixel (m, n) and $d_{tr_{m,n}}$ denotes the length of the portion of the ray line from transmitter t to receiver r passing through the pixel (m, n). The number of pixels in the imaging domain are $n_x \times n_y$. It is assumed that the sound-speed is constant in each pixel. The travel time, $\mathcal{T}_{tr}$, must be inferred from the arrival time of the received waveform. (In this paper, the calculation of this arrival time is performed using the modified energy ratio algorithm which will be descried later.) In most experimental systems the actual absolute time at which the waveform is transmitted is unknown, so we write (5.2) for both the incident (in the absence of the OI) and the total (in the presence of the OI) received waveforms. Then, the difference between the travel time for the total and incident waveform can be calculated as

$$\begin{aligned} \mathcal{T}_{tr}^{\text{tot}} - \mathcal{T}_{tr}^{\text{inc}} \triangleq \Delta\mathcal{T}_{tr} &= \sum_{m=1}^{n_y}\sum_{n=1}^{n_x} d_{tr_{m,n}}\Big[\frac{1}{c_{m,n}^{\text{tot}}} - \frac{1}{c_{m,n}^{\text{inc}}}\Big] \\ &= \sum_{m=1}^{n_y}\sum_{n=1}^{n_x} d_{tr_{m,n}}\chi_{m,n}^{c} \end{aligned} \tag{5.3}$$

where $\mathcal{T}_{tr}^{\text{inc}}$ and $\mathcal{T}_{tr}^{\text{tot}}$ are the travel times in the absence and presence of the OI for the particular transmitter/receiver pair. Here $c_{m,n}^{\text{inc}}$ and $c_{m,n}^{\text{tot}}$ are the sound-speeds for pixel (m, n) in the absence and presence of the OI, respectively. It should be noted that in both cases the ultrasound waves are assumed to propagate in a straight ray path between the transmitter and receiver and any potential refraction effect between different regions having different sound-speed is neglected.

Time of arrival calculation

In this paper, the modified energy ratio (MER) algorithm [57, 58] is utilized to calculate TOA of the MUBI signals. An odd DC bias exists in the experimental data and this is removed before applying this method. The MER automatic TOA picker method has been used in seismic [58] and in microwave radar imaging [57]. In this method, the energy ratio between two energy windows from each side of each time sample is calculated as [57, 58]

$$\text{ER}(j) = \Big[\sum_{i=j}^{j+N_w} S^2(i)\Big] / \Big[\sum_{i=j-N_w}^{j} S^2(i)\Big] \tag{5.4}$$

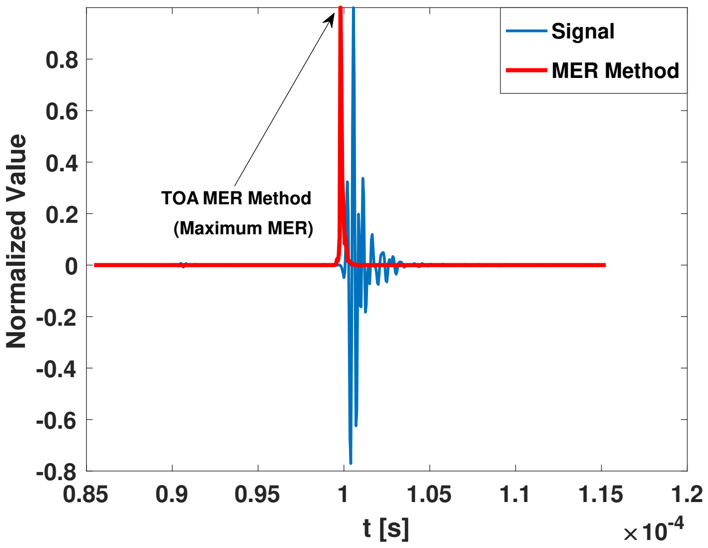

Figure 5.2: Calculation of the time-of-arrival of the signal using the MER method for the typical preprocessed signal obtained by the MUBI system.

$$S(i) = \begin{cases} \frac{S(1)+S(2)}{2} & \text{if } i \leq 0 \\ \\ \frac{S(N-1)+S(N)}{2} & \text{if } i > N \end{cases}$$

where N is the total number of data points in the time-domain signal and j is a value from 1 to N. N_w corresponds to the number of samples in the window. The method we use for choosing N_w is described in [57]. The modified energy ratio is then calculated as

$$\text{MER} = (|S| \times ER)^3 \tag{5.5}$$

The point corresponding to the maximum value of MER is utilized as the the arrival time of signal. For the representative signal shown in Fig 5.2 the MER curve is shown in red.

5.5.3 Attenuation Reconstruction

Attenuation is another quantitative ultrasonic property of the OI which is of importance due to the fact that cancerous tissues are better distinguished from benign tissues by their attenuation than by the difference in their sound-speed [53]. Herein, to reconstruct the tomographic attenuation image, three different ray-based methods are utilized: 1) amplitude decay, 2) spectral ratio method, and 3) complex signal energy ratio [3]. In these methods a ray-propagation assumption is made for modelling the ultrasonic wave between each transmitter and receiver pairs. In addition, a pixel-based attenuation is assumed. These amplitude decay method is briefly described below.

Amplitude Decay Method

The decay of the amplitude of the transmitted signal (source signal) after travelling between transmitter/receiver pair can be written as [3]

$$\mathcal{A}_{tr}^{\text{tot}} = \mathcal{A}_{tr}^{\text{inc}} \times e^{\left(-f_c \sum_{m=1}^{n_y} \sum_{n=1}^{n_x} \alpha_{m,n} d_{tr_{m,n}}\right)} \tag{5.6}$$

where $\mathcal{A}_{tr}^{\text{tot}}$ and $\mathcal{A}_{tr}^{\text{inc}}$ correspond to the amplitude of the signal in the presence and absence of the OI for the particular transmitter/receiver pair being considered. Here, $\alpha_{m,n}$ is the attenuation within pixel (m, n) at the central frequency of the spectrum of the signal being used, f_c. Equation (5.6) can be written as

$$\frac{1}{f_c} \ln \frac{\mathcal{A}_{tr}^{\text{inc}}}{\mathcal{A}_{tr}^{\text{tot}}} = \sum_{m=1}^{n_y} \sum_{n=1}^{n_x} d_{tr_{m,n}} \alpha_{m,n} \tag{5.7}$$

which now clearly shows the measured signal parameters as the data. The size of the column vectors and the matrix in the above equation are the same as in (5.3). For brevity, the details of the spectral ratio and complex signal energy ratio methods for the reconstruction of the attenuation are not described here, but can be found in [3].

5.5.4 Nonlinear Reconstruction of Compressibility and Attenuation

In addition to the ray-based methods above, the MR-GNI algorithm was adapted in [28] to reconstruct the ultrasonic properties of compressibility and attenuation (with the assumption of no variation of density). As will be seen, in this paper, we also utilize the MR-GNI algorithm to reconstruct ultrasonic (compressibility and attenuation) properties of an MRI-based breast numerical phantom.

5.6 Experimental Ultrasound Results

Developers of the MUBI system provide one set of data for a tissue mimicking phantom [54–56,144]. The tissue structure of this phantom is shown in Fig 5.1b. Water, gelatin, graphite powder, and alcohol are utilized to create this phantom. This phantom is composed of a homogenous background denoted as "BG". The structure within this BG region consists of two 0.25 mm diameter steel needles, and two cylindrical hollows: one filled with water and the other filled with a gelatin preparation. The ultrasonic properties of the gelatin-filled hollow are meant to mimick cyst tissue (the sound-speed of this cyst region has only a small difference compared to that of the BG region [55]). Measurements are taken with this phantom immersed in a water-filled tank. The sound-speed of the water used for this experiment was measured to be 1479.7 [m/s], provided by the MUBI developers. We assume that the attenuation in water is close to zero [148]. Using the provided data, we first show quantitative

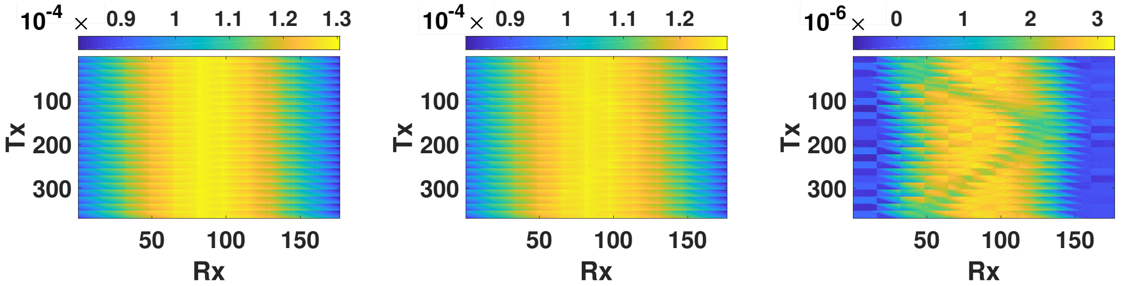

(a) $\mathrm{TOA}_{\mathrm{Inc}}$ (b) $\mathrm{TOA}_{\mathrm{Tot}}$ (c) $\mathrm{TOA}_{\mathrm{Inc}}$ - $\mathrm{TOA}_{\mathrm{Tot}}$

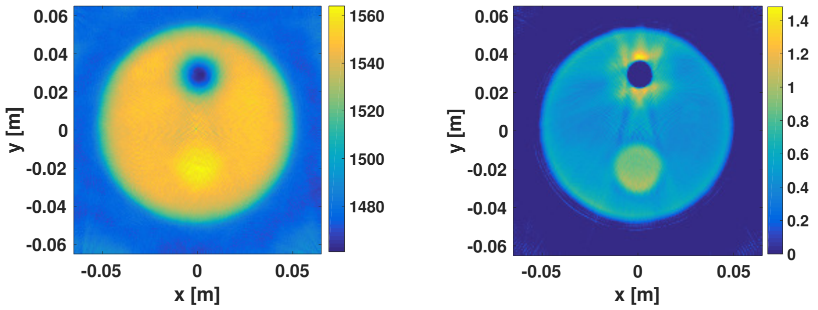

(d) sound-speed (e) α-Amplitude Decay

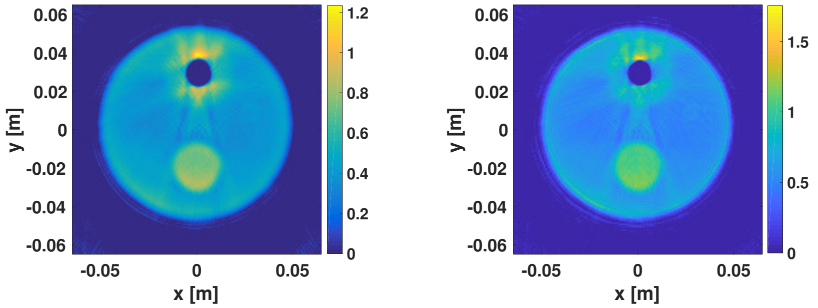

(f) α-Complex Signal Energy Ratio (g) α-Spectral Ratio

Figure 5.3: Reconstruction of the sound-speed and attenuation for the tissue mimicking phantom. The first row corresponds to time of arrival of incident, total signals and their difference. The second and third rows correspond to the reconstruction of the sound-speed and attenuation.

reconstruction of the sound-speed and attenuation. We then utilize these quantitative images to create one composite tissue-type image (cTTI) with its corresponding probability image.

5.6.1 Property Reconstructions using the MUBI System Data

The TOA of the incident, total signals, and their subtraction are shown in the first row of Fig 5.3. The reconstruction of the sound-speed is shown in Fig 5.3d. The reconstructed value of the sound-speed for the BG and cyst regions are very close to each other and it is difficult to distinguish these two regions from each other. In Fig 5.3 (e, f, g) the attenuation reconstructions are shown. The cyst region can be better distinguished from the BG region using the attenuation property because of the larger difference that exists in the attenuation contrast as compared to the sound-speed contrast for these two materials [51, 53, 55]. It should also be noted that in the reconstructed attenuation image, the size of the reconstructed water hollow is smaller than its actual size and we also see some wrongly reconstructed pixels having high values for the reconstructed attenuation around the water hollow. These artifacts show up irrespective of the attenuation algorithm being used.

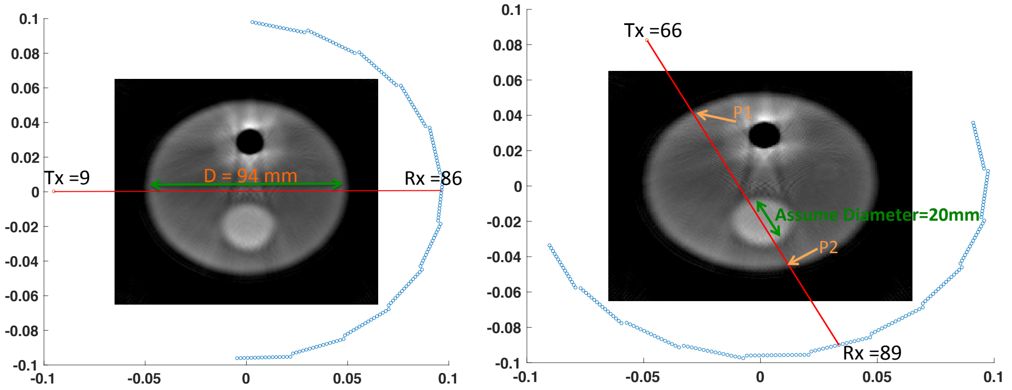

(a) Line $Tx = 9, Rx = 86$ (b) Line $Tx = 66, Rx = 89$

Figure 5.4: Calculate the sound-speed and attenuation for the cyst and BG regions in tissue mimicking phantom using two different straight ray-paths (transmitter/receiver pairs).

5.6.2 Estimation of the Actual Sound-speed and Attenuation

We now show how the quantitative property images obtained from the MUBI system can be used to create a cTTI along with the associated probability image. Unfortunately the MUBI developers do not provide the actual sound-speed and attenuation values for the different materials used in their phantom. To estimate the actual value of these two properties for the two tissue mimicking materials used in the phantom, cyst and BG, we consider two different straight ray-paths as shown in Fig 5.4. These two paths correspond to two different transmitter/receiver pairs also shown in the figure. The first pair is chosen to be between $Tx = 9$ and $Rx = 86$ as shown in Fig 5.4a. The straight line between this transmitter/receiver passes through the main diameter ($D = 94$ mm) of the phantom which includes only the BG material. Thus, the sound-speed and attenuation of the BG material can be estimated using the incident and total signal for this transmitter/receiver pair based on (5.3) and (5.6), respectively. The second transmitter/receiver pair path is chosen to be between $Tx = 66$ and $Rx = 89$ as shown in Fig 5.4b. The straight line path between this transmitter/receiver pair approximately passes through the main diameter of the cyst region (20 mm). The two points where this line intersects with the phantom are denoted as $P1$ and $P2$. We can calculate the sound-speed and attenuation for the cyst region based on the estimated distance between these two points as well as on the ultrasonic properties of the BG regions using (5.3) and (5.6). Using this method, the estimated sound-speed and attenuation for the different materials making up the tissue mimicking phantom are tabulated in Table 5.1.

Table 5.1: The calculated sound-speed and attenuation for different regions of the tissue mimicking phantom.

Tissue	Sound-Speed [m/s]	Attenuation [dB/cm]
Water	1479.7	0
BG	1546.7	0.4929
Cyst	1572.1	0.9227

5.6.3 Assigning the PDFs

Quantitative reconstruction of the object of interest as well as the probability density functions (PDFs) of each property for the different tissue types are required to create the cTTI and its corresponding probability image. The PDF of each property for each tissue type is approximated based on the expected range of that property for each tissue. Using the estimated sound-speed and attenuation tabulated in Table 5.1, we assume that these properties will be centered at the tabulated value and vary by ±15 [m/s] for the sound-speed and ±0.2 [dB/cm] for the attenuation. Then, the standard deviation of an assumed normally distributed PDF is calculated based on the assumption that the value of the PDF at the minimum and maximum values of the expected ranges is 40% of the maximum value of the PDF [2]. The multivariate normal PDF used for Method 2 of creating a cTTI is created using these standard deviations and mean values.

5.6.4 Single Property TTI Results

The sound-speed and attenuation property PDFs for all tissue types are shown in the first row of Fig 5.5. The single-property TTI and single-property probability images are shown in the second and third rows of Fig 5.5. The region filled with water is well distinguished with high probability in the single-property sound-speed

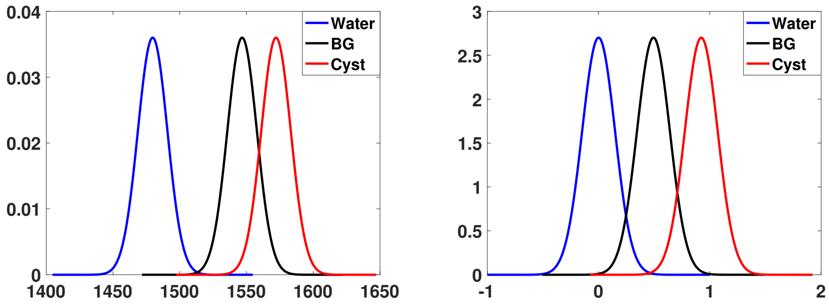

(a) PDF c (b) PDF α

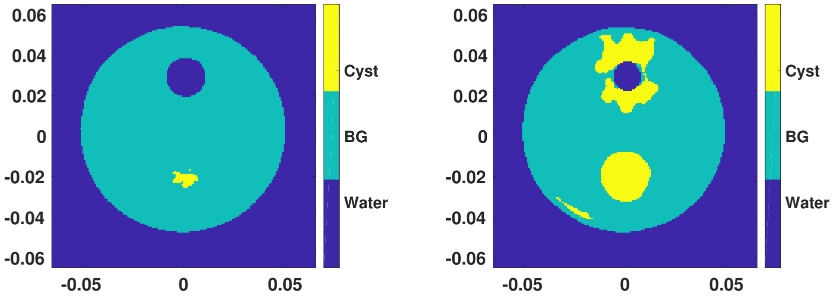

(c) Single-Prop TTI-c (d) Single-Prop TTI-α

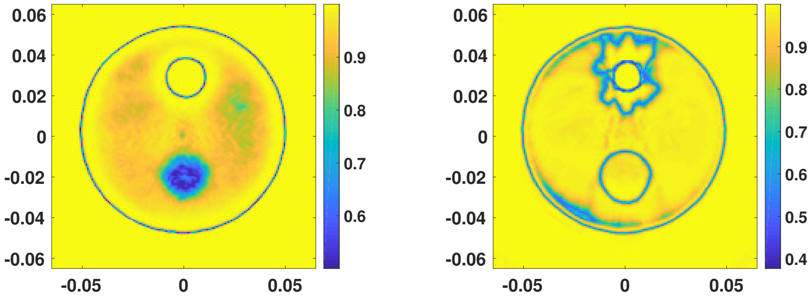

(e) Probability image c (f) Probability image α

Figure 5.5: PDF, single property TTI, and probability image for sound-speed (c) and attenuation (α) are shown in the first and second columns.

TTI. The sound-speed of the cyst and BG are close to each other [55] as shown in the Fig 5.3d and Table 5.1. This leads to the sound-speed PDFs for cyst and BG overlapping significantly. The result is that the probability of the cyst region in the associated probability image is low as shown in Fig 5.5e. The cyst region is well distinguished with high probability in the single-property attenuation TTI. However, some pixels close to the perimeter of the water hollow are wrongly chosen to be cyst in the single-property attenuation TTI. This is due to the fact that these pixels are wrongly reconstructed with high attenuation in the property image shown in Fig 5.3e.

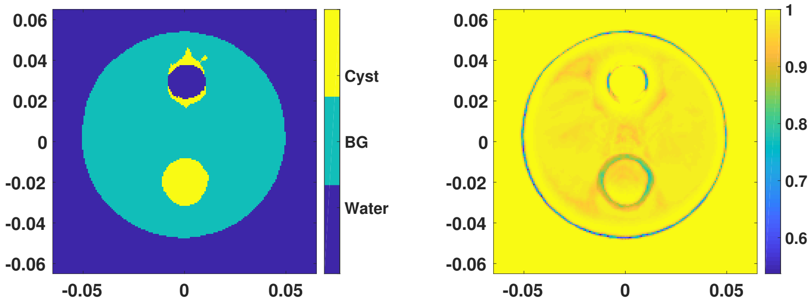

(a) CTTI-Method 1 (b) Probability image

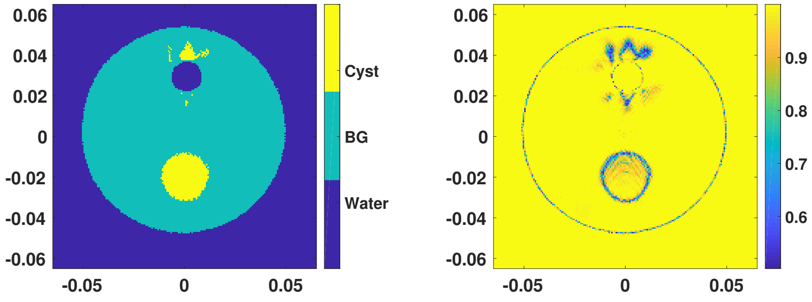

(c) CTTI-Method 2 (d) Probability image

Figure 5.6: Reconstruction of cTTI and composite probability image. The first and second rows correspond to the Method 1 and Method 2 respectively.

5.6.5 Composite Property TTI Results

We now show the benefits of utilizing either of the two composite tissue type reconstruction methods previously described. In Method 1, we utilize the single property

TTIs and associated probability images based on the sound-speed and attenuation. The cTTI and composite probability image, based on Method 1, are shown in the first row of Fig 5.6. Alternatively, in Method 2, all the property reconstructions are simultaneously used to create the cTTI and its probability image. The resulting images are shown in the second row of Fig 5.6. As expected, both methods produce TTIs that are an improvement over the single property TTIs. Note that the associated probability images indicate that some pixels are reconstructed with a low probability. This is especially true at the borders between regions, and around the water hollow where the attenuation reconstruction is poor. Methods of ameliorating the poor performance of the cTTI algorithm for some regions are now described.

5.6.6 Improvements Based on Trust in Property Reconstructions

In this section we propose some possible improvements to the TTI framework. First is the concept of potentially having more trust in the reconstruction of one property over another. For example for the MUBI phantom, the reconstruction of the sound-speed is more accurate than the reconstruction of the attenuation. This can be seen around the water hollow in the MUBI phantom as shown in Fig 5.3. In this region, the reconstruction of the attenuation is poor whereas the sound-speed reconstruction is good. It is obvious from the MUBI phantom imaging results that one might have more trust in the reconstruction of the water hollow over the cyst in the sound-speed reconstruction. This is clearly shown by the probability image associated with the single-property TTI for sound-speed in Fig 5.5e, where the reconstruction of the water hollow has a probability of close to 1. It is important to note that the low probability (≈ 0.6) associated with cyst reconstruction in the sound-speed image is not due to poor reconstruction; it is due to the fact that the PDFs of cyst and BG have much more overlap compared to with the water hollow (see Fig 5.5a).

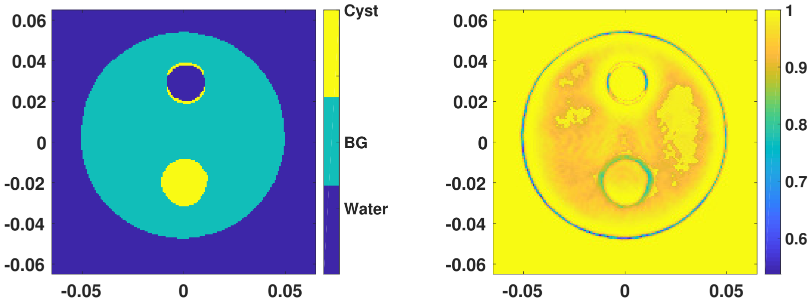

(a) cTTI-Method 1 (b) Probability Image

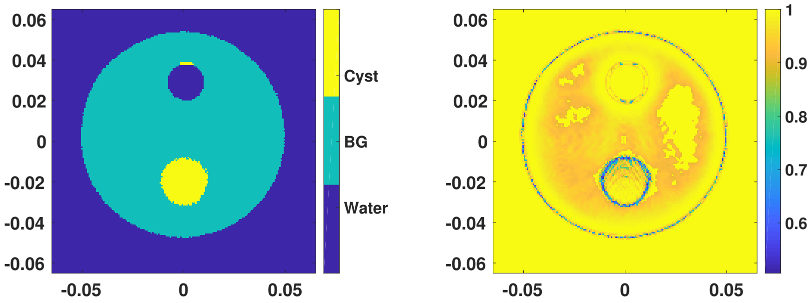

(c) cTTI-Method 2 (d) Probability Image

Figure 5.7: Reconstruction of cTTI and composite probability image using Method 1 and Method 2 with the prior information of having more trust in the reconstruction of the sound-speed compared to the attenuation. The tissue types with the high probability value (greater than 0.9) in the single-property TTI probability image based on the sound-speed are chosen in the cTTI.

Unfortunately, the cTTIs reconstructed using either Method 1 or 2, shown in Fig 5.6, erroneously reconstruct some cyst pixels around the water hollow instead of BG or water with high probability. Note that the water hollow itself is reconstructed with a slightly smaller radius than its true radius but those pixels on its perimeter are reconstructed with lower probability. Thus, if we decide to trust more in the quantitative reconstruction of the sound-speed property we could take the single-property TTI reconstructed using the sound-speed and keep the pixels that are associated with a probability that is greater than a chosen threshold. This is applicable to cTTI reconstruction using either method. This is a simple way of including prior information into the cTTI.

For our particular example of the MUBI phantom, we choose this threshold to be 0.9 in the single-property TTI probability image based on the sound-speed. Then in the cTTI these pixels are replaced using the pixels from this single-property TTI (including their associated probability). The new cTTI and composite probability image using this method is shown in Fig 5.7. Note the improvement, especially utilizing Method 2.

The prior information and/or the knowledge about the geometrical structure of the OI can be taken into account in the prior probability. This information can provide a better prior probability when utilizing Bayes' equation. The equal prior probability for different tissue types is utilized for the case that one has no prior information. On the other hand, we can infer some information based on any particular reconstruction. For example, for the MUBI phantom we now show how the single property TTI sound-speed and its associated probability image can be used to modify the prior probability of a pixel considering the reconstructed tissue type of neighbouring pixels and their corresponding probability values. If we consider a pixel (q, w) and neighbours up to m pixels away ($m = 1$ in this example), then all the pixels between rows $q - m$ and $q + m$ and columns $w - m$ and $w + m$ are utilized to calculate a prior probability for pixel (q, w). To calculate a prior probability for tissue type T_k occupying this pixel, we first check the neighbours including pixel (q, w) having tissue type T_k and then add the probability corresponding to these pixels. Finally, this number is divided by

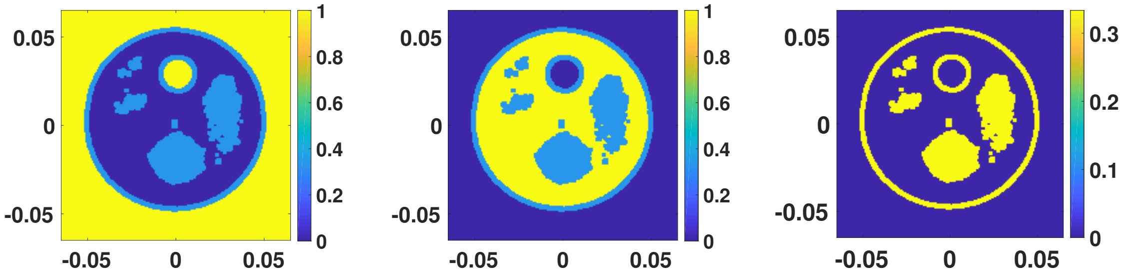

(a) Prior Prob Water (b) Prior Prob BG (c) Prior Prob Cyst

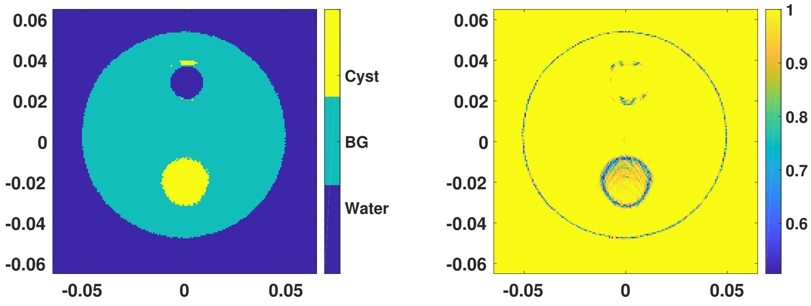

(d) CTTI - Method 2 - Prior prob (e) Probability Image

Figure 5.8: Reconstruction of the cTTI and composite probability image using the prior probability obtained from the single property sound-speed. The first row corresponds to the prior probability calculated using the single property TTI sound-speed.

total number of neighbouring pixels plus one. We perform the same procedure for all the tissue types to find the prior probability of each tissue type for pixel (q, w) and for all pixels. Then, the new prior probability is applied to the composite tissue type method to enhance the reconstruction of the cTTI. It should be noted that we only apply this method to those pixels having the probability greater than a threshold (0.9 in this example) in the probability image of the single property sound-speed. For the other pixels having the probability is less than 0.9 in the single probability of the sound-speed, equal prior probability for different tissue types are utilized. Using this method, the newly calculated prior probabilities of each pixel being water, BG, and cyst for the MUBI phantom are shown in the first row of Fig 5.8. The reconstruction of the cTTI and composite probability image using Method 2 based on the new prior probabilities is shown in the second row of Fig 5.8. As can be seen, the reconstruction of cTTI using the new prior probabilities is improved compared to the reconstruction using equal prior probabilities.

5.7 Experimental Microwave Results

The experimental data obtained from the human forearm using the MWT system at the University of Manitoba is utilized to create a tissue-type image along with the probability image. In this experiment, which was originally reported in [1], salt water is used as a background medium (Salt-15 in [1]). The reconstruction of the real and imaginary parts of the relative complex permittivity profile of the volunteer's forearm, denoted by ϵ_r and ϵ_i respectively, are shown in the first row of Fig 5.9 using the balanced MR-GNI algorithm at the frequency of 0.8 GHz. (The development of this MWT system and the reported inversion are from [1]; herein, we will use these to experimentally evaluate our TTI framework.)

To reconstruct the tissue-type image for the human forearm, only the real part of the complex permittivity is used. This is due to the fact that the reconstruction of the real part of the complex permittivity is much more accurate in comparison with the imaginary part of the complex permittivity as shown in the first row of Fig 5.9. The PDF for each tissue type of the real part of the complex permittivity is approximated based on the expected range of each tissue. The expected values of the relative complex permittivity for salt water, muscle, and bone at 0.8 GHz are $\epsilon^{\text{Salt Water}} = 77 - j17$, $\epsilon^{\text{muscle}} = 56 - j20$ and $\epsilon^{\text{bone}} = 13 - j3$ [1]. (A time-dependency of $\exp(j\omega t)$ is assumed.) We assume that these expected values will be centered and

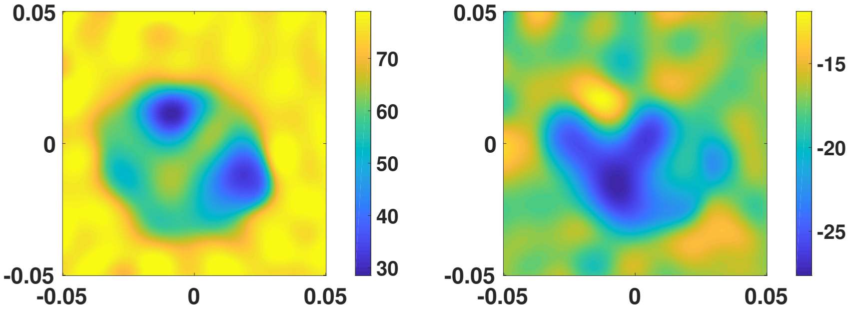

(a) Reconstructed ϵ_r (b) Reconstructed ϵ_i

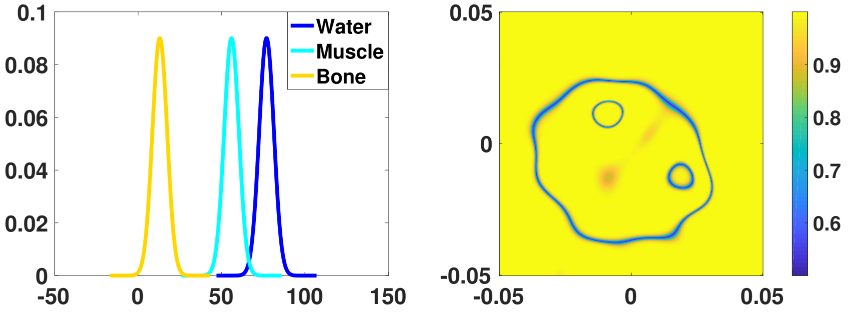

(c) PDF ϵ_r (d) Probability Image ϵ_r

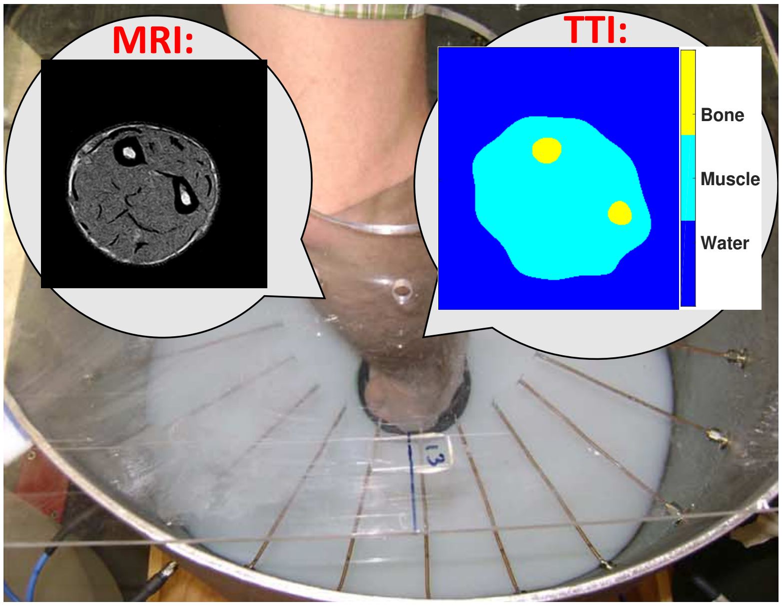

(e) Measurement of volunteer's forearm using MWT - MRI & TTI Reconstructions.

Figure 5.9: Experimental measurement of the forearm using MWT. The first row corresponds to the reconstruction of the complex permittivity. The second row corresponds to the PDF and probability image. Experimental MWT set up for measuring forearm as well as MRI and TTI of the volunteer's forearm are shown in the last row. (The photo of the experimental system and MRI image were taken from [1])

vary by ±6 for the real part of the complex permittivity. Then, the standard deviation of an assumed normally distributed PDF is calculated based on the method explained in Section 5.6.3. The PDF and probability image for the real part of the complex permittivity of the volunteer's forearm are shown in the second row of Fig 5.9. In the probability image of the single property ϵ_r, the probability of choosing specific tissue type for each pixel is high except for the pixels at the boundary between different tissue types. The single property TTI (using only ϵ_r property) and magnetic resonance image (MRI) of the volunteer's forearm are shown in Fig 5.9e. Comparing the reconstruction of the TTI with the MRI image of the volunteer's forearm, it can be seen that the reconstruction of the TTI (with only using one property-ϵ_r) for the volunteer's forearm is promising.

5.8 Synthetic combined UT and MWT Results

In this section, we reconstruct the composite tissue type along with the probability image using ultrasound, microwave tomography properties as well as their combination for an MRI-based numerical breast phantom having a more complicated structure compared to the tissue mimicking and human forearm used in the previous sections. (In addition to being a more complicated object, the use of this numerical phantom enables us to create a cTTI from combined UT and MWT data.) The effect of improving prior probability compared to having equal prior probability is also considered in the reconstruction of the cTTIs. The true tissue type image of this phantom is shown in Fig 5.10. The simulated data is provided by a two-dimensional (2D) forward solver and data is contaminated with 2% noise for both ultrasound and microwave imaging according to the equation presented in [109]. To avoid the inversion crime for both ultrasound and microwave tomography, the mesh used in the generation of the synthetic data is different from the one used for inversion. The background medium is chosen to be water and a 2D point source is utilized as a transmitting source. It should be noted that the error associated with applying a 2D inversion to a 3D object has not been considered. The number of transceivers for UT and MWT is set to be 120 and 40 respectively as shown in Fig 5.10. (Due to having a smaller wavelength for UT, the number of UT transceivers are more than those for MWT.) The formation of the true ultrasonic, electromagnetic properties of this breast phantom as well as the PDFs are based on [2]. The MR-GNI algorithm is utilized as a non-linear inversion algorithm for the reconstruction of the ultrasonic and electromagnetic properties of this MRI-based breast phantom. The cTTIs for this numerical phantom is reconstructed based on Method 2.

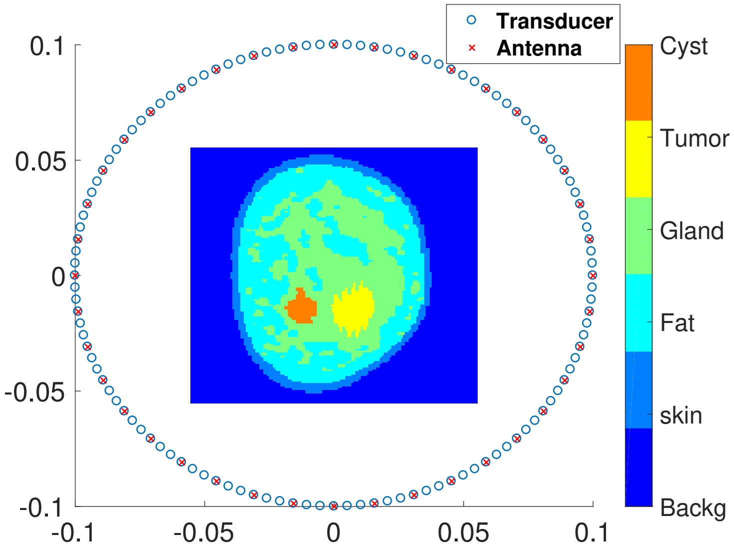

Figure 5.10: The true tissue type image of the MRI-based numerical phantom. The positions of transceivers for UT and MWT are also shown in this image.

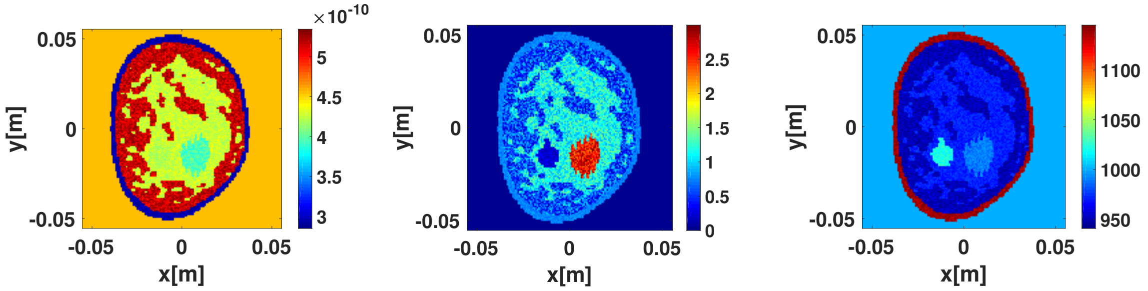

(a) True κ (b) True α (c) True ρ

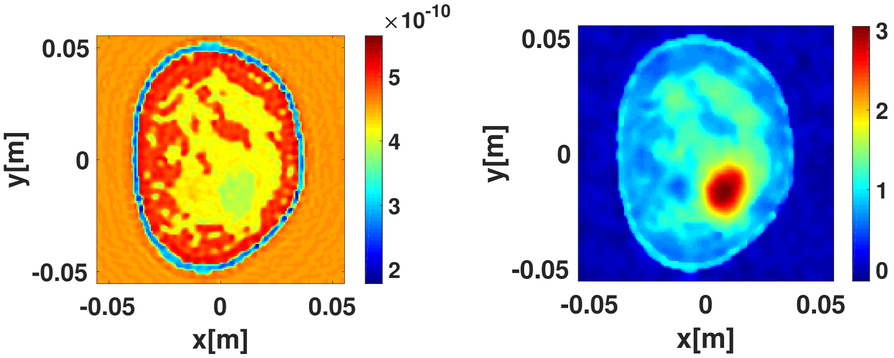

(d) Reconstructed κ (e) Reconstructed α

Figure 5.11: The first row corresponds to the true ultrasonic properties of the breast phantom used in the forward solver. The second row corresponds to the reconstruction of the compressibility and attenuation.

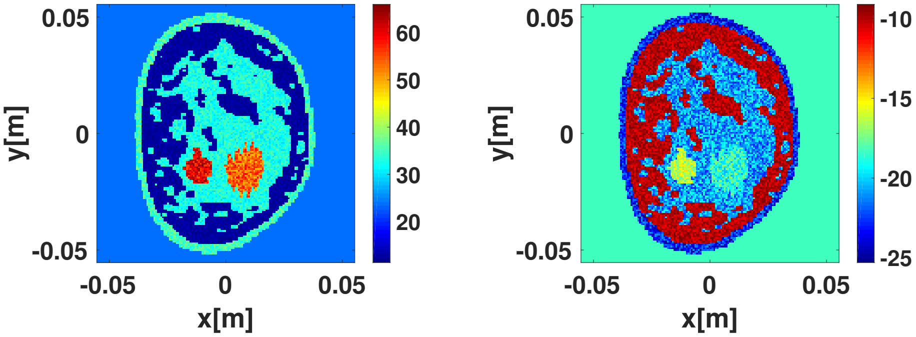

(a) True ϵ_r (b) True ϵ_i

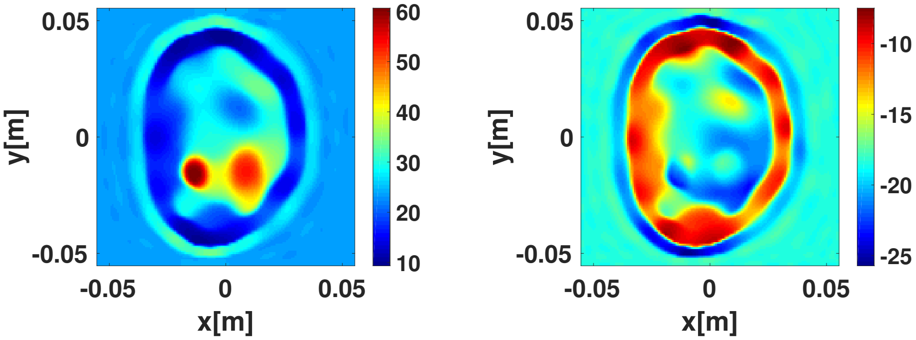

(c) Reconstructed ϵ_r (d) Reconstructed ϵ_i

Figure 5.12: The first and second row correspond to the true and reconstructed electromagnetic properties of the MRI-based breast phantom.

5.8.1 Single Property TTI Results

The true ultrasonic properties (*i.e.,* compressibility, attenuation and density) for this phantom are shown in the first row of Fig 5.11. The reconstruction of the compressibility and attenuation is shown in the second row of Fig 5.11. It should be noted that the variation of all three ultrasonic properties are considered in the creation of the simulated data. However, the variation of density is neglected in the non-linear inversion algorithm[**] (Scenario 3 in [28]). Three frequencies, $f = [110, 150, 200]$ kHz, are simultaneously utilized for this UT inversion algorithm. True and reconstructed electromagnetic properties (*i.e.,* real and imaginary parts of the complex permittivity) for this phantom are also shown in the first and second rows of Fig 5.12. Five frequencies, $f = [1.1, 1.5, 2, 2.4, 2.8]$ GHz, are simultaneously utilized for the MWT inversion algorithm. The PDF, single property TTI and probability image for compressibility, attenuation, real and imaginary parts of the complex permittivity are shown in different rows of Fig 5.13. In the reconstruction of these TTIs, the chance of each tissue-type occupying each pixels is assumed to be the same (equal prior probability). In other words, the chance of occupying each pixel for skin, fat, glandular, tumor and cyst is the same and equal to 0.2.

5.8.2 Forming Improved Prior Probabilities

The prior probability utilized in the Bayas' equation can be improved to enhance the reconstruction of TTIs. We consider two different sets of improved prior probability based on the estimated skin and fat regions for this breast phantom. To estimate

---

[**] Herein, although the density variation is considered in the generation of the synthetic data, the inversion of the density profile is not considered herein; i.e., the contrast of density is assumed to be zero. Of course, this results in modelling error in the inversion process. It should be noted that we have avoided this assumption in Chapters 2, 3 and 4 in which all the contrast functions are inverted.

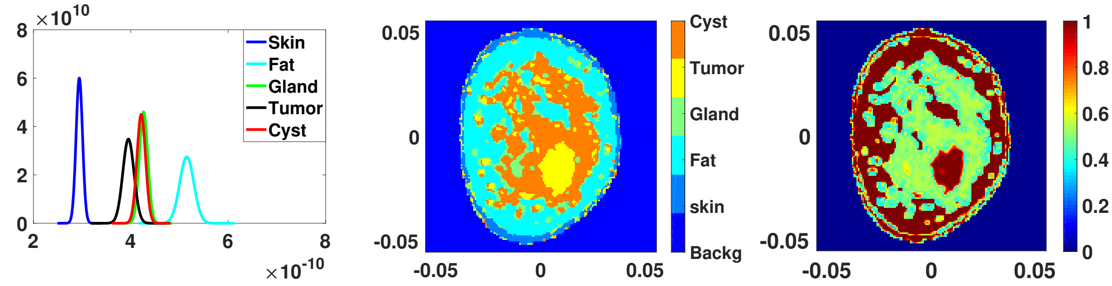

(a) PDF κ (b) TTI-κ (c) Probability Image κ

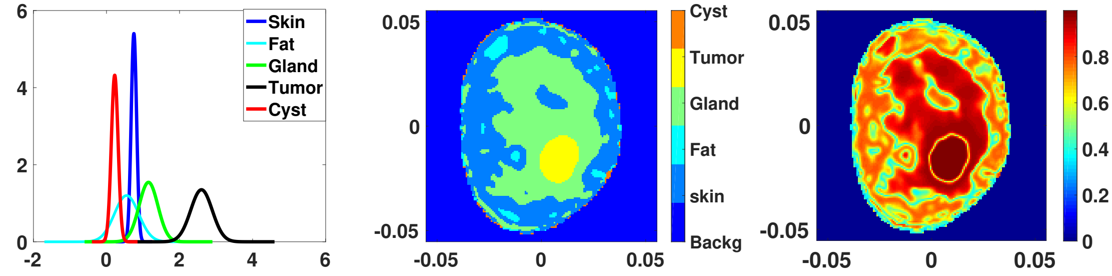

(d) PDF α (e) TTI-α (f) Probability Image α

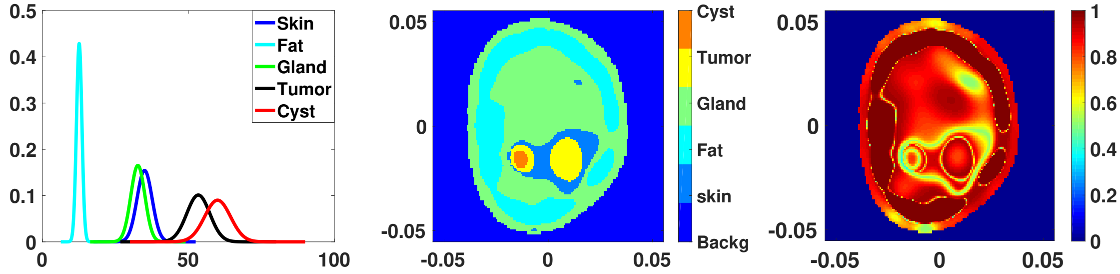

(g) PDF ϵ_r (h) TTI-ϵ_r (i) Probability Image ϵ_r

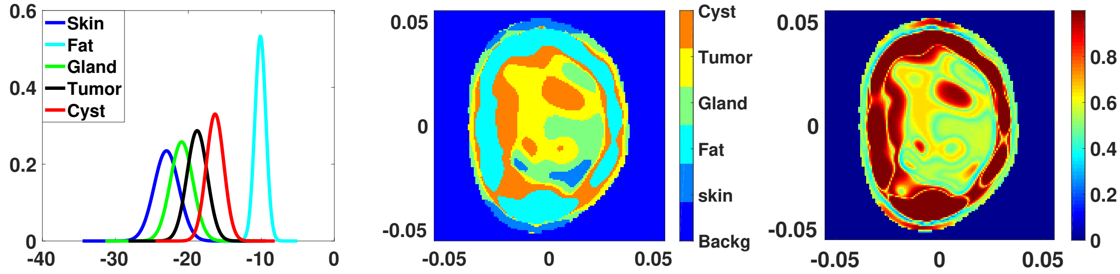

(j) PDF ϵ_i (k) TTI-ϵ_i (l) Probability Image ϵ_i

Figure 5.13: PDF, single property TTI, and probability image for compressibility, attenuation, real and imaginary parts of complex permittivity. It is assumed that the prior probability of each tissue type occupying each pixel is equal.

the skin region for this phantom, we utilize the reconstruction of attenuation as shown in Fig 5.11e. This is due to the fact that the attenuation of water is close to zero which leads to better classification of breast from the background medium. This classification based on attenuation image is shown in Fig 5.14a. Then, the intersection line between background medium and OI can be found as shown in Fig 5.14b. Finally, some thickness (4 mm from inner side and 2 mm from other side) are considered for the skin region as shown in Fig 5.14c. Once the skin region is identified, an improved prior probability based on its knowledge can be utilized to enhance the cTTI reconstruction. It should be noted that the skin is in the outer region of a breast. For the region shown in Fig 5.14c (estimated thickness of skin), we consider that this region can be skin or fat and the equal prior probabilities of 0.5 for the skin and fat for this region are utilized. In addition, the probability of having skin tissue in the central parts of the reconstructed breast volume is set to zero. The chance of having fat, glandular, tumor and cyst anywhere inside the breast but outside the skin region is set to be equal. The improved prior probabilities based on the estimated skin region is shown in the first column of Fig 5.15.

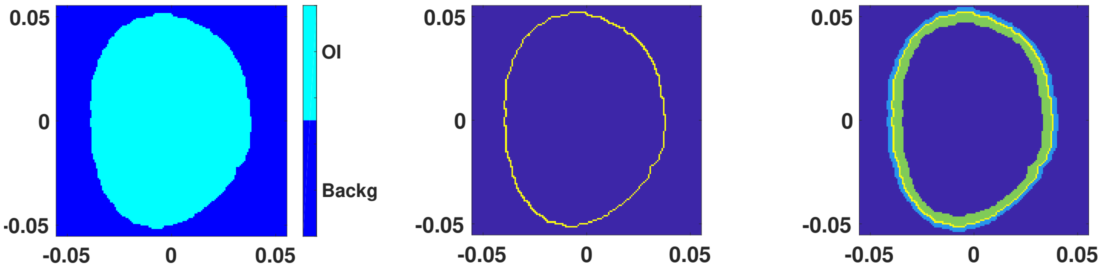

(a) (b) (c)

Figure 5.14: Find Skin region based on the reconstructed attenuation image. (a) Distinguish background from OI, (b) Outer Skin Region, and (c) Defined estimated thickness skin.

In the second improved prior probabilities, we consider both estimated skin and fat regions. The fat region is well distinguished in the single property TTI of compressibility with the probability close to one in the probability image as shown in Figs 5.13b,c. This is due to the fact that the range of the fat value in the compressibility property is totally different from the other tissue types as shown in Fig 5.13a. Once the skin and fat regions are identified, for the region shown in Fig 5.14c, we consider that this region can be skin or fat and the equal prior probabilities of 0.5 for the skin and fat for this region are utilized. For the region that is chosen as a fat in the single property TTI of compressibility property shown in Fig 5.13b, we consider that this region can be only fat and prior probabilities of one for the fat for this region is utilized. Finally, the chance of having skin and fat for the other pixels are considered to be zero and these pixels only have a chance to be glandular, tumor and cyst with the equal prior probability of 1/3. The second improved prior probabilities are shown in the second column of Fig 5.15.

5.8.3 Composite Property TTI Results from UT, MWT, and Their Combination

The cTTI, probability image and correct pixels with the assumption of having equal prior probabilities using solely ultrasound or electromagnetic properties are shown in the first and second columns of Fig 5.16. As can be seen in the cTTI reconstruction using electromagnetic properties with the assumption of equal prior probability as shown in Fig 5.16b, some pixels inside the breast are wrongly chosen to be skin. However, these pixels can be fixed using the first set of improved prior probability (based on skin region) as shown in the third columns of Fig 5.16. In this

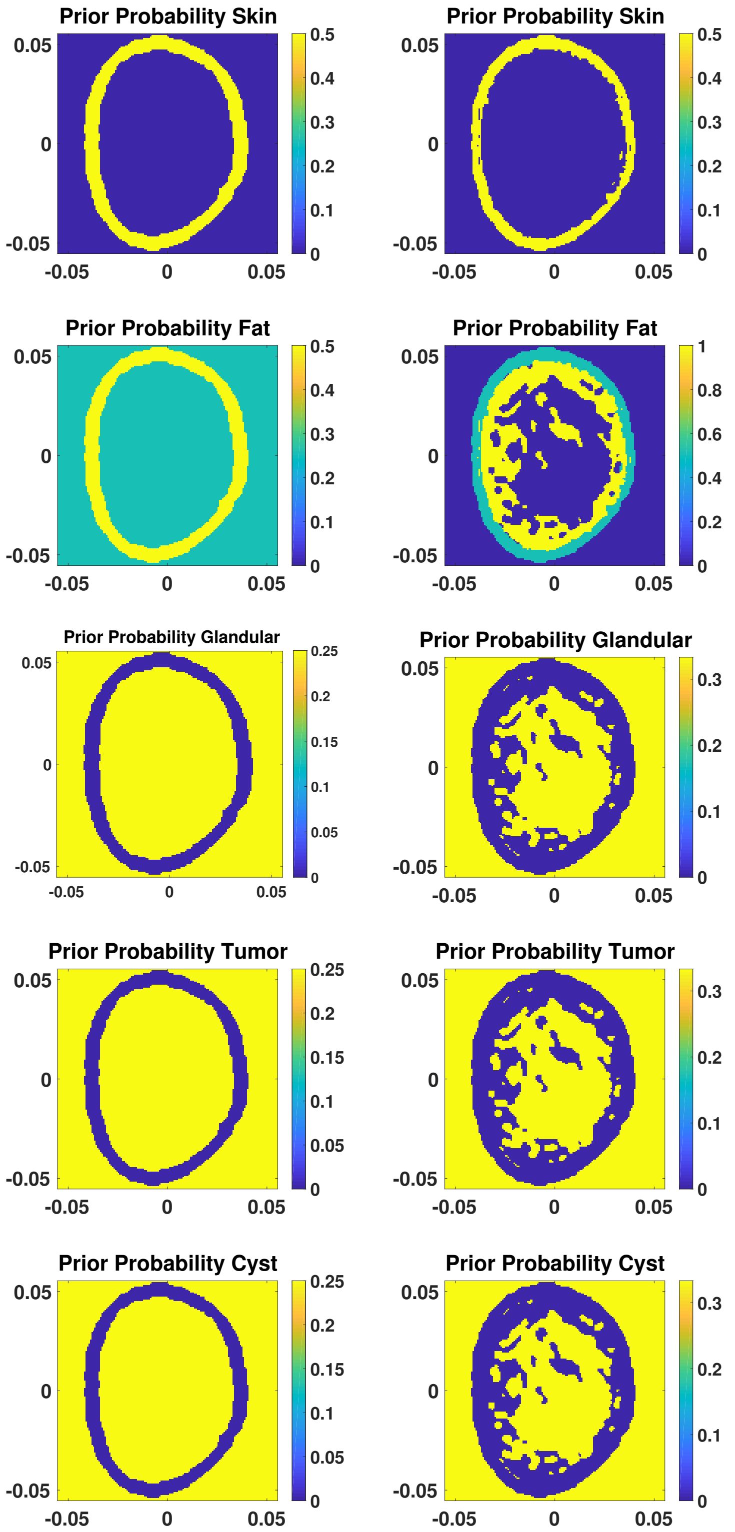

Figure 5.15: The improved prior probability for the reconstruction of the composite tissue type image. The first column corresponds to the set 1 of the improved prior probability based on the estimation of the skin region. The second column corresponds to set 2 of the improved prior probability based on the knowledge about the skin and fat regions.

case, the error decreases from 0.387 to 0.238 using the first set of improved prior probabilities.

It should also be noted that the cyst region is not detected in the cTTI reconstructions using solely ultrasonic or electromagnetic properties as shown in Figs 5.16a,b. When both ultrasound and electromagnetic properties are simultaneously used in the cTTI reconstructions, the cyst region starts to appear. (This further confirms the results obtained in [2].) The reconstruction of the cTTI, probability image and correct pixels using both ultrasound and electromagnetic properties with the assumption of having equal prior probability is shown in the first column of Fig 5.17. When both ultrasonic and electromagnetic properties are simultaneously used to create a cTTI as shown in Fig 5.17a, we lose some resolution compared to the cTTI using only ultrasonic properties as shown in Fig 5.16a. This is due to the fact that the ultrasonic wavelength is much smaller than electromagnetic wavelength. Thus, a higher resolution image can be obtained from the ultrasound properties. For example, the glandular region is well reconstructed with high resolution using the cTTI of the ultrasonic properties as shown in Fig 5.16a compared to the glandular region obtained from cTTI using only electromagnetic properties and combined ultrasound and electromagnetic properties as shown in Fig 5.16b and Fig 5.17a.

To solve this resolution problem, we can utilize the second set of improved prior probability instead of using equal prior probability. The reconstruction of cTTI, probability image and correct pixels using both ultrasonic and electromagnetic properties based on the second set of improved prior probability is shown in the second column of Fig 5.17. As can be seen in Figs 5.17a,b, we can obtain a higher resolution image using set 2 of improved prior probability compared to equal prior probability and the error also decreases from 0.204 to 0.098. The other approach to get a higher resolution image using both ultrasonic and electromagnetic properties is that we can first reconstruct cTTI image using ultrasonic properties having higher resolution then extract cyst from the cTTI using combined ultrasonic and electromagnetic properties. The reconstruction of the cTTI, probability image and correct pixel using this approach with the assumption of equal prior probability is shown in last column of Fig 5.17.

5.9 Conclusion

We have experimentally investigated the concept of tissue type image along with the probability image using ultrasound and microwave tomography properties. To this end, the ultrasound data for a tissue mimicking phantom was considered from the MUBI experimental system. The ray-based methods were utilized to create quantitative images of sound speed and attenuation for this phantom. The sound speed reconstruction was more accurate compared to the attenuation reconstruction for this phantom using ray-based methods. Thus, the cTTI algorithm was modified to take into account the differences between the accuracy of the sound speed reconstruction compared to attenuation reconstruction for this phantom. This modification led to improvement of the cTTI reconstruction.

We then considered evaluating this concept using experimental microwave imaging data. To this end, the microwave imaging data for a human forearm obtained from an in-house experimental microwave system at the University of Manitoba was considered. A full-wave tomographic inversion algorithm was utilized for the reconstruction of the complex permittivity profile of the human forearm. To reconstruct the TTI for the human forearm, only the real part of the complex permittivity was utilized. The TTI of the volunteer's forearm was also compared with its MRI image which demonstrated a good accuracy for the achieved TTI.

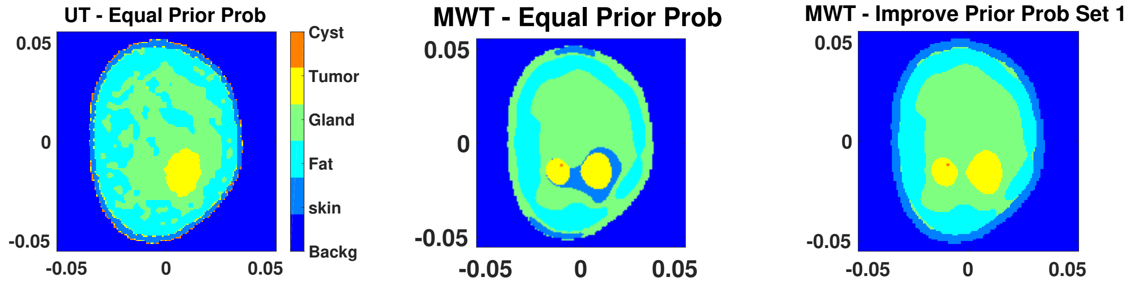

(a) cTTI-UT (b) cTTI-MWT (c) cTTI-MWT

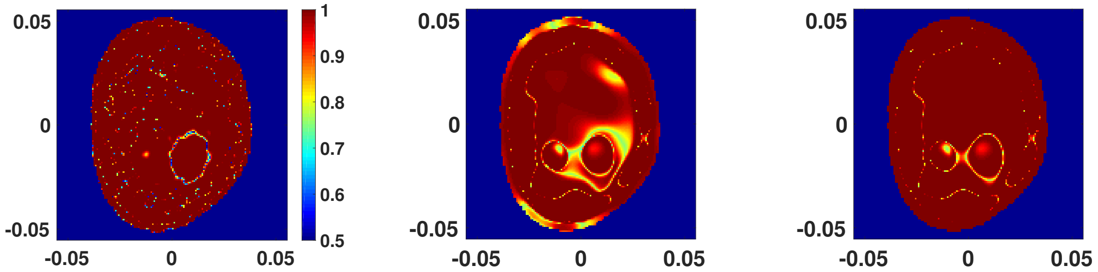

(d) Probability Image (e) Probability Image (f) Probability Image

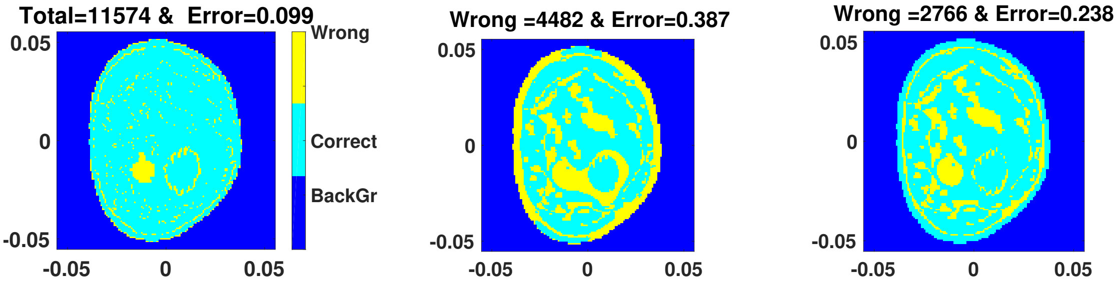

(g) Correct Pixels (h) Correct Pixels (i) Correct Pixels

Figure 5.16: Reconstruction of the cTTI, probability image and correct pixels. First column corresponds to the reconstruction of the cTTI using ultrasonic properties with the assumption of equal prior probability. Second and third columns correspond to the reconstruction of the cTTI using electromagnetic properties based on equal prior probability and set 1 of the improve prior probability.

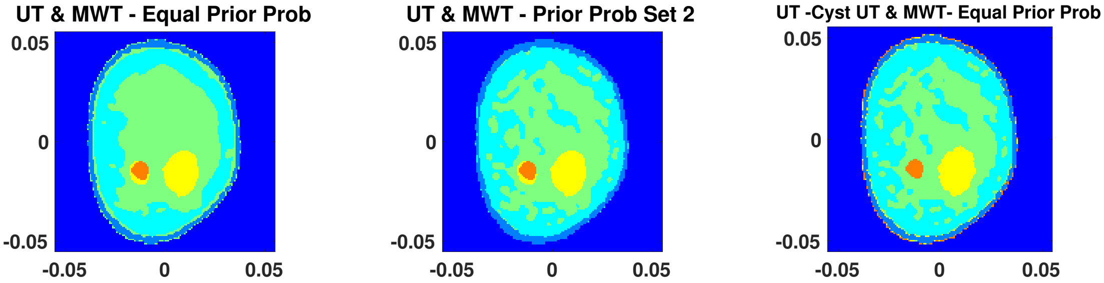

(a) cTTI-UT & MWT (b) cTTI (c) cTTI

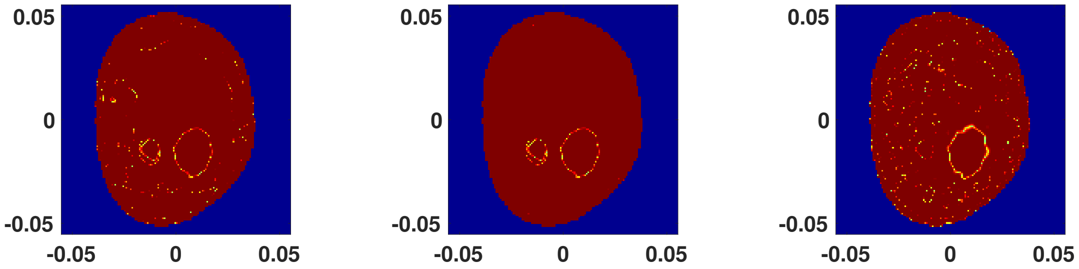

(d) Probability Image (e) Probability Image (f) Probability Image

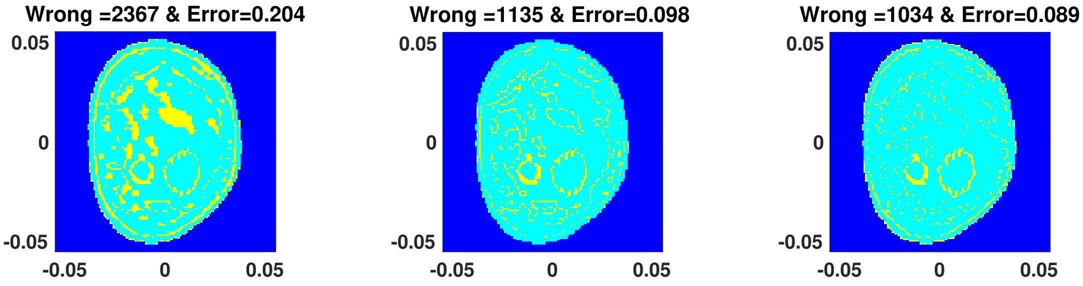

(g) Correct Pixels (h) Correct Pixels (i) Correct Pixels

Figure 5.17: Reconstruction of the cTTI, probability image and correct pixels. first and second columns correspond to the reconstruction of the cTTI using both ultrasonic and electromagnetic properties based on equal and set 2 of the improve prior probability. Last column corresponds to the reconstruction of cTTI using two ultrasonic properties and extract cyst from cTTI based on both ultrasonic and electromagnetic properties with the assumption of equal prior probabilities.

To further explore the potentials of this concept, the cTTI along with the probability images were also reconstructed for an MRI-based numerical phantom using ultrasound tomography properties, microwave tomography properties as well as their combination. When ultrasonic or electromagnetic properties of the breast phantom were separately utilized to create a cTTI, the cyst region was not detected. However, the cyst region started to appear for the case that both ultrasonic and electromagnetic properties were simultaneously utilized. The effect of improving the prior probability on the reconstruction of the cTTI of the breast phantom was also considered using two different sets of prior probabilities based on the estimated skin and fat regions. These sets of the improved prior probability enhanced the reconstruction of the cTTI compared to having the equal prior probability.

In summary, using experimental data, we have shown that the cTTI framework can be advantageously used with properties obtained from nonlinear inversion algorithms as well as simplified methods (ray-based methods in our case). In addition, using synthetic data, we have shown that the cTTI framework can accommodate different prior probabilities based on our knowledge about the object being imaged as well as the data from another imaging modality to improve the final image accuracy. This work motivates our plans to build a multimodal US/MW breast imaging system wherein US and MW data can be collected without moving the breast being imaged. The construction of up to five property images (three ultrasonic and two electromagnetic) should produce very high quality cTTIs of the breast.

ACKNOWLEDGMENT

The authors would like to thank the Ultrasound Systems and Technology Group at the Spanish National Research Council (USTG-CSIC) and Group of Nuclear Physics at the Complutense University of Madrid (GFN-UCM) where the Multimodal Ultrasound Breast Imaging (MUBI) system data was obtained. The authors would like to thank Dr. Majid Ostadrahimi for providing the experimental microwave data for the human forearm, and Dr. Puyan Mojabi for the MR-GNI algorithm. The authors would also like to thank Dr. Elise Fear at the University of Calgary for providing the MRI-based numerical breast phantom.

6

Conclusions and Future Work

6.1 Conclusions

In this thesis, ultrasound tomography (UT) and microwave tomography (MWT) were used as two nondestructive imaging modalities to reconstruct the quantitative ultrasonic and dielectric properties of an object of interest (OI). In this work, these properties are reconstructed using non-linear inverse scattering algorithms (for both UT and MWT) and ray-based methods (for UT). The quantitative ultrasonic properties are compressibility, attenuation, density (and, sound speed), while the quantitative dielectric properties are the real and imaginary parts of the complex permittivity. These quantitative images were then used in a new type of imaging technique that has been introduced by the author: the tissue-type imaging (TTI) method. The TTI is referred to as a composite TTI (cTTI) when more than one property is used to form the TTI. In the TTI, each pixel identifies a single tissue out of a set of potential tissues that may exist at the location of the pixel. An associated probability image whose pixels store the level of confidence in the tissue-type reconstruction is also constructed as part of the method. This TTI approach is novel as (1) we can combine different imaging modalities such as UT and MWT to yield one single image, and (2) the final tissue type image has a corresponding probability for each pixel within the image. The following summarizes the work presented in this thesis and draws some overall conclusions for this thesis.

- As background, the Born Iterative Method (BIM) in conjunction with the CGLS regularization was described as the techniques that was used as the non-linear inversion algorithm for UT. The actual research for this solver was performed during the author's MSc research. The forward solver used for this inversion algorithm was equipped with some acceleration features based on marching-on-source, fast Fourier transform, and the symmetric block Toeplitz matrix with symmetric Toeplitz blocks property of the Green's function matrix to increase efficiency and to only store the first row of this matrix to reduce memory requirements.

- For the breast imaging application, three scenarios were considered to evaluate the BIM inversion algorithms to reconstruct the ultrasonic properties of MRI-based breast phantoms. The first scenario corresponds to the case that all the ultrasonic properties (*i.e.,* compressibility, attenuation and density) are assumed to be independent and unknown. The assumption of a linear relationship between the contrast of compressibility and the contrast of inverse density is used in the second scenario, and finally the variation of density is neglected in the last scenario. The inversion algorithms for all three scenarios were equipped with the balancing method to enhance the reconstructions of all the properties. The reconstructions of the ultrasonic properties for the breast phantoms using the balanced BIM under three scenarios were shown and compared. It was shown that it is essential to use such a balancing technique.

- The multiplicative regularized Gauss Newton inversion (MR-GNI) algorithm, which was originally developed for microwave tomography by another member of the Electromagnetic Imaging Laboratory (EIL) at the University of Manitoba, was adapted for ultrasound tomography under the last scenario which assumes no variations for the density profile. (In addition, the MR-GNI algorithm was also used as a non-linear inversion algorithm for microwave tomography to reconstruct the dielectric properties of the OI.)

- The concept of tissue-type image was proposed and developed for the first time to integrate the information obtained from different reconstructed quantitative property images. These quantitative properties can be obtained from different physical modalities such as UT and MWT, which was the focus of our work. The output of this algorithm is one composite tissue-type image (instead of having multiple quantitative properties) along with the probability image. This composite tissue type image is advantageous for clinical applications as it integrates different types of quantitative images into a single image that can be used by medical doctors for diagnostics. In particular, this is useful for multi-modality imaging systems, e.g., MWT and UT systems. In addition, the concept of the probability image is also useful as it demonstrates the level of confidence in the diagnostics. For example, if a region of interest corresponds to a low probability value, the medical doctor may require a follow-up study on that region, possibly with a different imaging modality. The reconstruction of the cTTI along with the probability image for MRI-based breast phantoms using ultrasound tomography property images, microwave tomography property images and their combination were shown.

- The potential use of anatomical and epidemiological information to enhance the cTTI reconstruction for the breast imaging application was introduced. The improvement of the cTTI reconstruction based on the knowledge of skin and fat regions using ultrasound tomography property images, microwave tomography property images and their combination was shown. A new approach to properly combine all the ultrasonic and electromagnetic properties to get a high resolution cTTI was also shown using an MRI-based numerical phantom.

- Using experimental ultrasound data, ray-based methods were used to create quantitative (sound speed and attenuation) and qualitative images of simple targets as well as a simplistic 2D breast phantom. Calculating the time-of-arrival of the time-domain signal as well as the preprocessing of the raw data were also explained. (The experimental ultrasound data sets were obtained from two different experimental systems: one developed in the EIL and one by a Spanish group [54–56])
- The concept of cTTI along with the probability image from quantitative ultrasonic and electromagnetic properties was experimentally validated using the experimental data for the tissue mimicking phantom (obtained from the Multi-modal Ultrasound Breast Imaging system) and a human forearm (obtained from an in-house system at the University of Manitoba). The difference between the accuracy of the reconstruction of one property compared to another property was also considered in the reconstruction of the cTTI for the tissue mimicking phantom.

6.2 Future Work

- Creating an enhanced ultrasound experimental system having many more transducers compared to the current ultrasound system existing in the EIL, which has only 32 transducers in each ring, is an important goal for future work. (For our current in-house UT system, see Appendix A.) This is due to the fact that the minimum number of data points required to image an object in a circular ring, see (A.1) needs to be satisfied. This will enable the investigation of different reconstruction approaches and develop new ones by utilizing different forms of experimental data. It should be noted that the choice of the ultrasound reconstruction algorithms may affect the data acquisition system. For example, inverse scattering algorithms are computationally much more expensive than the ray-based methods. This may limit the choice of the maximum frequency of operation for the inverse scattering algorithms. This is due to the fact that if the frequency of operation becomes too large, the wavelength of operation becomes too small, and as a result the imaging domain will be very large with respect to the wavelength, thus making the inverse scattering algorithms even more computationally expensive. For example, in the Techniscan medical system presented in [52, pg. 421-422], two data acquisition arrays have been employed: one for the ray-based reconstruction, and the other for inverse scattering reconstruction. In addition, for inverse scattering algorithms, it is important that the inversion model is sufficiently close to the actual system; this can also affect the design of the ultrasound system.

- Other important future work will be to experimentally validate our balanced UT inversion algorithms under the three scenarios explained in this thesis. This can only be done once an enhanced system is built. Then, the tissue-type method can be applied to the UT quantitative reconstructions obtained from the inversion algorithms to create a composite tissue-type along with the probability image.

- The next step would be to perform research on integrating the ultrasound tomography system and the microwave tomography system. One of the advantages of integrating these systems is to remove the difficulty of image registration [149]. This integrated system would provide an opportunity to experimentally reconstruct the ultrasonic and dielectric properties of the OI. Then, these quantitative ultrasonic and dielectric properties of the OI could be used to create a composite tissue-type image.

- New inversion algorithms that simultaneously invert UT and MWT data can be developed, and their inversion results can be compared with individual inversion of each data set.

- The implementation of these algorithms can also be extended to three dimensions. This will be more computationally expensive and can benefit from parallel processing. For example, at each iteration of the inverse scattering algorithms, the solution of the forward problem corresponding to each transmitter is required for the BIM. That is, if we illuminate the object being imaged with 256 transmitters, each iteration of the BIM requires solving the forward problems 256 times. Noting that the BIM may take for example 10 iterations to converge, this will result in solving the forward problem 2560 times. To reduce the computational complexity of the problem, the forward problem corresponding to each transmitter may be solved in parallel using parallel processing techniques. In addition, three dimensional imaging will also increase the required number of measured data points which will make the resulting system more expensive and will make the acquisition time longer.

- In practice, we may encounter special situations, e.g., a patient with a metallic implant. We have not investigated these situations, which can be part of the future work of this thesis. However, some researchers have used similar microwave inversion algorithms to reconstruct metals, e.g., see [119]. This cited work included a metallic object in the vicinity of a dielectric object. When reconstructed, the metallic object demonstrated itself as an object with a high value for the imaginary part of the complex permittivity, which is associated with the high conductivity of the metallic object.

- In Chapter 3, we have considered the simultaneous inversion of the ultrasonic properties for breast imaging applications. It is also interesting to consider this simultaneous property inversion for other applications. For example, the authors in [150] have recently considered a simultaneous inversion of acoustic properties for human thorax imaging.

- The methods developed for solving ultrasound and microwave inverse (scattering) problems can also be investigated for other emerging imaging modalities, for example, photoacoustic tomography [151,152] and thermoacoustic tomography [153,154].

A

Experimental Results Using Ultrasound System at the University of Manitoba

The ultrasound system at the University of Manitoba is shown in Fig A.1 [155–158]. The diameter of this system, at the location of the piezoelectric transducers, is about 12.9 [cm]. This system consists of eight rings of transducers which are connected to arbitrary waveform generators and oscilloscopes via a switch. Each circumferential ring consists of 32 transducers*. The ultrasound transducers and switch that are used in this system were provided by Sonometrics Corporation [156]. The frequency range of optimal operation for these transducers is between 1.1 to 1.5 MHz and they have a resonant frequency near 1.3 MHz. The cylindrical piezoelectric crystals are made of lead zirconate titanate (PZT-5H).

The quantitative reconstruction algorithms used herein require that a specific spatial location be identified as the source of energy for each transducer (as well as for the receiver location). However, the size of our transducer is on the order of some millimetres as shown in Fig A.2. Thus, a specific spatial point should be identified as the transducer's location (its phase center). The multidimensional scaling (MDS) method [155, 159] has been used in the past to identify this position. The technique determines this location for an assumed background sound-speed and using the time-of-arrival (TOA) of the incident signal for different pairs of transmitter and receiver.

---

*Each transmitting transducer transmits a pulse waveform in this system.

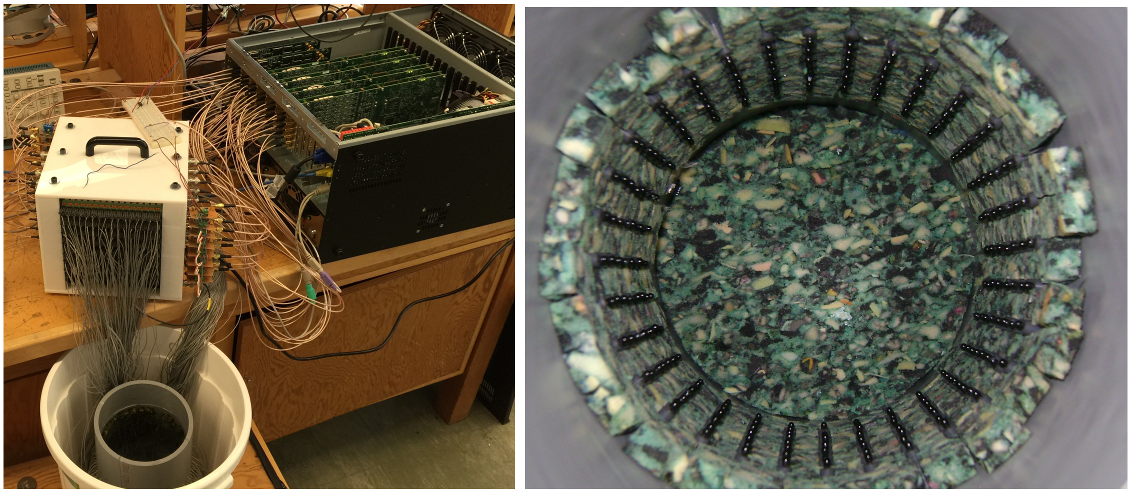

Figure A.1: Ultrasound tomography system at the University of Manitoba. This system has 8 rings, each of which consists of 32 transducers.

For this work, the TOA of the incident signal is found using methods described in Section A.2. It should be noted that water is used as a background medium its speed can be estimated based on its measured temperature [160]. The transducer locations, first based on the physical diameter of the system and then corrected using the MDS algorithm, are shown in Fig A.3. Note that only a slight correction is required for the position locations.

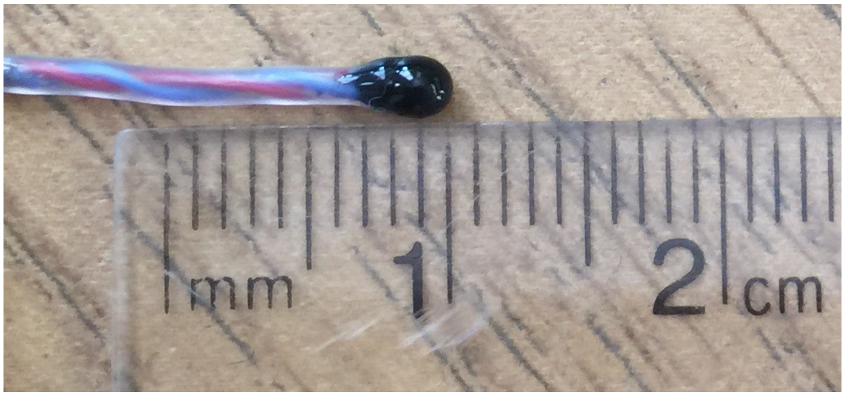

Figure A.2: A piezoelectric transducer used in our UT system.

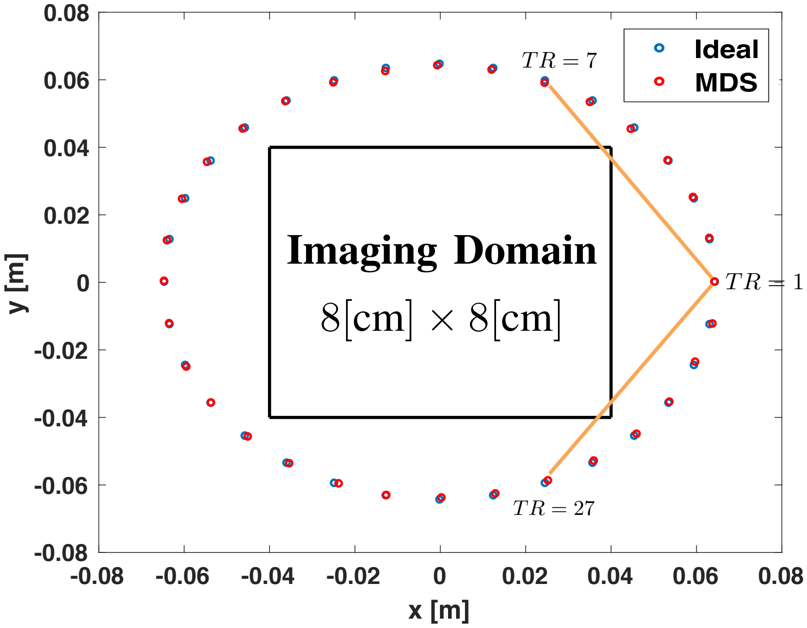

Figure A.3: Transducer localization for the University of Manitoba system, "ideal" based on physical construction and corrected using MDS.

As will be shown in the results section, a major disadvantage of this particular imaging setup is the small number of fixed transducers that are used. These stationary transducers only allow one to collect data from a fixed number of transmitter-receiver pairs. To understand how the number of transducers affects the image quality, a formula for an estimate of the minimum number of data sampling points required to image an object using a circular ring of transducers has been previously published [73, 161]:

$$\text{Minimum number of data points} > \frac{4\pi r_0}{\lambda} \tag{A.1}$$

where r_0 is the radius of the object of interest and λ is the wavelength. For example, the minimum number of the sampling points for the object with a radius of 3 [cm] at frequency of operation 1 MHz with the assumption of water as a background medium is about 252. The number of transducers in our circular ring is only 32, much smaller than the minimum number of sampling points required according to this formula[†]. In addition, for algorithms that reconstruct the sound-speed and attenuation based on a ray model of propagation, only the transmitter-receiver pairs having a corresponding ray line that passes through the imaging domain will contain useful information. In our system, for example, only 21 transducers ranging from 7 to 27 can be used as receivers for the case that transducer one operates as a transmitter (as depicted in Fig A.3). Thus, we only have 672 information containing rays for the size of the imaging domain shown. However, to handle the lack of sufficient data points in this work, we use simple objects (homogenous cylinders) as our test phantoms. The point herein is to evaluate our reconstruction techniques on our experimental data. More complicated tissue-mimicking phantoms are scanned using the MUBI system and shown in Section 5.6.

A.1 Preprocessing of Raw Data

In general, the raw data collected from any ultrasound system cannot be used directly when implementing these methods. Various amounts of random and systematic noise will corrupt the raw data, including the multi-path reflections generated within the system. The type and amount of noise will vary with the system being used. Thus, the experimentally collected time-domain data must be preprocessed before it can be used in the reconstruction algorithms.

The raw data from this system considered herein contained a DC bias of varying amount and a small amount of ripple, of unknown origin. We remove these unwanted signal components in the frequency domain. details can be found in [155]. A typical

---

[†] The choice of the ray-based methods for the experimental ultrasound imaging systems at the University of Manitoba is due to the following reason. The UM system does not satisfy the requirement for sufficient data sampling [161] for the inverse scattering algorithm at its frequency of operation. Due to this, we have used ray-based methods in conjunction with this system.

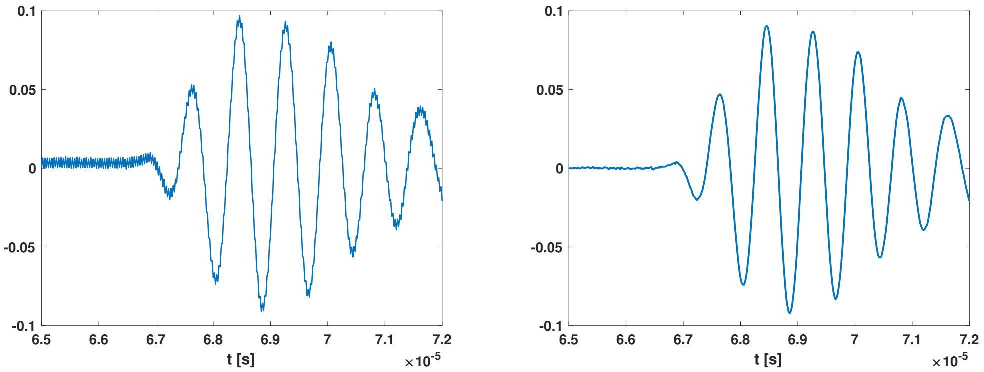

(a) Raw Signal (b) Preprocessed Signal

Figure A.4: Typical raw and preprocessed signal obtained by the UM system.

noisy raw signal measured in the University of Manitoba system, clearly displaying the DC bias and the small amount of ripple, as well as the preprocessed signal are shown in Fig A.4.

A.2 Calculating the Time-of-Arrival

Accurately calculating the time-of-arrival (TOA) of a signal is very critical for various different applications such as seismic and biomedical imaging [58,60]. TOA-based imaging algorithms can be used to study the internal structure of the earth and find the hypocenter location in seismic applications [58]. Different methods can utilized to find the TOA of the signal: manually, semi-automatically or automatically. Manually choosing the TOA is very time consuming and is also operator-dependent [162]. Different automatic TOA picker algorithms have been proposed. The easiest way is to use a thresholding algorithm that determines the TOA of the signal simply by setting a threshold as the detection point. This method does not perform well for low signal-to-noise ratio data [60]. Here, we investigate the performance of the Akaike information criterion (AIC) [60, 61] for its use in conjunction with the previously described sound-speed imaging algorithm which is described in Section 5.5.2.

The AIC function is defined as [60,61]

$$\begin{aligned} \mathrm{AIC}(k) &= k \log \Big[\mathrm{var}\big(S(1,k)\big) \Big] \\ &+ (N-k-1) \log \Big[\mathrm{var}\big(S(k+1,N)\big) \Big] \end{aligned} \tag{A.2}$$

where N is the total number of data points in the time-domain signal and k is a value from 1 to N. $S(1,k)$ and $S(k+1,N)$ corresponding to the (1 to k) and ($k+1$ to N) data points of the signal, respectively. In addition, *var* corresponds to the variance function. The value of k corresponding to the minimum value of AIC is chosen as the arrival time of the signal. A typical time domain signal obtained from the experimental system is shown in Fig A.5. The AIC function is shown as the red dashed line in the figure. The MER method explained in Section 5.5.2 for the calculation of the time-of-arrival of the signal is also shown in black in Fig A.5. For this particular example, it should be noted that both the AIC and MER methods identify the same sample point for the arrival time of the signal.

A.3 Results

Two examples are considered using the ultrasound experimental system at the University of Manitoba. In both examples water is used as a background medium. For each experiment the temperature of the water is measured so that the sound-speed of the background can be estimated for use in the different algorithms [160].

The first target is a non-centered cylinder where the size and position within the chamber are as shown in the first row of Fig A.6. The TOA of the incident, total,

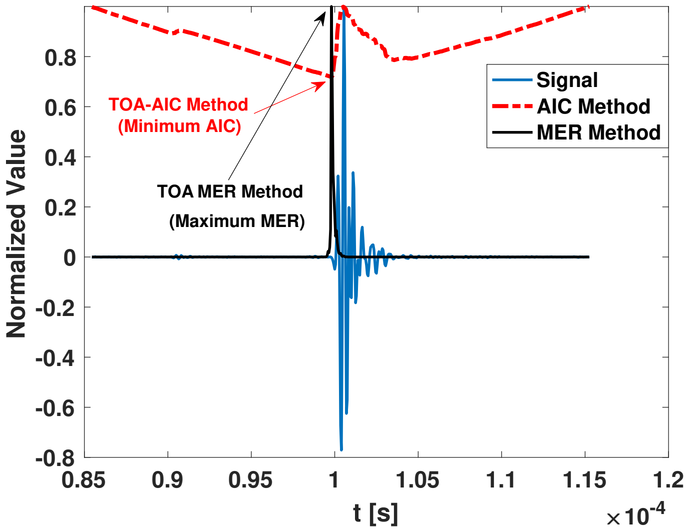

Figure A.5: Calculation of the time-of-arrival of the signal using the AIC and MER methods for the typical preprocessed signal obtained by the MUBI system.

and their subtraction are shown in the second row of Fig A.6. Each row corresponds to the particular transmitter while the column corresponds to the particular receiver. It should be noted that when one transducer operates as a transmitter, it cannot be used as a receiver so we give a zero value to that TOA. It is evident from this figure that the sound-speed of nylon cylinder is greater than the background sound-speed. The reconstruction of the sound-speed is shown in Fig A.7a. For this target, we also consider the reconstruction of the so-called reflection image using the Delay-and-Sum (DAS) method described in [21, 163]. This reconstruction is shown in Fig A.7b (in applying this algorithm it is assumed that the sound-speed everywhere is the same as the background sound-speed). The reconstruction of the attenuation using the three techniques previously described: amplitude decay, complex signal energy ratio, and the spectral ratio, are shown in Fig A.7 (c, d, e).

In the second example, we use two cylinders as shown in the first row of Fig A.8.

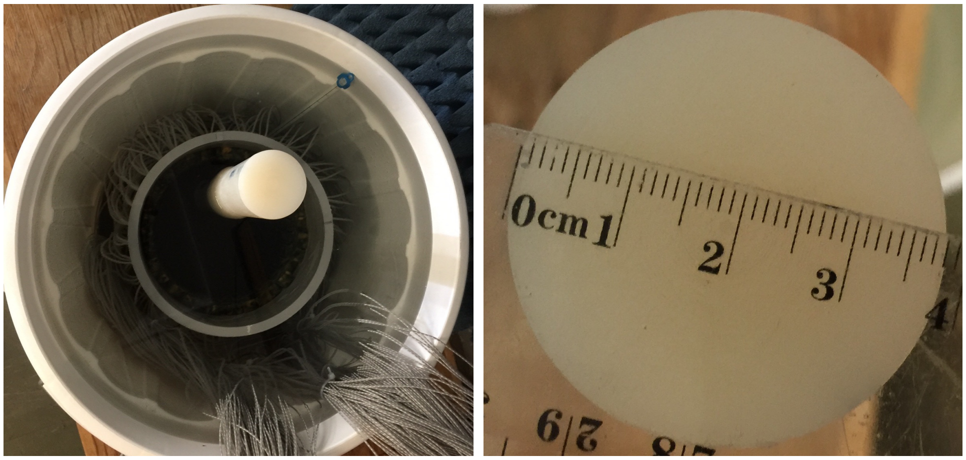

(a) Nylon cylinder in chamber (b) Nylon cylinder

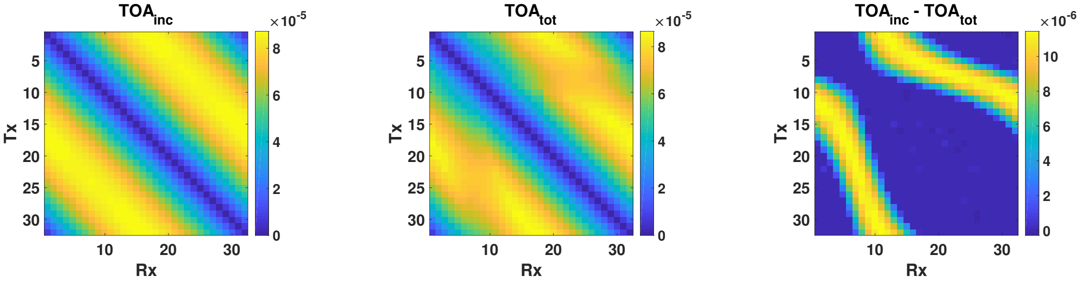

(c) $\mathrm{TOA}_{\mathrm{inc}}$ (d) $\mathrm{TOA}_{\mathrm{tot}}$ (e) $\mathrm{TOA}_{\mathrm{inc}} - \mathrm{TOA}_{\mathrm{tot}}$

Figure A.6: Experimental measurement of the Nylon cylinder using the ultrasound system at the University of Manitoba. The first row corresponds to the experimental set up for measuring the Nylon cylinder. The second row corresponds to the time of arrival for the incident, total and their subtraction.

The TOA of the incident, total, and their subtraction are shown in the second row of Fig A.8. The sound-speed reconstruction is shown in Fig A.9a. The attenuation reconstructions are shown in Fig A.9 (b, c, d). Two cases are considered for constructing the reflection image using the DAS method. In the first case, it is assumed that the sound-speed is homogeneous and equal to the background medium. The reflection image using this assumption is shown in Fig A.9e. In the second case, the inhomogeneous sound-speed calculated in Fig A.9a is used within the DAS algorithm

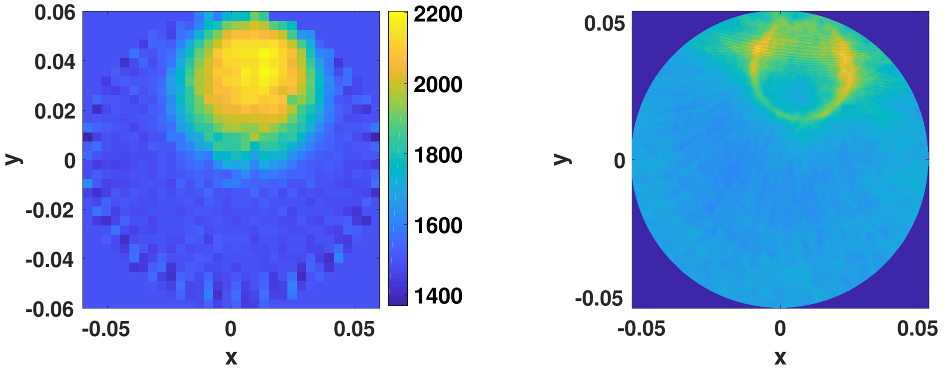

(a) Sound-Speed (b) Reflection Image

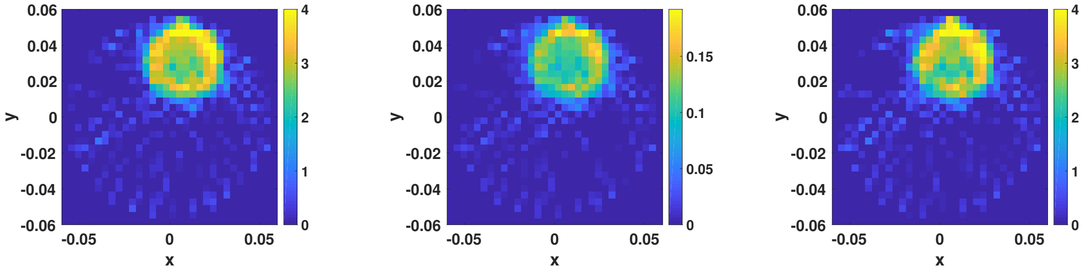

(c) α-Amplitude Decay (d) α-Complex Signal Energy Ratio (e) α-Spectral Ratio

Figure A.7: Reconstructions of the sound-speed [m/s], attenuation [db/cm] and reflection for the non-centered nylon cylinder. The reconstructions of the sound-speed and reflection are shown in the first row. The reconstructions of attenuation using amplitude decay, complex signal energy ratio and spectral ratio methods are shown in the second row.

by first finding the time between each transducer position and each pixel in the imaging domain. The reflection image based on this inhomogeneous sound-speed estimate is shown Fig A.9f. As can be seen in the last row of Fig A.9, only the boundary of the cylinders are reconstructed assuming a homogenous sound-speed, whereas more of the inside of the cylinders are reconstructed using the inhomogeneous sound-speed.

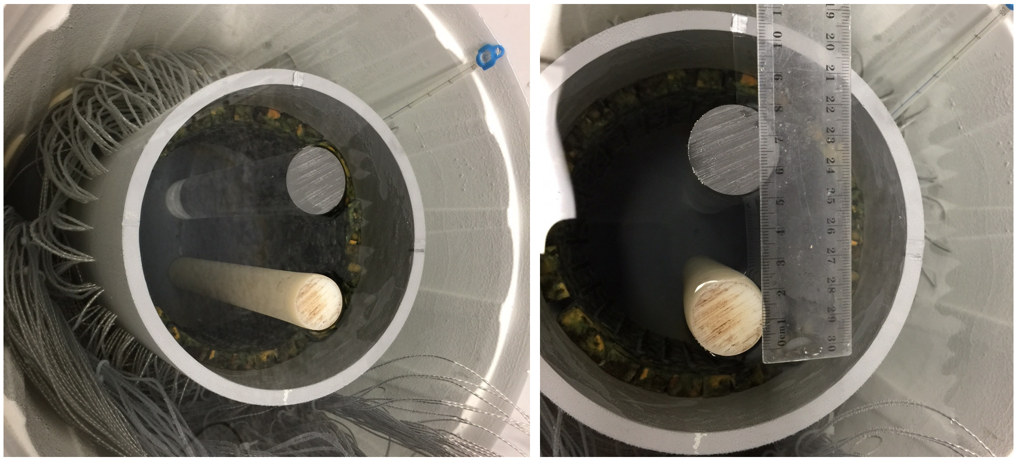

(a) Two cylinders in chamber (b) Two cylinders (top view)

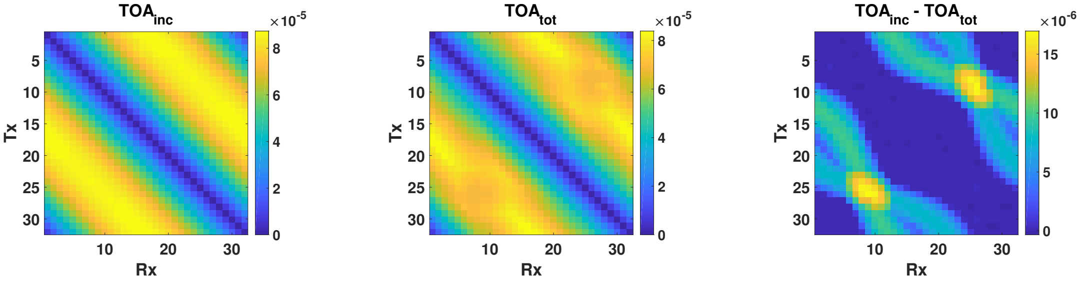

(c) $\mathrm{TOA_{inc}}$ (d) $\mathrm{TOA_{tot}}$ (e) $\mathrm{TOA_{inc}} - \mathrm{TOA_{tot}}$

Figure A.8: Experimental measurement of two cylinders using the ultrasound system at the University of Manitoba. The first row corresponds to the experimental set up for measuring two cylinders. The second row corresponds to the time of arrival for the incident, total and their subtraction.

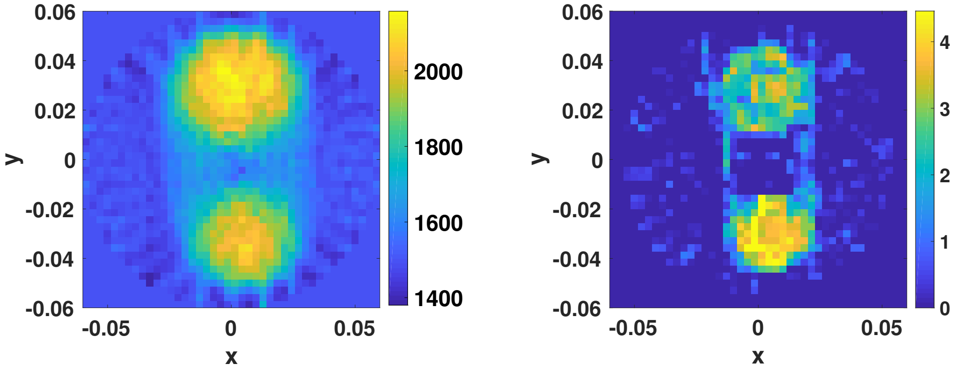

(a) Sound-Speed (b) α-Amplitude Decay

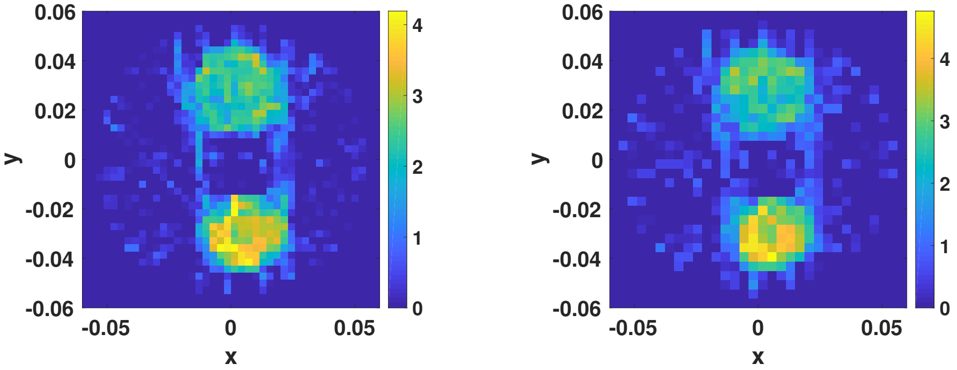

(c) α-Complex Signal Energy Ratio (d) α-Spectral Ratio

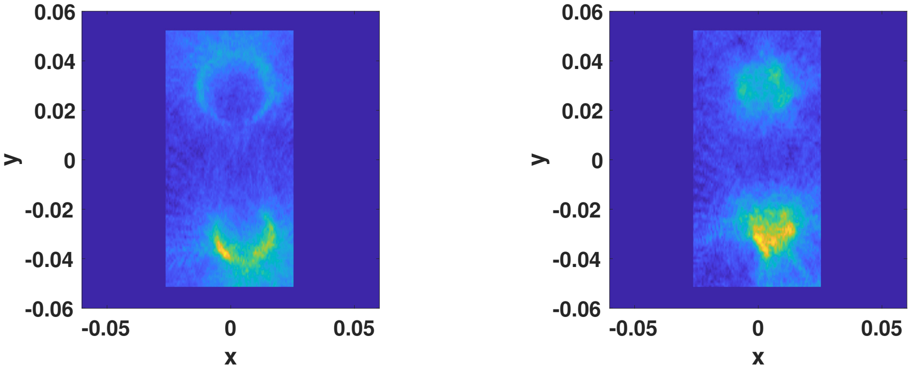

(e) Reflection-homogeneous-c (f) Reflection-inhomogeneous-c

Figure A.9: Reconstructions of the sound-speed [m/s], attenuation [db/cm] and reflection for two cylinders. The reconstructions of the sound-speed and attenuation are shown in the first and second rows. The reconstruction of the reflection image using the homogeneous and inhomogeneous sound-speed is shown in the third row.

B

On the potential use of anatomical and epidemiological information to enhance microwave and ultrasound breast imaging*

B.1 abstract

This paper proposes the use of available anatomical and epidemiological (statistical) information regarding breast cancer in conjunction with microwave and ultrasound breast imaging. This information, which can be extracted from the broader medical research effort, can be used in conjunction with image reconstruction algorithms to further guide those algorithms towards a more accurate solution. In particular, we propose to consider the following anatomical and statistical information into the image reconstruction process via the tissue-type framework. Anatomical information is utilized in assigning a tissue-type and its corresponding probability to a given pixel by considering the neighbouring reconstructed pixels (epidemiological information related to the anatomical surroundings of the pixel is used to modify the prior probabilities in the Bayes prediction model). Two types of epidemiological

---

*© 2018 IEEE. Reprinted, with permission, from Pedram Mojabi and Joe LoVetri, "On the potential use of anatomical and epidemiological information to enhance microwave and ultrasound breast imaging," *2nd URSI AT-RASC,* Gran Canaria, Spain, May 2018. (Invited).

information are used in reconstructing the tissue-type image to improve the discrimination between tumor and cyst: the quadrant of the breast within which a pixel is located provides statistical information regrading whether of being cancerous, and the age of the patient can provide similar information.

B.2 Introduction

Microwave and ultrasound imaging (MWI and UI respectively) can create quantitative images corresponding to the electromagnetic (*i.e.,* real and imaginary parts of complex permittivity) and ultrasonic (*i.e.,* sound speed, attenuation, compressibility and density) properties of the object of interest (OI) [2, 6, 17, 20, 28]. Integrating all these quantitative images into one image that incorporates the most important information of each individual image can be very useful; for example, in biomedical imaging applications, it is more practical and efficient for medical doctors to diagnose based on one single comprehensive image rather than checking several quantitative images with different range of color-bars. Furthermore, this concept (*i.e.,* integrating different images into one image) avoids the necessity for medical doctors to know the expected ranges of quantitative values for different tissue types of each quantitative image and also avoids the necessity for doctors to know which (part of the) quantitative image to trust more as compared to other images.

To this end, we introduced the concept of composite tissue-type image (cTTI) along with the probability image which can integrate all the quantitative images obtained from different modalities into one image; see [2]. Each pixel of this composite image corresponds to the special tissue type (e.g., breast tumor) as opposed to having quantitative values. In other words, reconstructed quantitative values of various images (e.g., conductivity image and sound speed image) can be combined to infer the tissue type. In addition, in this approach, the probability of choosing the special tissue type for each pixel is also provided in another image to help medical doctors determine the level of confidence for each pixel within the composite tissue type image. The reconstruction of cTTI along with its associated probability image based on the numerically generated data for ultrasound tomography and microwave tomography as well as their combination are presented in [2], in which, an inverse scattering approach (the Born iterative method or the Gauss-Newton inversion algorithm) is utilized to create the quantitative images. The experimental evaluation of this technique using ultrasound data for a tissue mimicking phantom based on ray-type methods is also described in [59].

In this approach, the prior probability of each tissue-type occupying each pixel is required to create a cTTI image based on Bayes' formula [2, 59]. When we do not have any prior information about the OI, we choose the prior probability of all the tissue types for each pixel to be the same. For example, in the case of breast imaging, we can consider five different tissue types: skin, fat, fibroglandular, tumor and cyst. Assuming that we do not have any prior information about where these tissue types are located within a breast, each pixel within the imaging domain will have a probability of 0.2 that it is occupied by one of these five tissue types. In this paper, we propose to take advantage of some anatomical information about the breast to provide a better prior probability for some of the pixels in the imaging domain, instead of naively assuming the same prior probability for each tissue-type. As will be shown in the presentation, this information can enhance the reconstruction of the cTTI.

A simple example of the use of anatomical information is the taking into account of the position of the skin tissue-type which is in the outer regions of the breast. Thus, the chance of having a skin tissue in the central parts of the reconstructed breast volume is zero. Therefore, we can assign a zero prior probability for skin tissue-type to the pixels residing in the central parts of the breast. Furthermore, the tissue-types of the neighbouring pixels can also help to provide a better prior probability for that pixel. For example, if we know that the chance of a tumor occurring inside the fibroglandular tissue is high [62], then we can always check the neighbouring pixels of that pixel that has been reconstructed as tumor. That is, the prior probability of a pixel reconstructed as tumor might be reduced if its neighbouring pixels are skin and fat. Similarly, we can apply the same procedure for any cyst regions.

The statistical information about relevant to breast cancer can also take into account the case in which we have an ambiguity of choosing a pixel as being tumor or cyst. For example, this might happen when the associated probabilities of a pixel for being tumor or cyst are close to each other. In this case, in addition to creating a cTTI along with the probability image, we also provide another cTTI to provide further insight and guidance regarding such pixels based on the statistical information to help medical doctors. For example, this statistical information can be based on the location of the pixel in the breast and also the age of the patient, or any other statistical information available from the medical research community.

The structure of this paper is as follows. In the next section, we briefly explain the formation of a cTTI. Then, in Section B.4, we discuss how to use anatomical and statistical information (available from epidemiological research) to enhance breast cancer diagnosis. Finally, our methodology will be described.

B.3 Composite Tissue Type Image (cTTI)

Two different methods are proposed in [2] to create a cTTI along with the probability image. In the first method, a single property tissue type along with the probability image is created for each property. Then, all these single property TTIs and probability images are utilized to create a cTTI. In the second method, all the properties are simultaneously used to create a cTTI. In both methods, Bayes' formula is utilized to calculate the probability of tissue-type T_k occupying the pixel of interest [2, 59]

$$P(T_k|x) = \frac{p(x|T_k)P(T_k)}{\sum_{i=1}^{N_t} p(x|T_i)P(T_i)} \tag{B.1}$$

where N_t and x correspond to the total number of tissue types and the quantitative value of that pixel in the corresponding property image. Also, $p(x|T_k)$ is the value of the conditional probability density function (PDF) for property value x assuming the tissue type is T_k. As noted earlier, the prior probability of assigning tissue type T_k for that pixel is denoted by $P(T_k)$. Without any prior information it is usual to choose the same prior probability for all the tissue-types.

B.4 Anatomical and Statistical Information

In this section, previously published reports related to breast cancer are discussed as an example of how one might extract prior information to improve our cTTI reconstructions. The specific information in these studies relates to the anatomical structure, the chances of a tumor being found in different breast quadrants, and the age of patients. We propose that taking into account this information can be very useful in the detection and identification of tumors via breast imaging. (This

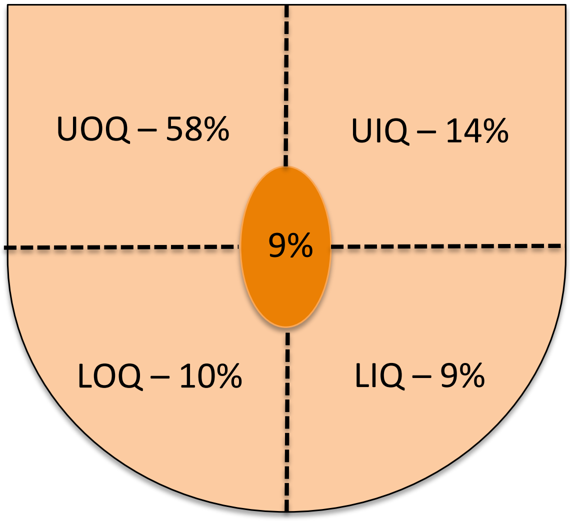

Figure B.1: The chance of tumor arising in four different breast quadrants (dented by Q). This figure corresponds to the right breast with U indicating the upper, L indicting the lower, O indicating the outer and I indicating the inner; e.g., UOQ denotes the upper outer quadrant. The orange ellipse represent the nipple area.

framework is general enough so that information obtained from other studies can easily be used to further enhance the reconstruction process.)

B.4.1 Anatomical Structure

Mammographic density (MD) which corresponds to the amount of fibroglandular tissue in the breast is one of the most important markers for breast cancer [62, 164]. The chance of breast cancer is four to six times for patients having dense breast tissue (occupying more than 75% of the breast) as compared to those having a low density (occupying less than 5% of the breast) [62, 164]. The study in [62] also shows that breast tumors emerge mainly within the radiodense tissue, specifically radiodense fibroglandular tissue. Furthermore, the fluid accumulation inside the glands leads to developing cysts in the breast [165]. Therefore, if a pixel is firstly identified to be

Table B.1: The average age of cancer and non-cancer cases based on 300 cancer cases and 200 non-cancer cases.

Decade	Cancer Cases [%]	Non-cancer Cases [%]
10-20	0	0.02
20-30	0.01	0.15
30-40	0.18	0.34
40-50	0.346	0.39
50-60	0.22	0.08
60-70	0.2	0.015
70+	0.043	0.005

tumor or cyst in the cTTI (using the equal prior probability assumption), we can subsequently check the neighbouring pixels of a pixel that has been identified to be tumor or cyst. Based on these studies, it is clear that the prior probability of a particular pixel being tumor or cyst can be reduced if the neighbouring pixels are skin and fat. The same procedure can also be considered for the skin tissue-type which should be in the outer region of the breast.

B.4.2 Epidemiological Information

A study conducted from 1990 to 2005 found that among 13,984 women having tumors that these breast cancer tumors occurred 58% of the time in the upper-outer quadrant (UOQ), 14% in the upper-inner quadrant (UIQ), 9% in the lower-inner quadrant (LIQ), 10% in the lower-outer quadrant (LOQ), and 9% in the nipple complex [63] (these anatomical regions are shown in Fig B.1 [63]). The same observation was also reported in [166]. Furthermore, an annual increase of breast cancer in UOQ was reported in [167]. Also, breast cancer in the UOQ is the highest among the youngest age group in this study (Age ≤ 49) [166, 167].

Table B.2: The average age of cancer based on 2248 cases.

Age	Number	Percentage
≤ 35	104	4.6
36-59	1503	66.9
≥ 60	641	28.5

The chance of having tumor and cyst varies among different ages. For example, 300 cancer cases and 200 non-cancer cases were used in [146]. The average age of people having cancer and non-cancer based on these samples is tabulated in Table B.1 [146]. Many more cancer cases (*i.e.,* 2,248) were considered in [147]. The percentage of cancer for three different age ranges using 2,248 cancer cases is tabulated in Table B.2 [147]. As can be seen in Table B.1, the percentage of cancer and non-cancer cases for the age below 30 is 0.01 and 0.17 respectively. Therefore, if after improving the cTTI using the previously discussed prior-modification methods we are still not sure whether to identify a pixel as being cancer or non-cancer (i.e., there is till an ambiguity), we can guess that the chance of being non-cancer is higher compared to cancer for a person in this age range. If in addition, the position of this pixel is not in the UOQ region (the quadrant having the highest chance of there arising a tumor), then the chance of being non-cancer may also be increased. For women of age greater than 60, the percentage of cancer and non-cancer cases is 0.243 and 0.02 respectively based on Table B.1. Therefore, if there is ambiguity that a pixel has a tissue-type of cancer or non-cancer, for a patient in this age range, the chance of being cancer would be reported as being higher, especially for pixels in the UOQ region.

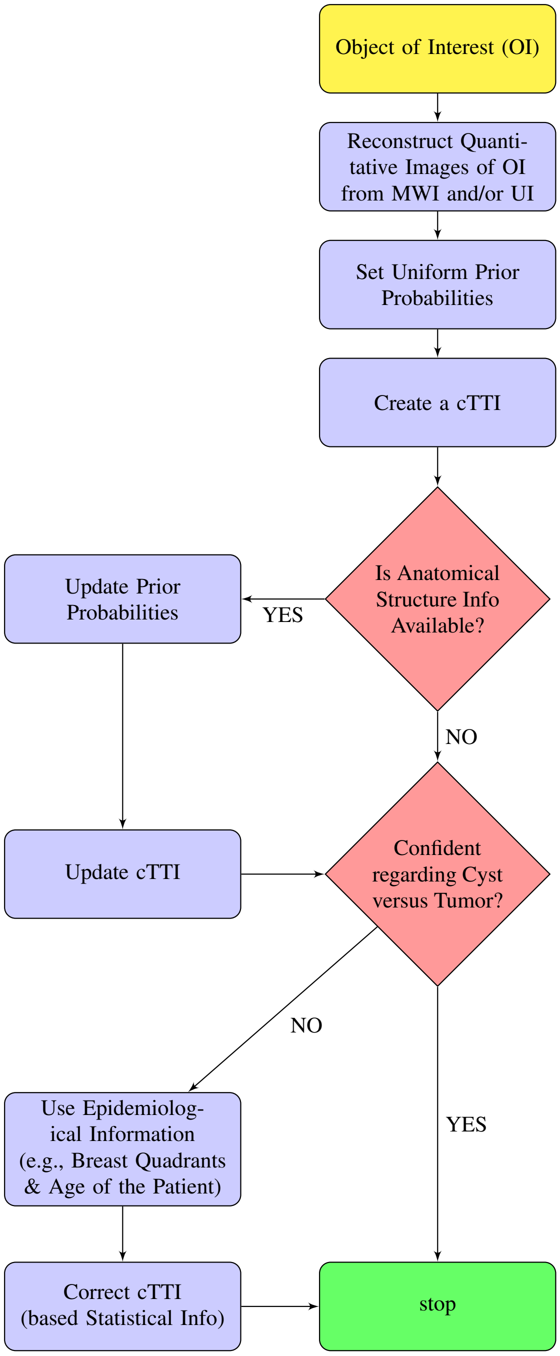

Figure B.2: Flowchart of the proposed method for using anatomical and epidemiological information to enhance the cTTI reconstruction for breast imaging

B.5 Framework

The flowchart of the framework for using anatomical structure and statistical information to improve the reconstruction of the cTTI for the breast is shown in Fig B.2. In this method, we first create quantitative images of the breast. These quantitative images can be of the electromagnetic (*i.e.,* complex permittivity) and/or the ultrasonic properties (*i.e.,* sound speed, attenuation, density, and compressibility) of the breast. Different methods such as full-wave non-linear inverse scattering algorithms, and ray based methods can be used to create these images [2,6,17,20,28,59]. In the next step, the prior probabilities of all the tissue-types occupying each pixel are set to be the same. The cTTI along with the probability image is then reconstructed based on the two methods explained in [2]. After creating a cTTI based on the equal prior probability, we can check the neighbouring tissue-types of each pixel to provide a better prior probability based on the anatomical structure of the breast as discussed in Section B.4.1. The new prior probability which is now modified based on the neighbouring tissue-types is used to enhance the reconstruction of the cTTI. Finally, if the cyst and tumor cannot be properly distinguished from each other (*i.e.,* the probability of being tumor or cyst is close to each other in a composite probability image), then the statistical information such as the chance of cancer in different breast quadrants, the age of patient (discussed in Section B.4.2) or any other statistical information can be used to better determine the tissue type. Finally, another cTTI image based on all the statistical information is created. This final cTTI could be provided to medical doctors who would make the final diagnosis.

B.6 Conclusion

We have proposed a framework wherein one can incorporate available anatomical and epidemiological information about a breast being imaged into microwave and ultrasound imaging algorithms. Herein, we discussed some of forms of useful information which can be utilized to provide enhanced imaging or increased certainty about the reconstructed breast tissue type. A particular framework on how to incorporate this information into the cTTI reconstruction algorithm has been described using a flowchart[†].

[†] Examples demonstrating this approach are shown in Chapter 5

References

[1] M. Ostadrahimi, P. Mojabi, A. Zakaria, J. LoVetri, and L. Shafai, “Enhancement of GaussNewton inversion method for biological tissue imaging,” *IEEE Transactions on Microwave Theory and Techniques*, vol. 61, no. 9, pp. 3424–3434, Sept 2013.

[2] P. Mojabi and J. LoVetri, “Composite tissue-type and probability image for ultrasound and microwave tomography,” *IEEE Journal on Multiscale and Multiphysics Computational Techniques*, vol. 1, pp. 26–35, 2016.

[3] C. Li, N. Duric, and L. Huang, “Comparison of ultrasound attenuation tomography methods for breast imaging,” *Proc. SPIE*, vol. 6920, pp. 692 015–692 015–9, 2008.

[4] M. Haynes and M. Moghaddam, “Large-domain, low-contrast acoustic inverse scattering for ultrasound breast imaging.” *IEEE Trans. Biomed. Engineering*, vol. 57, no. 11, pp. 2712–2722, 2010.

[5] P. Huthwaite and F. Simonetti, “High-resolution imaging without iteration: a fast and robust method for breast ultrasound tomography,” *The Journal of the Acoustical Society of America*, vol. 130, no. 3, pp. 1721–1734, 2011. [Online]. Available: http://scitation.aip.org/content/asa/journal/jasa/130/3/10.1121/1.3613936

[6] C. Li, N. Duric, P. Littrup, and L. Huang, “In vivo breast sound-speed imaging with ultrasound tomography,” *Ultrasound in Medicine & Biology*, vol. 35, no. 10, pp. 1615 – 1628, 2009.

[7] M. Beard and M. Lowe, “Non-destructive testing of rock bolts using guided ultrasonic waves,” *International Journal of Rock Mechanics and Mining Sciences*, vol. 40, no. 4, pp. 527 – 536, 2003.

[8] P. Mojabi and J. LoVetri, “Enhancement of the Krylov Subspace Regularization for Microwave Biomedical Imaging,” *IEEE Transactions on Medical Imaging*, vol. 28, no. 12, pp. 2015–2019, Dec 2009.

[9] T. Rubk, P. Meaney, P. Meincke, and K. Paulsen, “Nonlinear Microwave Imaging for Breast-Cancer Screening Using Gauss Newton’s Method and the CGLS Inversion Algorithm,” *Antennas and Propagation, IEEE Transactions on*, vol. 55, no. 8, pp. 2320–2331, Aug 2007.

[10] Z. Q. Zhang and Q. H. Liu, “Three-dimensional nonlinear image reconstruction for microwave biomedical imaging,” *IEEE Transactions on Biomedical Engineering*, vol. 51, no. 3, pp. 544–548, March 2004.

[11] Z. Q. Zhang, Q. H. Liu, C. Xiao, E. Ward, G. Ybarra, and W. Joines, “Microwave breast imaging: 3-D forward scattering simulation,” *IEEE Transactions on Biomedical Engineering*, vol. 50, no. 10, pp. 1180–1189, Oct 2003.

[12] T. Grzegorczyk, P. Meaney, P. Kaufman, R. di Florio-Alexander, and K. Paulsen, “Fast 3-D tomographic microwave imaging for breast cancer detection,” *IEEE Transactions on Medical Imaging*, vol. 31, no. 8, pp. 1584–1592, Aug 2012.

[13] N. K. Nikolova, “Microwave imaging for breast cancer,” *IEEE Microwave Magazine*, vol. 12, no. 7, pp. 78–94, Dec 2011.

[14] D. Tajik, F. Foroutan, D. S. Shumakov, A. D. Pitcher, and N. K. Nikolova, “Real-time microwave imaging of a compressed breast phantom with planar scanning,” *IEEE Journal of Electromagnetics, RF and Microwaves in Medicine and Biology*, pp. 1–1, 2018.

[15] E. Porter, M. Coates, and M. Popovic, “An early clinical study of time-domain microwave radar for breast health monitoring,” *IEEE Transactions on Biomedical Engineering*, vol. 63, no. 3, pp. 530–539, March 2016.

[16] E. Porter, E. Kirshin, A. Santorelli, M. Coates, and M. Popovic, “Time-domain multistatic radar system for microwave breast screening,” *IEEE Antennas and Wireless Propagation Letters*, vol. 12, pp. 229–232, 2013.

[17] E. C. Fear, S. C. Hagness, P. M. Meaney, M. Okoniewski, and M. A. Stuchly, “Enhancing breast tumor detection with near-field imaging,” *IEEE Microwave Magazine*, vol. 3, no. 1, pp. 48–56, March 2002.

[18] A. Diaz-Bolado and J. Laurin, “Experimental validation of the effect of compression on simplified phantoms in microwave tomography applied to breast cancer detection,” *IEEE Antennas and Wireless Propagation Letters*, vol. 11, pp. 1602–1605, 2012.

[19] P. Mojabi, N. Firoozy, N. Bayat, T. Brown, C. Narendra, P. Mojabi, C. Niu, T. Tiede, T. Neusitzer, X. Li, I. Jeffrey, J. LoVetri, and D. Barber, “Electromagnetic inversion for biomedical imaging, antenna characterization, and

sea ice remote sensing applications," in *2016 URSI Asia-Pacific Radio Science Conference (URSI AP-RASC)*, Aug 2016, pp. 586–589.

[20] P. Mojabi and J. LoVetri, "Ultrasound tomography for simultaneous reconstruction of acoustic density, attenuation, and compressibility profiles," *The Journal of the Acoustical Society of America*, vol. 137, no. 4, 2015.

[21] N. Duric, P. Littrup, L. Poulo, A. Babkin, R. Pevzner, E. Holsapple, O. Rama, and C. Glide, "Detection of breast cancer with ultrasound tomography: First results with the computed ultrasound risk evaluation (cure) prototype," *Medical Physics*, vol. 34, no. 2, pp. 773–785, 2007.

[22] A. Hormati, I. Jovanovic, O. Roy, and M. Vetterli, "Robust ultrasound travel-time tomography using the bent ray model," *Proc. SPIE*, vol. 7629, pp. 76 290I–76 290I–12, 2010.

[23] M. Krueger, A. Pesavento, and H. Ermert, "A modified time-of-flight tomography concept for ultrasonic breast imaging," *IEEE Ultrasonic Symposium*, 1996.

[24] H. Schomberg, "An improved approach to reconstructive ultrasound tomography," *Journal of Physics, Applied Physics*, vol. 11, no. 15, p. L181, 1978.

[25] D. J. Kurrant^{ast}, E. C. Fear, and D. T. Westwick, "Tumor response estimation in radar-based microwave breast cancer detection," *IEEE Transactions on Biomedical Engineering*, vol. 55, no. 12, pp. 2801–2811, Dec 2008.

[26] M. Slaney, A. Kak, and L. Larsen, "Limitations of imaging with first-order diffraction tomography," *Microwave Theory and Techniques, IEEE Transactions on*, vol. 32, no. 8, pp. 860–874, Aug 1984.

[27] T. J. Cui, W. C. Chew, X. X. Yin, and W. Hong, "Study of resolution and super resolution in electromagnetic imaging for half-space problems," *IEEE Transactions on Antennas and Propagation*, vol. 52, no. 6, pp. 1398–1411, June 2004.

[28] P. Mojabi and J. LoVetri, "Evaluation of balanced ultrasound breast imaging under three density profile assumptions," *IEEE Transactions on Computational Imaging*, vol. 3, no. 4, pp. 864–875, Dec 2017.

[29] M. Moghaddam and W. C. Chew, "Simultaneous inversion of compressibility and density in the acoustic inverse problem," *Inverse Problems*, vol. 9, no. 6, pp. 715–730, 1993.

[30] A. J. Hesford and W. C. Chew, "Fast inverse scattering solutions using the distorted Born iterative method and the multilevel fast multipole algorithm,"

The Journal of the Acoustical Society of America, vol. 128, no. 2, pp. 679–690, June 2010.

[31] A. J. Hesford and R. C. Waag, "Reduced-rank approximations to the far-field transform in the gridded fast multipole method," *Journal of Computational Physics*, vol. 230, no. 10, pp. 3656 – 3667, 2011.

[32] T. Tran-Duc, N. Linh-Trung, and M. Do, "Modified Distorted Born Iterative Method for Ultrasound Tomography by Random Sampling," in *Communications and Information Technologies (ISCIT), 2012 International Symposium on*, 2012, pp. 1065–1068.

[33] P. Mojabi, "Ultrasound Tomography: An Inverse Scattering Approach," MSc. dissertation, University of Manitoba, 2014.

[34] R. J. Lavarello and M. L. Oelze, "Density imaging using inverse scattering," *The Journal of the Acoustical Society of America*, vol. 125, no. 2, pp. 793–802, February 2009.

[35] R. Lavarello and M. Oelze, "Two approaches for tomographic density imaging using inverse scattering," in *Ultrasonics Symposium, 2008. IUS 2008. IEEE*, 2008, pp. 1298–1301.

[36] A. J. Hesford and R. C. Waag, "The fast multipole method and Fourier convolution for the solution of acoustic scattering on regular volumetric grids," *Journal of Computational Physics*, vol. 229, pp. 8199–8210, Oct. 2010.

[37] Y. M. Wang and W. C. Chew, "An iterative solution of the two-dimensional electromagnetic inverse scattering problem," *International Journal of Imaging Systems and Technology*, vol. 1, no. 1, pp. 100–108, 1989. [Online]. Available: http://dx.doi.org/10.1002/ima.1850010111

[38] W. Chew and Y. Wang, "Reconstruction of two-dimensional permittivity distribution using the distorted Born iterative method," *IEEE Transactions on Medical Imaging*, vol. 9, no. 2, pp. 218–225, Jun 1990.

[39] R. Lavarello and M. Oelze, "A study on the reconstruction of moderate contrast targets using the distorted Born iterative method," *IEEE Transactions on Ultrasonics, Ferroelectrics and Frequency Control*, vol. 55, no. 1, pp. 112–124, January 2008.

[40] P. M. van den Berg and R. E. Kleinman, "A contrast source inversion method," *Inverse Problems*, vol. 13, no. 6, p. 1607, 1997. [Online]. Available: http://stacks.iop.org/0266-5611/13/i=6/a=013

[41] K. W. A. van Dongen and W. M. D. Wright, “A full vectorial contrast source inversion scheme for three-dimensional acoustic imaging of both compressibility and density profiles,” *The Journal of the Acoustical Society of America*, vol. 121, no. 3, pp. 1538–1549, 2007. [Online]. Available: http://scitation.aip.org/content/asa/journal/jasa/121/3/10.1121/1.2431333

[42] A. Tikhonov and V. Arsenin, *Solutions of ill-posed problems*, ser. Scripta series in mathematics. Winston, 1977.

[43] T. Tran-Duc, N. Linh-Trung, M. L. Oelze, and M. N. Do, “Application of L_1 Regularization for High-Quality Reconstruction of Ultrasound Tomography,” *4th International Conference on Biomedical Engineering in Vietnam*, pp. 309–312, 2013.

[44] S. J. Kim, K. Koh, M. Lustig, S. Boyd, and D. Gorinevsky, “An Interior-Point Method for Large-Scale l_1-Regularized Least Squares,” *Selected Topics in Signal Processing, IEEE Journal on*, vol. 1, no. 4, pp. 606–617, 2007.

[45] A. Abubakar, P. van den Berg, T. Habashy, and H. Braunisch, “A multiplicative regularization approach for deblurring problems,” *Image Processing, IEEE Transactions on*, vol. 13, no. 11, pp. 1524–1532, Nov 2004.

[46] P. M. van den Berg, A. Abubakar, and J. T. Fokkema, “Multiplicative regularization for contrast profile inversion,” *Radio Science*, vol. 38, no. 2, 2003.

[47] P. C. Hansen, *Rank-deficient and Discrete Ill-posed Problems: Numerical Aspects of Linear Inversion*. Philadelphia, PA, USA: Society for Industrial and Applied Mathematics, 1998.

[48] P. Hansen, “The truncated SVD as a method for regularization,” *BIT Numerical Mathematics*, vol. 27, no. 4, pp. 534–553, 1987.

[49] P. M. Meaney, N. K. Yagnamurthy, and K. D. Paulsen, “Pre-scaled two-parameter Gauss Newton image reconstruction to reduce property recovery imbalance,” *Physics in Medicine and Biology*, vol. 47, no. 7, p. 1101, 2002. [Online]. Available: http://stacks.iop.org/0031-9155/47/i=7/a=308

[50] P. Mojabi and J. LoVetri, “A prescaled multiplicative regularized Gauss Newton inversion,” *Antennas and Propagation, IEEE Transactions on*, vol. 59, no. 8, pp. 2954–2963, Aug 2011.

[51] M. Andr, C. Barker, N. Sekhon, J. Wiskin, D. Borup, and K. Callahan, “Pre-clinical experience with full-wave inverse-scattering for breast imaging,” in *Acoustical Imaging*, ser. Acoustical Imaging, I. Akiyama, Ed. Springer Netherlands, 2009, vol. 29, pp. 73–80. [Online]. Available: http://dx.doi.org/10.1007/978-1-4020-8823-0_10

[52] J. Mamou and M. L. Oelze, *Quantitative Ultrasound in soft Tissues.* New York, USA: Springer, 2013.

[53] S. Johnson, T. Abbott, R. Bell, M. Berggren, D. Borup, D. Robinson, J. Wiskin, S. Olsen, and B. Hanover, “Non-invasive breast tissue characterization using ultrasound speed and attenuation,” in *Acoustical Imaging*, ser. Acoustical Imaging. Springer Netherlands, 2007, vol. 28, pp. 147–154. [Online]. Available: http://dx.doi.org/10.1007/1-4020-5721-0_17

[54] J. Camacho, L. Medina, J. Cruza, J. M. Moreno, and C. Fritsch, “Multimodal ultrasonic imaging for breast cancer detection,” *Archives of Acoustics*, vol. 37, no. 3, pp. 253–260, 2012.

[55] M. Prez-Liva, J. L. Herraiz, N. Gonzlez-Salido, L. Medina-Valds, J. Camacho, C. Fritch, and J. M. Udas, “Ultrasound computed tomography for quantitative breast imaging,” *Proc. IEEE Global Medical Engineering Physics Exchanges (GMEPE) & Pan American Health Care Exchanges (PAHCE)*, pp. 1–6, Madrid, Spain, 2016.

[56] N. Gonzlez-Salido, L. Medina, and J. Camacho, “Full Angle Spatial Compound of ARFI images for breast cancer detection,” *Ultrasonics*, vol. 71, no. Supplement C, pp. 161 – 171, 2016. [Online]. Available: http://www.sciencedirect.com/science/article/pii/S0041624X16300877

[57] K. Liu, E. C. Fear, and M. E. Potter, “Antenna aperture localization for arrival time correction using first-break,” vol. 62, pp. 105–120, 01 2015.

[58] J. Wong, L. Han, J. C. Bancroft, and R. R. Stewart, “Automatic time-picking of first arrivals on noisy microseismic data,” *CREWES Research Rep*, vol. 21, no. 30, 2009.

[59] P. Mojabi and J. LoVetri, “Experimental evaluation of composite tissue-type ultrasound and microwave imaging,” *Accepted in IEEE Journal on Multiscale and Multiphysics Computational Techniques*, 2019.

[60] C. Li, L. Huang, N. Duric, H. Zhang, and C. Rowe, “An improved automatic time-of-flight picker for medical ultrasound tomography,” *Ultrasonics*, vol. 49, no. 1, pp. 61 – 72, 2009. [Online]. Available: http://www.sciencedirect.com/science/article/pii/S0041624X08000863

[61] H. Zhang, C. Thurber, and C. Rowe, “Automatic p-wave arrival detection and picking with multiscale wavelet analysis for single-component recordings,” vol. 93, pp. 1904–1912, 10 2003.

[62] S. M. P. Pereira, V. A. McCormack, J. H. Hipwell, C. Record, L. S. Wilkinson, S. M. Moss, D. J. Hawkes, and I. dos Santos-Silva, “Localized fibroglandular tissue as a predictor of future tumor location within the breast,” *Cancer Epidemiology and Prevention Biomarkers*, vol. 20, no. 8, pp. 1718–1725, 2011. [Online]. Available: http://cebp.aacrjournals.org/content/20/8/1718

[63] V. Y. Sohn, Z. M. Arthurs, J. A. Sebesta, and T. A. Brown, “Primary tumor location impacts breast cancer survival,” *The American Journal of Surgery*, vol. 195, no. 5, pp. 641 – 644, 2008, papers from the North Pacific Surgical Association. [Online]. Available: http://www.sciencedirect.com/science/article/pii/S0002961008001025

[64] P. Mojabi and J. LoVetri, “On the potential use of anatomical and epidemiological information to enhance microwave and ultrasound breast imaging,” *2nd URSI AT-RASC*, Gran Canaria, Spain, 2018.

[65] ——, “Simultaneous reconstruction of compressibility and density profiles in multiple frequency acoustic inverse scattering,” in *2013 IEEE Antennas and Propagation Society International Symposium (APSURSI)*, July 2013.

[66] ——, “A fast and efficient MoM forward solver for ultrasound tomography of inhomogeneous compressibility and density profiles,” in *2013 IEEE Antennas and Propagation Society International Symposium (APSURSI)*, July 2013.

[67] M. Moghaddam, W. C. Chew, , and M. Oristaglio, “Comparison of the Born Iterative Method and Tarantola’s Method for an Electromagnetic Time-Domain Inverse Problem,” *International Journal of Imaging Systems and Technology*, vol. 3, no. 4, pp. 318–333, 1991.

[68] P. Mojabi and J. LoVetri, “Comparison of TE and TM Inversions in the Framework of the Gauss-Newton Method,” *Antennas and Propagation, IEEE Transactions on*, vol. 58, no. 4, pp. 1336–1348, 2010.

[69] W. Chew, G. Otto, W. H. W. andJ. H. Lin, and Y. M. Wang, “Nonlinear diffraction tomography the use of inverse scattering for imaging,” *International Journal of Imaging Systems and Technology*, pp. 120–129, 1993.

[70] J. W. Wiskin, D. T. Borup, and S. A. Johnson, “Inverse scattering from arbitrary two-dimensional objects in stratified environments via a Greens operator,” *The Journal of the Acoustical Society of America*, vol. 102, no. 2, 1997.

[71] O. S. Haddadin, S. D. Lucas, and E. S. Ebbini, “Solution to the inverse scattering problem using a modified distorted Born iterative algorithm,” in *1995 IEEE Ultrasonics Symposium. Proceedings. An International Symposium*, vol. 2, Nov 1995, pp. 1411–1414 vol.2.

[72] J. Wiskin, D. T. Borup, S. A. Johnson, and M. Berggren, “Non-linear inverse scattering: High resolution quantitative breast tissue tomography,” *Journal of the Acoustical Society of America*, vol. 131, no. 5, pp. 3802–3813, May 2012.

[73] F. Lin, A. I. Nachman, and R. C. Waag, “Quantitative imaging using a time-domain eigenfunction method,” *The Journal of the Acoustical Society of America*, vol. 108, no. 3, pp. 899–912, September 2000.

[74] T. D. Mast, A. I. Nachman, and R. C. Waag, “Focusing and imaging using eigenfunctions of the scattering operator,” *The Journal of the Acoustical Society of America*, vol. 102, no. 2, pp. 715–725, August 1997.

[75] S. A. Goss, R. L. Johnston, and F. Dunn, “Comprehensive compilation of empirical ultrasonic properties of mammalian tissues,” *The Journal of the Acoustical Society of America*, vol. 64, no. 2, pp. 423–457, August 1978.

[76] E. L. Madsen, W. A. Berg, E. B. Mendelson, and G. R. Frank, “Anthropomorphic Breast Phantoms for Qualification of Investigators for ACRIN Protocol 6666,” *Radiology*, vol. 239, no. 3, pp. 869–874, 2006.

[77] S.-J. Kwon and M.-K. Jeong, “Ultrasound inverse scattering determination of speed of sound, density, and absorption,” in *Ultrasonics Symposium, 1998. Proceedings., 1998 IEEE*, vol. 2, 1998, pp. 1631–1634 vol.2.

[78] R. F. Harrington, *Time-harmonic electromagnetic fields*, ser. IEEE press series on electromagnetic wave theory. Piscataway, NJ: J. Wiley and sons New York Chichester Weinheim, 2001. [Online]. Available: http://opac.inria.fr/record=b1105789

[79] J. Richmond, “Scattering by a dielectric cylinder of arbitrary cross section shape,” *IEEE Transactions on Antennas and Propagation*, vol. 13, no. 3, pp. 334–341, May 1965.

[80] R. F. Harrington, *Field Computation by Moment Methods.* Wiley-IEEE Press, 1993.

[81] L. Jebli, “A comparison of two methods for solving electromagnetic field integral equation,” *International Journal of Differential Equations*, 2011.

[82] M. R. Hestenes and E. Stiefel, “Methods of Conjugate Gradients for Solving Linear Systems,” *Journal of Research of the National Bureau of Standards*, vol. 49, no. 6, pp. 409–436, 1952.

[83] B. E. Barrowes, F. L. Teixeira, and J. A. Kong, "Fast Algorithm for Matrix-Vector Multiply of Asymmetric Multilevel Block-Toeplitz Matrices in 3-D Scattering," *Microwave and Optical Technology Letters*, vol. 31, no. 1, pp. 28–32, 2001.

[84] T. Chan and J. Olkin, "Circulant preconditioners for Toeplitz-block matrices," *Numerical Algorithms*, vol. 6, no. 1, pp. 89–101, 1994.

[85] M. Moghaddam and W. Chew, "Variable density linear acoustic inverse problem," *Ultrasonic Imaging*, vol. 15, no. 3, pp. 255 – 266, 1993.

[86] W. C. Chew, *Waves and Fields in Inhomogeneous Media (Electromagnetic Waves)*. IEEE Computer Society Press, 1995.

[87] J. De Zaeytijd, A. Franchois, C. Eyraud, and J. M. Geffrin, "Full Wave Three-Dimensional Microwave Imaging With a Regularized Gauss Newton Method Theory and Experiment," *Antennas and Propagation, IEEE Transactions on*, vol. 55, no. 11, pp. 3279–3292, Nov 2007.

[88] A. Tijhuis and A. Zwamborn, "Marching on in anything: solving electromagnetic field equations with a varying physical parameter," *Ultra-Wideband, Short-Pulse Electromagnetics*, vol. 5, pp. 655–66, 2002.

[89] A. Tijhuis, K. Belkebir, A. Litman, and B. De Hon, "Theoretical and computational aspects of 2-D inverse profiling," *Geoscience and Remote Sensing, IEEE Transactions on*, vol. 39, no. 6, pp. 1316–1330, Jun 2001.

[90] R. H. Chan and M. K. Ng, "Conjugate Gradient Methods for Toeplitz Systems," *SIAM Review*, vol. 38, no. 3, pp. 427–482, 1996.

[91] J. W. Cooley and J. W. Tukey, "An Algorithm for the Machine Calculation of Complex Fourier Series," *Mathematics of Computation*, vol. 19, no. 90, pp. pp. 297–301, 1965.

[92] P. C. Hansen, "Deconvolution and Regularization with Toeplitz Matrices," *Numerical Algorithms*, vol. 29, pp. 323–378, 2002.

[93] C. Van Loan, *Computational Frameworks for the Fast Fourier Transform*, ser. Frontiers in Applied Mathematics. Society for Industrial and Applied Mathematics, 1992.

[94] M. Moghaddam and W. C. Chew, "Nonlinear two-dimensional velocity profile inversion using time domain data," *IEEE Transactions on Geoscience and Remote Sensing*, vol. 30, no. 1, pp. 147–156, Jan 1992.

[95] P. Hansen, “Regularization tools: A matlab package for analysis and solution of discrete ill-posed problems,” *Numerical Algorithms*, vol. 6, no. 1, pp. 1–35, 1994.

[96] R. Waag and R. Fedewa, “A ring transducer system for medical ultrasound research,” *IEEE Transactions on Ultrasonics, Ferroelectrics and Frequency Control*, vol. 53, no. 10, pp. 1707–1718, October 2006.

[97] L. P. Duric, Neb, S. Schmidt, C. Li, O. Roy, L. Bey-Knight, R. Janer, D. Kunz, X. Chen, J. Goll, A. Wallen, F. Zafar, V. Allada, E. West, I. Jovanovic, K. Li, and W. Greenway, “Breast imaging with the Softvue imaging system: first results,” pp. 86 750K–86 750K–8, 2013.

[98] R. F. Bloemenkamp, A. Abubakar, and P. M. van den Berg, “Inversion of experimental multi-frequency data using the contrast source inversion method,” *Inverse Problems*, vol. 17, no. 6, p. 1611, 2001.

[99] W. Hu, A. Abubakar, and T. M. Habashy, “Simultaneous multifrequency inversion of full-waveform seismic data,” *GEOPHYSICS*, vol. 74, no. 2, pp. R1–R14, 2009. [Online]. Available: http://dx.doi.org/10.1190/1.3073002

[100] E. L. Madsen, M. A. Hobson, G. R. Frank, H. Shi, J. Jiang, T. J. Hall, T. Varghese, M. M. Doyley, and J. B. Weaver, “Anthropomorphic breast phantoms for testing elastography systems,” *Ultrasound in Medicine & Biology*, vol. 32, no. 6, pp. 857 – 874, 2006.

[101] E. L. Madsen, J. A. Zagzebski, and G. R. Frank, “An anthropomorphic ultrasound breast phantom containing intermediate sized scatterers,” *Ultrasound in Medicine and Biology*, vol. 8, no. 4, pp. 381–392, 1982.

[102] J.-H. Lin and W. C. Chew, “Ultrasonic imaging by local shape function method with CGFFT,” *Ultrasonics, Ferroelectrics and Frequency Control, IEEE Transactions on*, vol. 43, no. 5, pp. 956–969, 1996.

[103] T. D. Mast, “Empirical relationships between acoustic parameters in human soft tissues,” *Acoustics Research Letters Online*, vol. 1, no. 2, pp. 37–42, 2000.

[104] W. Chew and J.-H. Lin, “A frequency-hopping approach for microwave imaging of large inhomogeneous bodies,” *Microwave and Guided Wave Letters, IEEE*, vol. 5, no. 12, pp. 439–441, Dec 1995.

[105] O. Haddadin and E. Ebbini, “Imaging strongly scattering media using a multiple frequency distorted born iterative method,” *Ultrasonics, Ferroelectrics and Frequency Control, IEEE Transactions on*, vol. 45, no. 6, pp. 1485–1496, Nov 1998.

[106] E. L. Madsen, J. A. Zagzebski, G. R. Frank, J. F. Greenleaf, and P. L. Carson, "Anthropomorphic breast phantoms for assessing ultrasonic imaging system performance and for training ultrasonographers: Part ii," *Journal of Clinical Ultrasound*, vol. 10, no. 3, pp. 91–100, 1982. [Online]. Available: http://dx.doi.org/10.1002/jcu.1870100302

[107] D. Kurrant and E. Fear, "Regional estimation of the dielectric properties of inhomogeneous objects using near-field reflection data," *Inverse Problems*, vol. 28, no. 7, p. 075001, 2012. [Online]. Available: http://stacks.iop.org/0266-5611/28/i=7/a=075001

[108] H. Azhari, *Basics of Biomedical Ultrasound for Engineers*. Wiley, 2010. [Online]. Available: http://books.google.ca/books?id=FcuauV7dDCoC

[109] A. Abubakar, P. M. van den Berg, and S. Y. Semenov, "A robust iterative method for born inversion," *IEEE Transactions on Geoscience and Remote Sensing*, vol. 42, no. 2, pp. 342–354, Feb 2004.

[110] G. Y. Sandhu, C. Li, O. Roy, S. Schmidt, and N. Duric, "Frequency domain ultrasound waveform tomography: breast imaging using a ring transducer," *Physics in Medicine and Biology*, vol. 60, no. 14, p. 5381, 2015. [Online]. Available: http://stacks.iop.org/0031-9155/60/i=14/a=5381

[111] J. Wiskin, D. Borup, S. Johnson, M. Andre, J. Greenleaf, Y. Parisky, and J. Klock, "Three-dimensional nonlinear inverse scattering: Quantitative transmission algorithms, refraction corrected reflection, scanner design and clinical results," *Proceedings of Meetings on Acoustics*, vol. 19, no. 1, 2013. [Online]. Available: http://scitation.aip.org/content/asa/journal/poma/19/1/10.1121/1.4800267

[112] P. Mojabi and J. LoVetri, "Microwave and ultrasound imaging for biomedical tissue identification," in *Radio Science Meeting (Joint with AP-S Symposium), 2014 USNC-URSI*, July 2014, pp. 56–56.

[113] ——, "Tissue-type imaging using ultrasound tomography," in *2015 IEEE MTT-S International Conference on Numerical Electromagnetic and Multiphysics Modeling and Optimization (NEMO)*, Aug 2015, pp. 1–3.

[114] M. Lazebnik, D. Popovic, L. McCartney, C. B. Watkins, M. J. Lindstrom, J. Harter, S. Sewall, T. Ogilvie, A. Magliocco, T. M. Breslin, W. Temple, D. Mew, J. H. Booske, M. Okoniewski, and S. C. Hagness, "A large-scale study of the ultrawideband microwave dielectric properties of normal, benign and malignant breast tissues obtained from cancer surgeries," *Physics in Medicine and Biology*, vol. 52, no. 20, pp. 6093–6115, 2007.

[115] S. Hagness, A. Taflove, and J. E. Bridges, "Two-Dimensional FDTD analysis of a pulsed microwave confocal system for breast cancer detection: Fixed-focus and antenna-array sensors." *IEEE Transactions on Biomedical Engineering*, vol. 45, no. 12, pp. 1470–1479, 1998.

[116] P. Mojabi and J. LoVetri, "Microwave biomedical imaging using the multiplicative regularized gauss–newton inversion," *IEEE Antennas and Wireless Propagation Letters*, vol. 8, pp. 645–648, 2009.

[117] R. O. Duda, P. E. Hart, and D. G. Stork, *Pattern Classification (2Nd Edition)*. Wiley-Interscience, 2000.

[118] C. Gilmore, P. Mojabi, A. Zakaria, S. Pistorius, and J. LoVetri, "On super-resolution with an experimental microwave tomography system," *IEEE Antennas and Wireless Propagation Letters*, vol. 9, pp. 393–396, 2010.

[119] A. Abubakar, P. M. van den Berg, and T. M. Habashy, "Application of the multiplicative regularized contrast source inversion method on TM- and TE-polarized experimental Fresnel data," *Inverse Problems*, vol. 21, no. 6, p. S5, 2005. [Online]. Available: http://stacks.iop.org/0266-5611/21/i=6/a=S02

[120] E. Kerbrat, C. Prada, D. Cassereau, and M. Fink, "Ultrasonic nondestructive testing of scattering media using the decomposition of the time-reversal operator," *IEEE Transactions on Ultrasonics, Ferroelectrics, and Frequency Control*, vol. 49, no. 8, pp. 1103–1113, Aug 2002.

[121] N. Chakroun, M. A. Fink, and F. Wu, "Time reversal processing in ultrasonic nondestructive testing," *IEEE Transactions on Ultrasonics, Ferroelectrics, and Frequency Control*, vol. 42, no. 6, pp. 1087–1098, Nov 1995.

[122] M. Sak, N. Duric, P. Littrup, L. Bey-Knight, H. Ali, P. Vallieres, M. E. Sherman, and G. L. Gierach, "Using speed of sound imaging to characterize breast density," *Ultrasound in Medicine & Biology*, vol. 43, no. 1, pp. 91 – 103, 2017. [Online]. Available: http://www.sciencedirect.com/science/article/pii/S0301562916302575

[123] H. Gemmeke, T. Hopp, M. Zapf, C. Kaiser, and N. V. Ruiter, "3D ultrasound computer tomography: Hardware setup, reconstruction methods and first clinical results," *Nuclear Instruments and Methods in Physics Research Section A: Accelerators, Spectrometers, Detectors and Associated Equipment*, vol. 873, no. Supplement C, pp. 59 – 65, 2017, imaging 2016. [Online]. Available: http://www.sciencedirect.com/science/article/pii/S0168900217307593

[124] K. Wang, T. Matthews, F. Anis, C. Li, N. Duric, and M. A. Anastasio, "Waveform inversion with source encoding for breast sound speed reconstruction in

ultrasound computed tomography," *IEEE Transactions on Ultrasonics, Ferroelectrics, and Frequency Control*, vol. 62, no. 3, pp. 475–493, March 2015.

[125] P. M. Meaney, M. W. Fanning, D. Li, S. P. Poplack, and K. D. Paulsen, "A clinical prototype for active microwave imaging of the breast," *IEEE Transactions on Microwave Theory and Techniques*, vol. 48, no. 11, pp. 1841–1853, Nov 2000.

[126] L. M. Neira, B. D. V. Veen, and S. C. Hagness, "High-resolution microwave breast imaging using a 3-D inverse scattering algorithm with a variable-strength spatial prior constraint," *IEEE Transactions on Antennas and Propagation*, vol. 65, no. 11, pp. 6002–6014, Nov 2017.

[127] Q. H. Liu, Z. Q. Zhang, T. T. Wang, J. A. Bryan, G. A. Ybarra, L. W. Nolte, and W. T. Joines, "Active microwave imaging. i. 2-D forward and inverse scattering methods," *IEEE Transactions on Microwave Theory and Techniques*, vol. 50, no. 1, pp. 123–133, Jan 2002.

[128] M. Omer, P. Mojabi, D. J. Kurrant, J. LoVetri, and E. Fear, "Proof-of-concept of the incorporation of ultrasound-derived structural information into microwave radar imaging," *IEEE Journal on Multiscale and Multiphysics Computational Techniques*, vol. 3, pp. 129–139, 2018.

[129] N. Ozmen, R. Dapp, M. Zapf, H. Gemmeke, N. V. Ruiter, and K. W. A. van Dongen, "Comparing different ultrasound imaging methods for breast cancer detection," *IEEE Transactions on Ultrasonics, Ferroelectrics, and Frequency Control*, vol. 62, no. 4, pp. 637–646, April 2015.

[130] P. Kosmas and C. M. Rappaport, "Time reversal with the FDTD method for microwave breast cancer detection," *IEEE Transactions on Microwave Theory and Techniques*, vol. 53, no. 7, pp. 2317–2323, July 2005.

[131] N. K. Nikolova, *Introduction to Microwave Imaging*, ser. EuMA High Frequency Technologies Series. Cambridge University Press, 2017.

[132] M. Pastorino, *Microwave Imaging*, ser. Wiley Series in Microwave and Optical Engineering. Wiley, 2010.

[133] D. OLoughlin, B. L. Oliveira, A. Santorelli, E. Porter, M. Glavin, E. Jones, M. Popovic, and M. OHalloran, "Sensitivity and specificity estimation using patient-specific microwave imaging in diverse experimental breast phantoms," *IEEE Transactions on Medical Imaging*, pp. 1–1, 2018.

[134] R. C. Waag, F. Lin, T. K. Varslot, and J. P. Astheimer, "An eigenfunction method for reconstruction of large-scale and high-contrast objects," *IEEE*

Transactions on Ultrasonics, Ferroelectrics, and Frequency Control, vol. 54, no. 7, pp. 1316–1332, July 2007.

[135] M. Ostadrahimi, P. Mojabi, C. Gilmore, A. Zakaria, S. Noghanian, S. Pistorius, and J. LoVetri, "Analysis of incident field modeling and incident/scattered field calibration techniques in microwave tomography," *IEEE Antennas and Wireless Propagation Letters*, vol. 10, pp. 900–903, 2011.

[136] A. Abubakar, T. M. Habashy, V. L. Druskin, L. Knizhnerman, and D. Alumbaugh, "2.5D forward and inverse modeling for interpreting low-frequency electromagnetic measurements 2.5D modeling for low-frequency em," *Geophysics*, vol. 73, no. 4, p. F165, 2008.

[137] M. J. Burfeindt, T. J. Colgan, R. O. Mays, J. D. Shea, N. Behdad, B. D. V. Veen, and S. C. Hagness, "MRI-Derived 3D-printed breast phantom for microwave breast imaging validation," *IEEE Antennas and Wireless Propagation Letters*, vol. 11, pp. 1610–1613, 2012.

[138] M. Omer and E. C. Fear, "Automated 3D method for the construction of flexible and reconfigurable numerical breast models from MRI scans," *Medical & Biological Engineering & Computing*, vol. 56, no. 6, pp. 1027–1040, Jun 2018. [Online]. Available: https://doi.org/10.1007/s11517-017-1740-9

[139] ——, "Anthropomorphic breast model repository for research and development of microwave breast imaging technologies," *Scientific Data*, 2018.

[140] H. Jiang, C. Li, D. Pearlstone, and L. Fajardo, "Ultrasound-guided microwave imaging of breast cancer: Tissue phantom and pilot clinical experiments," vol. 32, pp. 2528–35, 09 2005.

[141] E. J. Feleppa, S. Dasgupta, A. Kalisz, J. Ketterling, S. Ramachandran, C. R. Porter, M. Lacrampe, D. Dail, D. Sparks, and F. Arias-Mendosa, "New developments in tissue-type imaging (TTI) of prostate cancer: combined ultrasonic and magnetic-resonance methods," in *IEEE Ultrasonics Symposium, 2005.*, vol. 2, Sept 2005, pp. 831–834.

[142] B. Malik, J. Klock, J. Wiskin, and M. Lenox, "Objective breast tissue image classification using quantitative transmission ultrasound tomography," *Scientific Reports*, vol. 6, pp. 1–8, 2016.

[143] N. V. Ruiter, M. Zapf, T. Hopp, H. Gemmeke, and K. W. A. van Dongen, "USCT data challenge," pp. 10 139 − 10 139 − 8, 2017. [Online]. Available: https://doi.org/10.1117/12.2272593

[144] 2D CSIC/UCM USCT data set. [Online]. Available: http://ipeusctdb1.ipe.kit.edu/~usct/challenge/?page_id=183

[145] E. Iuanow, K. Smith, N. A. Obuchowski, J. Bullen, and J. C. Klock, “Accuracy of cyst versus solid diagnosis in the breast using quantitative transmission (QT) ultrasound,” *Academic Radiology*, vol. 24, no. 9, pp. 1148 – 1153, 2017. [Online]. Available: http://www.sciencedirect.com/science/article/pii/S1076633217302076

[146] F. Foote and F. Stewart, “Comparative studies of cancerous versus noncancerous breasts,” *Annals of surgery*, vol. 121, no. 2, pp. 197–222, February 1945.

[147] M.-H. Hung, C.-Y. Liu, C.-Y. Shiau, C.-Y. Hsu, Y.-F. Tsai, Y.-L. Wang, L.-C. Tai, K.-L. King, T.-C. Chao, J.-H. Chiu, C.-H. Su, S.-S. Lo, C.-H. Tzeng, Y.-M. Shyr, and L.-M. Tseng, “Effect of age and biological subtype on the risk and timing of brain metastasis in breast cancer patients,” *PLOS ONE*, vol. 9, no. 2, pp. 1–8, 02 2014. [Online]. Available: https://doi.org/10.1371/journal.pone.0089389

[148] M. O. Culjat, D. Goldenberg, P. Tewari, and R. S. Singh, “A review of tissue substitutes for ultrasound imaging,” *Ultrasound in Medicine & Biology*, vol. 36, no. 6, pp. 861 – 873, 2010. [Online]. Available: http://www.sciencedirect.com/science/article/pii/S030156291000075X

[149] G. Boverman, C. E. L. Davis, S. D. Geimer, and P. M. Meaney, “Image registration for microwave tomography of the breast using priors from nonsimultaneous previous magnetic resonance images,” *IEEE Journal of Electromagnetics, RF and Microwaves in Medicine and Biology*, vol. 2, no. 1, pp. 2–9, March 2018.

[150] X. Song, M. Li, F. Yang, S. Xu, and A. Abubakar, “Feasibility study of acoustic imaging for human thorax using an acoustic contrast source inversion algorithm,” *The Journal of the Acoustical Society of America*, vol. 144, no. 5, pp. 2782–2792, 2018. [Online]. Available: https://doi.org/10.1121/1.5078590

[151] L. Lin, P. Hu, J. Shi, C. M. Appleton, K. Maslov, L. Li, R. Zhang, and L. V. Wang, “Single-breath-hold photoacoustic computed tomography of the breast,” *Nature Communications*, vol. 9, pp. 1–9, 2018. [Online]. Available: https://doi.org/10.1038/s41467-018-04576-z

[152] L. V. Wang, “Tutorial on photoacoustic microscopy and computed tomography,” *IEEE Journal of Selected Topics in Quantum Electronics*, vol. 14, no. 1, pp. 171–179, Jan 2008.

[153] X. Jin and L. V. Wang, “Thermoacoustic tomography with correction for acoustic speed variations,” *Physics in Medicine & Biology*, vol. 51, no. 24, p. 6437, 2006. [Online]. Available: http://stacks.iop.org/0031-9155/51/i=24/a=010

[154] M. Pramanik, G. Ku, C. li, and L. V Wang, “Design and evaluation of a novel breast cancer detection system combining both thermoacoustic (ta) and photoacoustic (pa) tomography,” *Medical physics*, vol. 35, pp. 2218–23, 06 2008.

[155] G. Faucher, “Calibration of an ultrasound tomography system for medical imaging with 2D Contrast-Source Inversion,” MSc. dissertation, 2013.

[156] C. Kumaragamage and P. Oramasionwu, “Design of an ultrasound tomography system for breast cancer imaging.” University of Manitoba, Tech. Rep, 2010.

[157] P. Mojabi and J. LoVetri, “Development of an ultrasound tomography system: Preliminary results,” *The Journal of the Acoustical Society of America*, vol. 140, no. 4, pp. 3419–3419, Honolulu, USA, 2016. [Online]. Available: http://dx.doi.org/10.1121/1.4970994

[158] ——, “Experimental reconstruction of sound speed and attenuation profiles,” *176th Meeting Acoustical Society of America, Victoria, BC, Canada*, 2018.

[159] K. W. Cheung and H. C. So, “A multidimensional scaling framework for mobile location using time-of-arrival measurements,” *IEEE Transactions on Signal Processing*, vol. 53, no. 2, pp. 460–470, Feb 2005.

[160] J. Lubbers and R. Graaff, “A simple and accurate formula for the sound velocity in water,” *Ultrasound in Medicine & Biology*, vol. 24, no. 7, pp. 1065 – 1068, 1998. [Online]. Available: http://www.sciencedirect.com/science/article/pii/S030156299800091X

[161] F. Simonetti, L. Huang, and N. Duric, “On the spatial sampling of wave fields with circular ring apertures,” *Journal of Applied Physics*, vol. 101, no. 8, p. 083103, 2007. [Online]. Available: http://dx.doi.org/10.1063/1.2717086

[162] J. I. Sabbione and D. Velis, “Automatic first-breaks picking: New strategies and algorithms,” *Geophysics*, vol. 75, no. 4, pp. V67–V76, 2010.

[163] T. D. Dorney, J. L. Johnson, J. V. Rudd, R. G. Baraniuk, W. W. Symes, and D. M. Mittleman, “Terahertz reflection imaging using kirchhoff migration,” *Opt. Lett.*, vol. 26, no. 19, pp. 1513–1515, Oct 2001. [Online]. Available: http://ol.osa.org/abstract.cfm?URI=ol-26-19-1513

[164] N. F. Boyd, H. Guo, L. J. Martin, L. Sun, J. Stone, E. Fishell, R. A. Jong, G. Hislop, A. Chiarelli, S. Minkin, and M. J. Yaffe, “Mammographic density and the risk and detection of breast cancer,” *New England Journal of Medicine*, vol. 356, no. 3, pp. 227–236, 2007, pMID: 17229950. [Online]. Available: https://doi.org/10.1056/NEJMoa062790

[165] “Non-cancerous breast conditions,” *American Cancer Society*.

[166] S. Chan, J.-H. Chen, S. Li, R. Chang, D.-C. Yeh, R.-F. Chang, L.-R. Yeh, J. Kwong, and M.-Y. Su, "Evaluation of the association between quantitative mammographic density and breast cancer occurred in different quadrants," *BMC Cancer*, vol. 17, no. 1, p. 274, Apr 2017. [Online]. Available: https://doi.org/10.1186/s12885-017-3270-0

[167] P. D. Darbre, "Recorded quadrant incidence of female breast cancer in great britain suggests a disproportionate increase in the upper outer quadrant of the breast," vol. 25, pp. 2543–50, 05 2005.